

# Tuning the plasmonic properties of metals by alloying - a computational study

---

**Bubaš, Matej**

**Doctoral thesis / Doktorski rad**

**2024**

*Degree Grantor / Ustanova koja je dodijelila akademski / stručni stupanj:* **University of Zagreb, Faculty of Science / Sveučilište u Zagrebu, Prirodoslovno-matematički fakultet**

*Permanent link / Trajna poveznica:* <https://um.nsk.hr/um:nbn:hr:217:753225>

*Rights / Prava:* [In copyright](#)/[Zaštićeno autorskim pravom.](#)

*Download date / Datum preuzimanja:* **2024-10-07**



*Repository / Repozitorij:*

[Repository of the Faculty of Science - University of Zagreb](#)





University of Zagreb  
FACULTY OF SCIENCE

Matej Bubaš

**TUNING THE PLASMONIC PROPERTIES OF  
METALS BY ALLOYING: A COMPUTATIONAL  
STUDY**

DOCTORAL DISSERTATION

Supervisor:  
Jordi Sancho Parramon

Zagreb, 2024





Sveučilište u Zagrebu  
PRIRODOSLOVNO-MATEMATIČKI FAKULTET

Matej Bubaš

**UGAĐANJE PLAZMONIČKIH SVOJSTAVA METALA  
LEGIRANJEM – RAČUNALNO ISTRAŽIVANJE**

DOKTORSKI RAD

Mentor:  
Jordi Sancho Parramon

Zagreb, 2024





This doctoral dissertation was made in the Laboratory of optics and optical thin films, Department of materials physics, Ruđer Bošković Institute under the supervision of dr. sc. Jordi Sancho Parramon, scientific advisor. The dissertation was made as a part of the Chemistry doctoral study course, field of Physical chemistry, at the the Department of Chemistry, Faculty of Science, University of Zagreb. The research was conducted as a part of two projects by Croatian science foundation: Plasmonic alternative materials for solar energy conversion (PKP-2016-06-4469) and Metal composites for ultrathin infrared coatings (IP-2019-04-5424).



## Acknowledgements

During the course of my doctoral studies and the making of this work, many people had an immediate positive impact that helped bring it to the finish line. However, due to the influence some teachers and professors had on the trajectory of my life, I would like to mention them too and start chronologically.

Big thanks to teacher Marčec and teacher Sukner for instilling in me an interest and love for natural sciences which directed me toward exploring them even since primary school. This continued in high school through positive influence of professor Kučak, professor Meštrovic, professor Vidović and professor Čoh.

Among many people who were a positive influence at the Faculty of Science, without a doubt the biggest contribution comes from both a mentor and a friend, Igor Rončević. I am very happy that I had, and still have to this day, the pleasure of collaborating with him.

I would also like to thank my peers and friends. There are a couple of them from the university I absolutely have to mention. I really could not have made it without them. The warmest thanks go to Špaco, Friga, Zlatan and Sović for being there when times were good, in times of need, and also when it was time to party. Special thanks go to Jura who has not only been a great friend but played a crucial role during my undergraduate, graduate and doctoral studies: Just as Virgil guided Dante through Inferno, so did Jura guide me through various administrative conundrums of academia and beyond.

Furthermore, I am pleased to say that, although the food at the canteen and the coffee at the machine were sometimes dubious, there was no doubt regarding the quality of the company during lunch and coffee breaks. Besides some friends I already mentioned, big thanks to Glo, Popov, Ivana L., Robić, Dunatov, Mia, Ena, Antun and Ana for fun and laughs, and for making lunch breaks much more than just ingesting sustenance.

I am also thankful to my former roommates and dear friends, especially these two: Thanks to Danijel for a lot of things, one being the captivating conversations in which he explained to me the wonders of theoretical physics. Also thanks to Matko, who showed me what science is really about by performing some inspired experiments using our kitchen microwave. I will never forget the results.

I tip my hat to several wonderful companions who have been with me on this journey. Mostly the members of the fellowship of Kajgana, and some others: Bibi, Žulić, Dara, Dusp, Antolko, Ruža, Dora, Nina, Bađ, Geč, Lorena, Lovro, Turk, Tomin and Konjić.

As for the lab at the institute, I really can say that I enjoyed coming to work because I would get to spend time with these people. Big thanks to Boris, Elizabeth and Petar for being true friends and for all the fun times we had both work and non-work related. Thanks to Vesna B.B. Selvi and Ivana F. for being almost like big sisters to me and looking out for me. Thanks to Vesna J. and Stefano for being wonderful senior colleagues to whom I could always turn for a helpful advice. I would also like to express my appreciation to newer colleagues, Isuf, Nirmala and Hrishikesh for interesting discussions and being a great company for this last year I spent at the institute. Lastly, I am truly thankful to Jordi. Jordi is one of the warmest people I have ever met and an exceptional mentor. I am grateful for all that I learned from him, for all the opportunities he opened for me, and for being such a kind person.

Finally, my deepest thanks to my mom, dad, and sister for all their love, support and encouragement.



## Table of contents

SAŽETAK.....	XI
ABSTRACT .....	XIII
PROŠIRENI SAŽETAK.....	XV
<b>§ 1. INTRODUCTION .....</b>	<b>1</b>
<b>§ 2. THEORETICAL BASIS .....</b>	<b>5</b>
<b>2.1. From orbitals to bands – band structure and density of states .....</b>	<b>5</b>
<b>2.2. Dielectric function .....</b>	<b>12</b>
<b>2.3. Density functional theory .....</b>	<b>15</b>
2.3.1. <i>Exchange correlation functionals and the derivative discontinuity.....</i>	<i>16</i>
2.3.2. <i>Calculations involving extended systems and the PAW method .....</i>	<i>18</i>
2.3.3. <i>Linear dielectric response time-dependent DFT and the dielectric function calculation.....</i>	<i>20</i>
<b>2.4. Electrodynamics calculations.....</b>	<b>21</b>
<b>§ 3. LITERATURE REVIEW .....</b>	<b>23</b>
<b>3.1. Plasmonic properties and their utilizations .....</b>	<b>23</b>
<b>3.2. Plasmonic properties tuning.....</b>	<b>26</b>
3.2.1. <i>Tuning by changing the size of the nanoparticle.....</i>	<i>27</i>
3.2.2. <i>Tuning by changing the shape of the nanoparticle .....</i>	<i>28</i>
3.2.3. <i>Tuning by changing the interparticle distance.....</i>	<i>28</i>
3.2.4. <i>Tuning by changing the refractive index of the environment.....</i>	<i>29</i>
3.2.5. <i>Tuning by changing the nanoparticle material .....</i>	<i>30</i>
<b>3.3. Use of DFT in plasmonics .....</b>	<b>31</b>
3.3.1. <i>Comparing the computational approaches.....</i>	<i>31</i>
3.3.2. <i>Choice of the exchange-correlation functional.....</i>	<i>34</i>
3.3.3. <i>Modeling metal alloys by DFT.....</i>	<i>39</i>
3.3.4. <i>Modeling intermetallics .....</i>	<i>40</i>
3.3.5. <i>Effects of configuration/disorder influence.....</i>	<i>44</i>
3.3.6. <i>Calculating hot carrier properties by DFT.....</i>	<i>50</i>
<b>§ 4. COMPUTATIONAL METHODS.....</b>	<b>54</b>
<b>4.1. Establishing a computational framework for optical and plasmonic properties calculation .....</b>	<b>54</b>
4.1.1. <i>The choice of the method .....</i>	<i>54</i>
4.1.2. <i>The choice of alloy systems.....</i>	<i>54</i>
4.1.3. <i>Structure optimization.....</i>	<i>55</i>

4.1.4. Density of states calculations.....	56
4.1.5. Band structure calculations .....	56
4.1.6. Dielectric function calculations .....	57
4.1.7. Electrodynamics simulations .....	57
<b>4.2. Hot carrier generation .....</b>	<b>58</b>
4.2.1. Unit cell optimization.....	58
4.2.2. Density of states calculations.....	59
4.2.3. Hot carrier energy distribution calculations .....	59
<b>§ 5. RESULTS AND DISCUSSION .....</b>	<b>61</b>
<b>5.1. Structure optimization.....</b>	<b>61</b>
<b>5.2. Establishing a computational framework for optical and plasmonic properties prediction.....</b>	<b>63</b>
5.2.1. Choice of the scattering rate .....	63
5.2.2. Choice of the optimal functional .....	63
5.2.3. DFT+U and derivative discontinuity.....	68
5.2.4. Alloy dielectric function calculation .....	70
5.2.5. Resolving interband and intraband contributions to the dielectric function: emergence of low energy interband transitions .....	74
5.2.6. Configuration influence on the dielectric function of alloys.....	81
5.2.7. Electrodynamics simulations of alloy plasmonic properties.....	86
<b>5.3. Elucidating a structure-property relationship .....</b>	<b>94</b>
5.3.1. Band structure calculations .....	94
5.3.2. Density of states calculations.....	100
<b>5.4. Influence of alloying on hot carrier generation .....</b>	<b>108</b>
5.4.1. Comparison of the DOS and the JDOS-based approach.....	108
5.4.2. Influence of unit cell configuration and disorder modeling.....	112
5.4.3. Effects of combining closed d-shell elements on hot carrier distribution.....	113
5.4.4. Effects of combining open and closed d-shell elements on hot carrier distribution .....	118
5.4.5. Effects of combining s-block and closed d-shell elements on hot carrier distribution .....	120
5.4.6. Effects of combining p-block and closed d-shell elements on hot carrier distribution .....	124
5.4.7. Effects of combining p-block and open d-shell elements on hot carrier distribution .....	126
<b>§ 6. CONCLUSION .....</b>	<b>128</b>
<b>§ 7. LIST OF ABBREVIATIONS .....</b>	<b>131</b>
<b>§ 8. REFERENCES.....</b>	<b>132</b>
<b>§ 9. APPENDIX.....</b>	<b>XXXVII</b>
<b>§ 10. CURRICULUM VITAE.....</b>	<b>LXIX</b>



Sveučilište u Zagrebu  
Prirodoslovno-matematički fakultet  
**Kemijski odsjek**

Doktorska disertacija

## SAŽETAK

### UGAĐANJE PLAZMONIČKIH SVOJSTAVA METALA LEGIRANJEM – RAČUNALNO ISTRAŽIVANJE

Matej Bubaš  
Bijenička cesta 54

Legiranje je potencijalno veoma učinkovit način ugađanja plazmoničkih svojstava metala u svrhu optimizacije za željenu funkciju. Metode temeljene na DFT-u imaju velik potencijal za proučavanje povezanosti strukture i svojstava legura jer omogućuju predviđanje svojstava i daju uvid u fundamentalna svojstva tvari čime produbljuju razumijevanje ovisnosti svojstava o strukturi. U ovom radu predstavljen je računalni okvir prilagođen učinkovitoj provedbi velikog broja računa te je GLLB-SC funkcional predstavljen kao opcija superiorna standardno korištenim GGA funkcionalima. Stvorena je baza predviđenih optičkih svojstava binarnih legura, opaženi trendovi su objašnjeni na temelju promjena u elektronskoj strukturi, te su istaknuta emergentna svojstva legiranja. Predstavljena je i metoda za računanje distribucije energija vrućih nosioca naboja, a dobiveni rezultati objašnjeni su na temelju elektronske strukture legura. Dobivene spoznaje daju temelj za racionalni inženjering distribucije energija vrućih nosioca naboja.

(138 stranica, 74 slike, 2 tablice, 185 literaturnih navoda, jezik izvornika: engleski)

Rad je pohranjen u Središnjoj kemijskoj knjižnici, Horvatovac 102a, Zagreb i Nacionalnoj i sveučilišnoj knjižnici, Hrvatske bratske zajednice 4, Zagreb.

Ključne riječi: DFT/ legure/ dielektrična funkcija/ gustoća stanja/ struktura elektronskih vrpaci/ vrući nosioci naboja

Mentor: dr. sc. Jordi Sancho Parramon

Rad prihvaćen: 03. 07. 2024.

Ocjenitelji: 1. prof. dr. sc. Višnja Vrdoljak  
2. dr. sc. Ivor Lončarić, v. zn. sur.  
3. dr. sc. Vito Despoja, v. zn. savj.







University of Zagreb  
Faculty of Science  
**Department of Chemistry**

Doctoral Thesis

## ABSTRACT

### TUNING THE PLASMONIC PROPERTIES OF METALS BY ALLOYING: A COMPUTATIONAL STUDY

Matej Bubaš  
Bijenička cesta 54

Alloying is a potentially very effective way of tuning the plasmonic properties by optimizing them for desired purposes. Methods based on DFT have a great potential for studying the connection between structure and properties of alloys because they enable prediction of properties and provide insight into the fundamental nature of materials thus enabling understanding of the structure-properties dependence. In this paper, a computational framework suitable for efficiently performing a large number of calculations is presented, and the GLLB-SC functional is highlighted as a superior option to standard GGA functionals. A database of predicted optical properties was created, trends were explained on based on the electronic structure changes, and emergent properties of alloys were highlighted. A method for calculating energy distribution of hot carriers is also presented, and the results are explained based on the electronic structure of alloys. These insights enable rational engineering of hot carrier energy distribution.

(138 pages, 74 figures, 2 tables, 185 references, original in english)

Thesis deposited in Central Chemical Library, Horvatovac 102A, Zagreb, Croatia and National and University Library, Hrvatske bratske zajednice 4, Zagreb, Croatia.

Keywords: DFT/ alloys/ dielectric function/ density of states/band structure/ hot carriers

Supervisor: dr. Jordi Sancho Parramon

Thesis accepted: 03. 07. 2024.

Reviewers:

1. prof. dr. sc. Višnja Vrdoljak
2. dr. sc. Ivor Lončarić, Senior research associate
3. Vito Despoja, Senior scientist





Sveučilište u Zagrebu  
Prirodoslovno-matematički fakultet  
**Kemijski odsjek**

Doktorska disertacija

## PROŠIRENI SAŽETAK

### 1. Uvod

S intenziviranjem proučavanja nanočestica i drugih nanostrukture znanstveno polje plazmonike ponovno je dobilo na važnosti. Napredak na području plazmonike tekao je u dva vala: U prvom valu plazmoničke su se nanočestice upotrebljavale za manipulaciju svjetlosne energije na način da se svjetlo usmjerava i fokusira na skali manjoj od valne duljine svjetla. Barijera na koju je naletio prvi val bili su optički gubici u materijalima koji su vodili do (neželjene) transformacije svjetlosne energije u druge tipove energije [S. V. Boriskina, T. A. Cooper, L. Zeng, G. Ni, J. K. Tong, Y. Tsurimaki, Y. Huang, L. Meroueh, G. Mahan i Gang Chen, *Advances in Optics and Photonics* **9** (2017) 775-827]. U drugom valu optički gubici su prihvaćeni te je znanstvena zajednica krenula s proučavanjem uporaba pretvorbe svjetlosne energije. Transformacija energije događa se kada plazmoni koji su pobuđeni svjetlom raspadaju. Pritom nastaju takozvani “vrući” nosioci naboja - elektroni i šupljine visoke energije - koji tu energiju mogu predati molekulama u okolini ili poluvodičima [Y. Hattori, J. Meng, K. Zheng, A. M. de Andrade, J. Kullgren, P. Broqvist, P. Nordlander i J. Sá, *Nano Letters* **21** (2021) 1083-1089]. Alternativno, energiju predaju drugim nosiocima naboja u čestici i naposljetku atomima u rešetci što dovodi do pretvorbe u toplinsku energiju [M. L. Brogersma, N. J. Halas i P. Nordlander, *Nature Nanotechnology* **10** (2015) 25-34]. Kako bi se postigla željena transformacija, svojstva nanostrukture potrebno je prilagoditi i optimizirati. To je moguće postići promjenom veličine i oblika nanočestica te njihove međusobne udaljenosti. Također, svojstva im se mogu podešavati odabirom materijala od kojeg su sačinjene. Najčešće korišteni materijali su metali poput zlata, srebra, bakra i aluminijska. Moguće je koristiti i druge metale no njihova svojstva najčešće su inferiorna navedenim dobrim plazmoničkim metalima što ograničava prilagodbu svojstava za željene svrhe.

---

Legiranje metala stoga se nameće kao zanimljiv način ugađanja plazmoničkih svojstava budući da omogućuje stvaranje kombinacija raznih metala u različitim omjerima. Zbog velikog broja kombinacija metala koje je potrebno istražiti kako bi se pronašla ona s najboljom funkcijom postoji potreba za računalnom metodom koja bi omogućila predviđanje svojstava i uz to pružala uvid u fundamentalnu povezanost strukture i svojstava tvari. Računalne metode temeljene na teoriji funkcionala gustoće (engl. *density functional theory*, *DFT*) potencijalno zadovoljavaju oba zahtjeva no njihova točnost, preciznost i računalna zahtjevnost drastično varira ovisno o odabiru parametara.

Stoga je glavni cilj ove disertacije uspostaviti računalni okvir temeljen na DFT računima koji pruža zadovoljavajuću kombinaciju točnosti i učinkovitosti. Pritom se pretpostavlja da je moguće pronaći pristup približno jednake računalne zahtjevnosti, uz veću točnost nego što to imaju trenutačno najčešće korišteni pristupi. Drugi cilj je dobiti odnos strukture i svojstava stvaranjem baze podataka predviđenih optičkih svojstava za legirane nanostrukture s različitim omjerima metala. Prateća je hipoteza da se evolucija optičkih svojstava u ovisnosti o sastavu može objasniti povezivanjem sastava, elektronske strukture i dielektrične funkcije. Zadnji je cilj ovog rada predstaviti metodu koja omogućava striktno i učinkovito predviđanje stvaranja vrućih nosioca naboja u legurama i proučiti utjecaj različitih elemenata uz hipotezu da se legiranjem može ugađati distribucija vrućih nosioca naboja.

## 2. Teorijska osnovica

Budući da neki od koncepata kojima se barata u okviru ovog rada nisu često korišteni u kemiji, pobliže su pojašnjeni u teorijskoj osnovici pri čemu je cilj intuitivno ih približiti i povezati sa standardnim konceptima u kemiji.

Jedan od tih koncepata je struktura elektronskih vrpce koja se standardno koristi u znanosti o materijalima i u fizici za proučavanje tvari u čvrstom stanju, pogotovo onih koje imaju kristalnu strukturu i sastoje se od mnogo atoma. Način na koji se elektronska struktura u kemiji proučava - uglavnom iz perspektive nekolicine atoma - može se povezati sa strukturom elektronske vrpce preko teorije molekularnih orbitala. U toj teoriji atomske orbitale nekolicine atoma zajedno tvore molekularnu orbitalu delokaliziranu preko dijela ili cijele molekule. Najjednostavniji način da se ta poveznica predstavi je da se zamisli slučaj (gotovo) beskonačnog jednodimenzionalnog lanca vodikovih atoma s pripadnim s orbitalama. Kada bi sve orbitale imale isti predznak, molekularna orbitala koju tvore imala bi potpuno

---

vezni karakter. Suprotno tome, kada bi se sa svakim sljedećim atomom predznak orbitale mijenjao rezultatna molekularna orbitala bila bi potpuno protuvezna. Promjena predznaka čija je periodičnost između te dvije krajnosti (nikada i sa svakim sljedećim atomom) vodila bi do postupnog povećanja energije od potpuno veznog do potpuno protuveznog stanja. Stoga se može reći da set energijski iznimno bliskih stanja u tom rasponu energija tvore vrpce. Na nekim dijelovima raspona energija stanja polagano varira te se, po jedinici enegije, tamo nalazi više stanja nego na dijelovima gdje energija stanja brže varira; drugim riječima, na nekim su dijelovima raspona energije stanja „gušća“, te je za proučavanje varijacije energije vrpce koristan koncept gustoće stanja.

Dielektrična je funkcija još jedan od koncepata koji su često korišteni u fizici čvrstog stanja. To je kompleksna frekventno ovisna funkcija elektromagnetskog polja koje djeluje na materijal. Realni je dio povezan s polarizacijom materijala uslijed vanjske perturbacije električnog polja, dok je imaginarni dio povezan sa slabljenjem elektromagnetskog vala u materijalu i optičkim gubicima. Dielektričnu funkciju metala karakteriziraju dva doprinosa: doprinos unutarvrpčanih prijelaza za koje su uglavnom zaslužni slobodni elektroni u vodljivoj vrpce i doprinos međuvrpčanih prijelaza pri čemu se elektroni koji su najčešće lokalizirani pobuđuju u više energijsko stanje.

Proučavanje tih koncepata teorijom funkcionala gustoće zahtjeva pridavanje posebne pažnje funkcionalu izmjene i korelacije. Pritom jedan od najvećih problema proizlazi iz toga što lokalni i semilokalni funkcionali pogrešno opisuju ovisnost ukupne energije sustava o broju elektrona u sustavu [P. Borlido, T. Aull, A. W. Huran, F. Tran, M. A. L. Marques i S. Botti, *Journal of Chemical Theory and Computation* **15** (2019) 5069-5079]. Takvi funkcionali nemaju diskontinuitet derivacije ukupne energije kod cijelog broja elektrona što dovodi do pogrešne procjene energije pobude elektrona u viša energijska stanja [J. P. Perdew i M. Levy, *Physical Review Letters* **51** (1983) 1884-1887].

Korištenje teorije funkcionala gustoće za račune vezane uz sustave u čvrstom stanju uključuje opis sustava u blizini atoma gdje valna funkcija brzo oscilira i nije osjetljiva na okolinu te u prostoru između atoma u kojem je valna funkcija relativno glatka i sporo se mijenja pa je vrlo osjetljiva na promjenu okoline. *Projector augmented wave* (PAW) metoda prilagođena je upravo takvim sustavima [P. E. Blöchl, C. J. Först i J. Schimpl, *Bulletin of Materials Science*, **26** (2006) 33-41]. U toj se metodi valna funkcija dijeli na prostor unutar sfere u blizini atomske jezgre i prostor van sfere. Zamjenom prave valne funkcije valnom

---

funkcijom koja je glatka na cijelom prostoru (i unutar sfere), a jednaka pravoj valnoj funkciji van sfere, omogućava se učinkovita provedba računa. Istovremeno, prava se valna funkcija može po potrebi reproducirati i unutar sfere što osigurava fleksibilnost PAW metode.

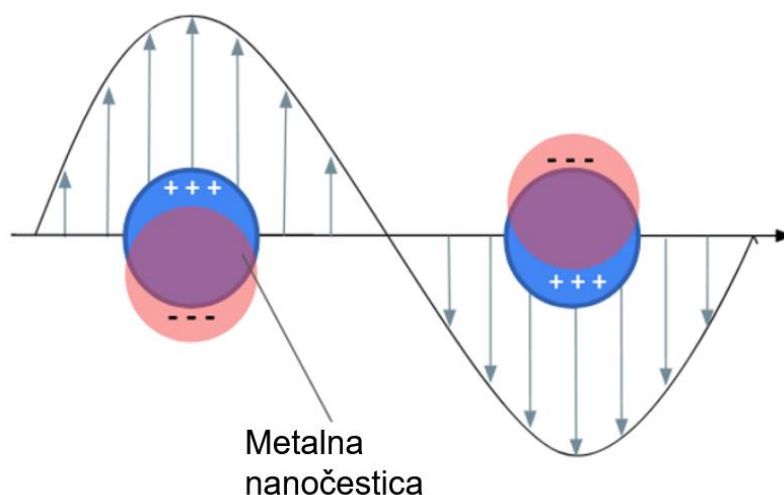
Računanje dielektrične funkcije teorijom funkcionala gustoće zahtjevalo bi proučavanje odaziva materijala na vanjsku perturbaciju elektromagnetskim valom, to jest, implicira potrebu za zahtjevnim računima koji uključuju vremensku ovisnost. No, ako je perturbacija dovoljno slaba, potrebno je uzeti samo prvi, linearni član ekspanzije kojom se predstavlja ta perturbacija. Kako taj član ovisi samo o svojstvima neperturbiranog sustava, račun dielektrične funkcije zasniva se samo na osnovnom stanju sustava što mu drastično smanjuje računalnu zahtjevnost.

Računi zasnovani na elektrodinamici omogućavaju povezivanje svojstava materijala na makroskali i na nanoskali. Korištenjem Mieove teorije moguće je izračunati optička i plazmonička svojstva nanočestica ekspanzijom elektromagnetskog polja u prikladan vektorski prostor (kugline funkcije). To omogućuje eksplicitno određivanje svojstava nanočestica koje su sferične (i za mali broj drugih geometrija) dok je za većinu geometrija potrebno numerički rješavati Maxwellove jednadžbe.

### 3. Literaturni pregled

Djelovanje elektromagnetskog polja na metalnu nanočesticu može uzrokovati gibanje vodljivih elektrona u metalu. Pritom se negativni naboj nakuplja na jednoj, a pozitivni na drugoj strani nanočestice, što stvara povratnu silu koja djeluje na elektrone i uzrokuje periodičko gibanje unutar nanočestice. Kada je frekvencija svjetla u rezonanciji s tim kolektivnim oscilacijama elektrona, pobuđuju se plazmoni – kvazičestice koje opisuju oscilacije plazme.

---



Slika I. Prikaz lokaliziranih površinskih plazmona u nanočesticama pobuđenih elektromagnetskim valom.

Zbog rezonancije površinskih plazmona metalne nanočestice pokazuju mnoga zanimljiva svojstva poput pojačanja lokalnog elektromagnetskog polja [H. Wang, H. Li, S. Xu, B. Zhao i W. Xu, *Scientific Reports* **7** (2017) 14630] i iznimno velikog ekstinkcijskog poprečnog presjeka [S. D. Rezaei, J. Ho, R. J. H. Ng, S. Ramakrishna i J. K. W. Yang, *Optics Express* **25** (2017) 27652-27664]. Ta su svojstva posebno korisna za upotrebu u sensorima. Oscilacija elektrona u nanočestici ima konačno vrijeme trajanja te kada gibanje elektrona izađe iz faze plazmoni se raspadaju. Pritom nastaju elektroni i šupljine koje karakterizira iznimno visoka energija. Iz tog ih se razloga naziva vrućim nosiocima naboja [M. L. Brogersma, N. J. Halas i P. Nordlander, *Nature Nanotechnology* **10** (2015) 25-34]. Vrući se nosioci naboja mogu injektirati u materijal s kojim je nanočestica u kontaktu, na primjer molekula, koje zbog toga potencijalno lakše stupaju u reakciju. Plazmoničke nanočestice stoga upotrebu nalaze i u katalizi [A. Marimuthu, J. Zhang i S. Linić, *Science* **339** 1590-1593]. Prijenos vrućeg nosioca naboja u poluvodič može rezultirati učinkovitijim prikupljanjem solarne energije [Z. C. Su, C. H. Chang, J.-C. Jhou, H.-T. Lin i C.-F. Lin, *Scientific Reports* **13** (2023) 5388]. Ako se energija vrućih nosioca naboja preda rešetci nanočestice, dolazi do snažnog lokalnog zagrijavanja koje se, na primjer, može iskoristiti za termičku razgradnju tumora [H. S. Han i K. Y. Choi, *Biomedicines* **9** (2021) 305].

Prilagodba plazmoničkih svojstava željenim svrhama od ključne je važnosti. Promjena veličine nanočestice može se upotrijebiti za ugađanje frekvencije rezonancije plazmona [K.-C. Lee, S.-J. Lin, C.-H. Lin, C.-S. Tsai i Y.-J. Lu, *Surface and Coatings Technology* **202**



(2008) 5339-5342] i promjenu omjera apsorpcije i raspršenja svjetla [P. K. Jain, K. S. Lee, I. H. El-Sayed i M. A. El-Sayed, *Journal of Physical Chemistry B* **110** (2006) 7238–7248]. Promjenom oblika nanočestice [W. Cao, T. Huang, X.-H. N. Xu i H. Elsayed-Ali, *Journal of Applied Physics* **109** (2011) 034310], kao i njene okoline [K. L. Kelly, E. Coronado, L. L. Zhao i G. C. Schatz, *Journal of Physical Chemistry B* **107** (2003) 668-677], rezonanciju plazmona moguće je ugađati u veoma širokom rasponu frekvencija. Prilagodba udaljenosti nanočestica često služi postizanju iznimno velikog pojačanja lokalnog polja u području između njih koje se naziva vrućom točkom [J. H. Kim, J. Y. Lee, E. S. Kim i M. Y. Jeong, *Photonix*, **4** (2023) 8] . Sva navedena svojstva moguće je mijenjati i odabirom materijala nanočestice. Legiranje je pritom posebno prikladno budući da omogućava fino ugađanje malim promjenama sastava, kao i odabir svojstava na temelju elemenata legure.

Teorija funkcionala gustoće posebno je prikladna za predviđanje svojstava legura, no dosad se uglavnom primjenjivala na u svrhu proučavanja nanostruktura čistih metala. Pritom su korištena tri pristupa modeliranja sustava: *jellium* modeli, atomističko modeliranje nanočestice i kombinacija računa na makroskopskom materijalu i elektrodinamike. Budući da *jellium* modeli nisu prikladni za modeliranje nekih metala, a atomistički modeli računalno prezahtjevni da se njima računaju svojstva bilo kakvih sustava osim veoma malih nanočestica, veoma često su korišteni računi na makroskopskim sustavima, katkad u kombinaciji s elektrodinamikom, što omogućava poveznicu sa svojstvima na nanoskali. Za provedbu takvih računa uglavnom je potrebno koristiti računalno učinkovite funkcionalne izmjene i korelacije, maksimalno na razini generaliziranog gradijenta gustoće. Najčešće korišten funkcional u te svrhe je PBE, koji uzrokuje veliku pogrešku kod tretmana d-vrpce dobrih plazmoničkih metala. Ipak, nekoliko je istraživanja pokazalo da podjednako učinkoviti funkcional GLLB-SC puno bolje tretira d-vrpce i bolje predviđa elektronsku strukturu i optička svojstva standardnih plazmoničkih metala [R. Sundararaman, P. Narang, A. S. Jarmyn, W. A. Goddard 3rd i Harry Atwater, *Nature Communications* **5** (2014) 5788]. Iako se sustav prilikom provedbe računa temeljenih na teoriji funkcionala gustoće modelira kao savršeni kristal, postoje indikacije da je moguće iskoristiti teoriju funkcionala gustoće da se odredi utjecaj konfiguracije i neuređenosti na svojstva legura [K. S. B. De Silva, A. Gentle, M. Arnold, V. J. Keast i M. B. Cortie, *Journal of Physics D: Applied Physics* **48** (2015) 215304]. Osim toga, u literaturi se pojavljuju i indikacije da se uslijed legiranja javljaju neočekivani prijelazi među vrpčama pri niskim energijama, te da ih je moguće predvidjeti teorijom funkcionala gustoće

[L. K. Skriver i H. P. Lengkeek, *Physical Review B* **19** (1979) 900-910]. Uz to, teorija funkcionala gustoće omogućava predviđanje distribucije energija vrućih nosioca naboja u materijalima [L. J. Krayner, K. J. Palm, C. Gong, A. Torres, C. E. P. Villegas, A. R. Rocha, M. S. Leite i J. N. Munday, *ACS Photonics* **7** (2020) 1689–1698]. To je posebno prikladno za legure koje bi potencijalno mogle biti iskorištene da se distribucija energija vrućih nosioca naboja ugađa za ciljane svrhe, no trenutno dostupne metode uključuju velike aproksimacije.

#### 4. Eksperimentalni dio

Računalni pristup istraživanju mogućnosti ugađanja optičkih i plazmoničkih svojstava legiranjem zasniva se na određivanju svojstava makroskopskih legura teorijom funkcionala gustoće. Pritom se koristi jedinična ćelija na temelju koje se upotrebom periodičkih rubnih uvjeta modelira kristalna struktura makroskopskog materijala. To omogućuje učinkovito određivanje fundamentalnih svojstava tvari poput elektronske strukture. Uz to omogućuje i određivanje dielektrične funkcije koja služi kao osnova za račune temeljene na klasičnoj elektrodinamici, kojima se određuju optička i plazmonička svojstva nanostrukture.

Za predviđanje optičkih i plazmoničkih svojstava nanostrukture odabrane su četiri binarne legure: Au-Cu, Au-Ag, Au-Pd i Ag-Cu. Sastav im je mijenjan u koracima od 12.5%, tako da je, uključno s čistim metalima, uzeto u obzir 9 različitih omjera dvaju metala u leguri za svaki sustav. Za sustave stehiometrije  $A_3B_5$  priređene su tri različite jedinične ćelije što je omogućilo procjenu utjecaja konfiguracije ćelije na svojstva.

Svi računi provedeni su u programu GPAW [J. Enkovaara *et al.*, *Journal of Physics: Condensed Matter* **22** (2010) 253202], koristeći funkcionalnosti koje pruža ASE (*Atomic simulation environment*) [A. H. Larsen *et al.*, *Journal of Physics: Condensed Matter* **29** (2017) 273002]. Brillouinova zona uzorkovana je Monkhorst-Pack mrežom a korištena DFT metoda bazira se na razvoju po ravnim valovima. Konvergencija je osigurana kod svih parametara računa, što za ravne valove uključuje graničnu vrijednost od 500 eV za optimizaciju, te do 450 eV za sve ostale račune, dok je kod optimizacije broj k-točaka bio  $24 \times 24 \times 24$  za ćelije s četiri atoma i  $24 \times 24 \times 12$  za 8 atoma te do  $40 \times 40 \times 40$  u ostalim računima za ćelije s četiri atoma i  $40 \times 40 \times 20$  za ćelije s 8 atoma. Kod određivanja distribucije vrućih nosioca naboja, zbog različitih veličina i oblika jediničnih ćelija, korištena je gustoća od 30 k-točaka po recipročnom Å za sve ćelije. Jedinične ćelije čistih metala optimizirane su pomoću PBE [J. P. Perdew, K. Burke i M. Ernzerhof, *Physical Review Letters* **77** 3865-3868] i PBEsol [J. P.

Perdew, A. Ruzsinszky i G. I. Csonka, *Physical Review Letters* **100** (2008) 136406] funkcionala, koji je modifikacija PBE funkcionala s ciljem boljeg opisa krutina. Jedinične ćelije legura optimizirane su samo pomoću PBEsol funkcionala budući da se pokazao boljim. Sustavno vrednovanje (engl. *benchmarking*) funkcionala izmjene i korelacije provedeno je na čistim metalima te se GLLB-SC [M. Kuisma, J. Ojanen, J. Enkovaara i T. T. Rantala, *Physical Review B* **82** (2010) 115106] pokazao najboljim. GLLB-SC i PBE korišteni su za provedbu svih ostalih računa za legirane sustave. Proučavanjem sustavima određena je gustoća stanja (engl. *density of states, DOS*), struktura elektronskih vrpca i makroskopska dielektrična funkcija (u daljnjem tekstu samo „dielektrična funkcija“) pri čemu nisu korišteni efekti lokalnog polja budući da se pokazalo da imaju malen utjecaj na rezultate a povećavaju računalnu zahtjevnost. Zatim su za Ag-Au sustav provedeni i računi na temelju klasične elektrodinamike pritom modelirajući nekoliko često istraživanih tipova nanostrukture.

Uz navedeno, modifikacijom programa GPAW određene su i distribucije energija vrućih nosioca naboja za legirane sustave od interesa. Korištena metoda uspoređena je s metodom koja se najčešće koristi u literaturi i temelji se na *density of states* računima. Metoda predstavljena u ovom radu temelji se na *joint density of states* (JDOS) računima i uzima u obzir očuvanje količine gibanja. Računi vezani uz distribuciju vrućih nosioca naboja provedeni su korištenjem GLLB-SC funkcionala budući da se na ostalim primjerima pokazao kao najbolji.

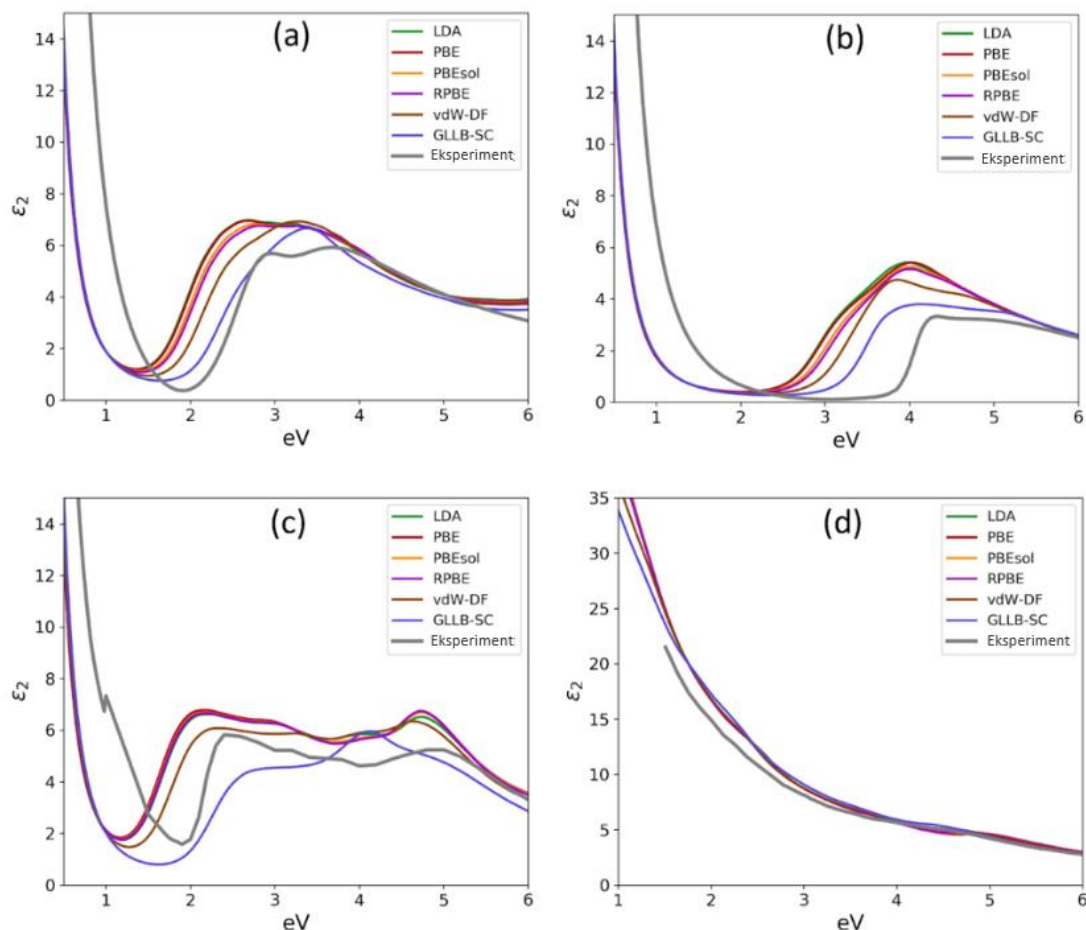
## 5. Rezultati i rasprava

Parametri jedinične ćelije određuju udaljenost atoma a time utječu i na elektronsku strukturu tvari. Stoga je, uz konvergenciju svih parametara računa, u svrhu pravilnog opisa svojstva tvari potrebno odabrati i prikladan funkcional izmjene i korelacije kako bi se parametri što točnije odredili. Usporedbom parametara određenih PBE i PBEsol funkcionalima i usporedbom s eksperimentalnim podacima pokazano je da PBEsol u prosjeku točnije određuje konstante ćelije Ag, Au, Pd i Cu metala, te da ta razlika može biti bitna kod određivanju optičkih svojstava metala. To je potvrđeno značajnom razlikom dielektričnih funkcija dobivenih računima s različitim konstantama jedinične ćelije.

*Benchmarkingom* funkcionala izmjene i korelacije na čistim metalima (Ag, Au, Cu i Pd) pokazano je da, u odnosu na eksperimentalne podatke, svi daju premale vrijednosti pri izračunu minimalne energije potrebne za pobudu međuvrpanih prijelaza. Pritom daleko

---

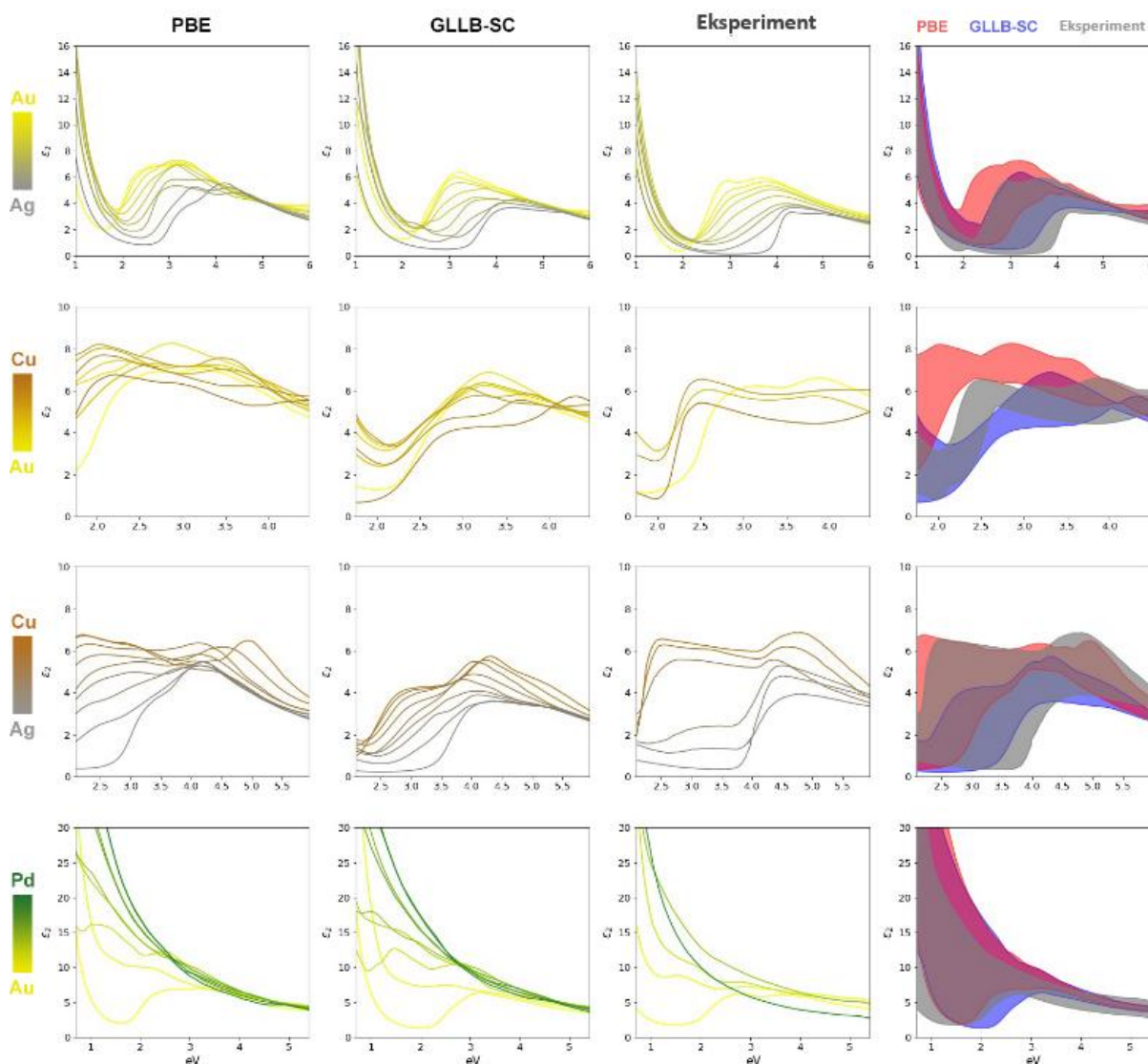
najbolje rezultate daje GLLB-SC iako je, kao i većina ostalih, to učinkovit funkcional na razini generaliziranog gradijenta gustoće (Slika II).



Slika II. Usporedba imaginarnih dijelova dielektrične funkcije za čiste elemente Au (a), Ag (b), Cu (c) i Pd (d) izračunate različitim funkcionalima s eksperimentalno određenim podacima.

Strukture elektronskih vrpce pokazuje da GLLB-SC bolje tretira d-vrpce od funkcionala poput PBE, predviđajući im niže energije, što dovodi do povećanja energije potrebne za međuvrpane prijelaze.

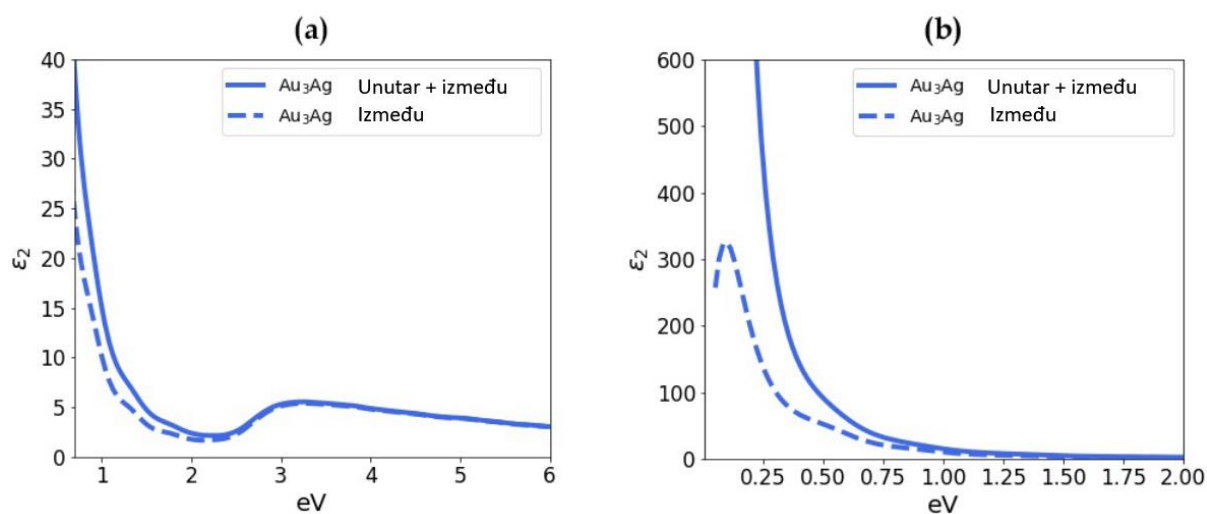
Pokazano je da se slični rezultati mogu dobiti provedbom PBE+U računa pri čemu faktor U označava korekciju temeljenu na Hubbardovom modelu, u ovom radu primijenjenu na d-vrpce. Budući da je parametar U potrebno podešavati za svaki sustav, korištenje funkcionala GLLB-SC kojem nije potrebna parametrizacija procijenjeno je kao praktičnije rješenje te su za legure uspoređeni PBE kao standardno korišten funkcional i GLLB-SC kao potencijalno superiorna alternativa.



Slika III. Imaginarni dio dielektrične funkcije za legure Au-Ag (prvi red), Au-Cu (drugi red), Ag-Cu (treći red) i Au-Pd (četvrti red). U prvom se stupcu nalaze rezultati dobiveni računima s PBE funkcionalom, u drugom redu s GLLB-SC funkcionalom, u trećem redu prikazani su eksperimentalno dobiveni podaci, dok su u četvrtom redu prikazane “ovojnice” određene minimalnom i maksimalnom vrijednošću imaginarnog dijela dielektrične funkcije za svaki sustav na danoj energiji. Eksperimentalni podaci za Au-Ag sustav dobiveni su iz [O. Peña-Rodríguez, M. Caro, A. Rivera, J. Olivares, J. M. Perlado i A. Caro, *Optical Materials Express* 4 (2014) 403–410], za Au-Cu sustav iz [W. Köster i R. Stahl, *Zeitschrift für Metallkunde* 58 (1967) 768–777], za Ag-Cu sustav iz [J. Rivory i M. L. Theye, *Journal de Physique Lettres* 36 (1975) 129-132] i za Pd-Au sustav iz [H. P. Myers, L. Walldén i Å. Karlsson, *The Philosophical Magazine: A Journal of Theoretical Experimental and Applied Physics* 18 (1968) 725-744].

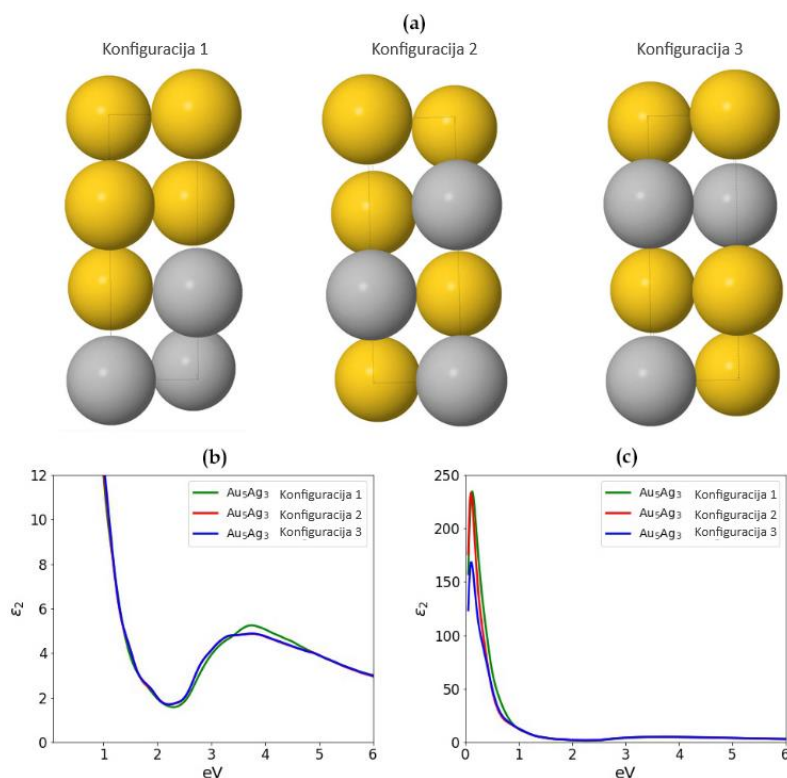
Na slici III vidljivo je da se dielektrične funkcije kod Au-Ag, Au-Cu i Ag-Cu sustava mijenjaju postupno s promjenom sastava dok je kod Au-Pd sustava prisutan nagli skok pri nižim energijama kada se uspoređuje sastav s čistim zlatom i sastav u kojem se nalazi makar malen udio Pd. Oba funkcionala uspješno predviđaju taj trend, kao i ostale kvalitativne trendove no u globalu GLLB-SC puno bolje kvantitativno predviđa vrijednosti dielektričnih funkcija.

U namjeri da se istraži pojava neočekivanih optičkih gubitaka u infracrvenom području uzrokovanih međuvrpanim prijelazima, što sugeriraju računalni i eksperimentalni podaci dostupni u literaturi, provedeni su računi dielektrične funkcije pri čemu je isključen doprinos unutarvrpanih prijelaza. Za razliku od čistih metala, kod svih legura dobivene su iznimno visoke vrijednosti dielektrične funkcije u području niskih energija, manjih od minimalne energije potrebne za d-sp prijelaze (kao što je vidljivo na slici IV), što implicira da je omogućavanje novih međuvrpanih prijelaza u tim slučajevima emergentno svojstvo legiranja.



Slika IV. Imaginarni dio dielektrične funkcije  $Au_3Ag$  sustava dobiven računima s GLLB-SC funkcionalom. Puna crta pokazuje zbrojeni doprinos unutar- i međuvrpanih prijelaza prijelaza, dok isprekidana pokazuje doprinos međuvrpanih prijelaza. Vidljivo je da je taj doprinos značajan i pri veoma niskim energijama te da dominira ne samo u ultraljubičastom i vidljivom području, već i u bliskom infracrvenom području.

Utjecaj konfiguracije na dielektričnu funkciju istražen je na temelju različitih konfiguracija jedinične ćelije za sustave  $A_3B_5$  stehiometrije. Utjecaj takve promjene nije velik i više je izražen pri niskim energijama gdje je zasjenjen utjecajem prijelaza unutar vrpce (slika V).

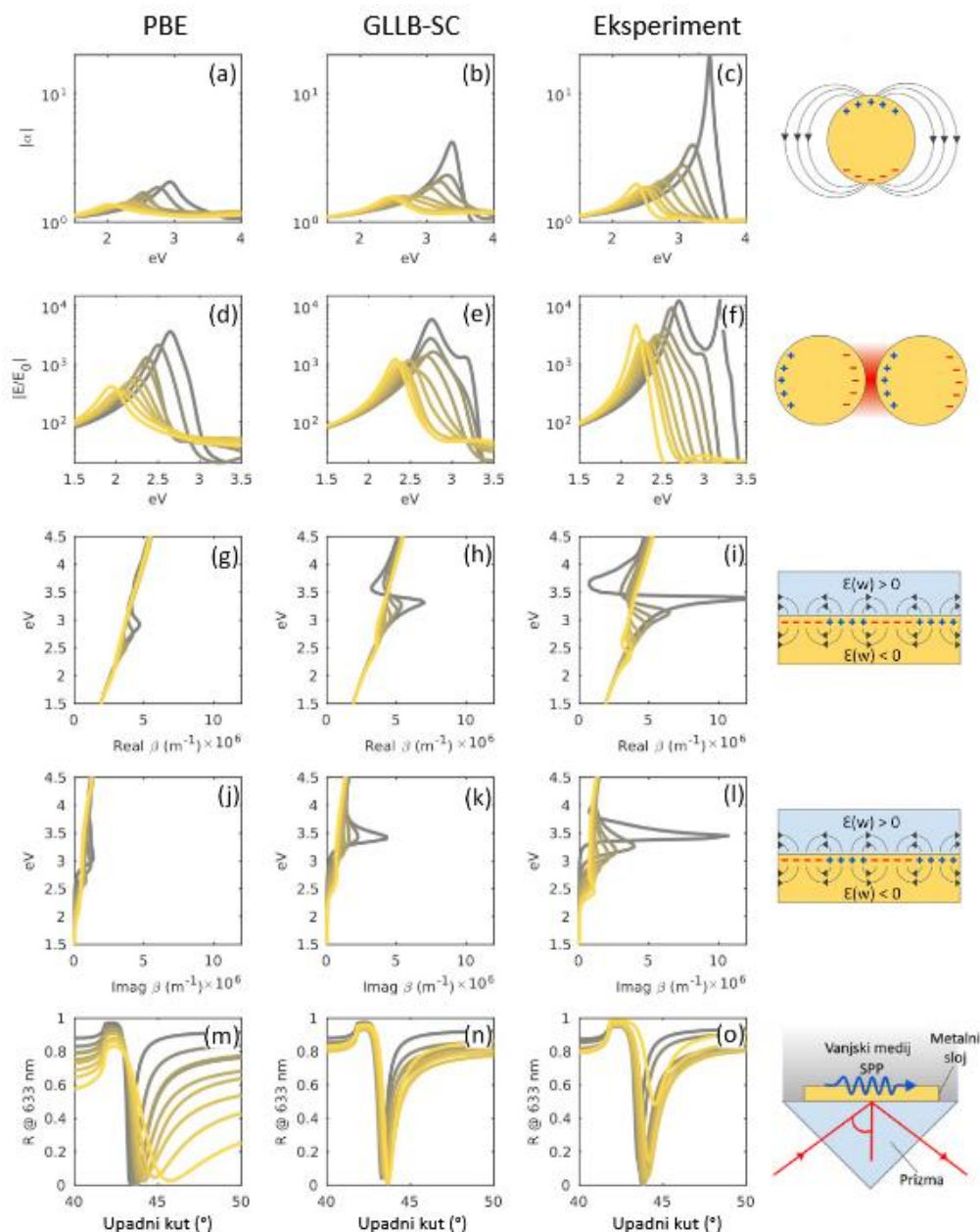


Slika V. Tri različite konfiguracije  $Ag_5Au_3$  jedinične ćelije (a) i pripadne dielektrične funkcije dobivene korištenjem GLLB-SC funkcionala prikazane u vidljivom i ultraljubičastom području (b) te od infracrvenog do ultraljubičastog područja (c). Utjecaj prijelaza između vrpce je relativno malen što je posebno izraženo kod konfiguracije 2 i 3 za koje se imaginarni dio dielektrične funkcije preklapa na velikom dijelu spektra.

Utjecaj uređenosti i neuređenosti procijenjen je usporedbom s podacima dobivenim iz literature [M. J. Rahm, C. Tiburski, T. P. Rossi, F. A. A. Nugruho, S. Nilsson, C. Langhammer i P. Erhart, *Advanced Functional Materials* **30** (2020) 2002122] za sustave legura s jednakim omjerom dvaju elemenata. Dielektrične funkcije dobivene računima sa samo 4 atoma veoma su slične onima koje su Rahm i suradnici dobili računima provedenim na temelju posebnih kvazinasumičnih struktura (*special quasirandom structure, SQS*) s 20-24 atoma. To dovodi do zaključka da je korištenje jednostavnih i malenih jediničnih ćelija opravdano kod računalnih metoda kojima je cilj učinkovita provedba mnoštva računa za velik broj legura različitog sastava.



Kao indirektni pokazatelj kvalitete funkcionala koji pomaže u procjeni odabira funkcionala u svrhu predviđanja optičkih i plazmoničkih svojstava legura provedeni su računi temeljeni na klasičnoj elektrodinamici (Slika VI).



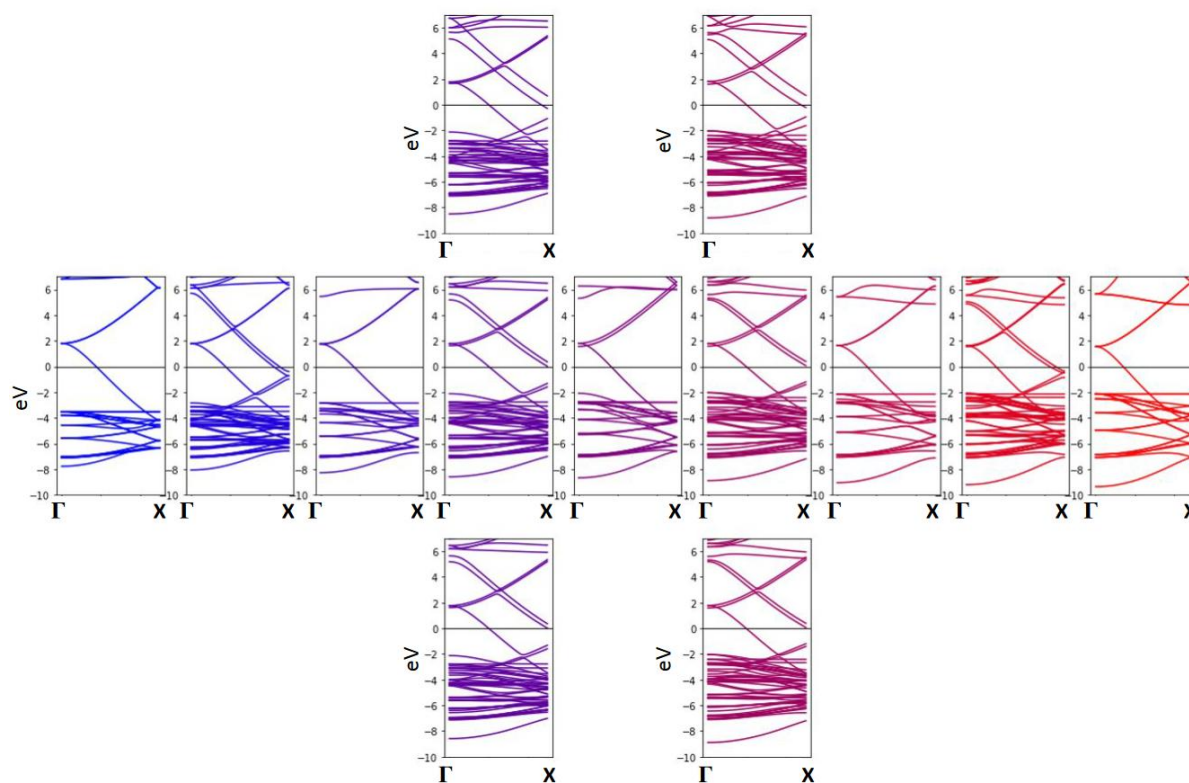
Slika VI. Plazmonička svojstva različitih sustava (desni stupac) Au-Ag legiranih nanostrukture dobivenih računima s PBE (lijevi stupac) i GLLB-SC funkcionalom (lijevo od sredine) te svojstva dobivena na temelju eksperimentalno određene dielektrične funkcije (stupac u sredini desno). Prikazano je 9 omjera Au/Ag s pomacima od 12.5%. Gornji red prikazuje vrijednosti polarizabilnosti sferičnih nanočestica, drugi prikazuje pojačanje intenziteta bliskog polja između dvije nanočestice, treći i četvrti prikazuju realni i imaginarni dio disperzijske relacije na granici zraka i metala, a peti prikazuje reflektanciju sustava staklo/metal/zrak kao funkciju upadnog kuta svjetla.



Iz dobivenih rezultata može se vidjeti je da je razlika u performansama dvaju korištenih funkcionala izraženija nego kod dielektričnih funkcija, te da PBE u nekim slučajevima gotovo potpuno podbacuje kod predviđanja plazmoničkih svojstava (npr. disperzijska relacija). Iako rezultati dobiveni na temelju dielektričnih funkcija određenih korištenjem GLLB-SC funkcionala puno manje odstupaju od rezultata dobivenih na temelju eksperimentalno određenih dielektričnih funkcija, slaganje i dalje nije kvantitativno. Ipak, rezultati dobiveni korištenjem GLLB-SC funkcionala pokazuju kvalitativno dobro slaganje te pravilno predviđaju trend promjene svojstava s promjenom sastava.

Računi struktura elektronskih vrpca pokazuju razliku u procjeni položaja d-vrpca dobivenih korištenjem PBE i GLLB-SC funkcionala, pri čemu su one, kao i kod čistih metala, niže kada se koristi GLLB-SC. Promjene koje nastaju zbog narušavanja translacijske simetrije, povećanjem jediničnih ćelija kod legiranih sustava, te promjene koje nastaju zbog kombiniranja dvaju elemenata različite elektronske strukture pomažu objasniti emergentne prijelaze među vrpcama: iz struktura elektronskih vrpca vidljivo je da se smanjenjem Brillouinove zone njihov položaj “preklapa” (jedna se nalazi iznad druge), te da se kombinacijom dvaju elemenata narušava degeneracija vrpca zbog čega se one “razdvajaju” (Slika VII). Između preklapljenih i razdvojenih vodljivih vrpca mogući su prijelazi, čak i pri veoma niskim energijama, što služi kao izvor dodatnih optičkih gubitaka kod legura.

---



Slika VII. Struktura elektronskih vrpci za Ag-Au sustav, počevši od Ag (lijevo) i završavajući s Au (desno). Za dva sastava korištene su po tri različite konfiguracije, a njihove su strukture elektronskih vrpci poredane vertikalno te je za njih korištena ista boja. Zbog različitih simetrija jediničnih ćelija prikazane su samo između  $\Gamma$  i X točaka budući da je taj dio puta visoke simetrije jedini zajednički kod svih sustava.

Računi gustoće elektronskih stanja komplementarni su računima strukture energijskih vrpci, a projekcija gustoće elektronskih stanja na atomske orbitale i razdvajanje na udio koji pripada svakom od elemenata ili čak svakom atomu omogućavaju dublji uvid u fundamentalna svojstva tvari i njihovu povezanost s plazmoničkim svojstvima nanočestica. Dobiveni rezultati ukazuju na zanimljivu evoluciju gustoće d-stanja prilikom legiranja pri čemu se kod nekih sustava, poput Au-Ag, d-vrpca mijenja s relativno ujednačenim doprinosom oba elementa, uz tek manju segregaciju stanja povezanih s atomima zlata kod gornjeg ruba d-vrpce. Suprotno tome, kod Ag-Cu sustava vidljiva je drastična segregacija stanja, pri čemu se d-vrpca cijepa na dva dijela od kojih se dio više energije može gotovo u potpunosti pridružiti atomima bakra, dok doprinos srebra gotovo potpuno određuje gustoću d-stanja pri nižim energijama. Svojstva d-vrpce kod Pd-Au sustava posebno su zanimljiva, pogotovo kad je udio paladija malen. Tada se kod gustoća d-stanja pojavljuje pik pri višim energijama, koji

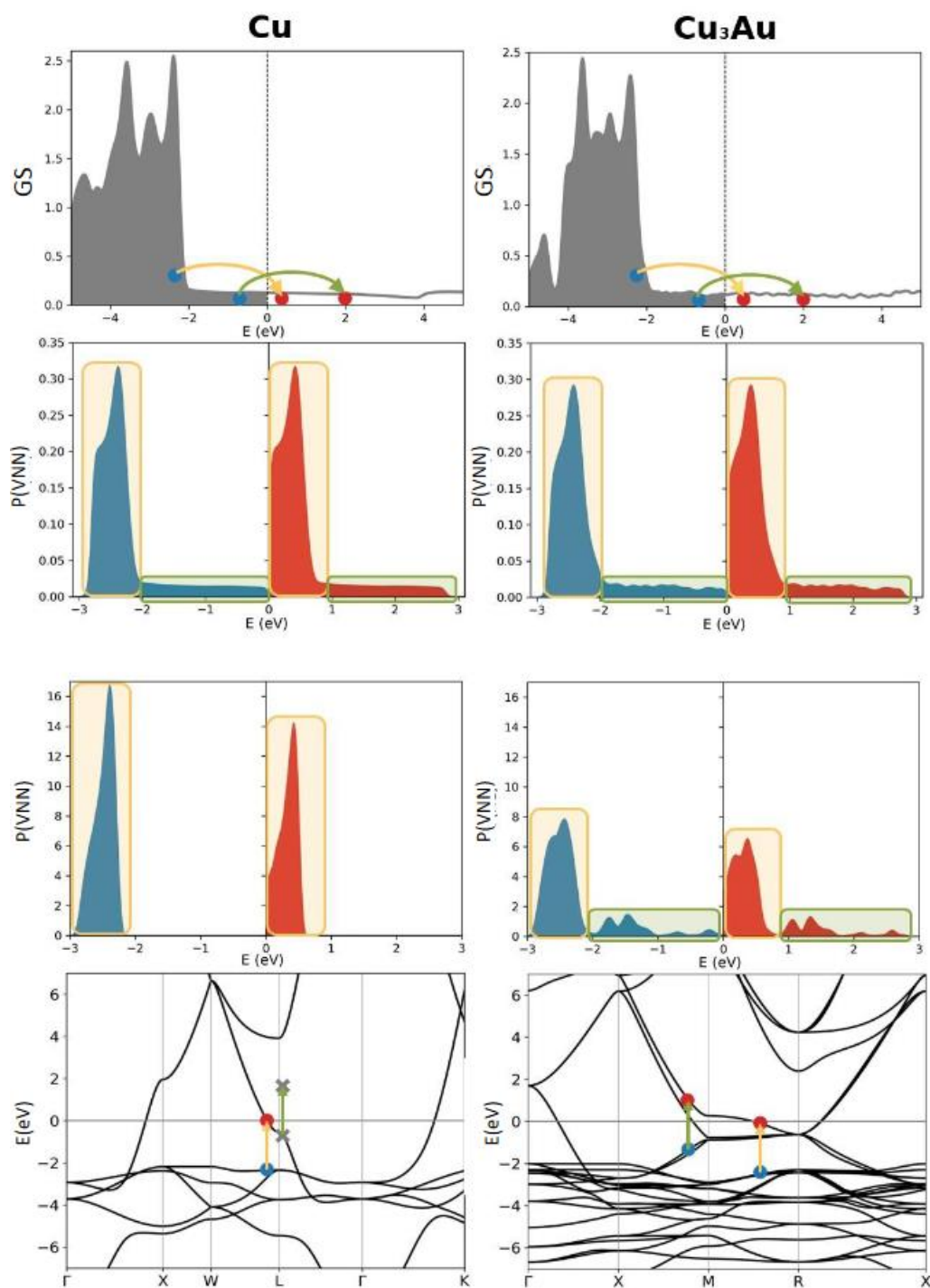
primarno određuje gornji rub d-vrpce i u najvećoj je mjeri određen utjecajem paladija. Nagla promjena dielektrične funkcija kod Au-Pd legura pri dodatku male količine paladija prilikom legiranja sa zlatom odražava taj pomak gornje granice d-vrpce koji se može objasniti doprinosom stanja pridruženih paladiju.

Uz to, projekcija stanja u blizini Fermijeve razine na atomske orbitale pokazuje da je udio d-karaktera tih stanja usporediv s udjelom s i p-karaktera, te da raste sa smanjivanjem udaljenosti gornjeg ruba d-vrpce od Fermijeve razine. Stoga utjecaj sastava na položaj d-vrpce mijenja i svojstva vodljive vrpce, koja, unatoč tome što ju se tako često naziva, nije (samo) sp-vrpca.

Naposljetku, proučen je i utjecaj konfiguracije na gustoću elektronskih stanja i može se pokazati da je relativno malen, u skladu s rezultatima računa dielektričnih funkcija i strukture elektronskih vrpce.

Navedeni rezultati daju naslutiti da se modifikacijama elektronske strukture legiranjem može utjecati na distribuciju energija vrućih nosioca naboja s obzirom na to da je ona određena dostupnim elektronskim prijelazima. Vrući nosioci naboja su elektrona i šupljina iznimno visoke energije koji mogu nastati raspadom plazmona ili direktnom pobudom fotonom te je njihova distribucija energija vanravnotežna. Trenutačno najčešće korištena metoda za procjenu distribucije energija vrućih nosioca naboja u literaturi temeljena je na gustoći stanja i zanemaruje očuvanje količine gibanja, zbog čega unutarvrpčane prijelaze i međuvrpčane prijelaze tretira jednako. Dosad prikazani rezultati ukazuju na to da su međuvrpčani prijelazi osjetljivi na legiranje, pogotovo zbog primijećene pojave emergentnih međuvrpčanih prijelaza. Stoga je u sklopu ovog rada predstavljena metoda koja uzima u obzir očuvanje količine gibanja i primarno proučava međuvrpčane prijelaze. Razlika tih dvaju pristupa i rezultati njihove primjene prikazani su na slici VIII.

---



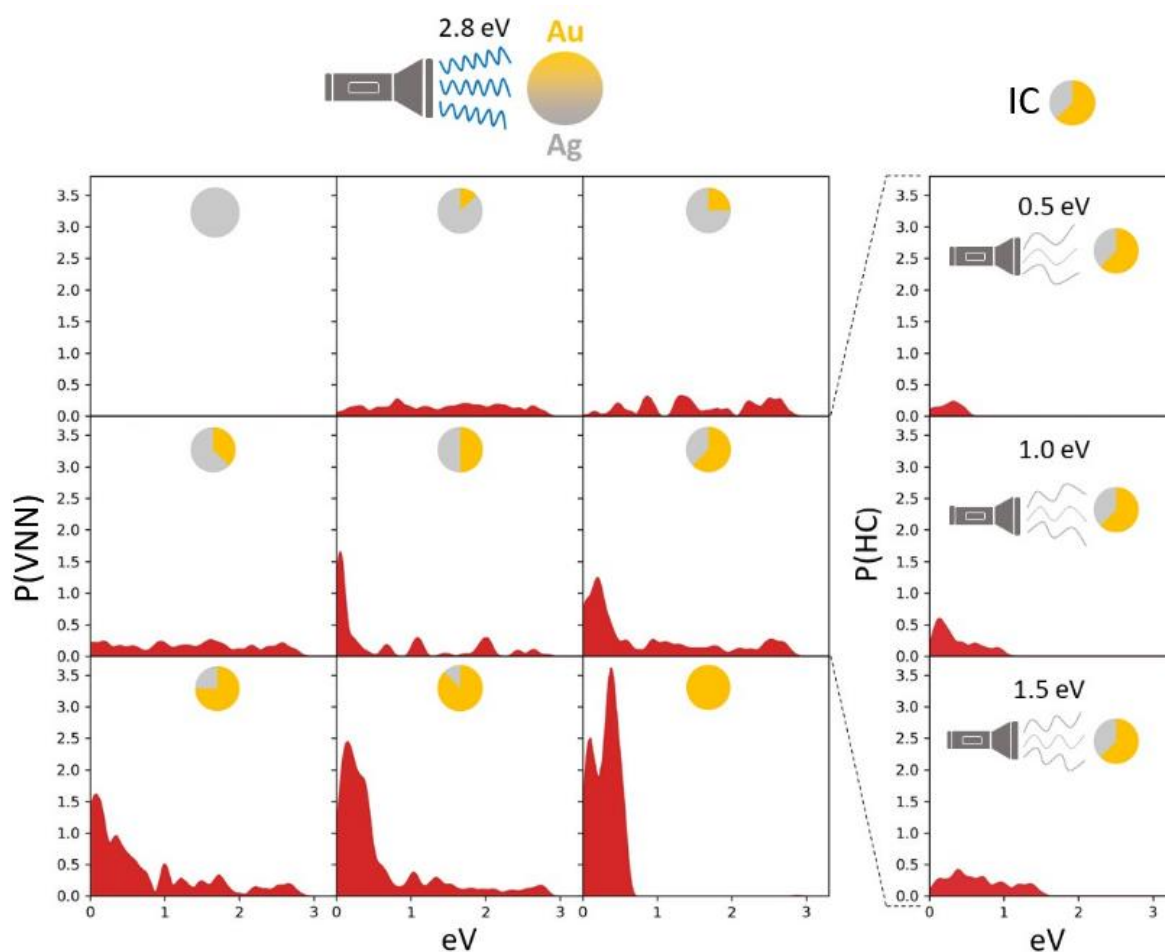
Slika VIII. Usporedba distribucija energija vrućih nosioca naboja (VNN) dobivenih metodom temeljenom na gustoći stanja (GS) (gornja dva reda) i metodom predstavljenom u sklopu ovog rada (donja dva reda). Žute strelice prikazuju prijelaze između d-vrpce i vodljive vrpce, dok zelene prikazuju prijelaze između vodljivih vrpce. Dijelovi distribucije energija vrućih nosioca naboja koji nastaju zbog navedenih prijelaza osjenčani su bojom u skladu s tipom prijelaza.

Iz dobivenih rezultata vidljivo je da prijelazi između vodljivih vrpca rezultiraju dijelom distribucije vrućih elektrona s energijama koje u rasponu sve do energije fotona. Taj efekt nije primijećen drugom metodom, što ukazuje na važnost uzimanja očuvanja količine gibanja u obzir.

Utjecaj konfiguracije, to jest modeliranja neuređenosti, provjeren je usporedbom rezultata za najjednostavniju jediničnu ćeliju CuAu sustava sa samo 2 atoma s rezultatima dobivenim korištenjem specijalne kvazinasumične strukture istog sastava. Modeliranje neuređenosti ne mijenja kvalitativno distribuciju vrućih elektrona; glavna razlika vidljiva je u nešto glađem izgledu distribucije dobivene korištenjem specijalne kvazinasumične strukture. S tim u vidu, u ostalim računima korištene su najjednostavnije jedinične ćelije koje odgovaraju određenom sastavu (ili kristalne strukture temeljene na eksperimentalnim podacima kada stvaranje jednostavne supstitucijske legure nije bilo opravdano).

S promjenom sastava u Au-Ag sustavu legura mijenja se položaj d-vrpca, kao što je ranije navedeno. To omogućuje ugađanje distribucije vrućih nosioca naboja na način da se dio distribucije koji proizlazi pobuda elektrona iz d-vrpca pomiče ovisno o sastavu (pri fiksnoj energiji fotona). Time se mijenja udio vrućih šupljina visoke energije i udio vrućih elektrona niske energije, kao što je vidljivo na slici IX.

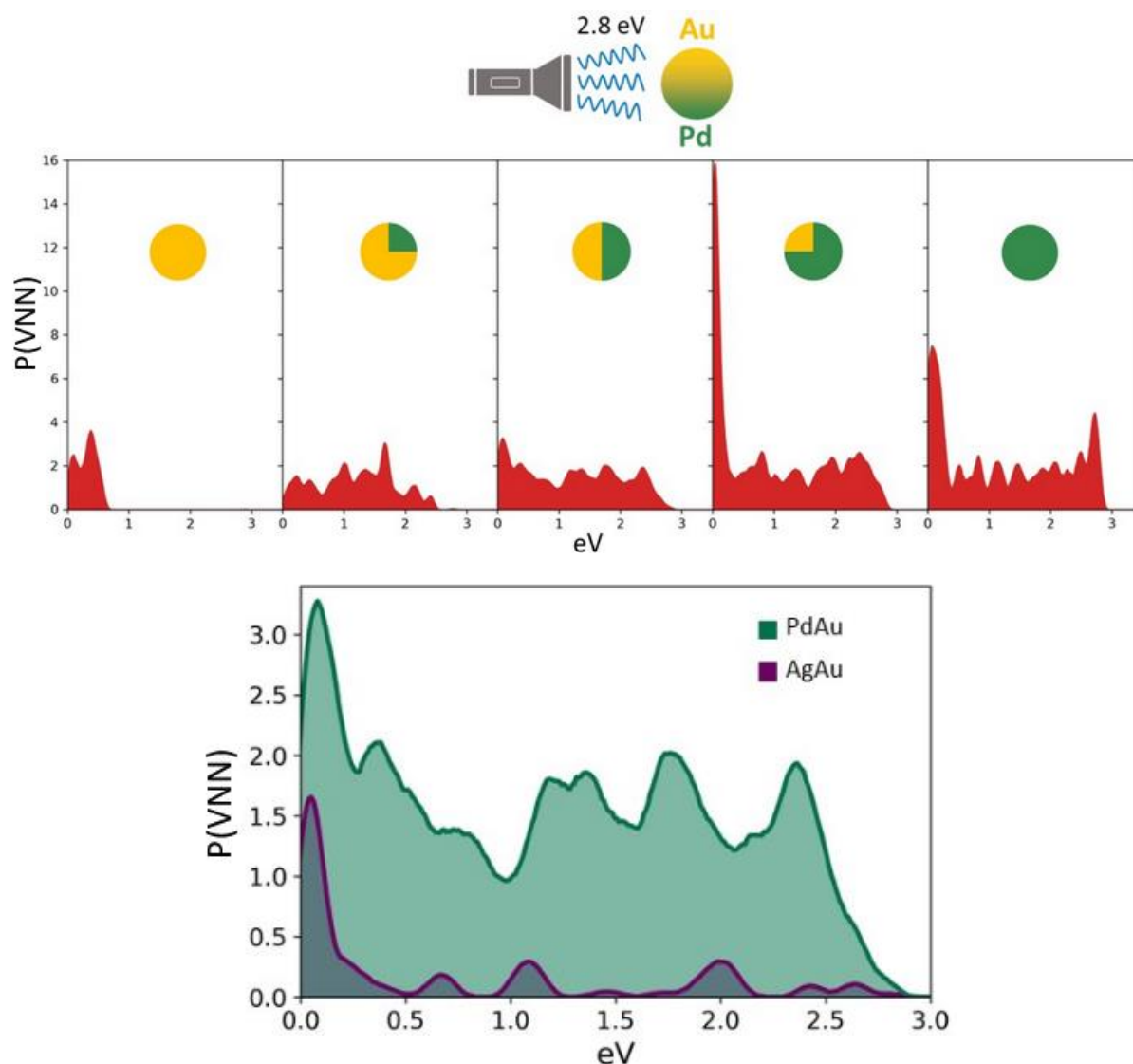
---



Slika IX. Distribucija vrućih elektrona pri pobudi svjetlom energije 2.8 eV za Au-Ag sustav. Stupac s desne strane pokazuje distribucije vrućih elektrona koje se mogu dobiti infracrvenim svjetlom za fiksni sastav legure, energijama daleko manjim od najmanje potrebne za pobudu elektrona iz d-vrpce.

U svrhu istraživanja utjecaja različitog tipa elektronske strukture na distribuciju vrućih nosioca naboja provedena je klasifikacija elemenata: Au, Cu i Ag klasificirani su kao elementi sa zatvorenom d-ljuskom, Pd kao element s otvorenom (iako je anomalija kod Aufbau principa s  $d^{10}$  konfiguracijom, kao krutina d-vrpca paladija nije potpuno popunjena što mu mijenja svojstva u odnosu na ranije navedene elemente), Na je klasificiran kao element s-ljuske, a Al kao element p-ljuske.

Pd-Au sustav, kao primjer legure elementa otvorene s elementom zatvorene d-ljuske daje drugačiju distribuciju vrućih elektrona od Au-Ag sustava, koji čine dva elementa zatvorene d-ljuske (Slika X).



Slika X. Gore: Distribucija energija vrućih elektrona kod Pd-Au sustava pri pobudi svjetlom 2.8 eV. Dolje: Usporedba distribucija energija vrućih elektrona za PdAu leguru i za AgAu leguru.

Vidljivo je da je predviđena puno veća generacija (pod pretpostavkom jednakog elektromagnetskog polja) vrućih nosioca naboja za Pd-Au sustav, čemu je vjerojatno razlog veća gustoća stanja na Fermijevoj razini zbog doprinosa d-vrpca.

$\text{Na}_8\text{Au}_4$  sustav uzet je kao primjer legure elementa s-ljuske i elementa zatvorene d-ljuske. Kod te je legure d-vrpca znatno niže nego kod čistog zlata, što ukazuje na mogućnost ugađanja. Gustoća stanja vodljive vrpce raste s porastom energije što rezultira distribucijom vrućih elektrona sličnoj kao kod Au-Ag legura, no s trendom veće generacije vrućih elektrona pri višim energijama, što može biti korisno kod upotreba kod kojih se oni moraju injektirati u molekulu ili poluvodič.

Legure aluminijska kao primjera elementa p-ljuske s bakrom kao elementom zatvorene d-ljuske i paladijem kao elementom otvorene d-ljuske vode do distribucije vrućih nosioca naboja srednjih vrijednosti u odnosu na ranije navedene sustave. Bitno je primijetiti da se d-vrpce i u tom slučaju pomiču prema nižim energijama, pogotovo u slučaju legure s paladijem, što može poboljšati plazmonička svojstva legure smanjujući optičke gubitke.

## 6. Zaključak

Kao primarni cilj ovog rada, uspostavljen je računalni okvir koji omogućuje učinkovitu provedbu računa temeljenih na teoriji funkcionala gustoće za određivanje optičkih i plazmoničkih svojstava legura. Pritom je GLLB-SC predstavljen kao superiorna alternativa tradicionalno često korištenim funkcionalima u optici i plazmonici jer daje točnije rezultate bez značajnog povećanja računalne zahtjevnosti. Pokazano je da je izbor funkcionala izmjene i korelacije bitan i kod optimizacije struktura legure.

Uspostavljena je i baza podataka s dielektričnim funkcijama nekoliko binarnih sustava legura pri čemu je pokazano da teorija funkcionala gustoće omogućuje kvalitativno predviđanje trendova. Uz to, teorija funkcionala gustoće omogućuje odvajanje doprinosa prijelaza između vrpce i unutar vrpce što je pomoglo da se optički gubici pri niskim energijama izoliraju te da se pokaže da nastaju zbog emergentnih svojstva legiranja. Navedeni optički gubici pripisani su prijelazima između “preklopljenih” i “razdvojenih” vodljivih vrpce, a uzroci navedenih efekata objašnjeni su pomoću rezultata izračuna strukture elektronskih vrpce. Uz to, računi gustoće elektronskih stanja upotpunili su opažanja vezana uz strukturu elektronskih vrpce i pružili objašnjenje za ovisnost dielektrične funkcije o sastavu legure. Proučen je i utjecaj konfiguracije na sva od navedenih svojstava te se pokazalo da u većini slučajeva nije značajan. Simulacije na temelju klasične elektrodinamike pomogle su povezati svojstva makroskopskih legura s optičkim i plazmoničkim svojstvima koja bi imale legirane nanostrukture čime je stvorena poveznica između strukture tvari, fundamentalnih svojstava (elektronske strukture) i optičkih te plazmoničkih svojstava.

Naposljetku, proučena je i mogućnost ugađanja distribucije vrućih nosioca naboja legiranjem u sklopu čega je predstavljena metoda koja uzima u obzir očuvanje količine gibanja prilikom elektronskih pobuda (eng. *momentum-resolved JDOS*). Elementi su klasificirani na temelju njihove elektronske strukture u makroskopskom materijalu što se pokazalo prikladnim za objašnjenje raznolikog utjecaja na distribuciju vrućih nosioca naboja

---



koji imaju. Pritom je razjašnjena uloga emergentnih svojstava legiranja, kao i drugih trendova povezanih s promjenom elektronske strukture legiranjem. Navedeni rezultati omogućuju racionalni dizajn, to jest, inženjering svojstava povezanih s generacijom vrućih nosioca naboja

---

## § 1. INTRODUCTION

More than a century has passed since the inception of the field of plasmonics<sup>1</sup>, with its intermittent progress accelerating rapidly once again in recent years. This resurgence in the field is based on exploring the exotic effects in plasmonic nanostructures and their promising utilizations, and can be divided in two waves:

In the first wave the goal was to manipulate the light energy by controlling the flow of light and guiding it by using plasmonic nanostructures as nanoantennas<sup>2</sup>. In this way, light could be directed and focused on a nanometer (subwavelength) scale, which spurred high hopes for advancements in sensing<sup>3</sup> and creation of miniature devices for optical communication<sup>3</sup>. While good progress was indeed achieved, the limiting factor for such utilizations became the loss of light energy by its transformation to other forms of energy, predominantly dissipation through heat<sup>4</sup>. Thus, the focus was shifted on minimizing the losses, with the metaphorical “Holy Grail” being the discovery of a lossless plasmonic material<sup>5,6</sup>. However, as was proven after years of struggle, the losses were here to stay. This brought about a collective shift in the field, wittily described by Boriskina *et al.* as “plasmonics Kübler-Ross grief cycle”<sup>7</sup>, shown on Figure 1. At the end, the “grief cycle” led to the acceptance of (optical) losses. This marked the start of the second wave of recent resurgence in plasmonics research.

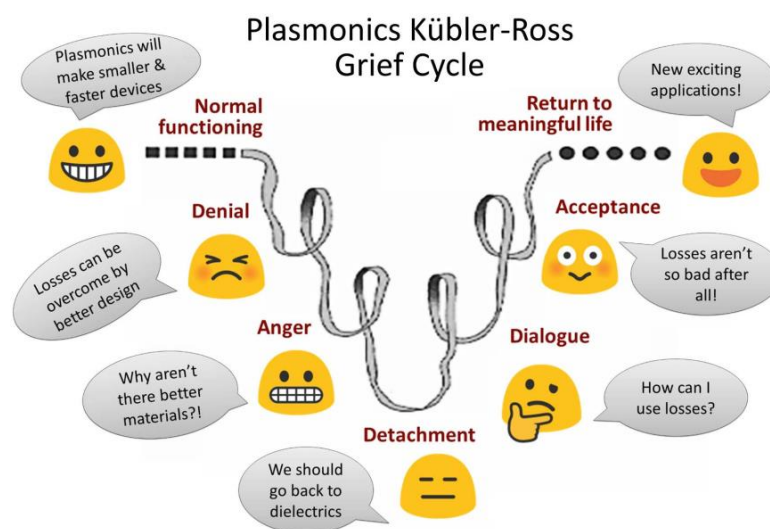


Figure 1. Kübler-Ross grief cycle figuratively depicting the shift in the field of plasmonics caused by the inability to eliminate optical losses.<sup>7</sup>

In the second wave, which is currently ongoing, optical losses are not only accepted but in many cases welcome. The goal of the second wave is to take advantage of the ability of nanostructures to transform light energy into other forms of energy and explore the opportunities this offers. The energy transformations in plasmonic nanostructures happen due to plasmon decay during which energy of the light that has been absorbed by the nanoparticle ends up in highly energetic (hot) charge carriers. These hot carriers can transfer the energy to the surroundings by injecting into the adjacent semiconductors<sup>8</sup>, for example in a photovoltaic cell<sup>9,10</sup>, completing the transformation of light energy into electrical energy. Alternatively, they can be injected into adsorbed molecules<sup>10,11</sup> inducing chemical reactions and turning light energy into chemical energy. If they instead remain inside the nanostructure, they will quickly scatter with other electrons and the lattice, thus transferring their energy to vibrational modes and turning the energy of the light into thermal energy<sup>12</sup>. The resulting intense local heating is explored for uses such as water vapor production<sup>13</sup> and thermal ablation of tumors<sup>14</sup>. Transformation of light energy into mechanical energy was tentatively achieved by creating “plasmonic tweezers”<sup>15</sup>. Hinting at future prospects in that regard, a concept of light-propelled machineries consisting of plasmonic nanoparticles was introduced very recently by Mezzasalma *et al.* showing that transformation to mechanical energy and useful work might soon become a topic of interest<sup>16</sup>.

*Recent developments thus show that the plasmonic nanostructures can abstractly be thought of as devices for manipulation and transformation of the energy of light (Figure 2).*

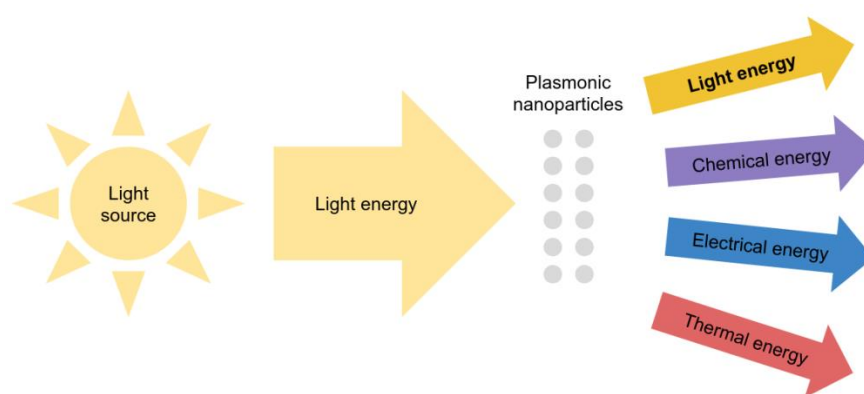


Figure 2. Manipulation of light energy (first wave of recent research in plasmonics, bold text depicts the change) and transformation of light energy into other forms of energy (second wave of recent research in plasmonics) by utilizing plasmonic nanoparticles as a means of manipulation and transformation.

It is important to note that not all plasmonic nanostructures can be useful for each of the aforementioned utilizations. For example, every nanoparticle has specific properties that are a function of its size, shape, and the material it is made of. Furthermore, in a system consisting of multiple nanoparticles, their spatial arrangement (relative distance) also plays a major role in how the light is manipulated and transformed. While their size, shape and spatial arrangement (when possible) have been controlled to tune the plasmonic properties of nanostructures to suit the desired purposes, material diversity of plasmonic nanoparticles is relatively low and provides very limited tuning opportunities<sup>6</sup>. Ag and Au have been used in the majority of research, with Cu and Al following as common alternatives<sup>13</sup>. Other metals are less suitable for such purposes either due to high losses, plasmon resonance far away from the spectral region of interest or low stability.

However, one way to tune the plasmonic properties by changing the material is through alloying different metals. Alloying unlocks a vast compositional space to be explored due to the large number of metal combinations and the possibility to finely adjust their respective ratios. Moreover, metals that can be combined in a plasmonic nanoalloy (alloy nanostructure) do not have to be only the aforementioned good plasmonic metals. Standard plasmonic metals can also be combined with less commonly used ones, thus opening the doors to introduction of new properties. However, it is not obvious which alloy composition could be most suitable for desired purposes. Finding the right alloy composition by producing many alloy combinations experimentally is exceedingly expensive, both monetarily and time-wise. The issue of finding the right alloy combination is exacerbated by the often rapid and nonlinear variation of alloy properties between the properties of the constituent elements. Adding to the problem, the alloy properties sometimes are not inherent from any of the constituent elements but emerge as a consequence of alloying. This reflects negatively on the use of empirical models as predictive tools since they are suitable only for systems with gradually varying optical and plasmonic properties and would not be suitable for prediction of emergent effects. Additionally, they would likely provide limited physical understanding of the observed predictions. For that reason, there is a need for a computational method that would predict plasmonic properties with as little empirical parameters as possible. It would also be preferable for the method to give insight into the structure-properties relationship, thus providing tools for a rational design.

---

A method based on density functional theory (DFT) could potentially meet all of the aforementioned requirements. It should, in principle, require almost no empirical data to predict the properties of materials that are being studied. On top of that, such a method should be especially useful in helping understand the fundamental properties of the material and how they determine its function. After the material properties have been determined they can be used for electrostatics simulations, to take into account the influence of shape and size of the nanoparticles and even interparticle distance. Such an approach enables the calculation of optical properties thus showing how to control the optical energy flow and the calculation of electronic structure to obtain fundamental insights into electronic transitions excited by light. Moreover, such an approach could also give insight into the properties related to transformation of energy, such as hot carrier energy distribution, and how it changes due to alloying. However, there are many levels of theory when considering a DFT-based approach, with dramatically varying degrees of computational cost associated with them, and also with varying adequacy for prediction of optical and plasmonic properties. Finding a suitable compromise between computational cost and quality of prediction is therefore crucial.

The principal goal of this dissertation is to establish a computational framework based on DFT calculations with a satisfactory combination of computational efficiency and accuracy. The accompanying hypothesis is that a same-cost alternative to the most commonly used approaches (currently at the generalized gradient approximation level of theory) with far superior performance for optical and plasmonic properties calculations can be found. The second goal is to obtain a structure-property relationship by creating a database of predicted optical properties for nanoalloys with different ratios of different plasmonic metals. It is hypothesized that the evolution of optical properties with composition can be explained by connecting composition, electronic structure, and the resulting dielectric function. The final aim of this work is to present a method that provides satisfactory predictions of hot carrier generation in alloys and use it to study the effects of elemental composition, with the hypothesis that alloying can be used to modulate and tune hot carrier generation.

---

## § 2. THEORETICAL BASIS

Some of the concepts that are a pivotal part of this work, such as the band structure and the dielectric function, are not commonly used in chemistry literature. For this reason, in the Theoretical basis they will be presented in a relatively intuitive and phenomenological manner, and connected to the concepts that are more commonly used in chemistry to describe the fundamental properties of matter.

### 2.1. From orbitals to bands - band structure and density of states

In chemistry, the theoretical representation of the electronic structure has traditionally been developed and adjusted to study molecules - units of substance usually characterized by a fairly limited number of atoms. The most suitable way of representing the electronic structure has thus been through the framework of atomic and molecular orbitals and the corresponding electronic states. Even in the study of molecular crystals, which can be thought of as a near-infinitely repeating lattice, theories such as crystal field theory focused on the local environment of the atomic centers of interest. Though this view holds merit, this conceptual framework based on a few atomic centers and discrete states is not practical when considering the electronic structure of an extended system. In this chapter a connection between traditional concepts and theories in chemistry towards the concepts more traditionally used in solid state physics is made, to provide a way to smoothly transition between them. The chapter is partially inspired by, and relies on, the work by Roald Hoffman in connecting these concepts for solids and surfaces<sup>17</sup>.

Starting from valence bonding theory, the picture of bonding is relatively simple and localized on the few atoms. Initially, the shape of the molecule of interest is either known or supposed, for example using valence shell electron pair repulsion (VSEPR) theory. Based on that shape, a hybridization of the atomic orbitals of a single atom is supposed such that the orientations of the resultant hybrid orbitals correspond to the desired shape (Figure 3).

---

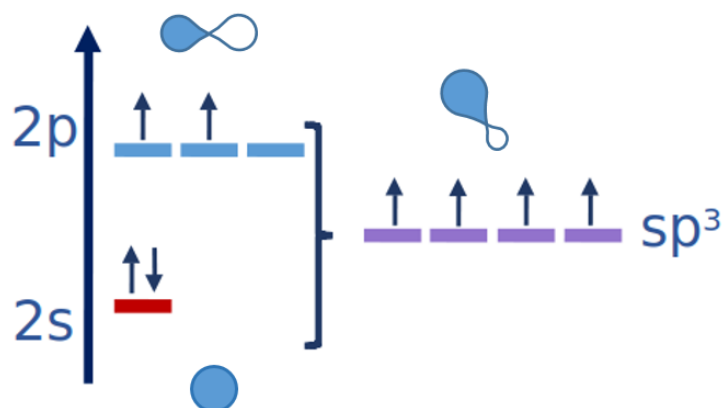


Figure 3. Hybridization of atomic orbitals, for example on the carbon atom: one s orbital hybridizes with the four p orbitals to form four  $sp^3$  orbitals.

In the molecular orbital theory the nature of bonding is viewed in a more complex, delocalized way. Here, the molecular orbitals can span multiple centers (atoms), with the corresponding electron density distributed between them. Such a view is necessary to represent the bonding nature of, for example, diborane ( $B_2H_4$ ) shown in the Figure 4.

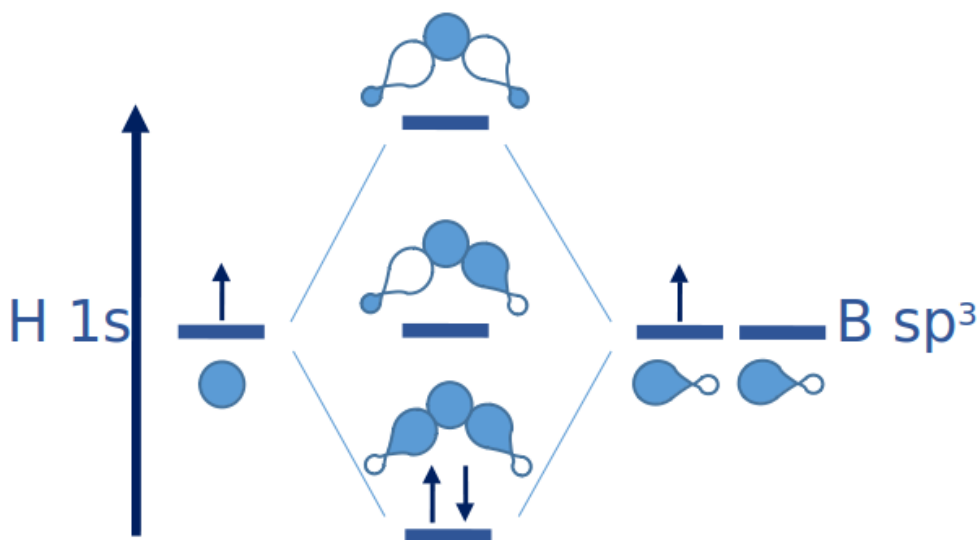


Figure 4. Formation of molecular orbitals by combining one hydrogen s orbital and two boron  $sp^3$  orbitals.

This delocalized view of bonding provides a suitable starting point to transition to the solid state physics point of view, by extending the system over many more centers. As the simplest

example, consider a one dimensional chain of equally spaced hydrogen atoms, labeled by the index  $n$ , such as on the Figure 5 a).

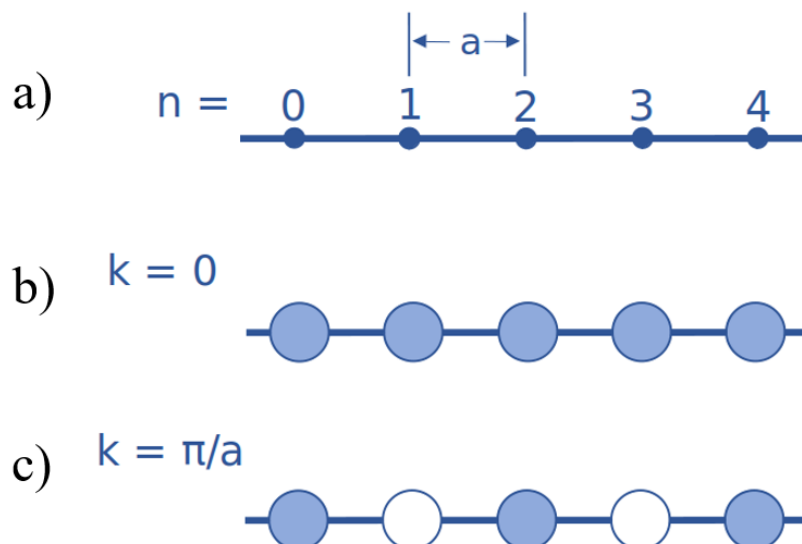


Figure 5. a) A chain of equally spaced H atoms. b) s orbitals of hydrogen atoms with the same sign (no sign change, fully bonding state) corresponding to  $k = 0$ . c) s orbitals of hydrogen atoms with maximally interchanging signs (fully antibonding state).

Let the 1s orbital of the H atom be a basis function, labeled  $\Phi_n$ . Taking into account the translational symmetry of the system, its wave function can be written as

$$\Psi_k = \sum_n e^{ikna} \Phi_n \quad (2.1)$$

where  $a$  is the atom spacing. Since  $k$  determines the periodicity of sign changes, and consequently the number of nodes, two extrema exist: one with no sign changes in the Figure 5 b) and another with the maximum number of sign changes in the Figure 5 c). For  $k = 0$  all the 1s orbitals have the same sign, so the corresponding molecular orbital of this hypothetical 1D molecule would be the lowest energy (best) bonding orbital.

$$\Psi_0 = \sum_n e^0 \Phi_n = \Phi_0 + \Phi_1 + \Phi_2 + \dots \quad (2.2)$$

Conversely, for  $k = \pi/a$ , the resulting molecular orbital is fully antibonding in nature.

$$\Psi_{\pi/a} = \sum_n e^{i\pi n} \Phi_n = \Phi_0 - \Phi_1 + \Phi_2 - \dots \quad (2.3)$$



Another such orbital exists for  $k = -\pi/a$ , and the total number of different values of  $k$  in the range between  $\pi/a$  and  $-\pi/a$  is determined by the number of translations in the chain. Therefore, an analogy with the crystal can be made: the space between the two atoms separated by the distance  $a$  can be thought of as a unit cell and the chain as a crystal lattice. It should be noted that extending the values of  $k$  beyond  $|\pi/a|$  results in repeating the wavefunctions that are already in the range. The range of values of  $k$  that result in unique periodicity is called the first Brillouin zone.

With that in mind, the simplest band structure can be represented using the framework of combining atomic orbitals. When atomic orbitals are combined, an equal amount of molecular orbitals is produced, with different energies: for example bonding (low), nonbonding (medium) and antibonding (high). If a large amount of atoms and their corresponding orbitals is combined, the resulting energy states form a near-continuous spread in a given energy range (a band). Resolved by the different values of  $k$ , the band is represented by the line which depicts how the energies of states in the atomic chain change with the periodicity of the sign change.

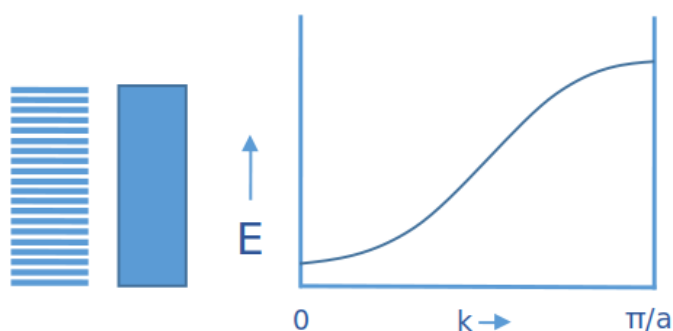


Figure 6. Discrete states in a certain energy range and a near-continuous spread of states in the same energy range, forming a band (left). Energies of a near-continuous number of states coming from  $s$  orbitals on a near-infinite chain (as shown in the Figure 5) plotted as a function of  $k$ -points in the range from  $k = 0$  to  $k = \pi/a$ . Fully bonding picture corresponds to the lowest energy, with rising energy of states up to the fully antibonding picture.

The direction of energy change with the changing  $k$  can be different for different types of orbitals, and depends on their symmetry. For example,  $p$  orbitals on a chain would have an antibonding interaction when  $k = 0$ , but a bonding interaction when  $k = \pi/a$ , meaning that the corresponding band has an opposite direction to the band corresponding to  $s$  orbitals.

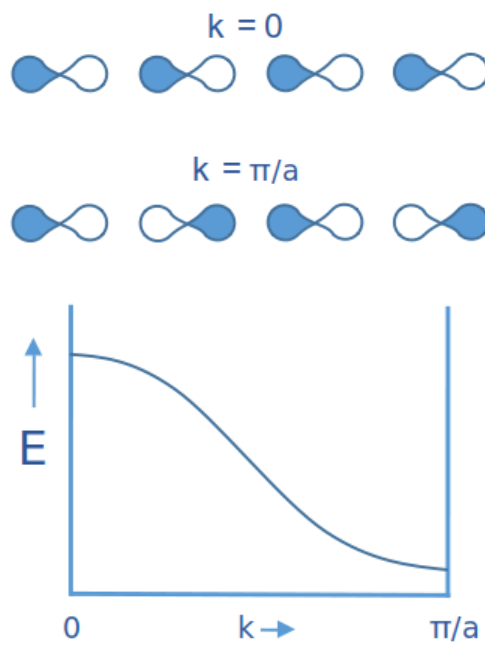


Figure 7. Orbitals of p-type aligned as on a 1D chain with no sign change ( $k = 0$ ) and with maximally interchanging signs ( $k = \pi/a$ ). (top) Unlike for the s-orbitals, due to the different symmetry, in this case no sign change leads to the fully antibonding picture while the opposite leads to the fully bonding picture. Therefore the energy band drops from  $k = 0$  to  $k = \pi/a$  (bottom).

A more complex band structure is formed for a 2D lattice such as depicted on the Figure 8.

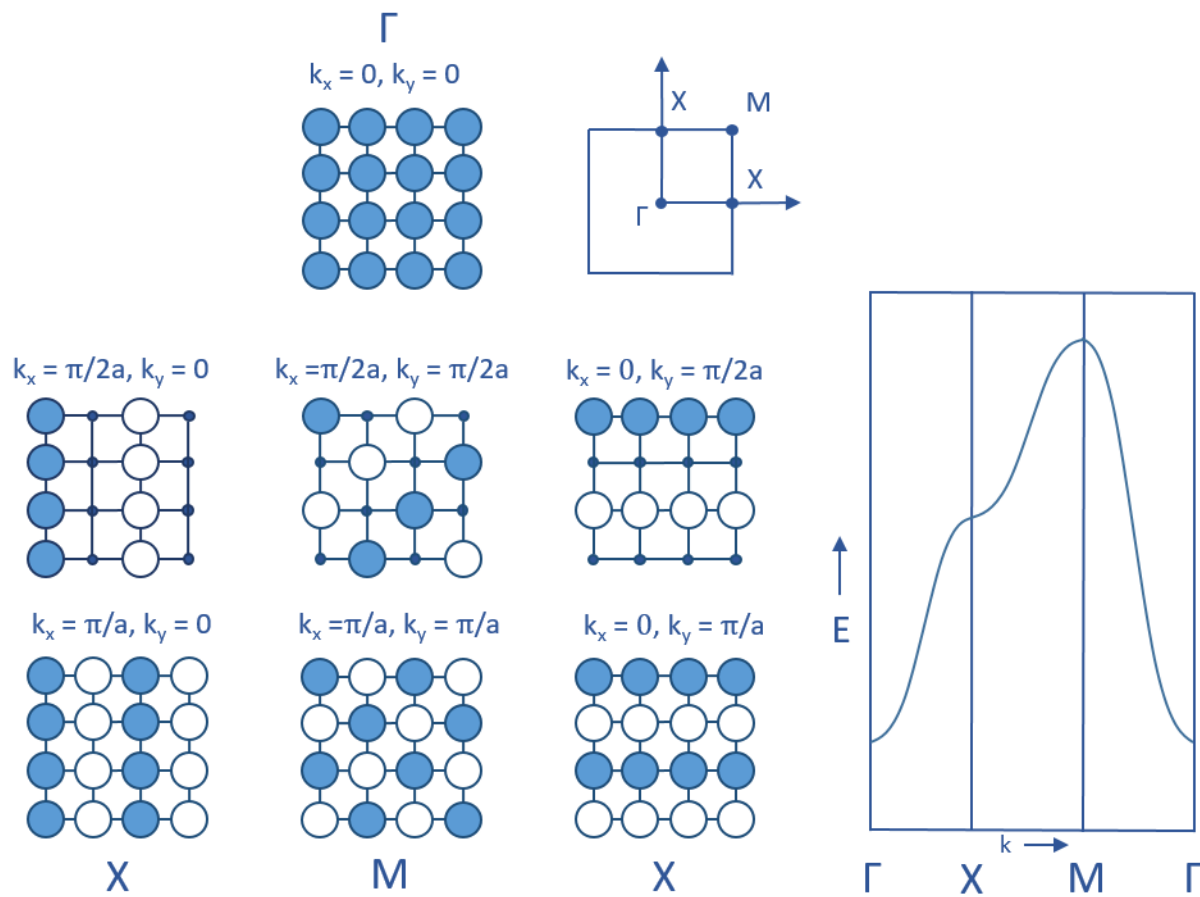


Figure 8. A 2D lattice with different periodicities of orbital sign changes corresponding to the high symmetry points and the resulting band structure. Figure adapted from the book by Roald Hoffman.<sup>17</sup>

Letters are used to label certain pairs of values of  $k$  that are called high symmetry points. Since these points depict the extrema (bonding and antibonding-like) as well as the nonbonding-like states, the energy change plotted between those lines well depicts the interesting properties of the electronic structure of the crystal. Since the slope of the bands near these points is relatively flat, more states are located in the vicinity (in the energy range) of such points. Therefore, the density of states (DOS) is greater in the vicinity of such points when compared to other areas of the band structure, as shown on the Figure 9.

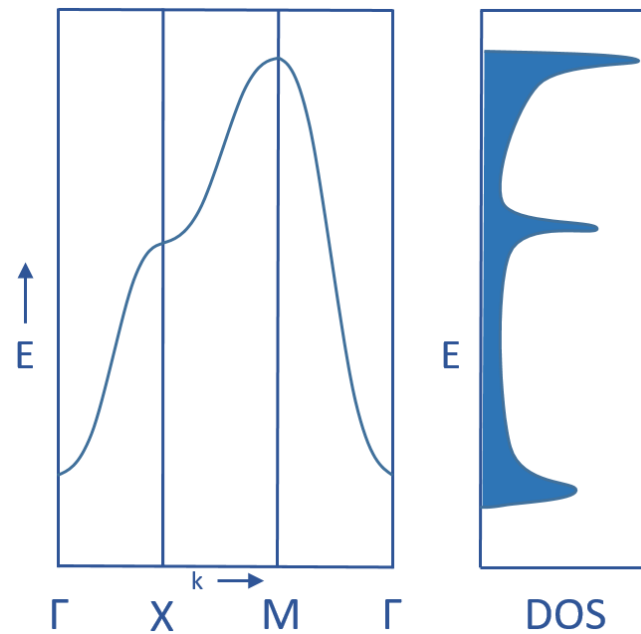


Figure 9. Band (left) and the corresponding density of states for the 2D lattice system shown on the Figure 8. Notice that the location of the peaks in the density of states corresponds to the „flatter“ areas at and near the critical points in the band structure.

Mathematically, DOS is defined as:

$$\rho(\varepsilon) = \sum_n \langle \psi_n | \psi_n \rangle \delta(\varepsilon - \varepsilon_n) \quad (2.4)$$

where  $\varepsilon_n$  denotes the eigenvalue of the eigenstate  $|\psi_n\rangle$

When a 3D crystal with several types of relevant orbitals is considered, the complexity of the band structure further increases (Figure 10).

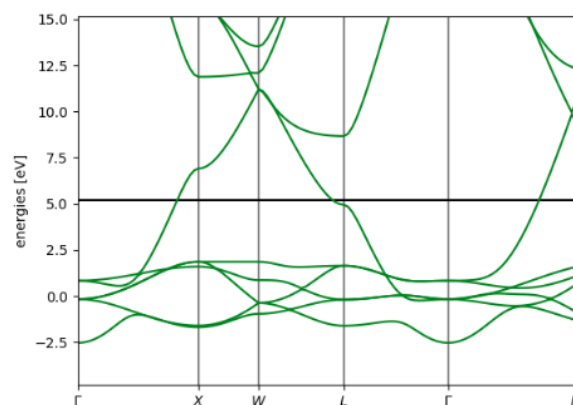


Figure 10. Band structure of the bulk Ag with a face centered cubic lattice.

The horizontal line on the Ag band structure shown on the Figure 10 represents the Fermi level. At 0 Kelvin, Fermi level represents the energy of the highest state occupied by an electron. At higher temperatures this level can be thought of as the energy which, at thermodynamic equilibrium, has a 50% chance of being occupied<sup>18</sup>. For conductors, such as Ag, band structure always has at least one band crossing the Fermi level. The bands lying far below the Fermi level are fully occupied. In the case of Ag these bands are formed by d orbitals and can be seen as the relatively flat set of bands several eV below the Fermi level. The bands above the Fermi level are unoccupied.

## 2.2. Dielectric function

In electrostatics, the dielectric constant describes how the material screens the external time-independent electric field and it is a real quantity. However, when the electric field is allowed to oscillate (in electrodynamics), the material screens the time-dependent electric field. Its response to the external perturbation by the electric field depends on the frequency of the oscillation and is described by the dielectric function. As the material adapts to the external perturbation there might be a phase shift (delay) in the response of the material with respect to the oscillation of the external field, which makes the dielectric function a complex quantity and leads to optical losses which are described by the imaginary part of the dielectric function.

In metals, upon the perturbation by the electric field the conduction electrons are able to move inside the lattice. Their motion can, in that case, be described mathematically as a damped oscillator,

$$-eE = m\ddot{r} + \gamma m\dot{r} \quad (2.5)$$

where  $m$  is the mass of electrons,  $-e$  is the elementary charge of an electron,  $E$  is the total electric field (including both the external electric field and the counteracting electric field created by the rest of the material),  $\gamma$  is the damping constant, attenuating the electron movement, and  $r$  is the electron displacement. By solving this equation and introducing polarization  $P(\omega)$ , it can be shown that

$$P(\omega) = \frac{ne^2}{m(\omega^2 + i\gamma\omega)} E(\omega) \quad (2.6)$$

Where  $n$  represents the charge density. Finally, by relating the polarization with the dielectric function

$$P(\omega) = \varepsilon_0(\varepsilon(\omega) - 1)E(\omega) \quad (2.7)$$


---

dielectric function can be expressed as

$$\varepsilon(\omega) = 1 - \omega_p/(\omega^2 + i\gamma\omega) \quad (2.8)$$

where the plasma frequency was introduced as

$$\omega_p = \sqrt{ne^2/m\varepsilon_0} \quad (2.9)$$

This classically described dielectric function, known as the Drude model, includes only the interband electronic transitions by the free electrons in the conduction band. However, if the frequency of the light is sufficient to excite electrons from one band to another, the interband contribution to the dielectric function is added. The frequency dependence of such transitions can be represented by Lorentzian oscillators, and thus the interband contribution can be represented as a sum of Lorentzian oscillators. In metals, direct interband transitions (transitions for which the momentum is conserved) usually strictly dominate over indirect interband transitions (those that require momentum transfer via photon-phonon coupling or some other mechanism). In such cases, the contribution of interband transitions for any given photon energy will be in large part based on the availability of the density of the pairs of occupied ( $N_{occ}$ ) and unoccupied ( $N_{unocc}$ ) states separated by that energy, also called the joint density of states (JDOS):

$$JDOS(E_{photon}) = \int N_{occ}(E)N_{unocc}(E + E_{photon})dE \quad (2.10)$$

By observing the band structure, it can be deduced that the highest JDOS for a given photon energy can be expected at the regions where two bands are near-parallel, or at the regions where at least one of the bands has low dispersion (is relatively flat), since this translates to an increase in the DOS at that energy, translating to either a high  $N_{occ}$  if the lower energy band is flat, or high  $N_{unocc}$  if the higher energy band is flat (or both). This can be mathematically described by the band having a (near) zero derivative, which is why such flat regions of the band are referred to as regions around critical points. As was shown in the Figure 8 for a 2D lattice, critical points are usually associated with a special, high symmetry k-point in the Brillouin zone. As expected from that fact, it can be seen from Ag band structure that the regions around critical points are located near the X and the L point in the band structure. Abundant interband transitions caused by the high JDOS near these points manifest themselves as a peak in the imaginary part of the dielectric function. The lowest energy required for interband transitions to be available is called the interband transition onset or

---

threshold. For Ag band structure it can be seen that the interband transition onset appears near the L point (it should be noted that even though a part of the L point is located below the Fermi level, due to Fermi-Dirac distribution, at temperatures above 0 Kelvin even some states slightly below the Fermi level can be unoccupied).

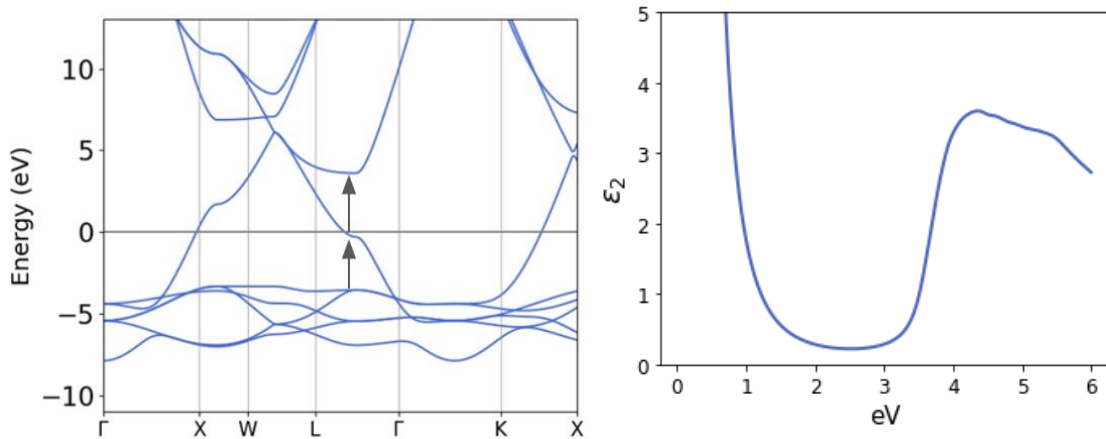


Figure 11. Band structure (left) and the imaginary part of dielectric function of the face-centered cubic Ag. The arrows near the L-point depict the lowest energy interband transition from a filled state to the unfilled state (near the Fermi level. It is visible that the abrupt rise in the imaginary part of the dielectric function, a bit above 3 eV, corresponds to exactly that energy, since it is caused by the interband transitions. For that reason it is often referred to as the interband transition threshold.

Thus, the dielectric function can be represented as the combination of the intraband contribution (called the Drude term) and the interband contribution (Figure 12).

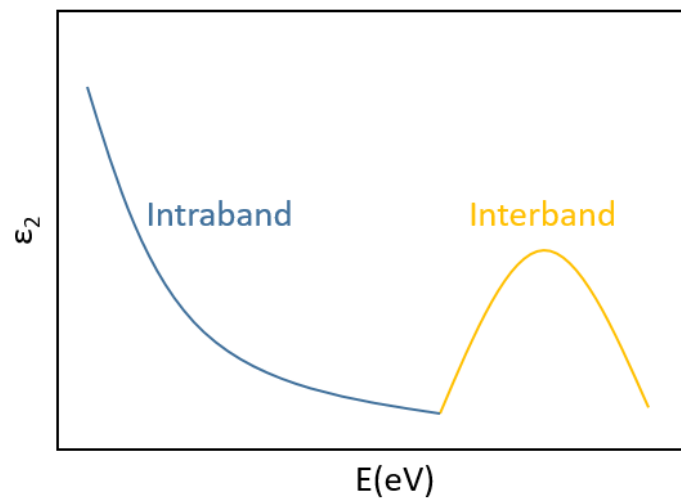


Figure 12. Interband (orange) and intraband (blue) contributions to the imaginary part of the dielectric function.

### 2.3. Density functional theory

Density functional theory provides a clever way of calculating the fundamental properties of the matter by avoiding the issue of solving the Schrödinger equation by reducing the  $3N$  dimensional problem, where  $N$  is the number of electrons in the system, to a 3 dimensional one.

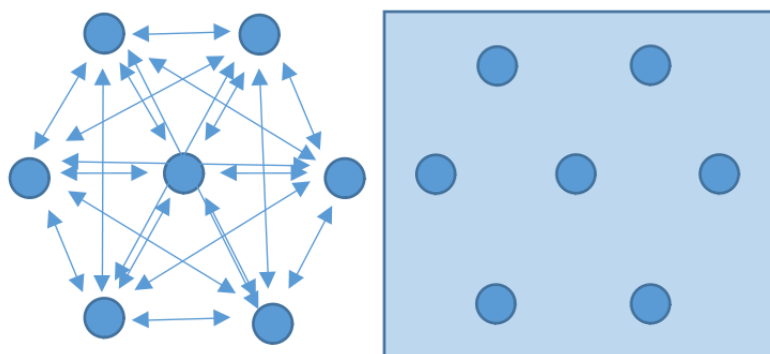


Figure 13. Left: Pictorial representation of a system of particles where each particle interacts with all other particles, which can be described by a wavefunction depending on the spatial coordinates of each particle. In this way solving the Schrödinger equation would require finding a solution to a  $3N$  dimensional problem where  $N$  is the number of electrons in the system. Right: Pictorial representation of the way the density functional theory reduces the dimensionality of the problem. In this case each electron contributes to the total electron density, a collective property which can be described with 3 dimensions, thus presenting a 3 dimensional problem.

The basis of this simplification is in two Hohenberg-Kohn theorems<sup>19</sup>:

1. All properties of a given system are determined by the electron density
2. True ground state electron density of a system minimizes the energy functional

It follows that the knowledge of the electron density is equivalent to the knowledge of the ground state wavefunction.

The energy functional mentioned in the second Hohenberg-Kohn theorem includes the kinetic energy and the energy corresponding to the electron-electron interaction which, along with the external potential (originating from the atomic nuclei) are the components of the total Hamiltonian  $\hat{H}$ :



$$\hat{H} = \hat{T} + \hat{U}_{ee} + \hat{V}_{ext} \quad (2.11)$$

where  $\hat{T}$  is the kinetic energy operator,  $\hat{U}_{ee}$  accounts for the electron-electron interactions and  $\hat{V}_{ext}$  to the potential by the external potential.

For calculation of the kinetic energy a total (many body) wavefunction is necessary. However, such a wavefunction is unknown, so an approximate way of determining it was established in Kohn-Sham theory<sup>20</sup>. Instead of a many body wavefunction, a system of one-electron Schrödinger-like equations including non-interacting particles in an effective potential is constructed using variational method based on expression for energy functional:

$$E[\rho] = E_{kin}[\rho] + E_{coul}[\rho] + E_{xc}[\rho] + E_{ext}[\rho] \quad (2.12)$$

where the  $E_{kin}[\rho]$  denotes the kinetic energy of the system,  $E_{ext}[\rho]$  the energy due to the influence of external potential,  $E_{coul}[\rho]$  denotes the Coulomb energy accounting for the electron repulsion, and the  $E_{xc}[\rho]$  the contribution of electron correlation and exchange. In this case the coulombic contribution has been separated from the electron-electron contribution, with the exchange-correlation term introduced to account for the remaining effects on the total energy coming from electron exchange and the many-body correlation. The effective potential  $V_{eff}$  is of the form

$$V_{eff} = V_{ext} + V_H + V_{XC} \quad (2.13)$$

where  $V_{ext}$  is the external potential,  $V_H$  the Hartree term which describes the electron-electron repulsion and  $V_{XC}$  the term that describes many-particle interactions. In principle, the potential would be such that it generates the same density as a system of interacting particles. Unfortunately, the formulation of the exchange correlation functional that would be needed to achieve that is not known and different formulations of the exchange-correlation functional, with different levels of complexity and accuracy are available.

### 2.3.1. Exchange correlation functionals and the derivative discontinuity

The simplest formulation of the exchange-correlation functional is based on the local density approximation (LDA)<sup>21</sup>. In this approximation the change in the electron density is assumed to be very gradual thus allowing the system to be treated as a homogeneous electron gas. Therefore, the exchange and correlation contributions at a given point depend only on the electron density at that exact point (locally).

Generalized gradient approximations (GGA) introduce semi-locality<sup>21</sup>. They account for the variations in electron density around the point where the exchange and correlation

contributions are being determined by the use of electron density gradient. This lowers the underestimation of the exchange term and overestimation of the correlation term, errors characteristic of LDA, which leads to improvement of many ground state properties.

However, both the LDA and the GGA functionals severely underestimate the band gap of the semiconductors, and also the interband transition threshold in metals<sup>22</sup>. An intuitive reason for this is in the self-interaction error inherent to the Kohn-Sham representation of the system. Since the electron is, in that case, technically interacting with itself, the excess repulsion increases the energy of the resulting filled states and pushes them upward. Unoccupied states do not experience the self-interaction as it does not contribute to the density, and do not experience the same upwards shift in energy. Therefore, the gap between occupied and unoccupied states is lowered.

Another way to describe the reason for the band gap lowering is by considering that, for a system with  $N$  electrons, band gap can be described as

$$E_g = (E_{N+1} - E_N) - (E_N - E_{N-1}) \quad (2.14)$$

Where  $E_g$  is the fundamental gap, and  $E_N$  the ground-state energy of the particle with  $N$  electrons<sup>23</sup>. The first term on the right-hand side of the equation is related to the electron affinity and the second to the ionization potential. Thus,  $E_g$  can in this case be obtained by calculating the ground-state energy of systems that correspond to the appropriate number of electrons in the equation 2.14. The qualitative depiction of the difference between the exact functional and LDA or GGA functionals in how the total energy of the system depends on the number of electrons the system can be seen on the Figure 14.

---

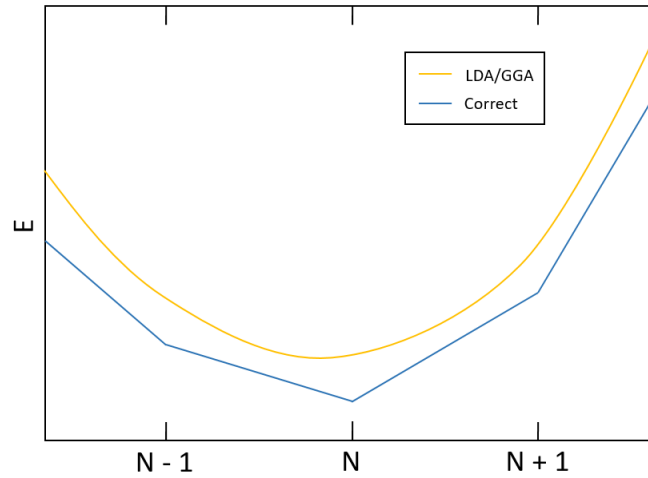


Figure 14. Dependence of the total energy of the system on the number of electrons in the system. The correct dependence includes a linear behavior between integer electron numbers, with slope coefficient changing at each integer. Unlike that, the behavior obtained by local and semilocal exchange-correlation functionals shows a smoothly changing total energy.

It is visible that the proper behavior of the total energy includes linearly changing energy between the integer (whole) number of electrons, whereas for local and semilocal functionals applied to the Kohn-Sham system this behavior is far smoother. It can be shown that the correct gap  $E_g$  always differs from the gap that can be obtained by the energies of the Kohn-Sham system  $\epsilon$ , with  $N$  denoting the number of electrons in the system, by the quantity  $\Delta_N^{xc24}$ , which is called the (electronic energy) derivative discontinuity:

$$E_g = \epsilon_{N+1} - \epsilon_N + \Delta_N^{xc} \quad (2.15)$$

Some of the ways the derivative discontinuity can be introduced and the gap energy corrected are mentioned in the Literature review section.

### 2.3.2. Calculations involving extended systems and the PAW method

When applying DFT to extended systems such as solids, two types of difficulties are usually encountered. Numerical difficulties near the core arise due to the rapid oscillations of the wavefunction. Such wavefunctions are characterized by the high kinetic energy of the electrons and by rigidity, meaning that in that region wavefunctions are almost fully independent on the environment. Conversely, in the bonding region, the wavefunctions are very smooth and large, meaning low kinetic energy. Almost a complete basis set is needed to

represent them, and they are very responsive to the changes in the environment. A suitable method to tackle these issues is the plane augmented wave (PAW) method<sup>25,26</sup>.

To make the representation of the full wave function suitable in both regions, it is divided in two parts, one near the core called the projection sphere and the bonding region, between the atoms. The true wavefunction is approximated by a smooth auxiliary wavefunction with a rapidly convergent plane wave expansion which can be efficiently tackled computationally. Outside the projector sphere the smooth part of the true wavefunction and the auxiliary wave function have to be the same. Frozen core approximation is used for the core states, which is justified due to rigidity of the true wavefunction in that region. Therefore only the valence states are included in the expansion of the wavefunction. In brief, the method can be mathematically described as follows (notation based mostly on papers by Blöchl<sup>26</sup> and Rostgaard<sup>27</sup>):

Auxiliary, smooth, wavefunction  $|\tilde{\Psi}_n\rangle$  can be transformed to the true all electron Kohn-sham single particle wavefunction  $|\Psi_n\rangle$  via a linear transformation  $\hat{T}$

$$|\Psi_n\rangle = \hat{T}|\tilde{\Psi}_n\rangle \quad (2.16)$$

where  $n$  denotes the quantum state. A Schrödinger-like equation is then be obtained

$$\hat{T}^\dagger \hat{H} \hat{T} |\tilde{\Psi}_n\rangle = \hat{T}^\dagger \hat{T} |\tilde{\Psi}_n\rangle \quad (2.17)$$

where  $\hat{H}$  is the Hamiltonian. Modification to the wavefunction is made close to the nuclei (inside the augmentation sphere)

$$\hat{T} = 1 + \sum_a \hat{T}^a, \quad |\mathbf{r} - \mathbf{R}^a| < r_c^a \quad (2.18)$$

where  $a$  stands for an atom index denoting that the transformation is centered on that atom. Outside the region beyond the cutoff radius  $r_c^a$  the transformation is not applied. Inside the sphere the true wavefunction is expanded in the partial waves  $\phi_i^a$  and the auxiliary wavefunction is expanded in corresponding auxiliary partial waves  $\tilde{\phi}_i^a$

$$|\phi_i^a\rangle = (1 + \hat{T}^a)|\tilde{\phi}_i^a\rangle \Leftrightarrow \hat{T}^a|\tilde{\phi}_i^a\rangle = |\phi_i^a\rangle - |\tilde{\phi}_i^a\rangle \quad (2.19)$$

If smooth partial waves form a complete set inside the augmentation sphere, the smooth all electron wave function can be expanded as a linear combination of smooth partial waves inside the sphere. The coefficients  $P_{ni}^a$  will be linear functionals of smooth all electron wave function

$$P_{ni}^a = \langle \tilde{p}_i^a | \tilde{\psi}_n \rangle = \int \tilde{p}_i^{a*}(\mathbf{r} - \mathbf{R}^a) \tilde{\psi}_n(\mathbf{r}) d\mathbf{r} \quad (2.20)$$

where the  $|\tilde{p}_i^a\rangle$  are smooth projector functions (some examples shown on the Figure 15).

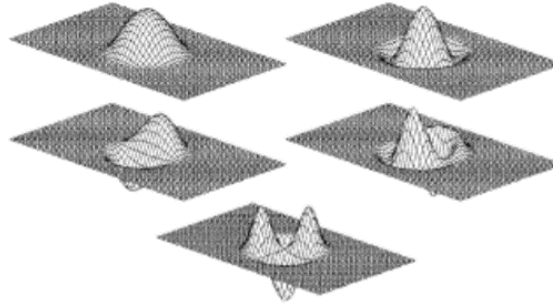


Figure 15. Projector functions of the Cl atom. Two topmost function correspond to two s-type partial waves the two functions in the middle to the p-type partial waves and the bottom one to the d-type.<sup>25</sup>

The smooth projector functions must satisfy the completeness relation

$$\sum_i |\tilde{\phi}_i^a\rangle\langle\tilde{p}_i^a| = 1 \quad (2.21)$$

The linear transformation can then be defined as

$$\hat{T}^a = \sum_i \hat{T}^a |\tilde{\phi}_i^a\rangle\langle\tilde{p}_i^a| = \sum_i (|\phi_i^a\rangle - |\tilde{\phi}_i^a\rangle)\langle\tilde{p}_i^a| \quad (2.22)$$

Finally, the all electron Kohn-Sham wave function can be constructed as

$$\psi_n(\mathbf{r}) = \hat{\psi}_n(\mathbf{r}) + \sum_a \left( \psi_n^a(\mathbf{r} - \mathbf{R}^a) - \hat{\psi}_n^a(\mathbf{r} - \mathbf{R}^a) \right) \quad (2.23)$$

### 2.3.3. Linear dielectric response time-dependent DFT and the dielectric function calculation

To obtain the dielectric function of a material computationally (using the DFT), the response to the optical (electromagnetic) perturbation has to be determined. In most cases of interest the perturbation by the external light source will be relatively small when compared to the strength of the interactions of charged particles in the material. Therefore, only a first (linear) term of the Taylor expansion with respect to the perturbation can be used. This means that the linear response depends only on the properties of the unperturbed system, which simplifies the calculation scheme.

In GPAW, the program package used in this work, the linear response function is calculated using the ground state electronic structure of the material, which is obtained on the real-space grid. Afterwards, the density response function is obtained as a function of frequency and the wave vector using the projector augmented wave method. The perturbation is assumed to vary slowly enough for the adiabatic local density approximation to be valid.

Also, the contribution of the total electric potential to the dielectric function is assumed to average out using random phase approximation (RPA), which simplifies the calculation procedure so that the dielectric matrix can be obtained using the non-interacting density response function:

$$\varepsilon_{GG'}^{RPA}(\mathbf{q}, \omega) = \delta_{GG'} - \frac{4\pi}{|\mathbf{q} + \mathbf{G}|^2} \chi_{GG'}^0(\mathbf{q}, \omega) \quad (2.24)$$

Where  $\mathbf{G}$  and  $\mathbf{G}'$  are the reciprocal lattice vectors,  $\mathbf{q}$  is the Bloch vector of the incident wave and  $\chi_{GG'}^0(\mathbf{q}, \omega)$  is the matrix element of the non-interacting density response function. The macroscopic dielectric function is then defined as:

$$\varepsilon_M(\mathbf{q}, \omega) = \frac{1}{\varepsilon_{00}^{-1}(\mathbf{q}, \omega)} \quad (2.25)$$

## 2.4. Electrodynamics calculations

The theoretical explanation for the well-known colorful optical response of spherical metallic particles was fully determined by Gustav Mie in his 1905 paper<sup>28</sup> much before the concept of localized surface plasmon resonance was coined. Essentially, the Mie theory solves the problem of the electromagnetic scattering of a spherical particle illuminated by a plane wave by expanding all the involved electromagnetic fields (incident field, field scattered by the particle and field inside the particle) in terms of a suitable vector basis (vector spherical harmonics) that take into account the spherical geometry of the problem. The coefficients of this expansion are found by imposing boundary conditions at the particle surface and once they are determined, any relevant electromagnetic quantity can be computed. In particular, the absorption and scattering efficiencies (or cross sections) quantify, respectively, the capacity of the particle to absorb or re-emit light in a direction different from that of the incoming beam. The extinction efficiency is then defined as the sum of absorption and scattering efficiencies and quantifies the ability of the particle to remove energy from an incoming beam.

Each term of the field expansion in the Mie theory is named a multipole and if the particle is much smaller than the wavelength, it suffices to consider only the first (dipole-like) term to get a good description of its electromagnetic response. This dipolar approximation permits to express the amount of light scattered, absorbed with efficiencies<sup>29</sup>:

$$Q_{abs} = 4x \text{Im} \frac{\varepsilon_1 - \varepsilon_m}{\varepsilon_1 + 2\varepsilon_m}, \quad Q_{sca} = \frac{8}{3} x^4 \left| \frac{\varepsilon_1 - \varepsilon_m}{\varepsilon_1 + 2\varepsilon_m} \right|^2 \quad (2.26)$$

where  $\varepsilon_1$  and  $\varepsilon_m$  are the dielectric function of the metal particle and its environment respectively and  $x$  is the size parameter defined as  $x = 2\pi r\sqrt{\varepsilon_m}/\lambda$ ,  $r$  being the particle radius and  $\lambda$  wavelength. The expressions for efficiencies indicate that when  $\varepsilon_1 = -2\varepsilon_m$  the absorption/scattering will present a resonant behavior, corresponding to excitation of the localized surface plasmon resonance in the particle.

The Mie theory can be applied only to spherical particles and there are few extensions to non-spherical particles. Electrodynamics calculations for arbitrarily shaped particles are usually addressed by means of numerical methods that discretize the particle into a large number of elements and consistently solve the Maxwell equations at each of these elements, taking into account boundary conditions between the particle and its environment. There are different approaches widely used in plasmonics, such as the discrete dipole approximation, the finite element method or the finite difference time domain<sup>30</sup>. Over the last years the boundary element method has gained popularity, because only the particle surface needs to be discretized, allowing optimization of computational resources<sup>31,32</sup>.

Calculation of single particle response by means of the Mie theory or numerically solving Maxwell equations are appropriate methods under the assumption that particles are isolated. In case that the particles are close enough so that their electromagnetic interaction is comparable to the effect of the incoming field, many-particle methods are required. The Mie theory can be extended for several particles taking into account that the field acting over every particle is the sum of the incoming field and the field scattered by the other particles, resulting in a coupled system of equations<sup>33</sup>. Numerical methods can be also extended to consider several particles.

In addition to localized surface plasmons in nanoparticles, one can consider plasmons propagating along a planar interface separating a metal and a dielectric<sup>34</sup>. This so-called surface plasmon polaritons are surface waves, i.e., with amplitude exponentially decreasing from the interface, that are defined by the propagation constant (wavevector component in the propagation direction along the interface): the real part quantifies the phase velocity of the surface wave and the imaginary part its attenuation in propagation direction. The dependence of the frequency with the wavevector, determined from the frequency-dependent dielectric function, defines the dispersion relation that characterizes the surface waves as a function of the light frequency.

---

## § 3. LITERATURE REVIEW

### 3.1. Plasmonic properties and their utilizations

Consider a metal nanoparticle, for example a nanosphere, in a changing electromagnetic field (depicted schematically in Figure 16), for example illuminated by light. Light — an electromagnetic wave — interacts with the charged particles in a material. Some of these charge carriers, namely delocalized and mobile (free) electrons, are induced to move and oscillate as the force is exerted on them by the changing electric field. Since a nanoparticle is confined on a nanoscale in all three dimensions, as the electrons are collectively moved through a nanoparticle by a light wave, they start to accumulate at the edge of the nanoparticle. The excess negative charge in that area then acts with a restoring force in the opposite direction, so the system acts as a harmonic oscillator. When the light frequency coincides with the mode of the described oscillator the system is in resonance and plasmons are excited. The plasmon resonance condition depends on many factors such as nanoparticle size, shape, material it is made of, and its environment. Due to the nanoscale localization in the nanoparticle such an effect is called localized surface plasmon resonance (LSPR). In general, plasmons can be described as quasiparticles representing quanta of plasma oscillation. In a more classical way, they can be thought of as self-sustaining collective oscillations of electrons in a material (for example conduction electrons in a metal) oscillating under the resonance condition.

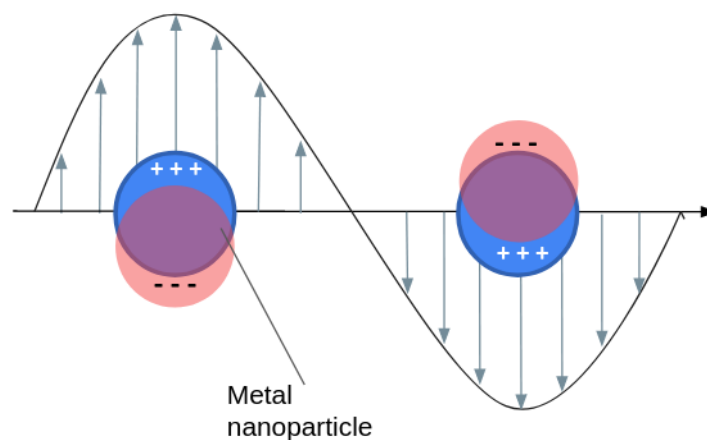


Figure 16. Depiction of localized surface plasmons excited in the nanoparticles by the electromagnetic wave.



LSPR in the nanoparticles gives rise to many interesting properties which is why plasmonic nanoparticles have been the focus of intensive research in recent decades. Such properties include extraordinary enhancement of the electromagnetic field in the immediate vicinity of the nanoparticle surface<sup>35</sup>. This local field intensity is further increased several orders of magnitude in the “hot spots” between nearly touching plasmonic nanoparticles. Effectively, light is being bent towards the nanoparticle and interacting with it, which results in a dramatic increase in the extinction cross section. As many photons get scattered by the nanoparticle or are absorbed by it, the extinction cross section (sum of the scattering and absorption cross sections) can become order(s) of magnitude larger than the geometric cross section of the nanoparticle<sup>36</sup>. The ratio of scattering and absorption at any given wavelength depends on the nanoparticle properties and are discussed in the next subsection.

Oscillating electrons in the nanoparticles have a finite lifetime and at some point dephase in a process called plasmon decay. Plasmon decay mechanisms can be radiative, with photons being reemitted, and nonradiative, exemplified by Landau damping, during which electron-hole pairs are created. These charge carriers are usually very energetic - such high energies would be exceedingly unlikely for charge carriers in a typical Fermi-Dirac distribution, except at exotically high temperatures - which is why they are called hot carriers. Hot carriers are typically short-lived (at the order of 100 fs) and lose energy by undergoing recombination while emitting a photon or by scattering with electrons of lower energy and with the lattice. Alternatively, hot carriers can be transferred to the matter that is in contact with the nanoparticle, e.g. molecules or semiconductors, provided that they possess enough energy to occupy the available energy level and to cross the energetic barrier for injection into that energy level. If they instead remain in the nanoparticle, they will distribute the kinetic energy throughout the nanoparticle by scattering with the lattice which effectively increases the temperature of the nanoparticle. Finally, thermalization is achieved by dissipating the energy to the surroundings as heat<sup>12</sup>.

These and other plasmonic properties are being explored in several different fields, with some of the most promising applications being for sensing purposes. The applications are many and diverse: At the cutting edge, sensors based on hot carrier generation and quantum plasmonics sensors<sup>37</sup> are being developed, offering exciting opportunities in the future. More standard applications include different types of colorimetric sensors and

---

refractive index sensors and surface-enhanced Raman scattering-based sensors. While providing abundant research opportunities, they are already finding applications and are at the beginning of commercialization<sup>38,39</sup>. Notably, the currently most applicable and pervasive sensor involving plasmonic nanoparticles has a rather simplistic design: it is a lateral flow test for virus antigens (Figure 17). Perhaps precisely due to its simplicity, such a device was widely adopted and played a crucial role in the recent global pandemic enabling rapid virus detection<sup>40,41,42</sup>.



Figure 17. A lateral flow test with two visible red lines formed by accumulation of plasmonic Au nanoparticles. Picture courtesy of dr. Juraj Nikolić.

Yet another positive contribution of plasmonic nanoparticle research to the field of medicine is in photothermal cancer therapy. Currently already in initial clinical applications, it utilizes local heat generation by plasmonic nanoparticles to precisely target and destroy cancer cells, with minimal damage to the surrounding tissue<sup>43,44,45</sup>

Plasmonic effects also show prospects in propelling the field of solar energy harvesting. Enhancement of solar harvesting efficiency could be achieved by improving the light harvesting properties in the existing solar cells, for example by light trapping<sup>46</sup>. Additionally, photons can be also harvested by using the plasmonic nanoparticles as primary light absorbers<sup>47</sup>, used in tandem with standard semiconductors<sup>48,49</sup>, perovskites<sup>50</sup> and even organic molecules<sup>51</sup> and polymers<sup>52</sup>.

Perhaps the most compelling use of plasmonic effects at the moment is for promoting and catalyzing chemical reactions. There are several ways by which plasmonic effects promote chemical reactions:

- 1) Due to local electromagnetic field enhancement, the rate of reactions that regularly involve photoexcitation can be substantially increased when molecules are located near the nanoparticles, especially in the “hot spots” with extreme field intensity.
- 2) Due to local heating of the plasmonic nanoparticles, the rate of reactions that regularly involve heating can substantially increase when molecules are located at the surface or in the immediate vicinity of the nanoparticles.
- 3) Hot carriers produced by plasmonic nanoparticles can be injected into the molecules adsorbed in the surface providing energy, destabilizing the molecules and inducing bond breaking and restructuring. Hot carrier generation can also induce desorption of unwanted products accumulated on the surface of the nanoparticle thereby promoting chemical reactions.

Whereas 1) and 2) just involve enhancement of the regular reaction-promoting mechanisms, 3) provides a largely novel way to initiate and catalyze chemical reactions. Hot electron catalysis unlocks new reaction pathways, potentially enhancing yield and selectivity<sup>12,53</sup>, and bypassing the limitations of regular catalysis for some of the most industrially important reactions<sup>54,55</sup>. Moreover, hot carrier-based reaction promotion opens up the possibility of conducting artificial photosynthesis and mimicking similar processes that play a pivotal role in nature<sup>56</sup>.

This chapter includes only a brief overview of plasmonic applications. Along the mentioned ones we note that there are a lot of other interesting applications such as surface-enhanced infrared absorption spectroscopy, metal-enhanced fluorescence for chemical analysis<sup>57</sup>, waveguiding<sup>58</sup>, nanophotonic signal processing<sup>59</sup>, photoacoustic tomography<sup>60</sup>, photodynamic therapy<sup>61</sup> and many more.

### **3.2. Plasmonic properties tuning**

There are multiple factors affecting the plasmonic properties of nanoparticles, mainly their size, shape, material they are made of, interparticle distance, and their environment.

---

### 3.2.1. *Tuning by changing the size of the nanoparticle*

Perhaps the simplest variable that can be leveraged to modulate plasmonic properties of a nanoparticle is its size. Changing the size of a nanoparticle provides a possibility of gradually and smoothly changing the plasmon resonance wavelength, albeit in a relatively limited range. As the nanoparticle size increases, the plasmon resonance generally shifts to the red, towards higher wavelengths, due to extrinsic size effects<sup>62,63</sup>. However, at very low sizes, intrinsic properties of matter are not constant and quantum effects also become noticeable, which can lead to trend reversal and a slight red shift with a decrease in size<sup>64</sup>. Since this results in shifting the extinction peak to longer wavelengths, changing the nanoparticle size is an effective way to change the color of the nanoparticle, and vice versa - by observing the change in color, all else being the same, an inference regarding nanoparticle size can be made. Influence of size on the field enhancement is less clear, as there is a strong interplay between size and other factors, but there are indications that size increase correlates positively with field enhancement<sup>65,66</sup>. Influence of nanoparticle size on the extinction, absorption and scattering is especially interesting: Size increases not only the extinction cross section, which seems intuitive since the geometrical cross section also increases, but also the extinction efficiency. The increase in extinction efficiency is wavelength dependent, as the peak shifts following the shift of the plasmon resonance, and nonlinear, as the increase in efficiency shows a trend of slowing down<sup>67</sup>. Interplay of absorption and scattering with size change is especially interesting: small plasmonic nanoparticles, typically under 40 nm in size, show almost no scattering at visible wavelengths - extinction is almost fully determined by absorption. However as the size of the nanoparticle increases above 40 nm, scattering increases rapidly, while the absorption eventually stops increasing and starts to decrease after that point, indicating a competitive relation between absorption and scattering<sup>34,67,68</sup>. Theoretical calculations have shown that the nanoparticle size also has an influence on hot carrier production. Namely, as the nanoparticle size increases the hot carrier generation rate also increases, but the energy of hot carriers generally decreases<sup>69</sup>. Furthermore, in small nanoparticles (sub 10 nm) the large proportion of hot carriers under the energy of interband transition threshold is generated by surface-assisted transitions. As the size increases, so does the influence of phonon-assisted transitions, but also of resistive losses that decrease the overall efficiency of hot carrier generation<sup>70</sup>.

---

### 3.2.2. *Tuning by changing the shape of the nanoparticle*

The shape change is an effective way to influence the plasmonic properties in many ways. Regarding the plasmon resonance, many deviations from sphericity will lead to a prominent red shift, be it the presence of sharp features such as points and ridges<sup>71</sup>, introducing a void or a hole to create a nanoshell-like structures<sup>72,73</sup>. However, the actual change in plasmon resonance with breaking the symmetry (for example of a spherical nanoparticle) is more complex, as several plasmons, depending on the polarization of the light, can be excited in such nanoparticles, some of which can be blue shifted. The blue shifted plasmons are usually more attenuated and can lose significance, with the red shift being the only noticeable effect. Changing the aspect ratio, such as elongation of the nanoparticle, enables plasmon resonance tunability in a rather large range. In elongated nanoparticles such as nanorods two extinction peaks can be observed, corresponding to two distinct plasmon resonances: one coming from plasmon polarization along the long axis and the other perpendicular to it. It is interesting to note that the influence of geometry on the plasmonic properties connects, through analogies, plasmonics and chemistry. For example, in nanoshells bonding and antibonding plasmon modes can be observed, resulting from the interactions of the sphere and cavity plasmons, with energy levels largely analogous to those of bonding and antibonding molecular orbitals created by the interaction of isolated atomic orbitals<sup>74</sup>. Similarly, splitting of plasmon modes due to nanoparticle geometry can be connected to the crystal field splitting in transition metal complexes<sup>75</sup>. Although the influence of geometry on field enhancement can be very complex, in general the field can be significantly enhanced at the sharp edges, ridges and other high aspect ratio features of the nanostructures, resulting in localized hot spots<sup>76,77</sup>. Atoms located at edges and ridges also serve as spots of efficient high energy hot electron production. Given the similar size and shape (for example polyhedral), the overall hot carrier distribution still depends on the exact geometry of the nanoparticle indicating a possibility of hot carrier distribution tunability<sup>78</sup>.

### 3.2.3. *Tuning by changing the interparticle distance*

When plasmonic nanoparticles are located close enough to each other, usually under several tens of nanometers, they are able to interact upon excitation with light as their plasmons couple. This leads to a red shift in case of light polarization along the axis of the dimer (blue shift in case of perpendicular polarization) of the plasmon resonance<sup>79,80,81</sup>, which progresses

---

until the nanoparticles are in proximity of around 1 nm, under which quantum effects become dominant and complicate the trend<sup>82</sup>. However, by far the most prominent and the most utilized plasmonic effect of the interparticle distance tuning is the creation of the hot spots due to extraordinary field enhancement in the area between interacting nanoparticles. While affected by other factors like plasmon resonance position, a correlation of interparticle distance and field enhancement can be inferred: when the gap between nanoparticles becomes lower than approximately 50 nm, the field enhancement increases dramatically, becoming the largest below 10 nm. At these distances slanting angle (and thus the shape of the neighboring nanoparticles) also becomes increasingly important<sup>83</sup>. Field enhancement due to plasmon coupling between metal plasmonic nanostructures is possibly the most effective field enhancement strategy, as can be inferred from the recent study in which the metal-based nanostructure outperformed the dipole antenna and a grating nanostructure by 15 times in enhancement of the local field<sup>84</sup>.

#### *3.2.4. Tuning by changing the refractive index of the environment*

The clearest effect, and thus the main purpose of changing the environment of the nanoparticle is in shifting the LSPR position or, in other words, changing the plasmon resonance. Strong response of the LSPR position to the refractive index change of the matter the nanoparticle is in contact with is the basis of refractive index sensors, some of the most utilized plasmonic sensors. If a nanoparticle would be moved from a low refractive index medium such as vacuum, air, or some particular gas-phase atmosphere to a higher refractive index medium such as water or silica, its plasmon resonance position would shift to higher wavelengths. In case of partial embedding of nanoparticle in two different dielectric media, the plasmon peak position shifts to red rapidly upon minor embedding in a higher refractive index material and proceeds to redshift more slowly as it is gradually fully transferred to that material<sup>85</sup>. Precisely because the LSPR is shifting with the change in the refractive index (dielectric properties) of the medium, establishing a clear dependence of the maximum field enhancement becomes complicated. Since dielectric properties of the nanoparticle itself are a function of frequency, there is a difference in the response of the nanoparticle to the conditions at different plasmon resonance frequencies. In general, for nanoparticles with a low aspect ratio (near-spherical nanoparticles) the field enhancement should increase with the increase in the refractive index of the environment, since the system effectively becomes

---

more polarizable<sup>34</sup>. This is supported by the work of Fukoka and Tanabe, although the same work also shows that the trend becomes less clear or even reversed when geometry of the nanoparticles is also changed<sup>86</sup>. Consequently, the influence of the environment on other plasmonic properties also has a complex dependence on many factors.

### 3.2.5. *Tuning by changing the nanoparticle material*

For a long time, tuning the plasmonic properties by changing the nanoparticle material was largely limited to discrete changes based on the choice of a material class and, if possible, the most suitable type of material in that class. If plasmon resonance was needed in the infrared range, doped semiconductors and transition metal nitrides along with some metals could be used<sup>6,87,88,89</sup>. However, for most applications the range of interest is the visible range, where metals dominate. Other than having LSPR in the visible range, a beneficial property is a high number of free charge carriers and chemical stability. Closed d-shell metals (ten electrons in the d-orbital), such as Au, Ag and Cu are especially suitable for plasmonic applications since their interband transitions can largely be avoided resulting in low losses and, consequently, sharp resonances. Alongside them, Al is also a good plasmonic metal but in most configurations has plasmon resonance in the UV. These metals exhibit very large extinction cross sections, mostly at wavelengths near plasmon resonance. Additionally, near the plasmon resonance they are also characterized by very large field enhancements<sup>87,89,90,91</sup>. Hot carrier production has also been studied for these elements, with the position of the d-bands showing importance for adjusting the ratio of highly energetic electrons and holes, and continuously available interband transitions distinguishing Al as a potentially important material for efficient hot carrier production<sup>70</sup>. Alkali metals should in principle possess similarly good plasmonic properties, but due to their characteristically high reactivity in practice alkali metal nanoparticles would be hard to create and require special conditions not to immediately deteriorate by reacting with the environment<sup>87</sup>. Catalytic metals such as Pt and Pd are very interesting due to their stability and the ability to lower the energy barrier for chemical reactions. However their high-lying d-bands, in part responsible for the good catalytic activity, are precisely the reason for high losses which disqualifies them from most plasmonic utilizations, seemingly limiting the functionality of the good plasmonic nanoparticles.

One strategy to achieve a finer tuning of optical properties is by combining metals, such as in core-shell or Janus morphology<sup>92,93</sup>. In this way, properties of both metals can be

---

combined and tuned by the ratio of each individual metal. For example, by introducing a shell of Au on top of Ag core the chemical stability of the nanoparticle should be increased when compared with pure Ag, with field enhancement superior when compared to pure Au. Additionally, this enables tuning of the LSPR position.

Another approach to tuning by combining metals is by alloying them. Experimentally there are many methods to achieve alloying, some of them straightforward and with a good degree of control. Alloying can thus also be a pragmatic way to combine properties of constituent elements, in some aspects with superior results in comparison with creating a core-shell structure. For example, tuning of the plasmon resonance position by changing the nanoparticle composition is much smoother when alloying Au and Ag than when creating a core-shell structure, which is also reflected in the trends obtained for extinction cross section for both nanoparticle types, field enhancement is higher for alloy Au-Ag nanoparticles than for the Ag core - Au shell nanoparticles of the same element ratio and size, and the stability of alloy nanoparticles much improved, even with just a minor addition of Au, when compared to pure Ag nanoparticles<sup>94</sup>. Improving stability by alloying could potentially enable the use of metals that are otherwise unsuitable in their pure state, paving a way towards expanding the research involving alkali metals for plasmonic purposes. Furthermore, alloying good plasmonic and good catalytic metals enables utilization of their beneficial properties in tandem, and also of their adjustments by influencing the electronic structure, namely the d-band position by adjusting the ratio of constituent metals. Some efforts have also been made in exploring the possibility of hot carrier energy distribution tuning by alloying<sup>95,96</sup>. Finally, besides providing a way to combine the properties inherent to constitutional metals, investigating the possible emergent properties of alloying might also lead to promising results.

### 3.3. Use of DFT in plasmonics

#### 3.3.1. Comparing computational approaches

In order to explore the opportunities that alloying brings in the field of plasmonics, it is important to research how the electronic structure of metals changes during alloying and to understand the composition-electronic structure-property relationship. This can be achieved by (*ab initio*) computational methods that are based on fundamental properties of the matter such as DFT.

---



There are three main approaches that are being used in DFT calculations to model the plasmonic properties of metal nanoparticles:

- Approaches representing nanoparticles by the use of jellium models
- Approaches utilizing an atomistic representation of nanoparticle
- Approaches combining bulk DFT calculations with electrodynamics

Jellium models are based on the assumption that the properties of interest can be represented well enough without taking into account the atomic nuclei with core electrons and the potential of the atomic lattice: the positive charge is distributed homogeneously within the object that is being modeled. Valence electrons are modeled as a homogeneous gas of delocalized negative charge that is bound by the positive potential of the desired geometry and treated on a quantum-mechanical level. Such models are suitable for calculating optical properties of model nanoparticles ranging from subnanometer scale to several tens of nanometers. Lower size limit is set by increasing deviation from the actual electronic structure of the nanoparticle and the inability to properly capture some of the quantum effects. Higher size limit is set by the computational cost of the calculations. Jellium models can be used adequately to calculate excitations of free gas-like electrons, which is the case for alkali-like metals and Al. For metals like Ag jellium models can be used in the visible range where only the transitions within the free electron-like states of the conductive *sp*-band are present<sup>69,97</sup>. However, when the plasmon resonance of a metal coincides with the energy range in which the metal has interband transition, which can be the case for Au, the jellium models are less suitable<sup>98</sup>. For the same reason, jellium models are not suitable for metals that have interband transitions present in the entire range from IR to UV. As such, they are very limited with regards to studying different metals, and their alloys. It will be shown later in this work that there is another limitation of jellium models with regards to alloys, related to the emergence of new interband transitions upon alloying.

For a long time atomistic-level models were limited to simulations of clusters consisting of up to a hundred atoms. However, with the rapid technological progress in the last decades, the available computational power increased by orders of magnitude. Increased processing power, combined with progress in computational methods, made atomistic-level models much more popular for studying the optical properties of metal clusters in the last couple of years. As of now, the maximum number of atoms in a studied system can be more

---

than a thousand, enabling calculations involving a cluster of up to 4 nm in diameter or in the other words, a small nanoparticle<sup>99</sup>. While promising, such studies have insofar involved a limited amount of different metals and there is very little research done on alloys, likely in part due to computational cost of such calculations. Also there is little to no research regarding some of the plasmonic properties that have come into focus lately, such as hot carrier generation. However, in a recent perspective paper by Sánchez and Berdakin<sup>100</sup>, alloys have been highlighted as a topic of interest for atomistic-level DFT calculations of hot carrier generation, and it is likely only a matter of time until the field progresses in that direction. At the beginning, however, computational cost will likely limit the research on a small number of compositions to be studied.

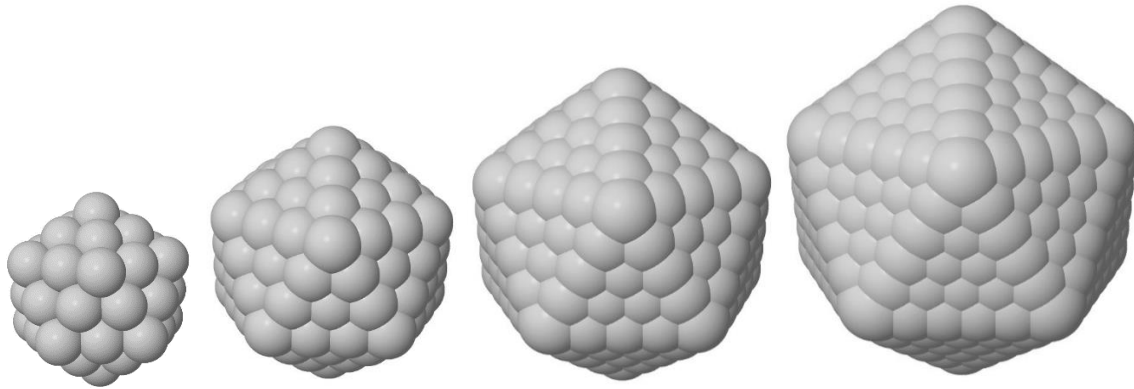


Figure 18. Atomistic models ranging from the nanocluster (left) to an icosahedral nanoparticle (right). Number of atoms in the particles is, from left to right, 55, 147, 309 and 561.

Probably the most ubiquitous approach has so far been combining the DFT calculations performed on an extended (bulk) system to obtain the properties of the material of interest. These properties, such as dielectric function - crucial to define how matter interacts with light - are then used as a basis for electrodynamics calculations to obtain the plasmonic properties of model nanostructures consisting of the material of interest. Such a DFT-based two-step approach is suitable for plasmonic properties calculations for several reasons: it is reasonably rigorous with respect to the material properties since it takes into account both the lattice and excitations of bound electrons; it is universal since it enables calculations of a wide variety of materials; it enables calculations involving a large number of systems since it is efficient - the calculations require setting up a unit cell, usually consisting of only one up to several tens of atoms which, due to periodic boundary conditions, reproduce the entire lattice. As classical

electrodynamics calculations are needed in the second step, this approach is most suitable for medium to large nanoparticles, those that are larger than 10 nm in diameter. 10 nm defines a tentative lower limit because below this threshold quantum effects become noticeable<sup>70</sup>. Nevertheless, the range of adequacy of classical electrodynamics can, for some properties, be pushed further below 10 nm, down to several nanometers - the size of small nanoparticles - if proper corrections for quantum effects are applied<sup>101</sup>. The aforementioned reasons make this approach especially suitable for calculations involving alloyed systems; finding the right composition of the alloy nanoparticle to optimize plasmonic properties for desired purposes can involve calculations performed on a large number of systems, including several different elements in a multitude of ratios.

In all of the approaches one of the main considerations is which level of theory, mostly pertaining to the choice of an exchange-correlation functional, is to be chosen having in mind the desired accuracy of the calculations and the limits imposed by the computational cost of the calculation.

### 3.3.2. *Choice of the exchange-correlation functional*

Two principal goals of an approach that uses DFT to obtain optical and plasmonic properties of metals are to describe their electronic structure and to predict their dielectric function to a satisfactory degree. The main issue then becomes a proper choice of an exchange correlation functional. Insofar, in the overwhelming majority of the studies, the functionals used for such calculations have been at the generalized gradient approximation (GGA) level, or even below, at the level of local density approximation (LDA). Since these functionals typically lack the derivative discontinuity of electronic energy at integer electron numbers<sup>24</sup>, they provide an improper treatment of highly correlated d-band electrons, resulting in overly delocalized d-states too with energy too close to the Fermi level<sup>70</sup>. This reflects particularly badly on the noble and coinage metals - the closed d-shell metals such as Au, Ag and Cu - which, unfortunately, are the most important plasmonic metals. In these metals the position of the d-bands determines the energy threshold for interband transitions that involve an excitation of an electron from fully occupied d-bands, below the Fermi level, to an unoccupied state in an sp-band, near or above the Fermi energy. Since the d-band is predicted to be too high for these metals, the interband transition onset is predicted to be too low; in other words, the d-sp interband transitions are available for lower photon energies than is the case in reality. This is

---

reflected quite clearly by the redshift of the interband transitions-related peak in the imaginary part of the dielectric function and the corresponding change in the shape of the real part of the dielectric function<sup>120</sup>.

To remedy the issue of shallow d-bands, corrections can be performed on top of LDA or GGA-based calculations. GW approximation, for example, includes quasiparticle and local field effects and corrects the energies of the states accordingly<sup>103</sup>. However, this comes at a cost increased by at least an order of magnitude when compared to uncorrected calculations. It has to be noted that even more precision can be obtained by including double particle excitations using the Bethe-Salpeter equation<sup>104</sup>. However, this comes at a yet another order of magnitude increase in computational cost which is why this approach is currently not utilized for purpose here discussed. GW correction has, on the other hand, been used in calculations involving a small number of pure metals performed with a high degree of accuracy<sup>103,105,106</sup>. Conversely, there is a type of correction less computationally involved even than GW approximation. It is based on correcting the overly delocalized d-bands using a so-called U-term based on the Hubbard tight-binding model<sup>107</sup>. In effect, the U term imposes an energy penalty to the atomic site occupancies with non-integer electron numbers, thereby favoring electron localization. The Hubbard-like U-term is an adjustable parameter and is rather useful when empirical data is available to provide a basis for tuning the degree of correction to achieve the best fit. Otherwise, however, it is of little predictive use. When calculations involve properties of materials for which there is a lack of empirical parameters that can be used to anchor the correction, this approach is much less suitable. There is progress in calculating the U-parameter *ab initio* but this estimation comes at a substantial computational cost, diminishing the affordability of the DFT+U corrections<sup>107</sup>. Alternatively, a hybrid-GGA functional can also be used to increase calculation accuracy, mainly by more properly describing the d-bands. Hybrid-GGA functionals are more sophisticated than GGA-level functionals since they use a certain ratio of exchange calculated at the Hartree-Fock level<sup>21</sup>. Greater sophistication brings with it a significant increase in the cost of calculations (order of magnitude difference) and poses an issue for simulations involving large unit cells (many electrons) or performing calculations on a multitude of systems. Additionally, since the amount of exchange is fixed and empirically determined on a certain class of systems, there is an issue of transferability for such functionals: while a certain amount of Hartree-Fock (HF) exchange works good for some elements and systems, it might not for different ones.

---

Three cornerstone studies provide information useful for the choice of an approach when determining the plasmonic properties of metals. Combined, they provide comparison of the performance of LDA, some standardly used GGA functionals, GW and DFT+U corrections applied on standard GGA functionals, as well as performance of one potentially suitable hybrid functional and a promising GGA-level functional that indicates a better performance for optical properties calculations<sup>103,106,108</sup>.

Lin *et al.* have compared three functionals for calculating optical properties of bulk gold and gold thin film - LDA, the simplest functional; PBE a GGA-level functional which is probably the most popular functional in physics and the standard functional for optical properties calculations; and GLLB-SC, a less commonly used GGA-level functional with adjustments useful for calculating optical properties<sup>108</sup>. They compared imaginary and real parts of complex dielectric function based on calculations with the experimental data. For bulk gold, they found that GLLB-SC results are the closest to the experimental results, and attributed that to the better description of the single-particle energies of noble metals compared to the other two functionals. Band structures along  $\Gamma$ -X and W-L- $\Gamma$  points of the Brillouin zone, as well as the corresponding density of states, were calculated and studied. It was shown that (mostly) the p-band - in this case the conduction band - was too low when calculated with LDA and PBE. Overall, in comparison with available experimental data, the calculations gave red shifted dielectric functions, with the deviation from the experiment being the smallest for GLLB-SC functional. For gold thin films, the  $\epsilon_2$  minimum calculated using GLLB-SC is slightly blue shifted, and red shifted using PBE and LDA. That is attributed to calculated d-bands of thin film being lower for GLLB-SC than for PBE and LDA. Compared to experimental data,  $\epsilon_2$  is slightly lower in the entire spectral range for GLLB-SC, but approximated the shape of the dielectric function quite well. PBE and LDA produced a higher  $\epsilon_2$  than is obtained by the experiments. There was also a larger discrepancy in the shape of the dielectric function for these two functionals. Data for the thin films was subsequently used for calculation of transmittance, reflection and loss using a software for electromagnetic simulations. Electromagnetic simulations based on metal properties calculated using GLLB-SC led to best reproduction of experimental data for optical and plasmonic properties of thin films.

---

Effects of different electronic structure methods on the description of the band structure for Al, Cu, Ag and Au were studied by Sundararaman *et al.* in order to find the best method for calculating hot carrier distributions from plasmon decay<sup>103</sup>. Band structure of aluminum was described similarly well regardless of the method used, which is to be expected since it is a third period element, meaning that it does not have filled and localized d-bands. For copper, gold, and silver, PBEsol, GGA-level functional based on ubiquitous PBE, with adjustments for solid state calculations, showed the worst performance when compared to experimental data. GLLB-SC, showed a significant improvement in the predicted d-band position. PBEsol corrected by the quasiparticle self-consistent GW approximation also improved the d-band description, but the improvement was comparable to the use of GLLB-SC despite it requiring much more computational power. DFT+U also showed comparable improvement, with the overall best performance after properly adjusting the U value.

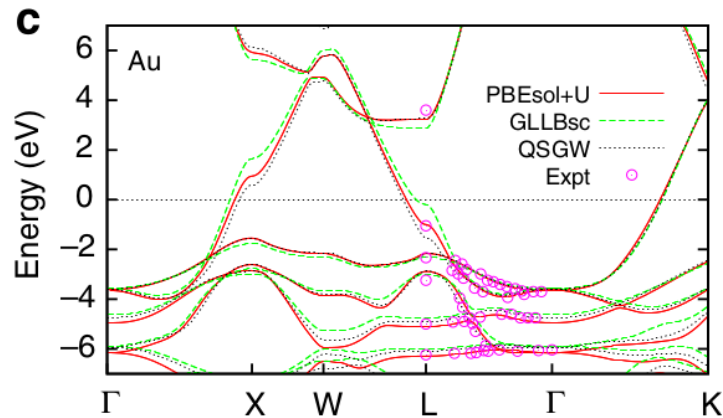


Figure 19. Comparison of band structures calculated by different methods and the experimental data.<sup>103</sup>

GW approach was thoroughly explored by Rangel *et al.* with different types of GW approximation being considered<sup>106</sup>. The study focused on Au, Ag and Cu, with GGA functional of choice being PBE. The effect of GW corrections on the calculation of the band structure was also compared to the effect of using HSE, a hybrid functional potentially suitable for bulk metal systems. The simplest version of GW, a single-shot  $G_0W_0$  approach (in which the quasiparticle equation is solved only once and not self consistently), corrects the DFT interband gap very well for Ag and Cu. It relies, however, on the assumption that the quasiparticle wavefunctions are close to the DFT ones, which does not always hold. Two schemes were explored to remedy such a situation - a SC-COHSEX +  $G_0W_0$  scheme, and a

QSGW (quasiparticle self consistent GW) scheme. All three GW schemes were used to calculate the band structure of Au and compared to uncorrected PBE and HSE. Inclusion of the semicore 5s and 5p states in the valence shell had negligible effects without including corrections, but it was of utmost importance in GW, leading to a correct ordering of bands at the Fermi level. The  $G_0W_0$  approach shifted the empty bands slightly upwards and the lowest occupied sp-band slightly downwards when compared to the experimental data, but not affecting the 5d states sufficiently. This was corrected using QSGW which also improved the 5d band energy. HSE bands showed a moderate discrepancy with the experimental data, which progressively worsened for higher states.

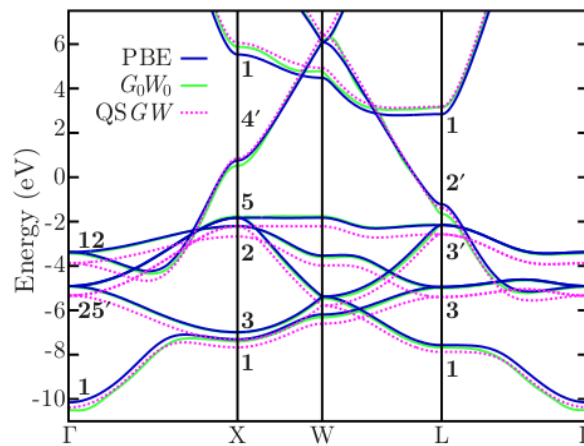


Figure 20. Comparison of band structures calculated using different methods.<sup>106</sup>

The combined results by the three aforementioned papers show that DFT calculations of band structure (and dielectric function) for noble metals such as Au and Ag underestimate the relevant interband transition energies regardless of the choice of functional. However, GLLB-SC seems to be a very interesting option, with significant improvements over LDA and PBE functionals, but a similar computational cost. Sundararaman *et al.* report that PBEsol+U improves the transition energy near the L-point in comparison with GLLB-SC but their data also seem to indicate that PBE+U performs worse than GLLB-SC for transitions near the X-point. Although the simpler versions of the GW approach such as  $G_0W_0$  obviously improve the overall band structure for Ag, Au, and Cu, as shown by both Sundararaman *et al.* and Rangel *et al.* it seems that significant problems, such as d-band positions and transition energy at the L-point, still remain. Therefore even more computationally expensive versions of the GW approach (QSGW for example) are necessary to achieve a meaningful improvement over

hybrid functionals such HSE and even a GGA functional such as GLLB-SC. Due to higher sophistication but not a higher computational cost than GGA-level PBE and PBEsol, GLLB-SC presents itself as a same-cost alternative to standardly used functionals in the field of plasmonics. In fact, there are several more papers stating a good performance of GLLB-SC for pure noble metals<sup>109,110,111</sup>.

GLLB-SC seems to meet several requirements for calculations of plasmonic properties of alloys, indicating that it could prove to be excellently suited for that class of systems. Since calculations on alloyed systems involve setting up a unit cell consisting of several atoms (unlike only one atom for pure metals), and since thoroughly exploring the compositional space requires many systems of different element ratios, the preferred approach should be efficient. Moreover, to avoid the redshift of the interband threshold and to properly predict the plasmonic properties the approach of choice should provide a proper treatment of the d-bands. Finally, the approach should be universal in the sense that it works well for a multitude of different systems without requiring empirical parametrization. The reasons for the suitability of GLLB-SC lie in its clever construction: It is based on PBEsol for obtaining the energy density and correlation but uses a GLLB exchange response potential that was developed by Gritsenko *et al.*<sup>112</sup>. The use of GLLB potential results in the correction of a known problem for GGA functional, the lack of derivative discontinuity. By restoring the exchange discontinuity contribution to quasiparticle band gap, the gap for interband transitions is widened. In particular, for noble metals, this is reflected by lowering of the d-bands, thus mitigating the ailments of GGA functionals for these important plasmonic materials. GLLB-SC introduces orbital energy-dependent localization of the exchange hole and is thus not dependent on parametrization. Additionally, the GLLB potential is formulated by following physically sound arguments such as fitting to the homogeneous electron gas, proper asymptotic behavior and exchange scaling relation.

### 3.3.3. Modeling metal alloys using DFT

When alloys are simulated using DFT a couple of approximations and idealizations have to be made in order to perform the simulations. There are several possible sources of errors arising from performing most common, not highly demanding calculations. The first and perhaps the most obvious idealization is in representing alloys as ordered periodic structures - perfect crystals - which neglects both local and long-range disorder. As a consequence an artificial

---



anisotropy of the supercell can be introduced, meaning that the dielectric function obtained from such a supercell is not the same for every axis. This can be partially remedied by averaging the dielectric function with respect to all directions. Furthermore spin-orbit coupling is oftentimes neglected in the calculation of optical properties which can sometimes result in improper band degeneracy and other issues. Finally, random phase approximation (RPA) is commonly used, which means that the quasiparticle and local field effects are disregarded to cut computational cost. This can oftentimes be justified, especially for well conducting metals, however in some cases these effects can prove to be quite significant. Finally, due to the high computational cost of using the Bethe-Salpeter equation, double particle excitations are very commonly disregarded at the expense of obtaining very accurate results.

#### 3.3.4. Modeling intermetallics

With the first source of error in mind - disregarding disorder in alloys - it is still possible to find alloys that fit into the constraint of being fully ordered, with well defined periodic structures. Such alloys are called intermetallic and appear at very precise stoichiometric ratios of elements. Prediction of their properties by DFT methods can therefore lead to more accurate results (since modeling disorder is not an issue in case of intermetallics), which makes them an appropriate starting point for analysis of alloy modeling using DFT. There are several studies that focus directly on the intermetallics, providing valuable insight into their structural and optical properties<sup>113,114,115,116,117</sup>.

Blaber *et al.* have performed a number of DFT calculations on intermetallics that show promise as possible low loss plasmonic materials<sup>113</sup>. They investigated how band edge and plasma frequency vary with composition to find the intermetallics for which plasma frequency is as close to the band edge, which should diminish the loss due to interband transition. To achieve that they calculated the interband transition component of the imaginary part of dielectric function for each of the compounds, as well as their plasma frequency. Primary and secondary band edges were determined and compared to the position of plasma frequency. KAu was found to be the most promising intermetallic as it has a band edge at almost the same energy as the plasma frequency, a finding which was later on confirmed by Blaber *et al.* in another study performed using a more thorough calculation scheme<sup>115</sup>. Plasma frequency of KAu is relatively low which promises good plasmon resonances at very short

---

wavelengths. NaAu and KAg also showed promise for IR plasmonics. Band structure was also calculated and a “fat-band” analysis was performed to connect the dielectric function with the band structure. In the fat-band analysis the parts of the band structure are depicted wider (“fatter”) the more they are involved in transitions. Very interestingly, it was shown that the studied intermetallics have bands that are closely aligned and near-parallel at some points in the band structure, and that these fragments of band structure cause energy transitions at very low energy. This is reflected as a low energy peak in the imaginary part of the dielectric function. In fact, the magnitude of the increase of the low energy interband component when alloying Au and Ag with group III metals is particularly interesting. For example, Al has  $\epsilon_2$  less than 50 at 1.5 eV with Drude term included, while AgAl<sub>2</sub> and AuAl<sub>2</sub> show  $\epsilon_2$  larger than 50 at 1.5 eV even without the Drude term.

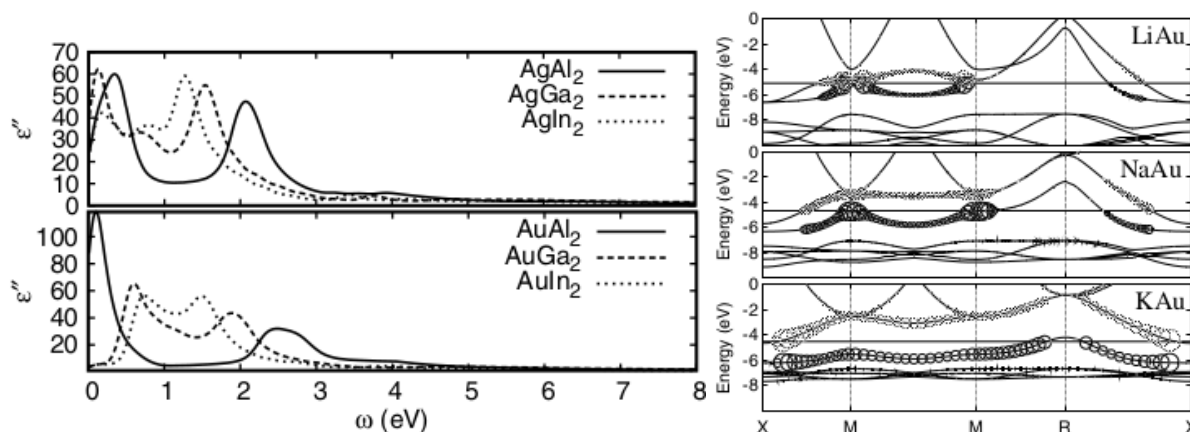


Figure 21. Purely intraband contribution to the imaginary part of the dielectric function (left) and the „fat band“ analysis showing the regions in the band structure where the interband transitions occur („fatter“ regions correspond to more transitions).<sup>113</sup>

Some of the same intermetallics that include Au as one of constituent elements were examined in another study, but in this case the Drude term was included in all calculations and the peak that appeared due to interband transitions in alloys was missed, as it was overshadowed by the (intraband) contribution of the Drude term<sup>114</sup>. The coloration of AuAl<sub>2</sub> causing the absorption peak in the visible range is attributed to transitions due to excitations of electrons in the sp-band, unlike the d-band as is the case for pure Au. As found in a later study, this is the reason for much more accurate prediction of the color of this intermetallic compound by DFT, since the relevant transitions in the visible spectrum do not include the d-bands problematic for GGA functionals such as PBE<sup>118</sup>. Interestingly, authors discuss the

onset of interband transitions being above 2 eV although the earlier study of the same system by Blaber *et al.* shows the peculiar peaks in the  $\epsilon_2$  coming from interband transitions at much lower energies. This highlights the importance of careful examination of both interband and intraband contribution to the dielectric function. A shoulder in the  $\epsilon_2$  is also visible for DyMg intermetallic compound in the region typically dominated by the Drude term and not commented on<sup>117</sup>, indicating that the low energy interband transitions could be an overlooked feature of alloys, with implications for plasmonic properties.

Similar features were also present, but passed relatively unnoticed, for many Au-based alloys and intermetallic compounds studied in a very extensive investigation of optical and plasmonic properties performed by Keast *et al.*<sup>116</sup> Their examination was focused on finding a second element that would, alloyed with gold, make an alloy suitable for low-loss plasmonic applications. Based on the previous prediction of AuAl<sub>2</sub> intermetallic compound having a better plasmonic performance than Au in the blue-green part of the visible spectrum<sup>114</sup>, alloys of many elements were investigated, and their performance compared to best performing pure metals. Choice of the elements was based on their bleaching properties, because bleaching the color of Au might be an indication that the d-band has shifted in energy. Substitutional alloys were constructed by creating an 8 atom FCC cubic gold supercell and replacing one of the gold atoms with another element which in some cases caused the stoichiometry of the cell to overshoot the solubility limit of the alloy, thereby introducing possible errors. Anisotropy was handled by averaging dielectric functions. The effect of lattice parameter optimization on the calculated dielectric function was also a matter of interest, and the authors claim it had just a negligible effect. Alloying with Al, Cd, Mg, and Zn showed promise because it shifted d-band downward in energy with the shift increasing with the increasing content of the alloying element. Quasiparticle effects have not been included, as well as spin-orbit coupling and local field effects. It is argued that these last two effects are minor. Based on the calculated quality factor, a couple of alloys showed a slight improvement over pure Au, but only at about 2 eV, where Au interband transitions start to quench the plasmon by introducing an additional plasmon decay channel. Overall, AuAl<sub>2</sub>, Au<sub>3</sub>Cd, AuMg, AuCd and AuZn were found to be candidates for low-loss plasmonic applications. However, the plasmon position would require significant tuning, most likely via shape adjustment, to be shifted to the position where losses are low. In fact, only AuAl<sub>2</sub> would not require a shape that significantly differs from spherical to achieve a strong plasmonic resonance in the visible spectral region. The results of this

---

study show the difficulty of avoiding optical losses. Despite the large number of promising materials included in the study, there was little to no success in finding new candidates for low-loss plasmonics. One of the reasons might be the appearance of the low-energy transitions in alloys that were found by Blaber *et al.*<sup>113</sup> but that possibility was not investigated. Overall, finding a low-loss material with performance competing or outperforming that of noble and coinage metals seems to be a hard task: it would require either a large number of calculations on a vast compositional space or understanding how to engineer electronic structure of the alloys to avoid unwanted transitions leading to optical losses.

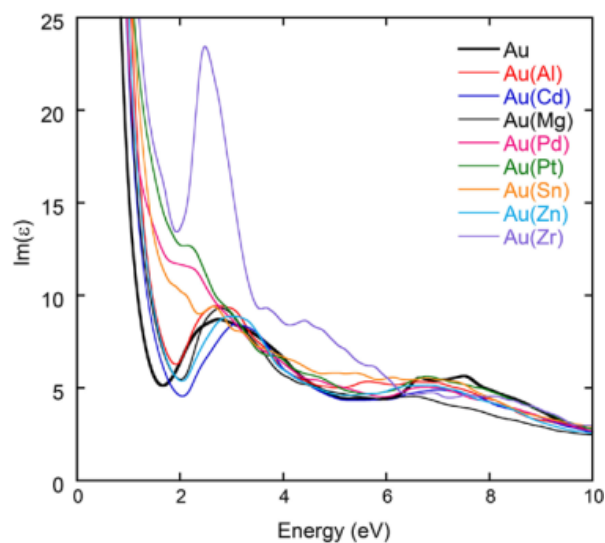


Figure 22. Imaginary part of the dielectric function calculated using DFT for many Au-based alloys (left). It can be seen that at almost no point are the alloy optical losses smaller than for the pure Au. This is reflected in the plasmon quality factor (right), indicating that the plasmonic properties of Au outperform the properties of all Au-based alloys.<sup>116</sup>

From the aforementioned studies of intermetallics a couple of points can be concluded: Since they can, ideally, be found almost as perfect crystals in nature, they are a good starting point for DFT studies of the properties of alloys. Reason for that is because the idealized, perfectly periodic structure imposed by periodic boundary conditions, in principle, holds. Furthermore, optical properties of various intermetallics have been predicted by the DFT calculations and some of them show promise as plasmonic materials. However, there is a severe lack of experimental data to compare the calculated data with. Also, stability and therefore practical usefulness of such intermetallics is in some cases questionable. It is interesting to note that

oftentimes absorption in the low energy region deviates from the Drude behavior. From some calculations it can be seen that such behavior stems from the interband transitions. For some intermetallics such absorption can closely follow the shape of Drude behavior, so it can be hard to distinguish such contribution to the low-energy imaginary part of dielectric function of alloys from the similar behavior caused by various scattering mechanisms. Finally, the low-energy interband transitions can be predicted by looking at the band structure. Close lying, parallel bands can be observed for intermetallics that show low-energy interband transitions. These insights are further substantiated by the fat-band analysis performed by Blaber *et al.*<sup>113</sup>

### 3.3.5. *Effects of configuration/disorder influence*

While the previous chapter focused on ordered alloyed systems, ending with the thorough exploration of Au-based alloys and intermetallics by Keast *et al.* a tentative exploration of the effects of configuration and disorder has been performed in that same study<sup>116</sup>. Although the study focused on intermetallics, some of the structures were experimentally observed to have a disordered structure, which was impossible to properly reproduce by the calculation setup. However, it is argued in the paper that the effect of structural disorder is expected to have a minor effect on the results when compared to the composition, based on configuration changes introduced by simulating alloy supercells. They investigated an effect of placing 2 Cd atoms next to each other in a 16 atom Au-Cd alloy supercell (12.5% Cd) and compared to the regular 8 atom supercell with 1 Cd atom which produces a structure with Cd placed apart. The dielectric function was reported to be almost indistinguishable. Furthermore, DOS of different crystal structures with the same stoichiometry was also investigated and shown to have the same overall shape, furthering the argument that configurational differences might not have a substantial influence on the properties. However, while providing a tentative indication, the effects of disorder are not accounted for by this research, which prompts further investigation.

A logical next step is to study systems that can be probed experimentally, and can vary from highly ordered to disordered. Such systems are gold-copper alloys such as CuAu and CuAu<sub>3</sub>, with known crystal structures. A 1974 paper by Rivory on optical properties of ordered and disordered Au-Cu alloys sheds light on the effect of disorder on dielectric function<sup>119</sup>. AuCu and AuCu<sub>3</sub> superlattices were obtained, and their (mostly) ordered structures compared to the disordered phases of the same composition. Imaginary part of the

---

dielectric function for an alloy film with 81% of copper (with AuCu<sub>3</sub> phase present) was studied as the degree of order decreased. A peak around 3.6 eV almost disappeared as the disorder increased, while the peak just above 2 eV remained of similar shape, but reduced in value. The degree of disorder on the AuCu phase (present in an alloy with about 40% Cu) had only a minor effect on the shape of  $\epsilon_2$ . Overall, the shape of the absorption edge and the value of the interband transition onset were not significantly modified by ordering. The part of  $\epsilon_2$  most affected by disordering was the peak at 4 eV. As disorder increases it becomes less pronounced and moves from 3.75 eV to higher energies, while the rest of the  $\epsilon_2$  remains almost unchanged.

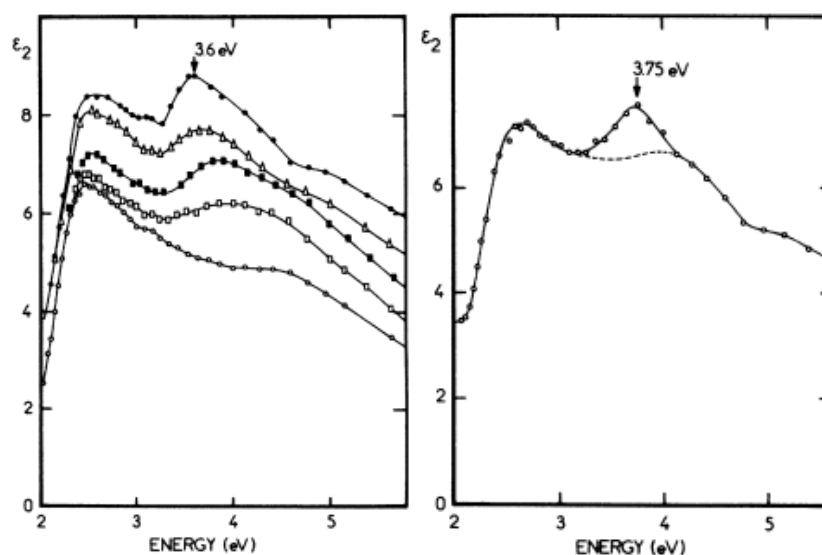


Figure 23. Reduction of the 3.6 eV peak in the dielectric function of Au<sub>0.25</sub>Cu<sub>0.75</sub> system with the transition from order to disorder.<sup>119</sup>

It has to be also noted that the difference in the sensitivity to order/disorder of the UV peak in Cu rich alloys is speculated to originate from transitions involving only conduction bands. Conversely, the lack of such an effect in Au-rich alloys was explained by d-sp transitions, which are supposed to be less affected by alloying. In general, the effect of disorder could be described as smoothing of the features of  $\epsilon_2$  with some, such as the peak around 3.7 eV, being more affected than others - a rather interesting effect, later explored in other works<sup>118,120,121</sup>.

De Silva *et al.* used both experimental and DFT results to probe the effect of disorder on Au-Cu alloy<sup>120</sup>. They list several reports from literature that point to ordering having a significant

effect on the shape of dielectric function of AuCu<sub>3</sub> and AuCu. One of them is a change in the crystal structure of AuCu from cubic to tetragonal in ordering transition. The effect of that phase transformation is not experimentally known. Furthermore, a research by Scott and Muldrew<sup>122</sup> is cited, reporting that ordering decreased  $\epsilon_2$  from 1.5 to 1.1 at 1.8 eV and to 0.5 between 0.5 and 1 eV. On the other hand Köster and Stahl report an increase of  $\epsilon_2$  from 3.4 to 4.4 at 1.8 eV<sup>123</sup>. Lastly, Rivory found little change in  $\epsilon_2$  on ordering<sup>119</sup>. Knowing the change in  $\epsilon_2$  in that range due to ordering is important because of possible LSPR in nanostructures being excited by similar energies.

The effect of disorder was explored using three different periodic structures with various atomic arrangements: a body centered cubic structure with the same arrangement as the ordered AuCu(I) alloy, but with cubic packing and the lattice parameter as in a disordered alloy and two face centered cubic supercells, one with 8 and the other with 1 atoms.

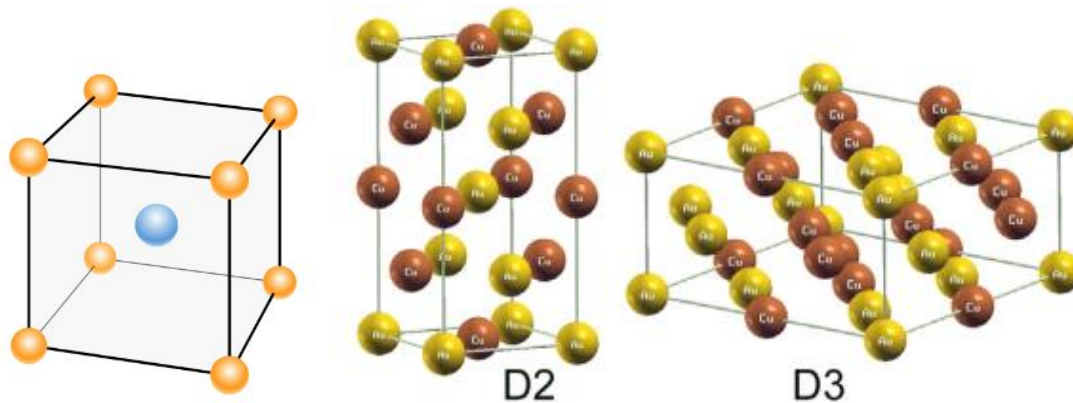


Figure 24. Three unit cells used to explore the effect of configuration and disorder in the work of De Silva *et al.*<sup>120</sup>

Dielectric functions that correspond to these cells, as well as those that correspond to pure gold and copper were calculated. The shapes of the calculated dielectric functions and the set of experimentally determined dielectric functions were qualitatively similar with the main source of discrepancy coming from a red shifted d-sp interband transition onset and an overestimation of  $\epsilon_2$  values - a known issue for PBE functional with RPA calculation scheme. Still, some differences were quite notable: all three structures representing the unit cell of Au-Cu alloys resulted in similar dielectric function, none of which managed to reproduce a large enough flattening of the 3.7 eV peak, although some reduction did occur. The authors

conclude that the effect of ordering is relatively minor and actually masked by the characteristic scatter band of experimental measurements.

However, it was later shown by Prandini, Rignanese and Marzari that the use of unit cells specially designed for proper representation of disordered systems - special quasirandom structures (SQS) - manages to reproduce the flattening of the 3.7 eV peak quite well<sup>118</sup>. It is fortuitous that in that work the functional of choice was PBE, and that the number of atoms in the cells was 16 - the same functional and number of atoms as in the largest unit cell used by De Silva *et al.*<sup>120</sup>, which did not fully reproduce the flattening of the said peak, thus showing that the benefits of the approach by Prandini *et al.* did not come from the size of the system nor the level of theory, but the way of representing the alloy structures. It follows that when probing the configurational influence on the alloy properties, the configurations deliberately designed to model the disordered structure will be needed to reliably model the influence of disorder.

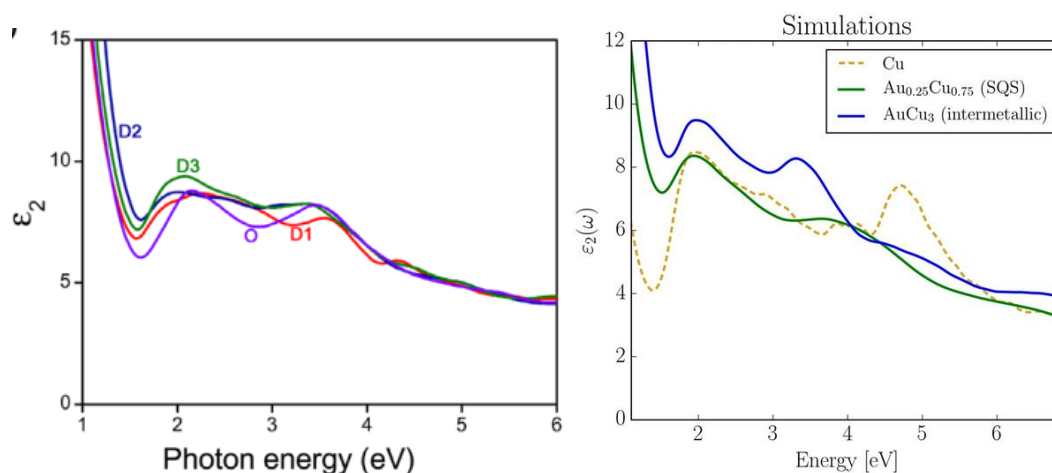


Figure 25. Dielectric functions obtained by Au-Cu unit cells of different configurations (left)<sup>120</sup>, and dielectric functions obtained in a different work<sup>118</sup>, in which simple unit cell and SQS were used. It can be seen that only by using SQS that peak near 3.6 eV disappears, showing that only the use of SQS leads to the reproduction of that experimentally observed phenomenon.

The concept of SQS was first proposed in the year 1990 By Zunger *et al.* as a technique for selecting a small number of not-too-large supercells containing special periodic “quasirandom structures” that mimic the first few radial correlation functions of an infinite substitutional random alloy<sup>124</sup>. Disorder is thus modeled by occupying a given (finite) number of sites of a periodic cell in a binary or a pseudobinary alloy. This approach works well because although



due to periodicity of such structures (periodic boundary conditions) there will be spurious effects beyond a certain distance, most of the important properties are governed by a couple of nearest neighbors. In this way costly statistical sampling methods can be circumvented, since good results can be obtained sometimes starting even at 8 atoms<sup>125</sup>. The method was tested both by comparing thermodynamic and optical properties to experimental results and computational results obtained using cells larger than 2000 atoms. Moreover, the development of newer and improved iterations is still ongoing<sup>126</sup>.

Among the other methods used for estimating the effects of disorder the simplest one is the virtual crystal approximation (VCA)<sup>127</sup>. Stated simply, this method averages the potentials of the constituent elements and constructs a lattice out of “composite” atoms with a potential constructed by the weighted contributions of the constituents. Thus it completely neglects the effects of a different local environment for each atom in a supercell, but provides exceptional computational efficiency due to the negligible increase in the computational cost when it is used. A recent comparison to the SQS method shows that this can be a reasonable compromise when alloys of very similar elements are used, but problematic otherwise<sup>128</sup>.

Yet another approach involves using a coherent potential approximation (CPA), for alloyed systems usually implemented using a Korringa-Kohn-Rostoker method (KKR-CPA). In it a lattice of effective potentials is constructed in a self-consistent way around impurities (alloy constituent elements). Similarly to the VCA method, KKR-CPA does not include effects of the local environment, only the long-range effects. Computationally inexpensive, it was one of the first methods used to model disorder-related effects in alloy electronic structure<sup>129,130</sup>, and still finds use for calculating related properties, including density of states (DOS) and band structure<sup>131,132</sup>.

It has to be noted that, as disorder is introduced, there is a loss of translational symmetry, and Bloch’s theorem is no longer applicable to such systems. Although to some extent, band structure picture can be applicable to alloys<sup>133</sup>, and experimental measurements of alloys are sometimes interpreted in terms of alloy band structures, the notion of bands and a band structure somewhat loses its meaning in disordered systems. In a relatively recent letter by Popescu and Zunger a new approach is laid out<sup>134</sup>. It produces an effective band structure (EBS) from supercells of random substitutional alloys, which shines the light on the extent to which the band characteristics are preserved for different compositions, band indices and k-points. Similar and even more recent band unfolding approaches claiming suitability for

---

simulating disorder are being introduced, showing ongoing interest in modeling the effects of disorder<sup>96,135</sup>.

However, there are indications that modeling disorder is not of crucial importance for alloy optical properties prediction. Recently, DFT calculations, albeit based on a very simple structure of a perfect crystal, helped explain experimental results and showed qualitative and even semiquantitative agreement with experimental data for Au-Ag alloys that form a (substantially disordered) solid solution<sup>136</sup>. XPS measurements showed the same trend as the DFT calculations for the shift of the interband transition threshold with the d-band position, with the influence of the d-band to the DOS identified as crucial for fine tuning the optical properties. Band structure engineering is proposed as a way to connect the electronic structure and optical properties of alloys. It has to be noted that low energy band splitting was observed for model alloys, resulting in close aligned near-parallel bands, reminiscent of the previously mentioned observations for intermetallic structures.

Finally, in the work by Skriver and Lengkeek, experimental measurements performed on an alloy system of Cu<sub>3</sub>Au stoichiometry showed that the optical absorption spectrum remains almost unchanged upon the order-disorder transition, barring the 10% reduction close to 3.6 eV that flattens the corresponding peak<sup>121</sup>. This is corroborated by some of the other earlier mentioned studies<sup>118,119,120</sup> and also shown in DOS calculations for Cu<sub>3</sub>Au system, along with Cu<sub>3</sub>Pt and Cu<sub>3</sub>Pd systems, which exhibit no shift of the DOS features between the ordered and disordered states, with the main difference being partial or complete smearing of some prominent features<sup>137</sup>. Echoing both findings, a study comparing experimentally determined colors with the DFT-based predictions showed that no significant change in the color between ordered and disordered structures can be seen. It is stated that there is no significant effect because the position of the onset of optical absorption is not modified by the presence of long-range order, and thus neither is the color<sup>118</sup>. Influence of ordering was also deemed unlikely to change the plasmonic properties of nanostructures by De Silva *et al.*<sup>120</sup>

It should be noted that an unusual low-energy peak, reminiscent of the ones observed in intermetallics calculations, is found by Skriver and Lengkeek in ellipsometric measurement of the  $\epsilon_2$  of the Cu<sub>3</sub>Au ordered system. They ascribe the lower reflection at the same energy range to the contribution of this observation. Similar deviations from the Drude-like behavior at low energies are also present in other experimental studies<sup>119,138,139</sup>. Band structure and joint density of states (JDOS) calculations show that transitions between close-lying bands are

---

likely to be responsible for the observed peak. This is especially important since it indicates that, at least when considering a system with a high degree of ordering, alloying can result in close-lying near parallel features of the band structure, which unlock low-energy interband transitions below the nominal d-sp transition onset/threshold.

In summary, insights regarding the effects of configuration of the unit cell for alloy systems of the same stoichiometry can be obtained relatively simply using small unit cells, but this might not be enough to properly model disordered systems. This is best demonstrated by comparing the results of different computational approaches with experimental data available for a system of  $\text{Cu}_3\text{Au}$  stoichiometry that can vary from disordered to ordered with an  $\text{L1}_2$  crystal structure. Use of SQS seems to be a good approach to properly reproduce the experimental data, but it does require one or more supercells to be created for any given stoichiometry. Depending on the level of precision that is required in the study there are other options such as using efficient approaches (KKR-CPA or VCA) that neglect the effects of local structure but account relatively well for the long-range effects. Moreover, it was shown for some systems that disregarding the effects of disorder completely still leads to qualitative or even semiquantitative agreement with experimental results. In other cases effects of disorder have been noted for intermediate results, such as dielectric function, but have shown to be irrelevant for the final results such as coloration. The choice of whether and how to introduce the effects of disorder is a nuanced one, as there is, as of now, no universal solution. As such, problems should be approached on a case-by-case basis and results compared until, with accumulation of data, best practices gradually emerge.

### 3.3.6. *Calculating hot carrier properties by DFT*

All three aforementioned computational approaches (section 3.3.1) used for obtaining plasmonic properties by DFT-based methods have been utilized to study hot carrier-related properties. Jellium models were among the first ones to be used to study both the generation and the relaxation of the hot carriers in plasmonic nanoparticles<sup>69,97</sup> as well as extraction to adjacent molecules<sup>140</sup>. Some of the pivotal studies using the jellium model provided first theoretical predictions regarding the dependence of the hot carrier energy distribution on the size of the nanoparticle and the relaxation time. However, in terms of calculations related to hot carriers, such models were insofar generally applied using only spherical geometry and in most cases, two metals - Au and Ag - although jellium model should in principle be better

---

suited for alkali-like metals. Jellium models are only applicable below the interband transition threshold, where only indirect transitions in the conduction band, which is free electron like, are available. However, if transitions between different bands are available, which is the case in many other metals, the use of a jellium model, which consists of free flowing gas of electrons, should be avoided<sup>98</sup>. For Au and Cu the jellium model can thus be highly imperfect, especially for photon energies higher than 2 eV, as d-sp interband transitions become available above that energy. In terms of hot carrier-related properties, for elements such as Al which have available interband transitions in the broad energy range<sup>70,98,103</sup>, jellium models are actually not suitable (although for obtaining many other properties jellium models are reasonably well applicable to Al). Narang *et al.* even state that, in the context of hot carrier generation, jellium models are “inapplicable to aluminum”<sup>98</sup>. While the model has been extended to bimetallic systems, the only metals studied were Au and Ag, and in a core-shell structure, meaning no alloying<sup>141</sup>. Due to limitation to a low number of elements, and since some of the aforementioned research found newly available interband transitions even below the d-sp transition threshold upon alloying Au and Cu, use of jellium models for alloyed nanostructures is not appropriate.

Unlike jellium models, atomistic models are much more exact and provide invaluable data including detailed evolution of plasmon excitation, hot carrier distribution and hot carrier injection propensity given the exact size and shape of the nanoparticle. Influence of geometry on the hot carrier distribution is found to be particularly important, showing that hot electrons are preferentially distributed on the areas of lower atom coordination such as edges, corners and certain facets of a nanoparticle, and that nanoparticles with larger proportion of such features generate more energetic hot electrons<sup>78</sup>. Decay mechanisms have also been explored shedding light on the different contributions of sp-bands and d-bands<sup>78,99,142</sup>. Important mechanistic information regarding hot carrier transfer from the metal nanoparticle to molecules and to semiconductors has recently been obtained using atomistic models<sup>143,144,145</sup>. This is a unique advantage of atomistic models since explicit modeling of both the donor and the acceptor system is best suited for elucidating the mechanistic details of such a process, which as of now cannot be obtained by other computational or experimental methods. Currently two relatively similar approaches have been used, TDDFT with RPA or adiabatic GLLB-SC and time-dependent density functional based tight binding (TD-DFTB). However, atomistic models for hot carrier-related calculations have insofar been limited to less than

---

1000 atoms, with Au and Ag as the metals of choice. Studying alloying by atomic-level models is as of now quite computationally expensive and not suited for an extensive study of many different systems and configurations. However, in a recent perspective paper, Sánchez and Berdakin highlight alloyed nanoparticles as interesting systems for future studies related to hot carrier generation using atomic-level calculations<sup>100</sup>.

Bulk-based DFT models have been used for more than a decade, starting approximately in parallel with jellium models, to calculate properties related to hot carrier generation. Some of the pivotal earlier works do not yet include nanoparticle geometry, but focus only on thin films and surfaces<sup>103,105</sup>. Later iterations of bulk-based methods include modeling of both the plasmons and the nanoparticles of different sizes which improved the applicability of the results and enabled better analysis of the surface-based effects on hot carrier generation and, very importantly, estimation of relative importance of different hot carrier generation channels to total hot carrier energy distribution<sup>70,145</sup>. Such methods are computationally involved but quite versatile regarding the choice of a pure metal, with most studied being Au, Ag, Al and Cu, but also alkali metals such as Na and K being included. However, applying a method that relies on a bulk-based model to alloy systems is not straightforward. There are two problematic requirements of such methods and the models used insofar include one or both of them: the first is the use of empirical parameters which are not readily available for alloys and the second is the use of expensive computational methods. For example, the approach by Bernardi *et al.* includes the calculation of self-energy which requires a correction using a costly GW approximation on a dense k-point grid<sup>105</sup>. That makes it inapplicable for multiatom unit cells and many different alloy systems. The approach by Sundararaman *et al.*<sup>70</sup> requires DFT+U with empirically fitted U parameter and the use of experimentally determined dielectric functions which is an issue if the large composition space of alloys consisting of different components and in different ratios is to be studied. Approach by Dal Forno<sup>146</sup> also requires the use of experimentally determined dielectric function. Moreover, in that work they also use experimentally determined work functions, which requires knowledge of the surface (its Miller indices), often not even known for alloys. Additionally they use the Matthiesen's rule, which requires empirical parameters and for alloys deviates a lot in cases of phase transitions due to appearance of ordered phases for certain alloy compositions. Bulk calculations have been used for estimation of alloy hot carrier energy distribution, but in a much more simplified way, based on a method by White

---

---

and Catchpole<sup>147</sup>, expanded by Gong *et al*<sup>95</sup>. Put in simple terms, this approach involves a product of two DOS separated by the photon energy, and with Fermi distribution in mind to account for filled and empty states. However, this method carries in it a relatively large approximation: it completely neglects the momentum conservation, which means that all the direct and indirect transitions are being treated the same. Despite the crudeness of the approximation and the relatively old origin of such an approach, it is still being used, and results are published in prominent journals<sup>96,148</sup>. Therefore, there is a need in the field for a new method for alloy hot carrier generation estimation, one with sufficient efficiency and simplicity to replace the currently used one, but one which also takes momentum conservation into account.

---

## § 4. COMPUTATIONAL METHODS

The fundamental part of this work is based on density functional theory (DFT). All DFT calculations were performed using the GPAW package<sup>149</sup> and atomic simulation environment (ASE)<sup>150</sup>. Brillouin zone was sampled with Monkhorst-Pack grid<sup>151</sup> and plane waves were used as a basis set. Smearing was of Fermi-Dirac type with the value of 0.1 eV.

### 4.1. Establishing a computational framework for optical and plasmonic properties calculation

#### 4.1.1. *The choice of the method*

The choice of the computational approach is based on the goal of this work, which is to find the combination of efficiency and accuracy suitable for performing calculations on a large number of alloyed systems. These calculations ought to have predictive value and also provide fundamental insight. For these reasons alloys are represented as a bulk material. This is done by first forming a unit cell of a binary alloy with a desired stoichiometry with periodic boundary conditions, meaning that the unit cell is effectively extended to infinity in all directions, thereby representing a quasi-infinite (bulk) system. To extend the results to nanostructures, the dielectric functions obtained for bulk alloys are used as a basis for electrodynamic simulations for plasmonic nanoparticles.

#### 4.1.2. *The choice of alloy systems*

Four binary alloy systems were chosen for this part of the study: Au-Cu, Au-Ag, Au-Pd and Ag-Cu. The choice of the constituent elements is based on several factors:

- In their pure state these elements form bulk crystals with a face centered cubic (FCC) lattice.
  - When alloyed they form substitutional alloys with a FCC-like structure, which makes modeling of the alloys more straightforward.
  - Adequate experimental data exists for both the stable (Au-Cu, Au-Ag, Au-Pd) alloys, and for the metastable Ag-Cu which does not form stable alloys in the larger part of the compositional range. This enables evaluation of the computational results.
-

Increments of 12.% were chosen for sampling of the compositional space which translates to 9 systems - 2 for pure metals at the extremes and 7 for their alloys with varying element ratios. For pure metals 1 atom cells were used, for 25%, 50% and 75% ratios 4 atom cells were used, and for 12.5%, 37.5%, 62.5% and 87.5% ratios 8 atom cells were used. 8 atom cells are roughly two times longer in the z-direction that in the x and y-directions and resemble two 4 atom FCC unit cells stacked one on top of the other.

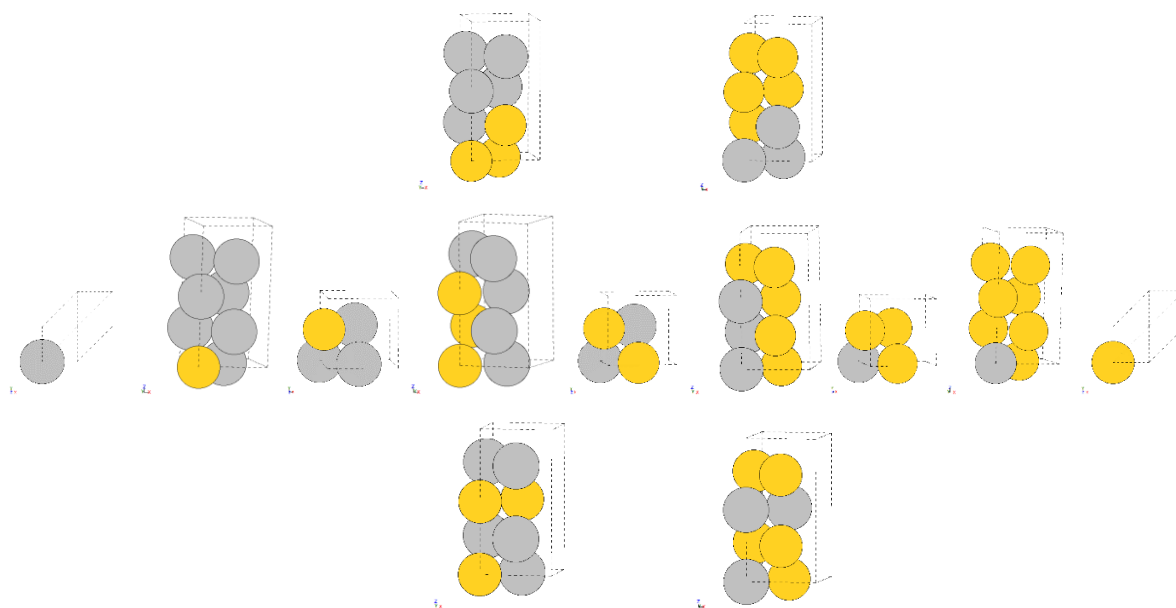


Figure 26. Different unit cells used to represent Au-Ag alloyed systems.<sup>152</sup>

It has to be noted that setting up cells in this way results in three possible configurations of  $A_3B_5$ -like cells (37.5% or 62.5% ratio), all of which are used in calculations and used to study the effects of configuration change. Three different configurations of those cells are shown in the Figure 26.

#### 4.1.3. Structure optimization

Broyden–Fletcher–Goldfarb–Shanno (BFGS) algorithm<sup>153</sup> was used for structure optimization. For simultaneous optimization of atom positions and unit cell parameters the UnitCellFilter method was included in the optimization procedure. Unit cells of all four pure elements were first optimized using two different functionals – PBE<sup>154</sup> and PBEsol<sup>155</sup>. A 44x44x44 k-point grid was shown to be sufficient for 1 atom unit cell optimizations. Compared to experimental cell parameters PBEsol outperformed PBE for Au, Ag and Pd, with comparable results for Cu. Table 1 with the results is presented in the Results and



discussion section. Due to better performance for pure elements, PBEsol was chosen for all subsequent alloy unit cell optimizations.

Initial unit cells for structure optimization were set up by creating an FCC unit cell of an appropriate size (4 or 8 atoms) of one element and then substituting the appropriate number of chosen atoms with the atoms of another element. Afterwards, the optimization procedure was initiated. 4 atom alloy unit cells were optimized using sampling on a 24x24x24 k-point grid. For 8 atom cells, due to one dimension being roughly double in the z-direction in the real space, the k-points were halved in the z-direction since the reciprocal cell is twice smaller in that direction, resulting in 24x24x12 k-point sampling. For both the pure and alloy unit cell optimizations a high plane wave cutoff energy of 500 eV was used to mitigate the effect of Pulay stress during the structure optimization. Pulay stress is an error in the stress tensor that arises due to incompleteness of the basis set with respect to the changes in volume which can lead to errors in the optimized geometry. Therefore increasing the number of plane waves by imposing a relatively high cutoff mitigates the error. The convergence criterion in all of the optimization procedures was set to 0.03 eV/Å meaning that the geometry is declared to be converged when the force on all the individual atoms drops below the chosen criterion.

#### 4.1.4. Density of states calculations

Density of states calculations were performed using optimized unit cell geometries as a starting point. Ground state calculations were performed both with PBE and GLLB-SC using a 36x36x36 k-point grid for 4 atom cells and 36x36x18 k-point grid for 8-atom cells. Plane wave cutoff was set to 400 eV. In all cases additional empty bands were used. All parameters were tested for convergence. Calculations of atomic orbital projected density of states (PDOS) and individual atom projected densities of states were performed based on the same ground state calculation. Since GPAW does not provide normalized PDOS, it was subsequently normalized and checked for accuracy using a total DOS calculation.

#### 4.1.5. Band structure calculations

Ground state calculations were performed using PBE and GLLB-SC functionals. A 40x40x40 k-point grid for 4 atom cells and 40x40x20 k-point grid for 8-atom cells was used, with a 400 eV plane wave cutoff. Number of the bands was set to the number of filled bands with 6 empty bands added to each system. Convergence was tested for all parameters.

---

These ground states were used to obtain the band structure. The same number of bands was used to calculate the band structure for each system following the relevant high symmetry path based on the optimized unit cell geometry. At least 200 points along the high symmetry path were taken for each band structure calculation. All band structures were calculated using both PBE and GLLB-SC functionals so their performance could be compared.

#### 4.1.6. Dielectric function calculations

One LDA and several GGA-level exchange-correlation functionals were benchmarked based on the agreement of calculated dielectric functions and the experimentally available data for pure metals: LDA<sup>156</sup>, PBE<sup>154</sup>, PBEsol<sup>155</sup>, RPBE<sup>157</sup>, vDW-DF<sup>158</sup> and GLLB-SC<sup>159</sup>.

Additionally, dielectric functions of Au and Ag calculated with PBE+U were produced for various values of U applied to d bands: U = 1 eV, U = 2 eV, U = 3 eV, U = 4 eV.

The same ground state as for the band structure is used as the basis for dielectric function, with k-mesh and number of bands and plane wave cutoff being the same as for the band structure. The value of the broadening parameter  $\eta$  was chosen to be 0.15. Scattering rate parameter was set to 0.01 eV for all dielectric functions. Although relatively low, this value was previously used in the literature and allows for comparison to other works and for obtaining a good distinction between the Drude term and the interband-related features of the dielectric function. For electrodynamic calculations  $\gamma$  was linearly interpolated between experimental values for pure Au and Ag obtained from the work of Peña-Rodríguez<sup>160</sup> to obtain the least possible discrepancy between results in the infrared range where the scattering rate strongly influences the dielectric function values. In this way the best possible results for calculated dielectric functions were used as initial values for electrodynamics simulations.

#### 4.1.7. Electrodynamics simulations

Electrodynamics simulations for alloyed systems were performed using dielectric functions obtained by DFT calculations and by experimental data obtained from the work of Peña-Rodríguez *et al.*<sup>160</sup>. Standard mathematical expressions from literature were used to calculate analytically the electrostatic dipole polarizability as

$$\alpha = 4\pi a^3 \frac{\varepsilon - \varepsilon_m}{\varepsilon + 2\varepsilon_m} \quad (4.1)$$

where  $a$  is the radius of the sphere,  $\varepsilon_m$  is the dielectric constant of the surrounding medium and  $\varepsilon$  is the dielectric response of the sphere material. Dispersion relation calculated at the interface of glass and metal is defined as

$$\beta = k_0 \sqrt{\frac{\varepsilon_1 \varepsilon_2}{\varepsilon_1 + \varepsilon_2}} \quad (4.2)$$

where  $k_0$  is the component of the wavevector perpendicular to the interface  $\varepsilon_1$  is the real and  $\varepsilon_2$  the imaginary part of the dielectric function. Reflectance is calculated as

$$R = \frac{(n-1)^2 + k^2}{(n+1)^2 + k^2} \quad (4.3)$$

with  $n$  and  $k$  being the real and complex parts of  $N = \sqrt{\varepsilon}$ , and reflectance in Kretschmann configuration which was calculated using the transfer matrix approach<sup>161</sup>. Own code for implementing the multiple-particle Mie theory (not developed as a part of this work) was used to calculate near field properties of nanoparticle systems<sup>162</sup>. For the optical response of nanorods the MNPBEM toolbox was used<sup>163</sup>. As explained in the Theoretical basis section, the calculations are based on taking into account that the field acting over every particle is the sum of the incoming field and the field scattered by the other particles. All the fields are expressed as a sum of vector spherical harmonics and the resulting system of coupled equations is solved numerically using MATLAB built-in functions. This approach utilizes a boundary element method to solve Maxwell equations in geometries that are unsuitable for analytical solutions.

## 4.2. Hot carrier generation

In case of hot carrier generation, instead of explicitly defining the k-point grid, a k-point density was set for calculations. This choice was made to ensure proper k-point spacing in all directions, in particular due to higher diversity of unit cells and difference in their shapes when compared to the cells used for optical and plasmonic properties predictions.

### 4.2.1. Unit cell optimization

Unit cells of FCC-like alloys that do not have an ordered and experimentally known crystal structure were optimized using a PBEsol functional. Density of k-points for optimization was set to 15 k-points per reciprocal Å. When experimental data for the crystal structure of a particular alloy was available, that crystal structure was used and the structure was not

optimized. Plane wave energy cutoff was set to 500 eV to lower the effects of Pulay stress. Geometry optimization cutoff was set to 0.03 eV per Å for forces acting on all individual atoms.

#### 4.2.2. *Density of states calculations*

Density of states calculations were performed using a k-point density of 30 k-points per reciprocal Å and a 400 eV plane wave cutoff and using a GLLB-SC exchange-correlation functional.

#### 4.2.3. *Hot carrier energy distribution calculations*

##### DOS-based approach

Hot carrier energy distributions were obtained in two ways. In one approach they are obtained from the DOS calculations following the method presented in the work by White and Catchpole with a Gong and Munday addition of Fermi-Dirac distribution<sup>95,147</sup>. The hot electron distribution is obtained by calculating, for each point in the energy range, a product of two DOS at energies that are a photon energy apart, keeping in mind their respective occupancies at a given energy level (product of a density of filled states with the density of unfilled states one photon energy apart). Since DOS is not k-point resolved, momentum conservation is completely neglected, because transitions from all states are being treated the same, regardless of whether they might be direct or indirect, interband or intraband.

##### JDOS-based approach

In the other approach, which is presented as an alternative in this work, momentum conservation is strictly taken into account when calculating hot carrier energy distributions. The results therefore reflect solely the effect of interband transitions. The basis of this method is the calculation of joint density of states (JDOS). From it a hot carrier energy distribution is obtained by summing all the available transitions between two states a photon energy apart, that also have the same wave vector. To avoid band folding, each unit cell is first transformed to a primitive unit cell, meaning that the smallest possible number of atoms that recreates the same lattice remain in the cell. This is performed using the Python spglib module<sup>164</sup>. As an added benefit, reducing the unit cells also increases efficiency of the approach. Energy states and their occupancies are then calculated. To ensure the meaningful occupancies are used, for

---

these calculations the width of the Fermi-Dirac distribution is not set to 0.1 eV, as is the case for other calculations to achieve quicker convergence, but to 0.0257 eV, which is the width at the room temperature. For these calculations the density of k-points is increased to 50 per reciprocal Å, which is a relatively high number. While a lower density is likely to also be sufficient, in this case a high number is used to ensure that all features of the resulting hot carrier distribution are properly distinguished. Several empty bands are included in all cases. Plane wave cutoff is set to 450 eV.

Similarly to the DOS-based approach, the available excitations are counted between all states separated by a certain photon energy. However, in this JDOS-based approach only the states located at the same k-point are considered as available for transitions (only direct transitions are allowed). A broadening of  $\pm 8$  meV is also implemented when considering the energy difference between states because of the low band width at a certain k-point. The hot carrier generation probability is also weighted by the respective occupancies of the initial and final states. For each transition hot hole generation is counted and added to the total at the energy of the initial state (relative to the Fermi level that is set to 0). Likewise, a hot electron generation is counted and added to the total at the energy of the final state relative to the Fermi level. The expression is as follows:

$$N(E, E_{ph}) = \sum_{k \in BZ} \sum_n \sum_{m>n} (f_{kn} - f_{km}) \delta[E - (E_{km} - E_F)] \delta[E_{ph} - (E_{km} - E_{kn})] \quad (4.4)$$

where  $N(E, E_{ph})$  is the hot electron distribution,  $f_{kn}$  is the occupancy of the initial state  $n$ , and  $f_{km}$  is the occupancy of the final state  $m$ , the  $\delta$  function on the right side ensures that the photon energy has to be equal to the difference between the initial and final states, while the  $\delta$  function on the left ensures that of all the valid transitions only the ones that result in hot electrons of energy  $E$ , which is equal to the energy difference between the final state and the Fermi level, are being counted. Hot holes are being counted in a similar way but focusing on the energy differences between initial state (from which electron is being excited and the hole is created) and the Fermi level. After all transitions have been considered, histograms representing hot hole and hot electron energy distributions are made. Finally, Gaussian convolution is used for smoothing of the energy distributions.

## § 5. RESULTS AND DISCUSSION

### 5.1. Structure optimization

Since the atomic arrangement in the lattice influences the eigenstates of the resulting structure, for example through greater orbital overlap due to lower interatomic distance, it follows that structure optimization affects the transitions between states, and thus also the dielectric function of the material. However, it is not obvious to what extent the dielectric function of the alloys can be affected by the lattice parameter differences resulting from different optimization parameters such as the choice of the functional. Unlike most of the other parameters for structure optimization that can be tested for convergence, the choice of the functional has to be made by benchmarking with respect to the experimental data or extrapolating from the information available in the literature. In this work two functionals that are commonly used for optimizing the structure of solid state systems are compared: PBE and PBEsol - a PBE-based functional optimized for solids. It has been shown that PBEsol is particularly successful for lattice optimizations of many bulk solids and, most importantly for this work, some noble metals<sup>165,166</sup>. This is also reflected in the results using our optimization parameters and the GPAW package (Table 1): PBEsol outperformed PBE for lattice constant calculations of three of the four metals - Au, Ag, and Pd - while showing comparable discrepancy from the experimental data as PBE for Cu.

Table 1. Comparison of lattice constants (in Å) for Au, Ag, Cu and Pd calculated using PBEsol and PBE functionals with experimental data obtained from the work of Lubarda for Ag, Au and Cu<sup>167</sup> and from the work of Arblaster for Pd<sup>168</sup>.

	<b>PBEsol</b>	<b>PBE</b>	<b>Experiment</b>
<b>Au</b>	4.100	4.166	4.078
<b>Ag</b>	4.052	4.138	4.086
<b>Cu</b>	3.576	3.634	3.615
<b>Pd</b>	3.880	3.940	3.889

The influence of the resulting lattice constant difference on the dielectric function is also explored and shown in the Figure 27. It can be seen that, although the difference in the lattice parameter of Ag does not seem to be large, the influence on the dielectric function (calculated using the same parameters except the lattice constant) is not negligible and can be comparable to the influence of the choice of functional or implementing a correction such as GW. In this case it is more so important since the part of the dielectric function reflecting the onset of interband transitions is affected by the different lattice constant value, which can have an outsized influence on the resulting plasmonic properties. This fact should not be neglected because the choice of the structure optimization approach usually ends up overlooked in computational studies of plasmonic properties, while these results imply that it can be important for reducing the discrepancy from the experimental data and approaching quantitative agreement.

Since PBEsol showed better performance than PBE, and due to relatively close agreement with the experimental data, structure optimizations for all other systems are performed using only PBEsol.

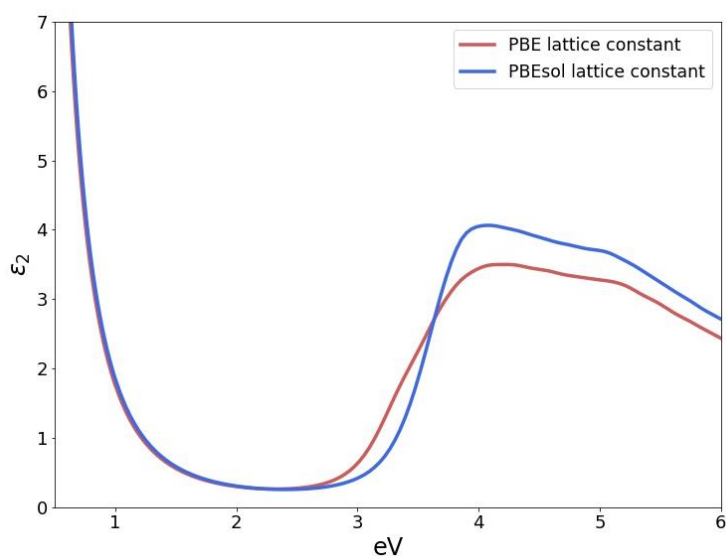


Figure 27. Imaginary part of the dielectric function of Au calculated using GLLB-SC functional. Starting geometries were optimized using PBE (red) and PBEsol (blue).<sup>152</sup>

## 5.2. Establishing a computational framework for optical and plasmonic properties prediction

### 5.2.1. Choice of scattering rate

Due to the way the dielectric function calculation is implemented in most DFT codes, one parameter - the scattering rate - is usually either empirically determined or set arbitrarily as a suitable guess. As was shown in the Theoretical basis section, in terms of transitions that contribute to the optical response of the material, the dielectric function is comprised of intraband (within the band) and interband (between different bands) contributions.

Interband transitions are calculated ab initio, but the intraband typically are not, so their effect is usually introduced through the expression derived from Drude model of electrical conductivity:

$$\epsilon_{intra} = \frac{\omega_p^2}{(\omega + i\gamma)^2} \quad (5.1)$$

Where  $\gamma$  is the scattering rate,  $\omega$  is the light frequency and  $\omega_p$  is the plasma frequency. It is very important to note that, to follow the linear response formalism, the implementation of the rate parameter in GPAW differs from typical expression of the Drude term

$$\epsilon_{intra} = 1 - \frac{\omega_p^2}{\omega(\omega + i\gamma)} \quad (5.2)$$

which can result in the factor of 2 discrepancy between the resulting dielectric function value if some of the literature values for the scattering rate are used.

To achieve the best agreement with experimentally measured dielectric function, it is usually the best to use values from the literature, if possible. However, an arbitrary value can be chosen if there are no experimentally determined results, or to better suit the cause (for example, to eliminate one variable for comparison purposes of other factors). Usually this value is 0.01 eV which is a physically meaningful but relatively low scattering rate. That value is used for all the calculations in this work, except for a specific case in electrodynamics simulations where calculation results in the low energy region, where the Drude term dominates, are compared to experimental results. In that case the values of the scattering rate for alloys were interpolated between the values for pure elements.

### 5.2.2. Choice of the optimal functional

With all of the other relevant parameters converged and determined, the choice of the exchange-correlation parameters is the most important factor in achieving a satisfactory

---



agreement with experiments. For that reason, benchmarking of several different functionals was performed for elements in their pure bulk state, since good experimental data is available for comparison. The functionals were chosen based on their availability in the GPAW code and computational efficiency - thus up to the GGA level: LDA, PBE and its upgrades RPBE and PBEsol, vdW-DF and GLLB-SC. The results are shown in Figure 28:

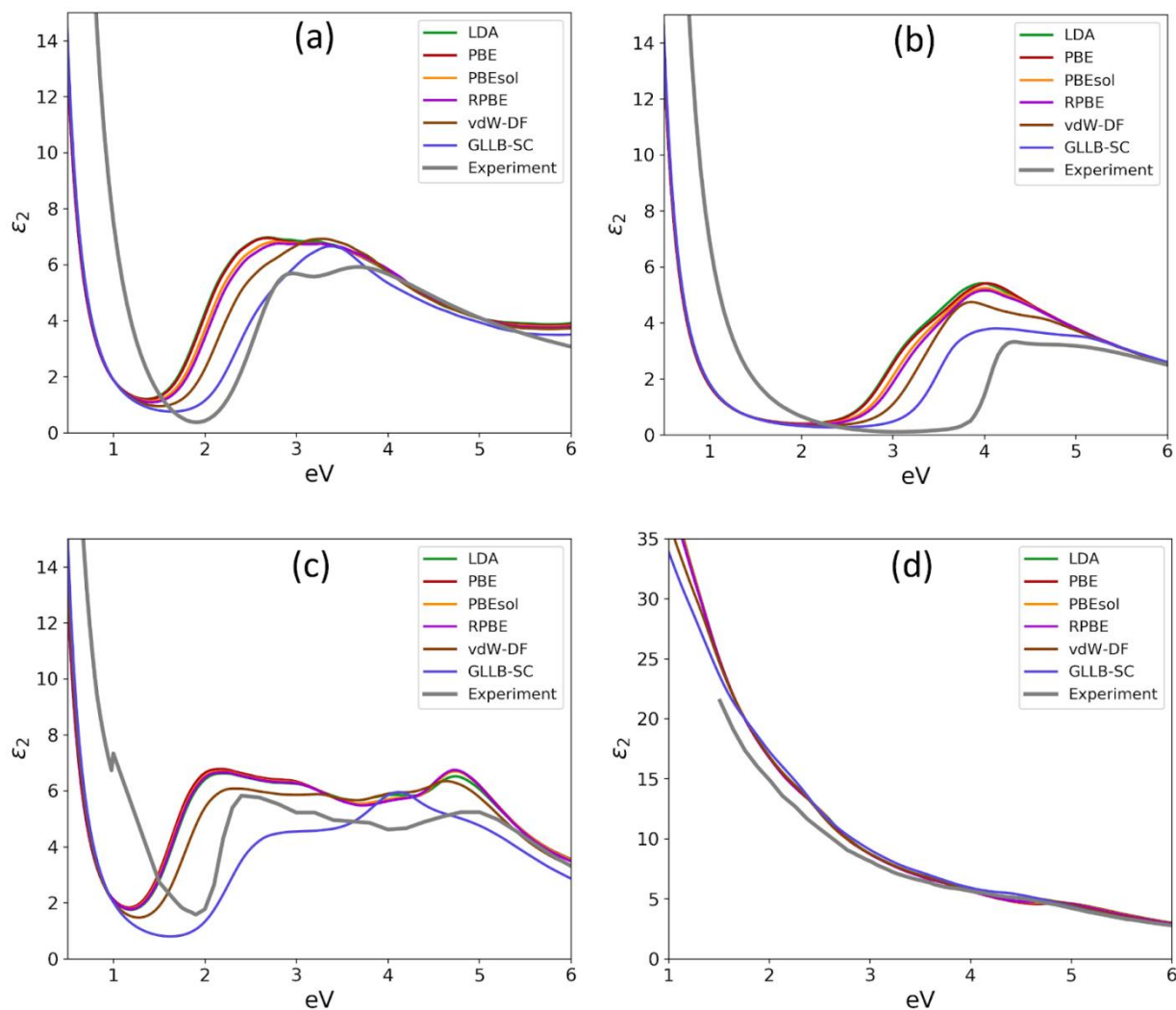


Figure 28. Comparison of the imaginary part of the dielectric functions of pure Au (a), Ag (b), Cu (c) and Pd (d) calculated using different functionals with the experimentally measured dielectric functions. The lack of agreement in the lower energy region is due to the scattering rate of all pure elements being set to 0.01 eV. Experimentally determined lattice constants were used for calculations. Both choices were made to isolate the effect of different functionals on the dielectric function calculation.<sup>152</sup>

In Figure 28. only the imaginary parts of the dielectric functions are shown since they are most suitable for comparison, with mild variations of values in the most of the energy range, and with clear delineation of interband and intraband contributions for some of the elements. Comparison of the DFT-based dielectric functions and the experimental data shows that all of the functionals perform quite similarly and relatively well for Pd, but that there are large differences in performance for Ag, Au and Cu. For the latter metals we see somewhat of a clustering of the data for LDA and PBE-based functionals, with vdW-DF performing similarly, but slightly better, and GLLB-SC showing the closest agreement with the experimental results, especially with regards to the interband onset. It is hard to define an objective parameter by which to evaluate the performance of different functionals. Not surprisingly, having in mind well known issues of GGA-level functionals in electronic structure and dielectric function calculations, visual inspection obviously shows that all of the calculations lead to a slight red shift of the interband transitions onset and an overestimation of the  $\epsilon_2$  values in the most of the energy range for Au, Ag and Cu. One exception is GLLB-SC which actually gives a bit lower  $\epsilon_2$  values and a very similar interband transitions onset for Cu. Since the interband transitions onset is of crucial importance for plasmonic and optical properties prediction it can be a relatively good, although a somewhat simplistic, figure of merit for benchmarking. We define the interband transitions onset as the the energy at which  $\epsilon_2$  reaches 200% of its minimum value. In Table 2 the values of interband transition onset determined in this way for all of the calculated and experimentally determined dielectric functions are listed. This quantification of interband transition onset shows in a more objective way that GLLB-SC has by far the best performance, erring less than all other functionals for Ag and having almost exactly the same value as the experiment for Au and Cu. For all other functionals the interband transition onset value is substantially red-shifted.

---

Table 2. Comparison of interband transition onsets determined from DFT-based dielectric functions and from experimentally determined dielectric functions for Au, Ag and Cu. In some cases the values are exactly the same since the energy array used for calculations does not have increments small enough to distinguish between different functionals. Experimental data for Au and Ag is from Peña-Rodríguez *et al*<sup>160</sup> and for Cu from Arblaster *et al*<sup>169</sup>.

	<b>LDA</b>	<b>PBE</b>	<b>PBEsol</b>	<b>RPBE</b>	<b>vdW-DF</b>	<b>GLLB-SC</b>	<b>Experiment</b>
<b>Au</b>	1.80	1.84	1.80	1.84	1.97	2.13	2.15
<b>Ag</b>	2.60	2.68	2.60	2.68	2.85	3.06	3.65
<b>Cu</b>	1.63	1.59	1.59	1.59	1.71	2.09	2.20

The variation in the computationally predicted dielectric functions is much larger than the variation between different experimentally determined dielectric functions for the same element in the interband region. For example, the experimentally determined  $\epsilon_2$  for Au<sup>170</sup> and Ag<sup>171</sup> do vary slightly in shape and value of the maxima in the interband region, but unlike for different functionals, there seems to be a very close agreement in the interband transition onsets for experimental data.

Since PBE is the standardly used functional for dielectric function and electronic structure calculations and all of the other benchmarked functionals except GLLB-SC show very similar results, in the calculations for alloy systems only PBE and GLLB-SC are used and compared. Therefore, GLLB-SC was tested as a same cost alternative to PBE with prospects of being a suitable new standard if it also performs substantially better for alloys.

The underlying reason for the better performance of the GLLB-SC functional can be elucidated by observing the differences in the band structures calculated using PBE and GLLB-SC shown in the Figure 29.

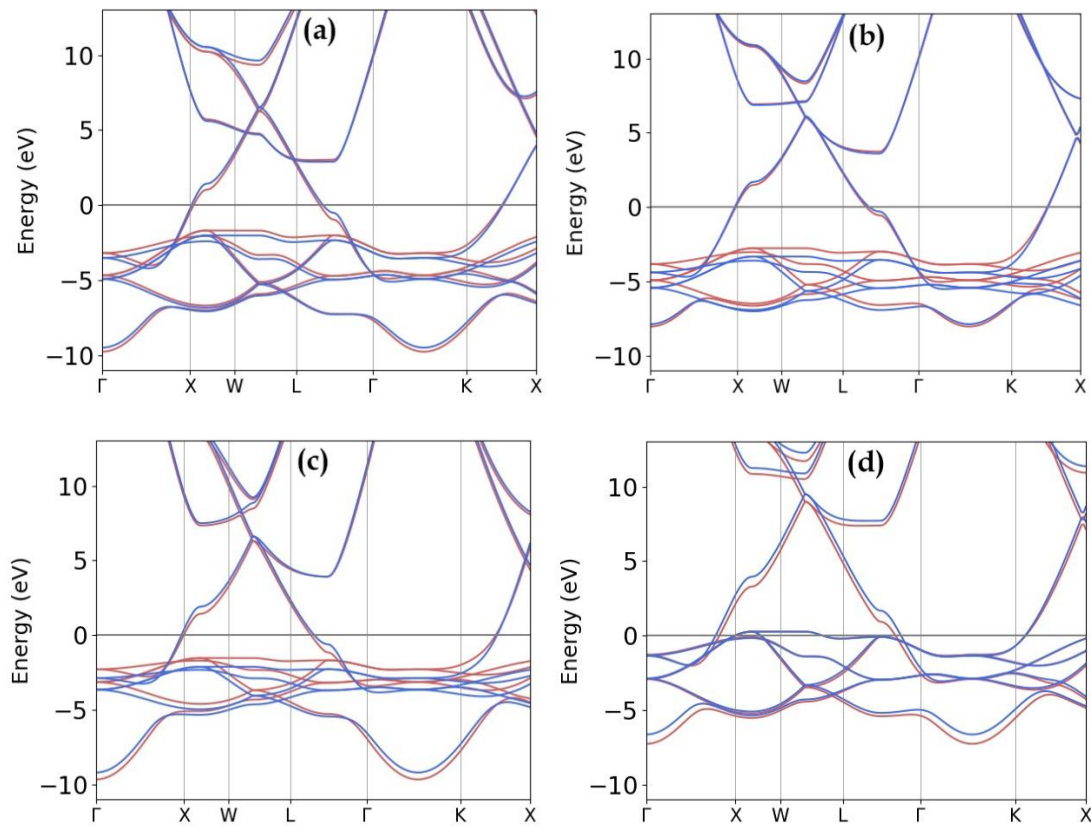


Figure 29. Comparison of band structures calculated by PBE (red color) and GLLB-SC (blue color) functionals for Au (a) Ag, (b) Cu (c) and Pd (d).<sup>152</sup>

It is visible that for the good plasmonic metals with the filled d-shell (Cu, Au, Ag) GLLB-SC predicts significantly lower lying d-bands, thus correctly shifting the interband transition onset to higher energies. Although of GGA-level, this functional seems to avoid the issues of too disperse and shallow d-bands that is characteristic for GGA functionals. Results for the less localized sp-bands seem to be quite similar for both functionals. For Pd with the unfilled d-shell and d-bands that cross the Fermi level, PBE and GLLB-SC give similar results. As stated in the Literature review, d-states of good plasmonic metals are more localized when calculated using GLLB-SC, and thus also lower in energy. Dielectric function shape can be connected to the corresponding band structure by observing that nowhere in the band structure is there a band below the Fermi level separated by an energy that would correspond to an IR photon for Au, Ag, and Cu. Thus, in the low energy range such as IR range, interband contribution to the dielectric function is either low or nonexistent for these metals. Above the interband transition threshold however, interband transitions dominate. Pd, on the other hand,

has high lying d-bands which cross the Fermi level and thus even in the low energy range interband transitions contribute to the dielectric function.

### 5.2.3. DFT+U and derivative discontinuity

As another way to correct the d-band treatment by functionals such as PBE, a DFT+U method was tested. Several values of the Hubbard-like U term were applied to the d-orbitals of Au and Ag and the dielectric function was calculated. This dielectric function was compared to the dielectric function calculated using the GLLB-SC functional.

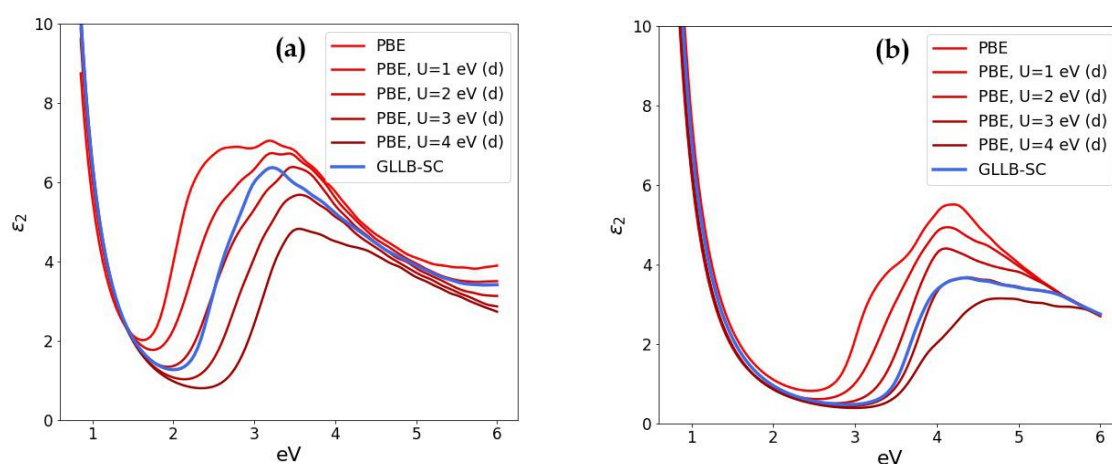


Figure 30. Comparison of the imaginary part of the dielectric function calculated using PBE and PBE+U with various values of Hubbard-like term U (red, shaded progressively with increasing U parameter), and the one using GLLB-SC (blue). For Au, PBE+U closely resembles GLLB-SC in shape when value of U applied to d-orbital is 2 eV (a) while for Ag PBE+U resembles GLLB-SC closely in shape when U applied to d-orbital is 3 eV (b).<sup>152</sup>

As can be seen from the Figure 30, as the value of U is increased, the interband transition onset is blue shifted, which contributes favorably to the agreement with experiments up to a point, but afterwards results in an erroneous blue shift and the overall shape deterioration. For a certain value of U, the dielectric function calculated using PBE+U becomes very similar to the one calculated using GLLB-SC (U = 2 eV for Au and U = 3 eV for Ag).

This similarity is not accidental. Both the localizing potential applied by the Hubbard-like U and the energy-dependent localization of the exchange hole present in the GLLB-SC act in the fundamentally similar way: they introduce the derivative discontinuity and thus correct the description of the d-states. The difference in the potential acting on the d-orbitals

localizes them, lowers their energy, and thus adds to the gap between the filled d-bands and the unfilled sp-bands. This means that the interband transition onset is shifted to higher energies and the known GGA issue is corrected. Moreover, another similarity is in GLLB-SC being based on PBEsol functional, which is just an upgraded version of the PBE functional. Comparison of all three functionals can be seen in the Figure 31. The value of  $U$  of 3 eV used to correct PBE and PBEsol since it was shown on Figure 30 that this value brings the PBE+ $U$  results the closest to the GLLB-SC ones. It is interesting to note that in the paper by Sundararaman *et al.* a value of 2.45 eV was found by fitting as the optimal value for the  $U$  parameter applied on the d-orbitals of Ag using PBEsol to bring the d-bands the closest to the experimental data for the band structure. GLLB-SC seems to achieve a similar type of correction in the d-band treatment without any empirical input.

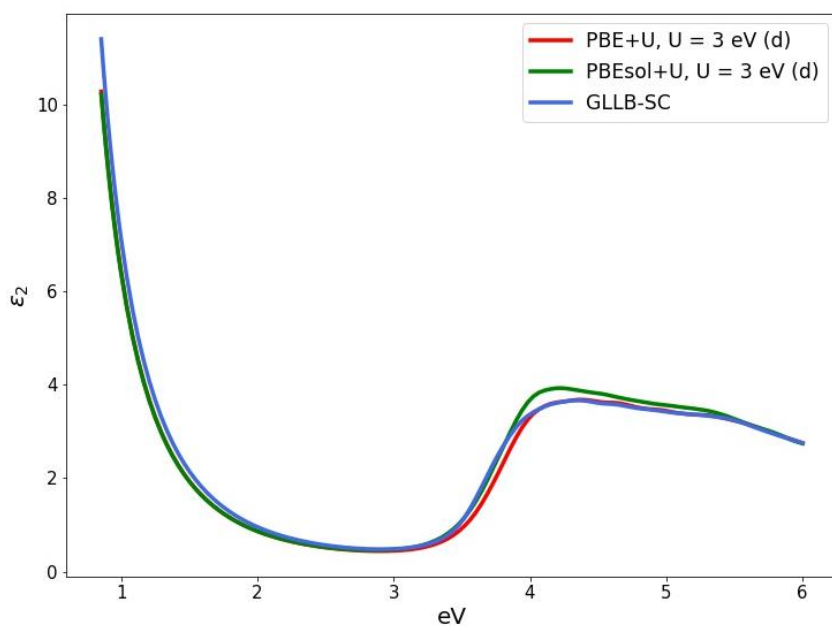


Figure 31. Comparison of PBE+ $U$ , PBEsol+ $U$  and GLLB-SC dielectric function for silver with Hubbard-like  $U$  term of 3 eV applied on d-orbitals.<sup>152</sup>

In fact, the Hartree-Fock exchange added in the hybrid functionals essentially produces the same effect - introduces the derivative discontinuity - thus in some ways acting as a correction of the GGA-like treatment of the d-bands, just like the ones in the GLLB-SC and DFT+ $U$  approaches. With the underlying similarity of using DFT+ $U$  and GLLB-SC in mind, a decision regarding which approach to test as an alternative to pure PBE for alloy plasmonic

properties comes down to their differences. Since it was shown in Figures 30 and 31 that the PBE+U and PBEsol+U calculations can result in extremely similar shape of the dielectric function as the ones obtained using GLLB-SC, these approaches can be, in terms of absolute accuracy, thought of as equal or better than GLLB-SC. In other words, if by fitting the U parameter the shape of the calculated dielectric function can be made to almost perfectly fit the shape obtained using GLLB-SC, then if any discrepancy with the experiment remains, for example a slight red shift, there is probably a U value that brings the overall shape slightly closer to the experimentally measured data. However, for predictive purposes, when no anchoring to experimental results is available, picking the right value of U is rather problematic. While it can be calculated ab initio in some packages for each system that requires substantial computational resources and in part defeats the purpose of using such a correction when more sophisticated ones are also available. Additionally, the formulation of the U parameter differs between different DFT software, thus making the comparison and transferability of the findings an issue. Moreover, the advantage in accuracy that might be obtained using DFT+U can be considered to be small to negligible for alloyed systems that are the focus of this work, since GLLB-SC predicts the interband transition onset with great accuracy for pure constituent elements. The advantage of having an accurate, physically grounded, and automatically adjusting correction implemented in an efficient way within the GLLB-SC functional thus outweighs the advantages of a DFT+U approach. For these reasons, we performed all of the alloy calculations using PBE as a current standard and GLLB-SC as a potentially advantageous alternative.

#### 5.2.4. Alloy dielectric function calculation

Dielectric functions were calculated for Au-Ag, Au-Cu, Au-Pd and Ag-Cu binary alloys. Since, as stated earlier, the imaginary part of the dielectric function is more suitable for analysis, in the Figure 32 the visualization enabling the comparison of dielectric function obtained from calculations using PBE, GLLB-SC and the experimental measurements contains only the  $\epsilon_2$ . Additionally, due to the limitations of the experimental data, the focus is mostly on the visible range, with part of the UV and small part of the IR (mostly NIR) range also present. For unit cells that are anisotropic the presented dielectric function is the average of dielectric functions in all three directions. Additionally, for the cases where more than one configuration was created for the same stoichiometric ratio, the presented dielectric function

---

---

is the average of all three configurations. Comparing each individual  $\epsilon_2$  for a certain alloy composition would be hardly legible and is further complicated by a mismatch in compositions for some of the experimentally used ratios and the ones used in calculations. This being the case, collective trends were captured by showing the envelopes for each method of obtaining the alloy dielectric functions (Figure 32, fourth column). The envelopes are defined by the highest and the lowest  $\epsilon_2$  values in the alloy system at each point in the energy range. Real part of dielectric functions from the calculations using PBE and GLLB-SC is shown in the Appendix, Figure A5, also clearly showing that alloying enables the tunability of the dielectric function.

---



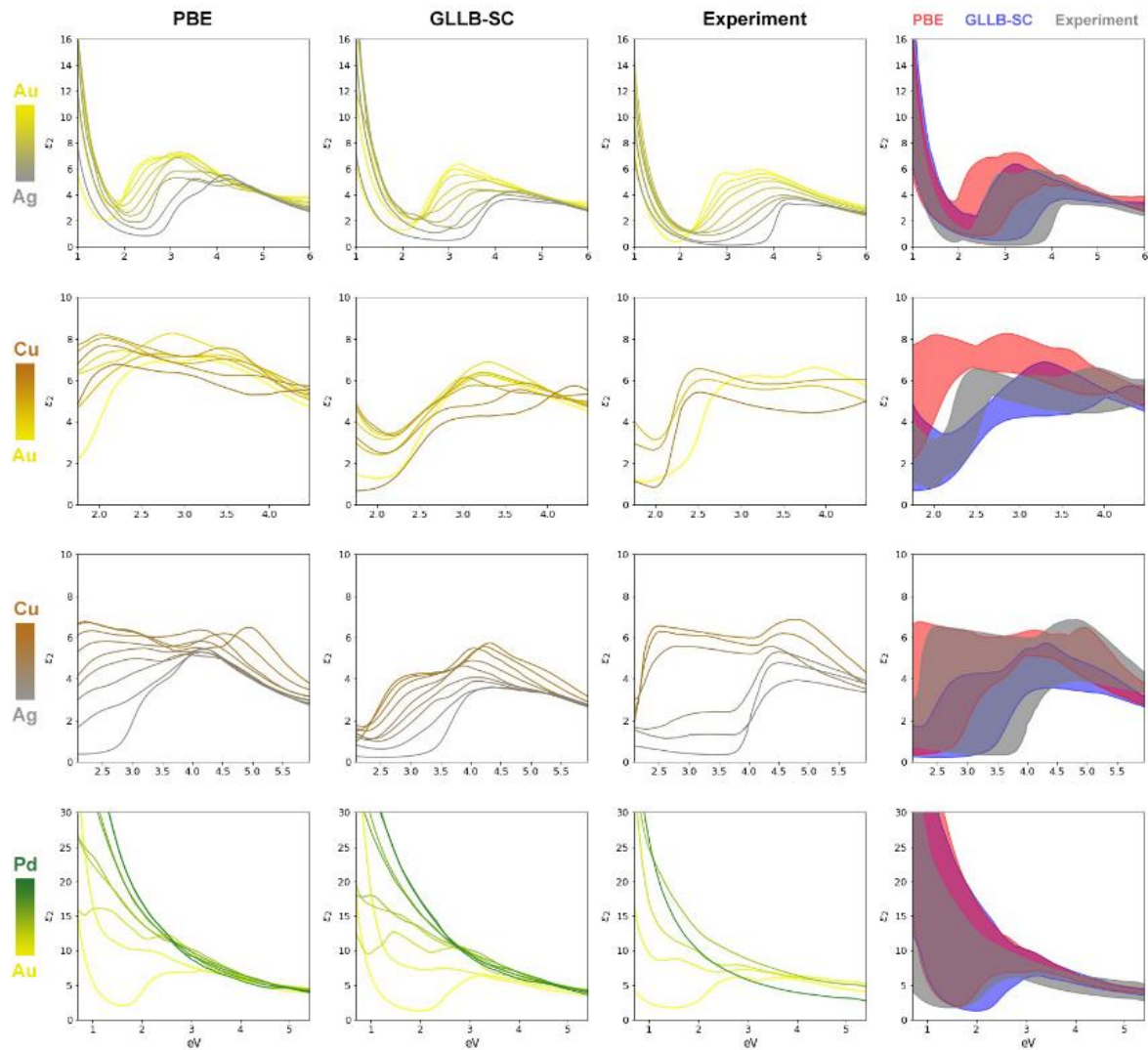


Figure 32. Imaginary part of alloy dielectric functions for Au-Ag (first row), Au-Cu (second row), Ag-Cu (third row) and Au-Pd (fourth row) shaded according to the elemental ratios. First column shows data calculated using PBE, second column shows data obtained using GLLB-SC, third column shows experimentally determined dielectric functions and the fourth column shows their respective envelopes determined by minimum and maximum value of  $\epsilon_2$  at a given photon energy. Blue envelope corresponds to GLLB-SC, red to PBE and gray to experiments. Experimental data is obtained from Peña-Rodríguez *et al.*<sup>160</sup> for Au-Ag, from Köster and Stahl<sup>172</sup> for Au-Cu, from Rivory and Theye<sup>173</sup> for Ag-Cu, and from Myers *et al.*<sup>174</sup> for Pd-Au alloy.<sup>152</sup>

Two different types of behavior with changing of the alloy compositions can be observed. For Au-Ag, Au-Cu and Ag-Cu the change in the dielectric function is smooth and gradual, almost linear, with the composition change. Dominant influence of the interband transitions in the UV/Vis range is also clear. These two observations hold both for the experimentally determined functions as well as for the ones calculated using PBE and GLLB-SC, therefore showing that DFT is able to qualitatively capture the defining features of alloy dielectric functions for these systems. A different behavior is observed for the Au-Pd system. Unlike the smooth variation observed in the other systems, even with intermixing a small amount of Pd in the alloy with Au, an abrupt shift can be observed in the dielectric function, which strongly deviates from the dielectric function of pure Au, especially at lower energies. This change is strongly nonlinear as the composition shifts to more Pd-abundant alloys, slowing down considerably for alloys that are rich in Pd and have little Au. For this system DFT calculations using both functionals also qualitatively captures the defining features of the dependence of alloy dielectric function on the elemental composition.

These two qualitatively different behaviors - smooth and gradual change when alloying good plasmonic metals, and abrupt and nonlinear change when alloying Pd and Au - become more understandable when elements are classified according to their electronic structure. Ag, Au, and Cu, are all closed d-shell elements. Therefore, they possess fully filled d-bands which, consequently, lie below the Fermi energy. By intermixing two filled d-shell elements, the nature of the resulting d-states (or d-bands) remains similar in the sense that they remain fully filled. The d-sp interband transition onset is therefore not drastically affected by the composition change if it is gradual. Conversely, although Pd is considered an exception to the Aufbau principle in its elementary state, with a fully filled d-orbital at the expense of 2 s-orbital electrons, in the bulk crystal the states hybridize and the range of their energies broaden with some of them crossing the Fermi energy (and some of the s-states ending up below it). Therefore, not all of the resulting d-states remain fully filled, so in bulk state Pd can be considered an unfilled d-shell element and will, for simplicity, be referred to as such in the rest of this work. The unfilled d-shell character is evidenced by the d-bands of Pd crossing the Fermi level. When Pd is mixed with the filled d-shell elements the alloy seems to inherit the nature of its d-states, which even in small amounts seem to be located near the Fermi energy, thus strongly affecting the interband transitions and thus also their contribution to the dielectric function. Therefore, such a classification could explain the

---

different behavior between Pd-Au and the rest of the alloyed systems. A more detailed discussion of the electronic structure will be presented along with the results of band structure and DOS calculations later in the text.

Although both functionals qualitatively predict the trend of alloy dielectric function change upon composition change, their quantitative agreement with the experimental data shows important differences. These differences can be best observed by contextualizing the trend by its limiting cases, which are the pure metals. Also, since the dielectric functions of the studied alloys almost exclusively lie between the pure element dielectric functions, the limiting cases can be well visualized as the borders of the envelopes on the Figure 32 with the alloy dielectric functions falling within the envelope. As already known from the benchmarking of functionals for pure elements, GLLB-SC performs very well for these limiting cases, and since it predicts the trend well it also shows good performance for alloy dielectric functions. This is especially evident in the UV and visible region, while the IR region should not be compared in these cases due to the rate parameter being set very low which affects the Drude term and causes large discrepancies. PBE, on the other hand, systematically overestimates the values of the  $\epsilon_2$  and predicts the red-shifted alloy dielectric functions. In the both cases the quality of prediction of specific features of the  $\epsilon_2$ , such as subtle variations in shape vary from system to system. For example PBE correctly captures two peaks in the interband region of Au. However, the shape of Ag dielectric function is much better predicted by GLLB-SC. Nonetheless, such features are of little importance for the resulting plasmonic and optical properties as evidenced in the case of ordered and disordered Cu-Au alloy system in the work of Pradini *et al.*<sup>118</sup> Much more importance lies in the correct prediction of the d-sp interband transition onset. Wrong estimation of the d-sp interband transition threshold shifts the entire dielectric function and thus results in very large differences in the imaginary part of the dielectric function in the range defined by the size of the error.

#### 5.2.5. *Resolving interband and intraband contributions to the dielectric function: emergence of low energy interband transitions*

Motivated by the occurrence of low energy interband contribution to the dielectric function presented for some alloyed systems the literature and the seeming lack of attention given to this effect all of the alloy dielectric functions were also calculated without the intraband contribution (Drude term). Separating the interband from intraband contribution helps to show

---

whether any low-energy losses still remain without the Drude term which would indicate that alloying promotes low-energy transitions even for the elements which do not show them in their pure bulk state. Again, both PBE and GLLB-SC are used for these calculations and the results are presented in Figures 33-36.

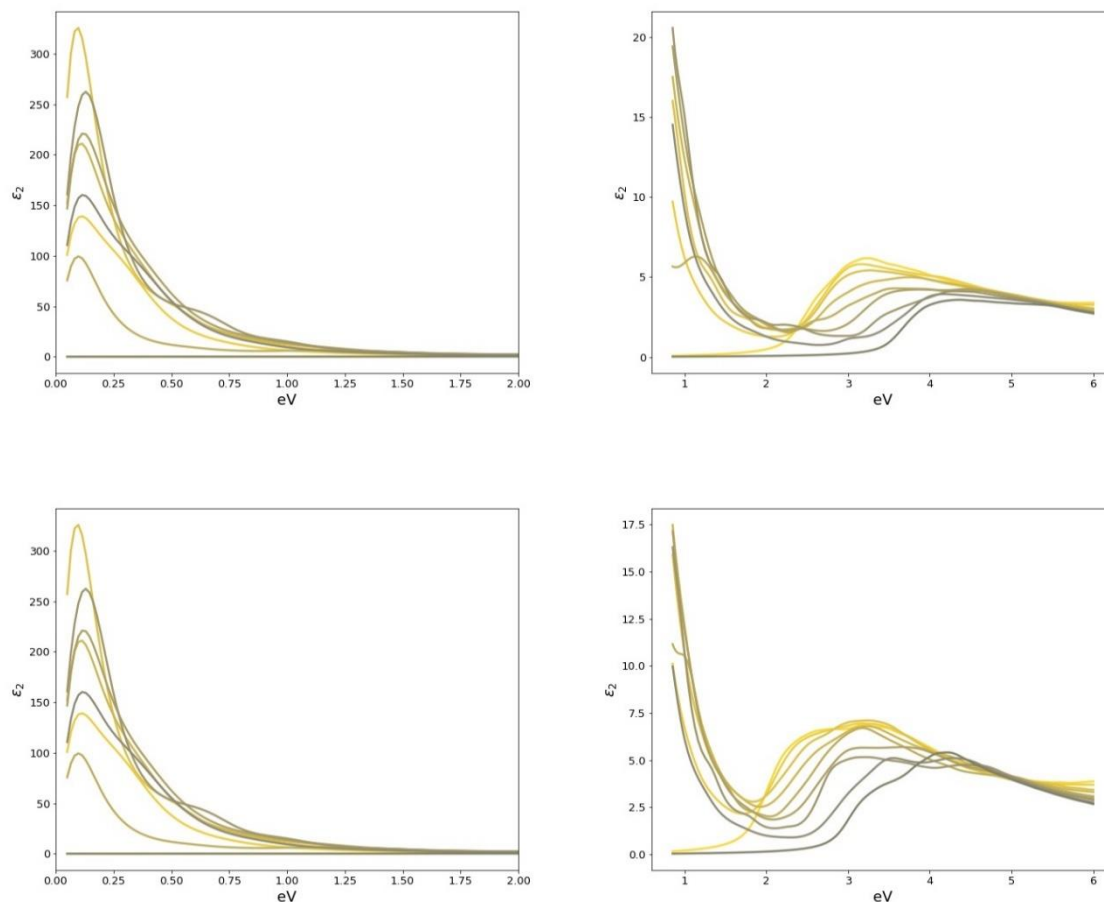


Figure 33. Interband contribution to the imaginary part of dielectric functions for Au-Ag calculated using GLLB-SC (first row) and PBE (second row). The elemental ratios change in the increments of 12.5%. First column shows the behavior in the IR region where values of the dielectric function are higher. The second column enables better inspection of the UV/Vis region where the values of dielectric function are lower. Note that for alloys in all cases there are peaks in the IR region although for pure metals they are not present and the dielectric function instead slowly approaches zero.<sup>152</sup>

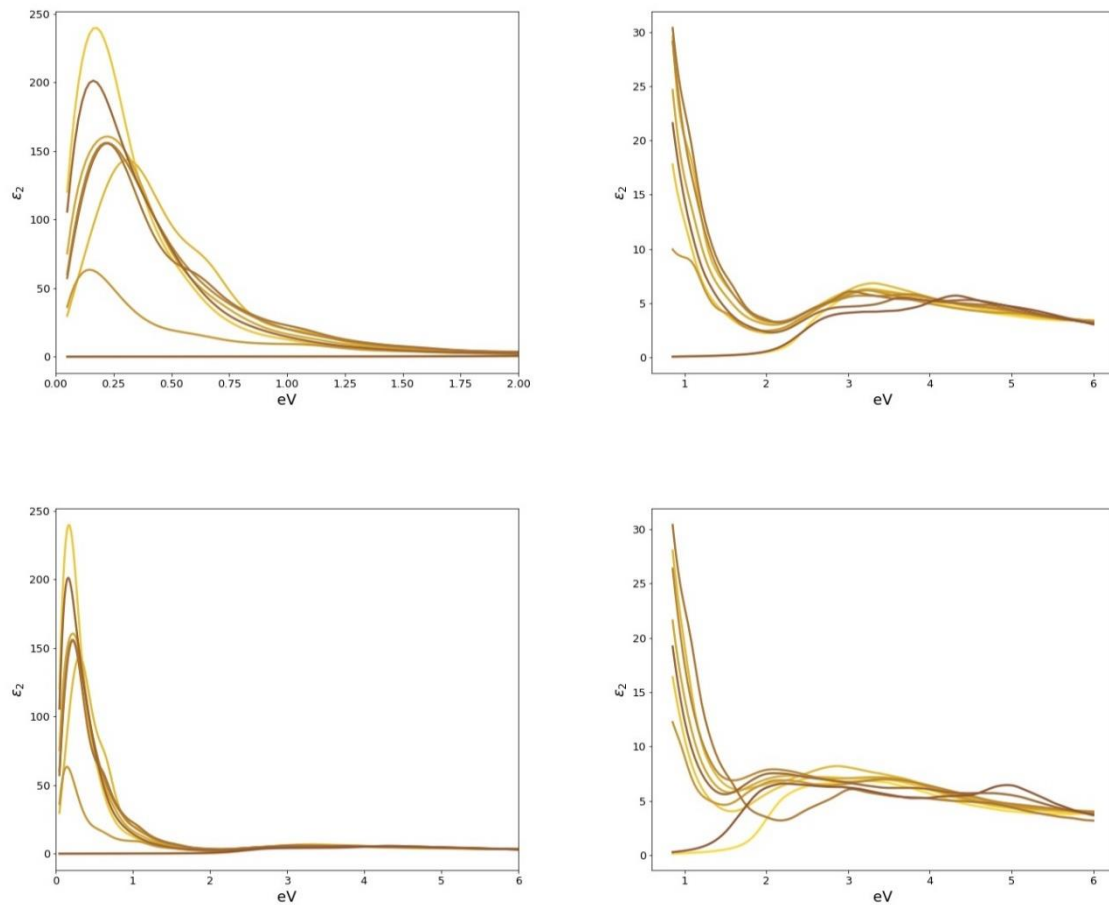


Figure 34. Interband contribution to the imaginary part of dielectric functions for Au-Cu calculated using GLLB-SC (first row) and PBE (second row). The elemental ratios change in the increments of 12.5%. First column shows the behavior in the IR region where values of the dielectric function are higher. The second column enables better inspection of the UV/Vis region where the values of dielectric function are lower. Note that for alloys in all cases there are peaks in the IR region although for pure metals they are not present and the dielectric function instead slowly approaches zero.<sup>152</sup>

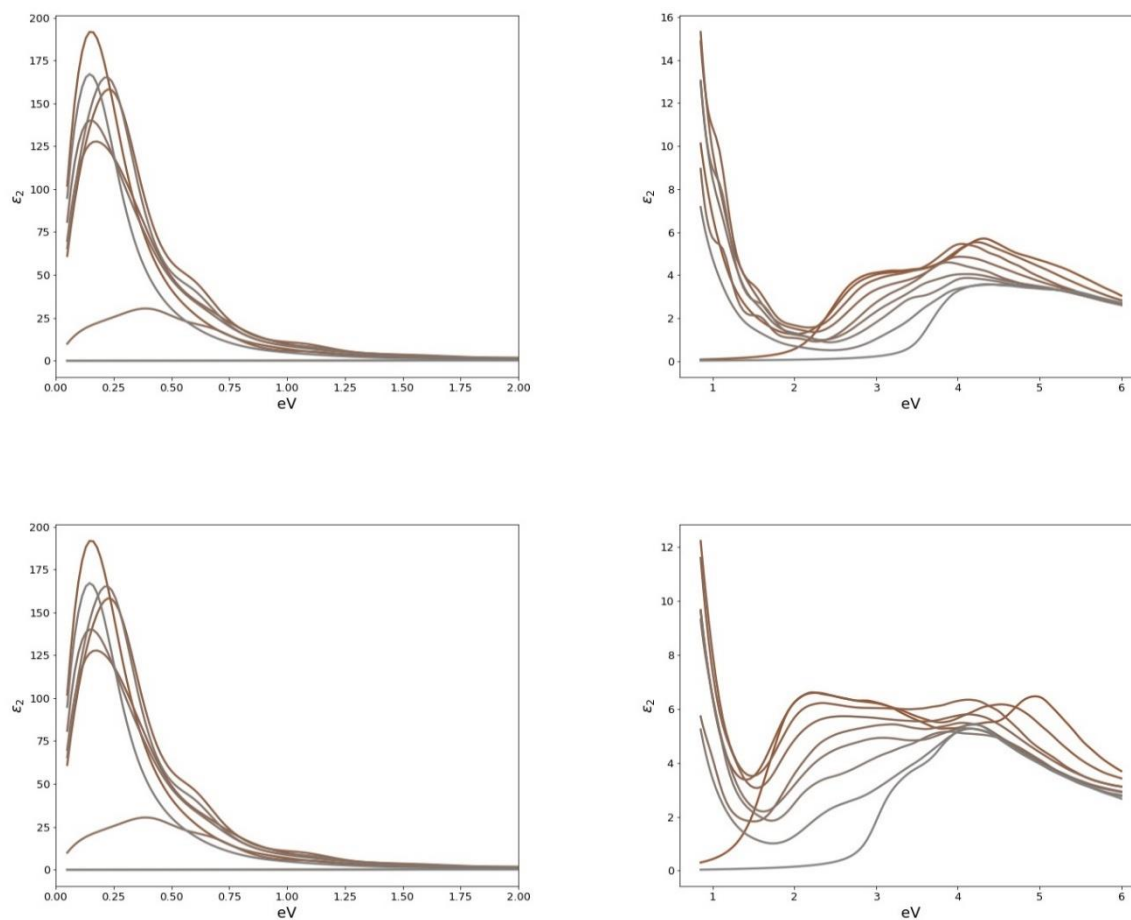


Figure 35. Interband contribution to the imaginary part of dielectric functions for Ag-Cu calculated using GLLB-SC (first row) and PBE (second row). The elemental ratios change in the increments of 12.5%. First column shows the behavior in the IR region where values of the dielectric function are higher. The second column enables better inspection of the UV/Vis region where the values of dielectric function are lower. Note that for alloys in all cases there are peaks in the IR region although for pure metals they are not present and the dielectric function instead slowly approaches zero.<sup>152</sup>

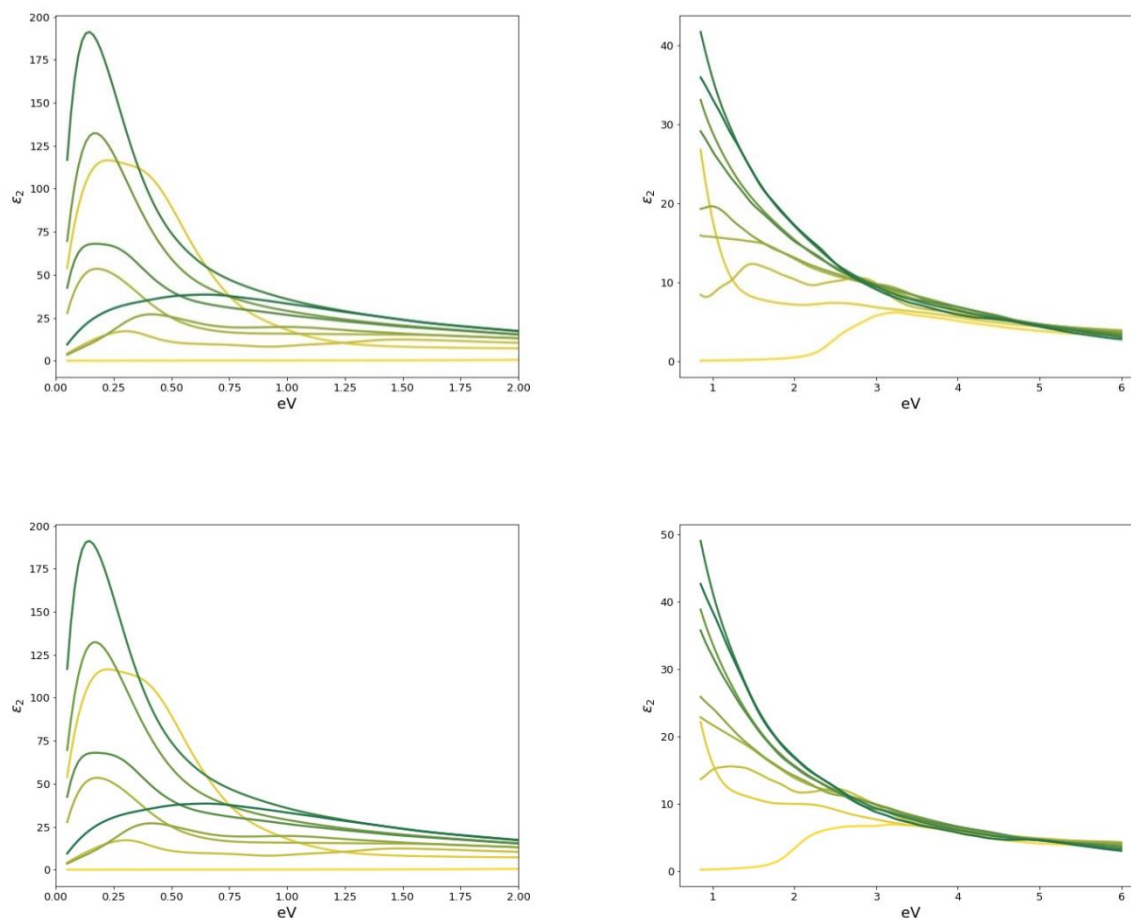


Figure 36. Interband contribution to the imaginary part of dielectric functions for Au-Pd calculated using GLLB-SC (first row) and PBE (second row). The elemental ratios change in the increments of 12.5%. First column shows the behavior in the IR region where values of the dielectric function are higher. The second column enables better inspection of the UV/Vis region where the values of dielectric function are lower. Note that for alloys in all cases there are peaks in the IR region although for pure metals they are not present and the dielectric function instead slowly approaches zero.<sup>152</sup>

By observing the right columns of each figure, strikingly, the shape of alloy dielectric function still strongly resembles the shape expected from including both interband and intraband contributions. On the other hand, this is not the case for the pure metals: as expected, for alloys of closed d-shell elements the imaginary part of the dielectric function approaches zero for energies below the known interband transition onset. Conversely, for alloys of closed d-shell elements, there is still a minimum below what is usually considered to

be an interband transition onset and then, following the energy range from visible into NIR, a supralinear rise in the values of the dielectric function, shape-wise resembling the Drude term. This rise continues to extremely high values when compared to the UV and visible region, as shown on the left columns in the figures 33-36 which focuses more on the IR energy region. Unlike the Drude term, this feature of the dielectric function reaches maximum values at 0.1 eV or higher, resulting in a distinct peak near the edge of the far infrared region. It has to be noted that the very similar behavior of the low-energy interband contribution to the dielectric function is predicted both by PBE and GLLB-SC. Although these features are rather pronounced, Figure 37 shows that such a behavior might be ascribed to the intraband transitions in the NIR due to the similar shape of the dielectric function (a), while further in the IR region the features would be overshadowed by the much higher values of the Drude term (b).

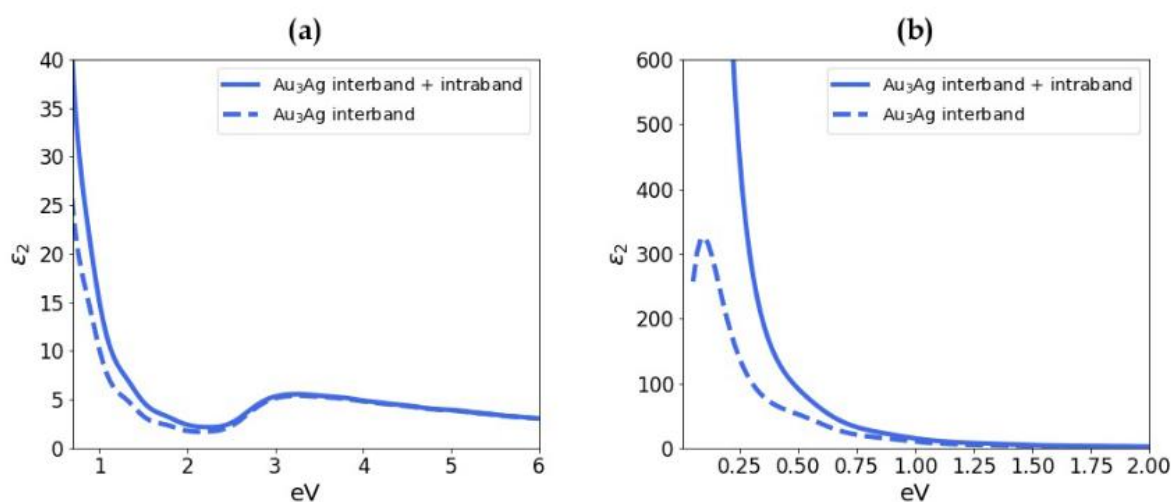


Figure 37. Imaginary part of  $\text{Au}_3\text{Ag}$  dielectric function calculated using GLLB-SC with both interband and intraband contribution included (full line) and with only interband contribution (dashed line). Interband contribution is dominant even below the nominal d-sp interband transition onset (a), but is overpowered by intraband (Drude) contribution in the mid- and far-infrared region despite taking far larger values than in the UV/Vis region (b).<sup>152</sup>

It can also be seen that the interband contribution alone qualitatively reproduces the behavior of the imaginary part of the dielectric function before the nominal (d-sp) interband transition onset for alloys, at the local minimum (Figure 38).



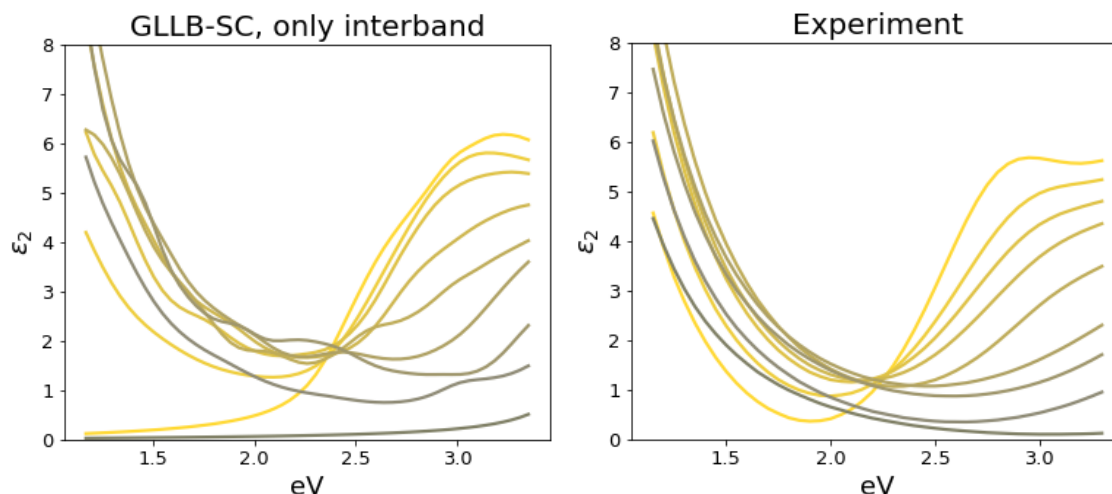


Figure 38. Comparison of the behavior of the dielectric functions for Au-Ag system below the nominal interband threshold. On the left the purely interband contribution to the dielectric function calculated using GLLB-SC is shown. On the right, the experimentally determined dielectric functions are shown.

In the trend resembling an inverted parabola, the values of the minima in the experimental measurements rise from one pure metal to alloys nearing 50% of each metal, and again fall as the composition shifts to the other pure metal. Traditionally ascribed to larger scattering probability due to rising disorder upon element mixing in alloys, this trend may instead be connected to mechanisms not involving momentum transfer and to the changes in the electronic structure by alloying. These results, therefore, indicate an alternative or complementary hypothesis to the dielectric function behavior usually ascribed to the changing (classical) scattering rate.

The aforementioned low energy interband contribution is not present for any of the constituent elements in their pure state but appears for each one of their alloys. Therefore, it can be considered an *emergent property of alloying*.

Au-Pd alloys show a similar behavior, with the difference being that, unlike closed d-shell elements, pure Pd also exhibits low energy interband transitions. Therefore it is not clear whether, or to which extent, the observed low energy contribution of the interband transitions is an emergent property of alloying, and to which extent it is an inherited property from Pd, since in the pure bulk state it has high lying d-bands crossing the Fermi level and allowing such interband transitions.

### 5.2.6. Configuration influence on the dielectric function of alloys

The effects of configuration were explored using three different configurations of 8-atom cells with  $A_5B_3$  stoichiometry, in one of which the atoms of different elements are more segregated, while in the other two they are more evenly spaced, as visible on the Figure 39 (a), for the case of  $Au_5Ag_3$  system.

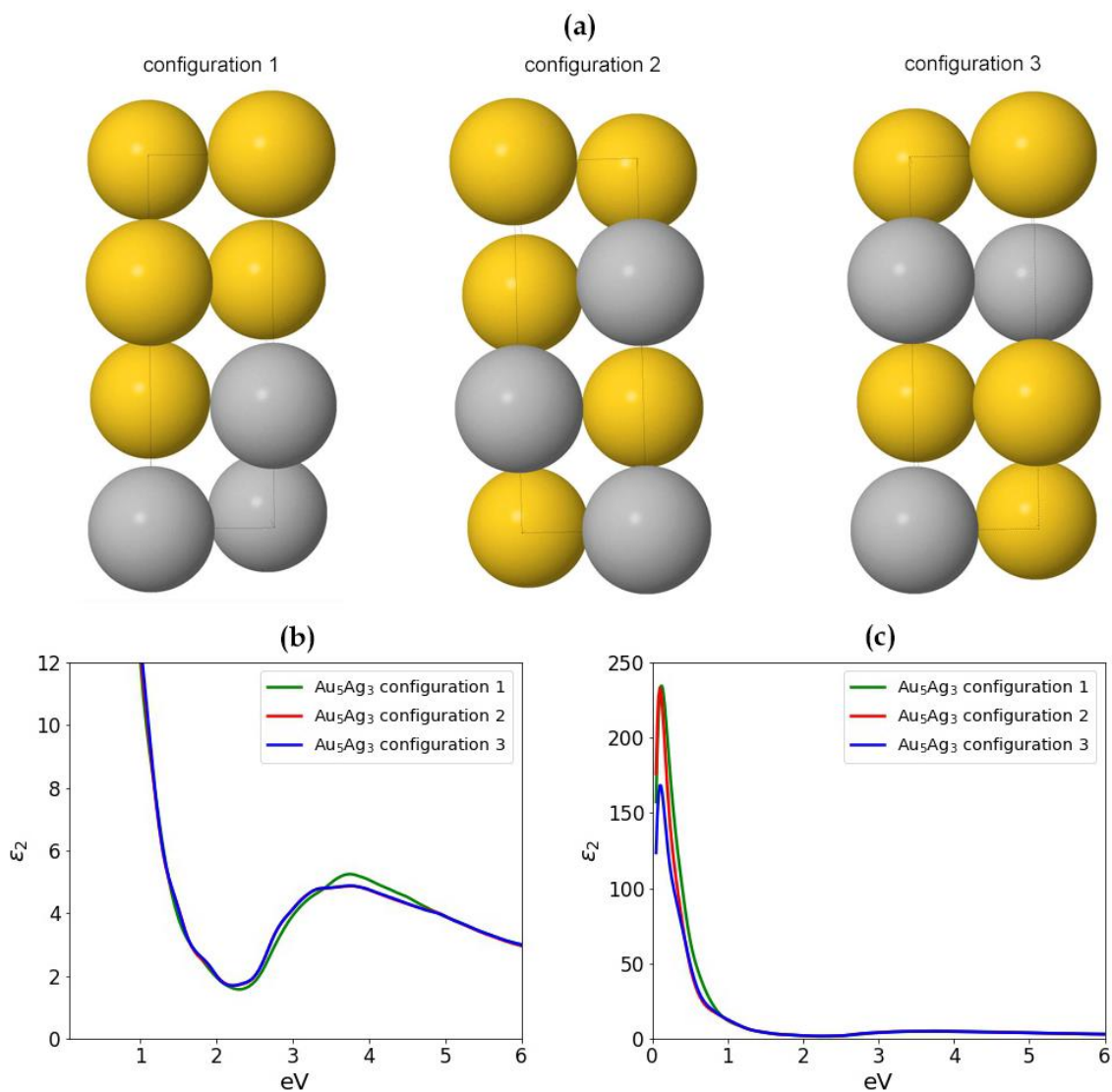


Figure 39. Three different configurations of  $Au_5Ag_3$  unit cell (a) and the corresponding dielectric functions in UV/Vis range (b) and from IR to UV (c). Interband contributions to the imaginary part of dielectric function of these unit cells calculated using GLLB-SC functional. We note that configurations 2 and 3 show almost perfect overlap in the UV and visible range, while configuration 2 differs slightly. In the lower energy range differences between all three configurations are slightly more pronounced, especially near the peak values.<sup>152</sup>

It is evident that the effect of configuration on the imaginary part of the dielectric function is not very pronounced in the UV and visible region, with  $\epsilon_2$  of two dielectric functions almost fully overlapping. The differences in the IR region are a bit more pronounced, especially at the peak values, although the importance of this difference can be put to question since at these energies the intraband term strictly dominates. The results for all of systems with the same stoichiometry but different configurations are presented in the Figure 40, largely reflecting the same behavior. It is notable that there seems to be slightly more variation with configuration change for the dielectric functions calculated using PBE than for those using GLLB-SC. The reason could be in the underestimated localization of (predominantly) d-states when calculating using PBE, since more delocalized wave functions should be more influenced by the changes in the environment.

These results show that the computational method could be even more simplified, by using only one 8-atom cell of the appropriate ratio, probably with a configuration with a less segregated and more diverse local environment of atoms, since this likely better reflects the local environment in the solid solution.

---

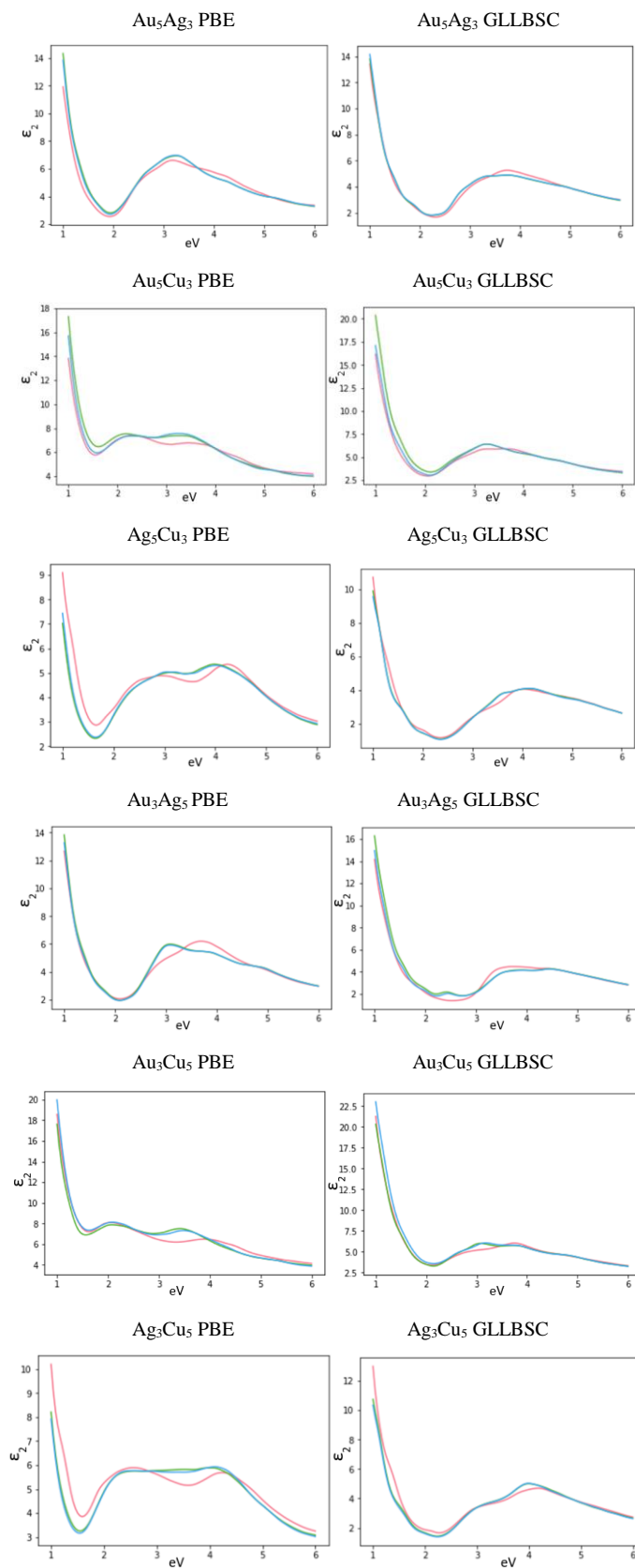


Figure 40. Comparison of the imaginary parts of the dielectric function for each of the three different configurations used to represent an alloy of  $A_3B_5$  or  $A_5B_3$  stoichiometry.

To gain insight into how configuration changes of the unit cell that best represent the influence of disorder, special quasirandom structures (SQS) have to be used. In a very recent work by Rahm *et al.*<sup>175</sup> SQS of 20-25 atoms were used to calculate dielectric functions of certain alloys using a very similar method to the one in this work. Although they used a different optimization procedure, and some of the parameters used to obtain dielectric function also differ from the ones used in this work, GLLB-SC functional was used in both cases, leading to rather similar results for pure metals, as visible in the Figure 41.

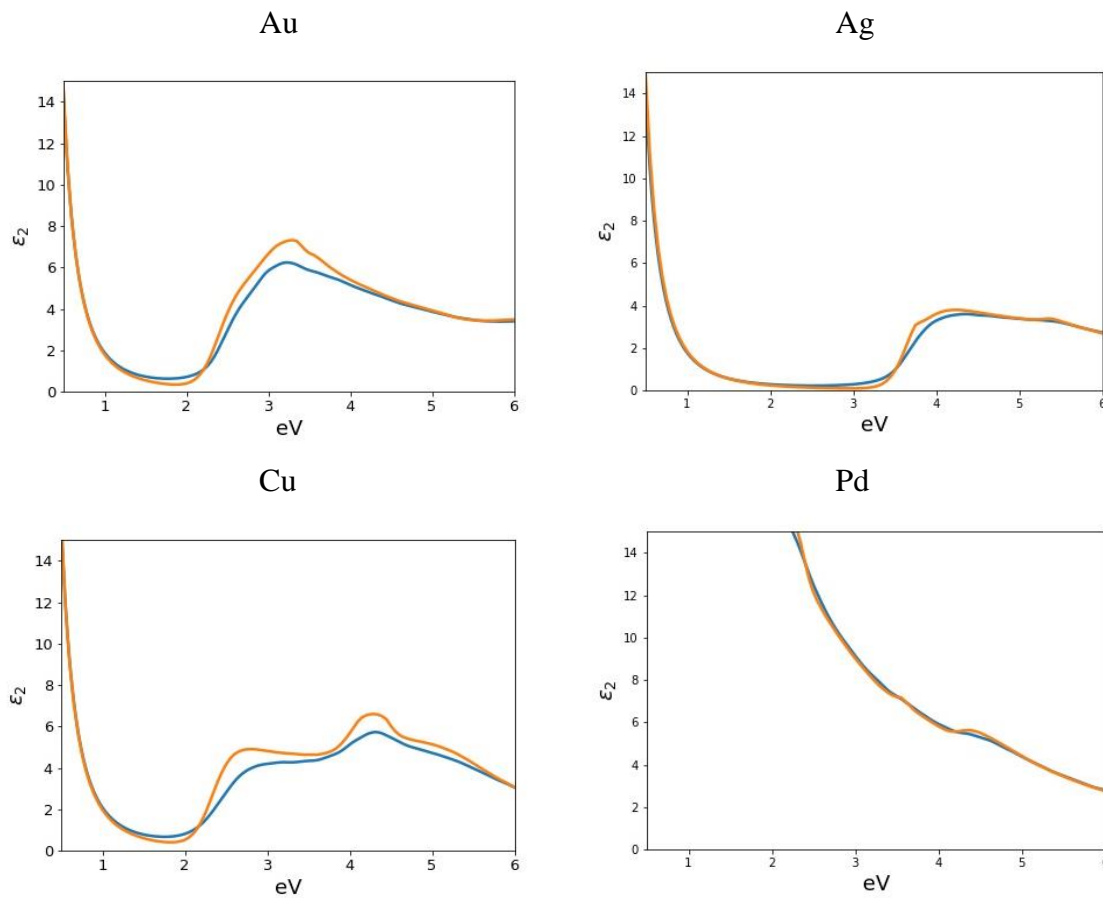


Figure 41. Comparison between dielectric functions obtained by Rahm *et al.*<sup>175</sup> (orange) and in our work (blue) for pure metals (Ag, Au, Cu, Pd). GLLB-SC was used as an exchange-correlation functional both in this work and by Rahm *et al.*<sup>175</sup>

The comparison of the results obtained for pure elements enables the assessment of the differences in calculation parameters, and to assess the influence of using a minimal unit cell instead of SQS. It is visible that, for the most part, the dielectric functions obtained by both works coincide very well, giving almost the same interband transition threshold although some minor shape differences are present. Overall, the results of these two works are more

similar than the results obtained using GLLB-SC and some different functional in our work, with all other parameters being the same.

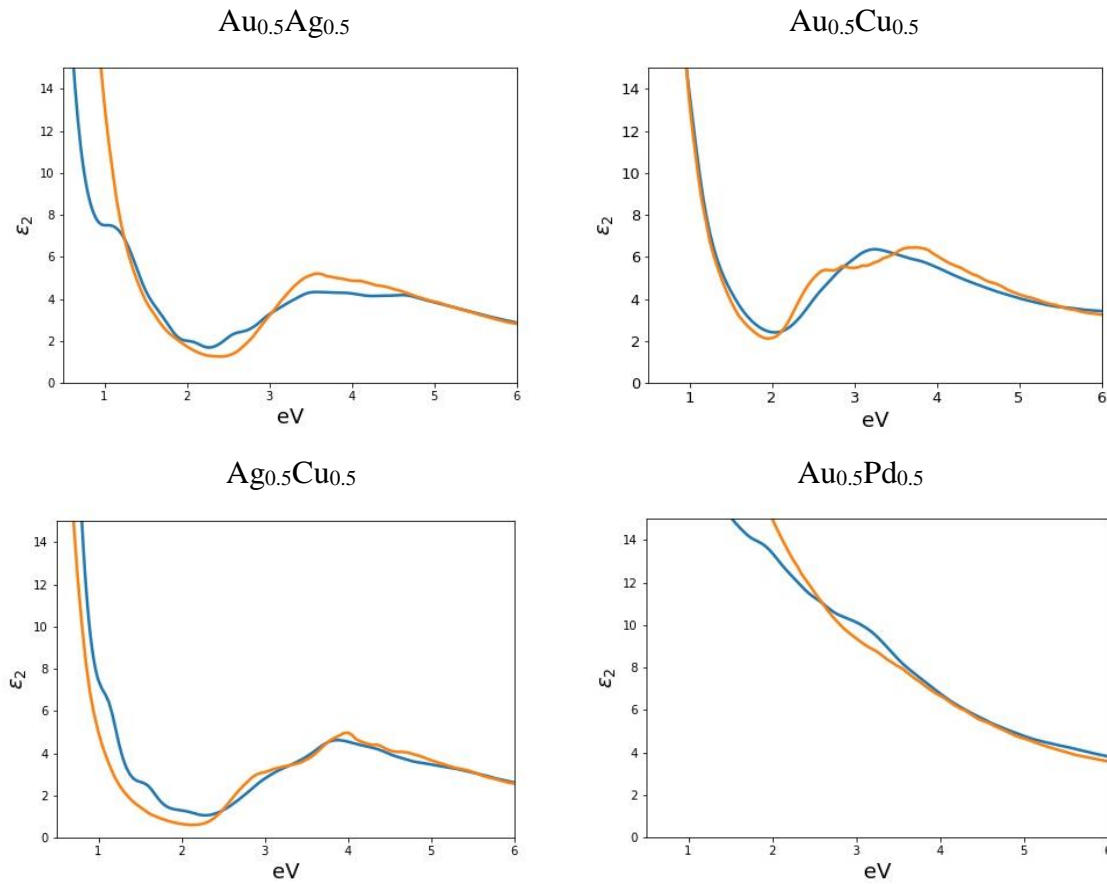


Figure 42. Comparison between dielectric functions obtained by Rahm *et al.*<sup>175</sup> (orange) using special quasirandom structures with 20–24 atoms and in our work (blue) using cells with 4 atoms. GLLB-SC was used as an exchange-correlation functional both in this work and by Rahm *et al.*<sup>175</sup>

In the Figure 42 dielectric functions calculated based on binary alloyed systems with equal number of atoms of two elements are shown. In our work simple 4 atom cells were used for calculations and the results are compared to SQS-based calculations of up to 24 atoms from the work of Rahm *et al.* It is visible that the resultant dielectric functions show a strong similarity. It is hard to pinpoint the exact causes for the differences that are observed due to the multifactorial nature of the problem: they could arise from the different optimization methods affecting the average atom spacing, different calculation parameters, and different choices of alloy representation - small and simple cell versus large SQS. However, by gauging the total influence of different optimization methods and calculation parameters by

comparing the dielectric functions in the Figure 41 additional discrepancy in the alloy dielectric functions (Figure 42) can be very roughly ascribed to the influence of using different unit cells. Based on that premise it seems that using large SQS have a rather minor impact when compared to using much smaller and simpler unit cells. The discrepancy in the alloy dielectric function obtained with different unit cell representation is comparable to the discrepancy shown when 1 atom unit cells of pure elements are used. A difference that can probably be assigned to the use of SQS is a slightly smoother dielectric function behavior in the lower energy region. Additionally, the double-peaked shape of the Au-Cu alloy is properly captured by the SQS while it is not by the simple unit cell which might be due to a better representation of a random alloy. However, for the calculation of optical and plasmonic properties these differences are mostly unimportant, except possibly at specific wavelengths in the infrared range. Using up to 24-atom with low symmetry cells would increase the computational cost of most of the calculations by orders of magnitude. Keeping in mind small impact that such a choice would have, we believe that the choice of a small and simple unit cell is justified and preferable when a high number of systems has to be taken into account and included in the calculations. Therefore, SQS were not used in this part of our work.

#### 5.2.7. *Electrodynamics simulations of alloy plasmonic properties*

To finalize the comparison of the predictive ability of PBE and GLLB-SC for alloy plasmonic properties, electrodynamic simulations were performed, focusing on the Au-Ag alloy system. Dielectric functions that were obtained by PBE, GLLB-SC, and from experimental measurements are used as input parameters for nanostructure material and the details of the desired system (size, shape, etc.) are modeled. One of the principal properties of plasmonic nanoparticles is their polarizability. In this case we use quasistatic approximation, which is most applicable for small nanoparticles. Since the size of such nanoparticles is much smaller than the wavelength of light, the particle can be treated like a point-dipole. In such cases only dipolar plasmon modes are excited, so the obtained results pertain to dipolar polarizability (Figure 43). The results show that Ag presents a sharp and intense peak and that a gradual quenching and broadening of the peak, as well as the red shift of the plasmon resonance as composition changes towards pure Au. In terms of comparing results based on experimental and computational data, the nanoparticle polarizability obtained using experimental data is predicted to be significantly larger than the polarizability obtained using calculated dielectric

---

functions because of overestimated optical losses in calculated dielectric functions, in large part due to improper estimation of the d-band position. However, while both functionals provide data that enables the reproduction of the general trend of polarizability change with composition change, the results obtained using GLLB-SC show a much better agreement with the experimental results than the PBE-based ones. This is true both for the peak position, as PBE gives significantly red-shifted peak positions (approximately 0.5 eV) while GLLB-SC shows a slight blue-shift (0.1 eV), and for peak height which, although underestimated, is predicted much more accurately using GLLB-SC.

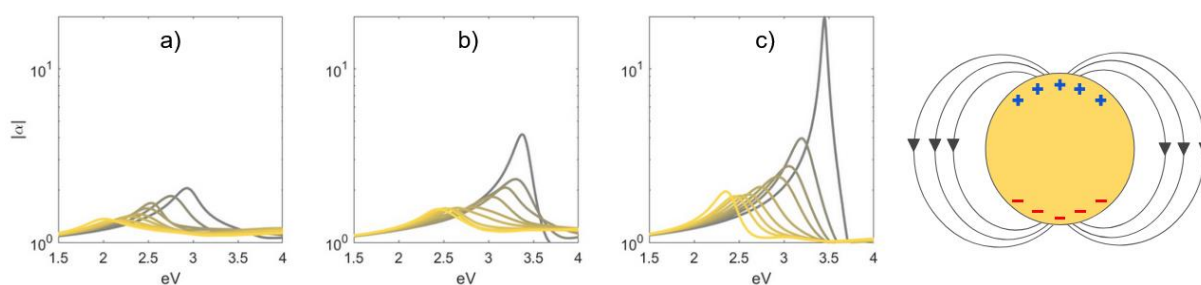


Figure 43. Absolute value of particle polarizability of small spherical Au/Ag alloy particles (schematically depicted on the right) in vacuum, i.e. in a matrix with dielectric function  $\epsilon_{\text{host}} = 1$ . The elemental ratios change in the increments of 12.5%. a) shows the results based on PBE, b) the results based on GLLB-SC and c) shows the results based on experimental data.<sup>152</sup>

Another common way to tune the plasmonic properties of bimetallic nanoparticles is by creating a core-shell bimetallic system and changing the size of the core and thickness of the shell. To compare these two ways we also simulated core-shell particles consisting of pure Au and Ag with equivalent compositions as for the alloyed nanoparticles. As can be seen on Figure 44 GLLB-SC again shows superior performance to PBE in predicting the extinction cross section of nanoparticles, with PBE-based results almost completely missing the characteristic plasmon peak for Au and Au-rich nanoparticles. Comparing the tuning capabilities of core-shell and alloyed nanoparticles, it is evident that alloying enables somewhat smoother (more gradual) tuning, especially for the compositions with similar amounts of both elements, while the results for core-shell nanoparticles show that they skew more strongly towards the characteristics of the more abundant constituent element, with a rapid shift at near-equal amounts of both elements.



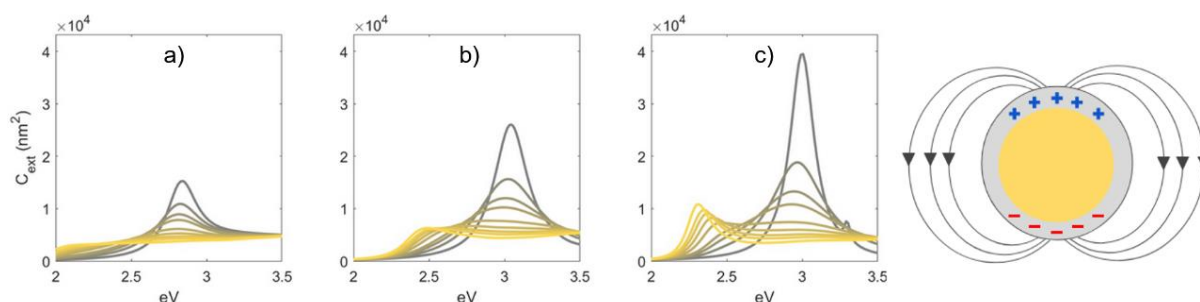


Figure 44. Extinction cross section of a Au@Ag core-shell particle (schematically depicted on the right) in water environment with shell radius 25 nm and core to total particle volume ratio 0 (pure Au, dark yellow), 0.125, 0.25, 0.375, 0.5, 0.625, 0.75, 0.875 and 1 (pure Ag, grey) as a function of photon energy computed using dielectric functions obtained with a) PBE, b) GLLB-SC and c) experimentally obtained dielectric functions.<sup>152</sup>

Since the plasmon resonance of the spherical Au-Ag nanoparticles is located in the visible and UV range, their plasmonic properties mostly depend on the shape of the dielectric function in that range. In Au and Ag nanorods the change of the aspect ratio causes a red shift of the plasmon resonance, moving it to NIR range. Therefore, the extinction cross section due to longitudinal plasmon resonance reveals the ability of DFT calculations to predict the behavior of the dielectric function in that range. It has to be noted that the quality of the results depends on one empirically determined factor, the scattering rate. In this case scattering rate was set to the experimental values for pure metals and linearly interpolated for alloys. Results show a mild variation of plasmon resonance with the composition change. The agreement of computational and experimental results in terms of peak height and width is better than in the UV and visible range. This is possible since the excitations starting from the d-bands (problematic for DFT) do not contribute to the dielectric function in the IR range. GLLB-SC is again slightly better than PBE in enabling proper prediction of plasmonic properties of Au-Ag nanoalloys.

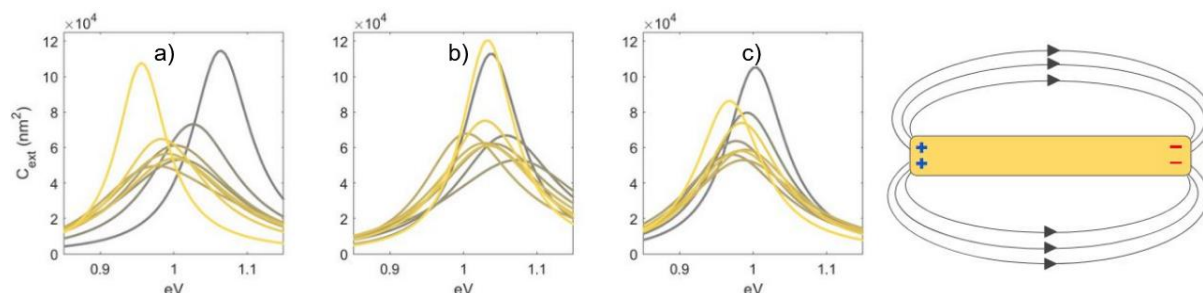


Figure 45. Extinction cross section of an Au/Ag alloy nanorod of 160 nm length and 20 nm diameter (schematically depicted on the right) in water excited by light polarized along the nanorod long axis as a function of photon energy and composition computed using dielectric functions obtained with a) PBE, b) GLLB-SC and c) experimentally obtained dielectric functions. Elemental ratios change in increments of 12.5%.<sup>152</sup>

As one of the most prominent properties of plasmonic nanoparticles, the field enhancement is also explored. The system of interest is a nanosphere dimer, due to exceptional field enhancement between closely spaced nanoparticles, resulting in so-called “hot spots”. Upon interaction with light polarized along the axis passing through the center of the nanoparticles the coupled plasmon modes are excited. As in the previous examples, it can be seen that alloying provides a way to smoothly tune the field enhancement between the peak positions of pure metals. Ag shows the best field enhancement, with the field between the nanoparticles enhanced four orders of magnitude with respect to the incident field. Both functionals predict the peak position well: PBE with a systematic shift of approximately 0.2 eV and GLLB-SC with a blue shift of approximately 0.1 eV. However, PBE severely underestimates the magnitude of the field enhancement. GLLB-SC once again shows superior performance even predicting the second (quadrupolar) peak for pure Ag, although too shallow.

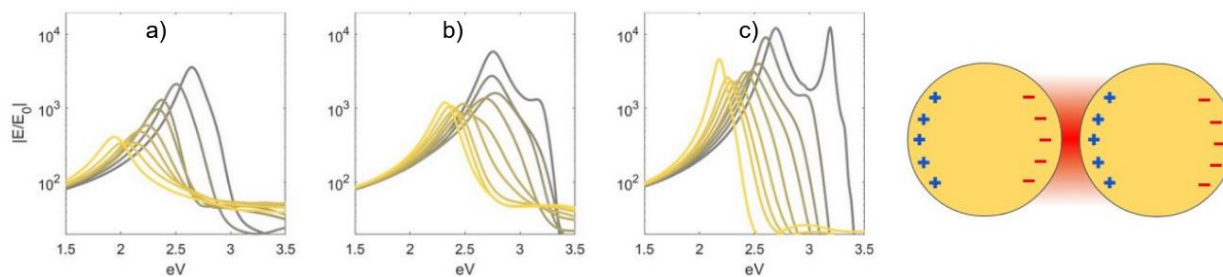


Figure 46. Near-field intensity enhancement at the gap between two Au/Ag alloy particles with radius 20 nm separated by 5 nm (schematically depicted on the right) excited by polarization parallel to the dimer axis placed in water ( $\epsilon_{\text{host}} = 1.77$ ) obtained with a) PBE, b) GLLB-SC and c) experimentally obtained dielectric functions. Elemental ratios change in increments of 12.5%.<sup>152</sup>

Next, several cases of thin films and metal-dielectric interface characteristic in plasmonic research are studied. Dispersion relation is calculated to gain insight into surface plasmon polariton characteristics for alloyed metals at the interface with glass. Real part of the wave propagation constant (as defined in the section 2.3.3) is shown in the Figure 47 and the imaginary part of the wave propagation constant shown in the Figure 48, with units of energy used instead of frequency, for comparison purposes with other plots. Results based on experimental data resemble an ideal lossless system particularly for Ag and Ag-rich alloys. For such alloys bound and propagating modes can be clearly distinguished, represented by lower and upper branches separated by a region with a large imaginary part of the propagating constant, which results in quenching of the propagation length for that mode. Au-rich alloys show less ideal behavior due to larger losses. Results based on DFT calculations show lower variation and are in general much smoother. The distinction between propagating and bound modes is much more subtle and the forbidden propagation region less prominent to barely evident. There is a considerable difference between the two functionals though: GLLB-SC qualitatively captures all of the features of the dispersion relations that are evident from the experiment-based results, while PBE barely captures even the most prominent features and seems to almost fully fail to capture the less evident ones, most notably for Au and Au-rich alloys.

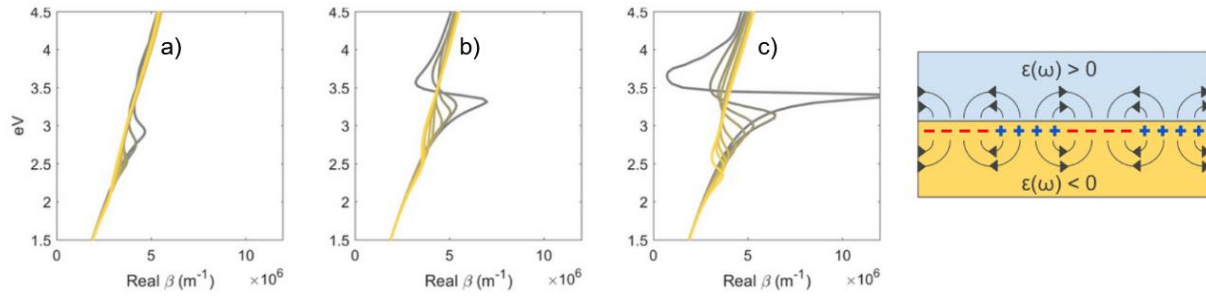


Figure 47. Real part of the dispersion relation for an Au/Ag alloy metal/glass system (schematically depicted on the right). a) shows the results based on PBE, b) the results based on GLLB-SC and c) shows the results based on experimental data. Elemental ratios change in increments of 12.5%.<sup>152</sup>

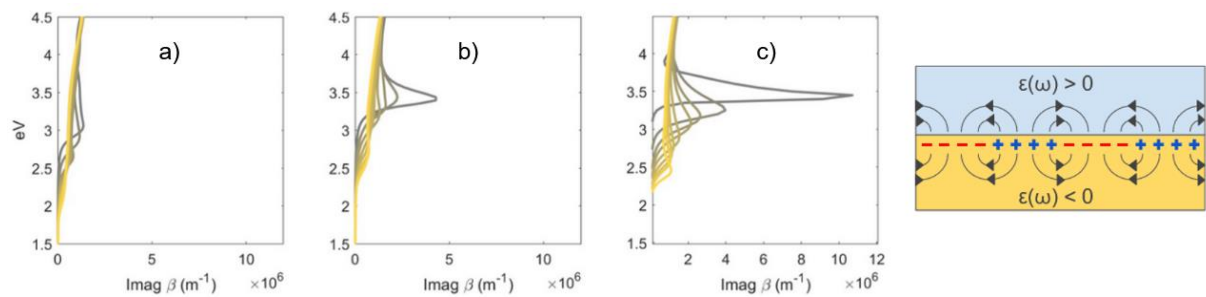


Figure 48. Imaginary part of the dispersion relation for an Au/Ag alloy metal/glass system (schematically depicted on the right). a) shows the results based on PBE, a) the results based on GLLB-SC and c) shows the results based on experimental data. Elemental ratios change in increments of 12.5%.<sup>152</sup>

Reflectance of the air-alloy system in the case of normal incidence of light is studied although plasmons are not excited in this case. Nonetheless it is important since it defines the color of metals and predicts the performance of inferential systems with metal layers. For different methods the differences in reflectance are not particularly prominent. High reflectance is expectedly located in the low energy region where Drude term dominates due to free electron excitations. Afterwards the reflectance drops almost in a stepwise fashion to values below 0.5, with the transition between the behavior in the low and high energy region defined by effective plasma frequency. Except for a very sharp dip to near zero reflectance for Ag, the shape features of the reflectance curves are relatively well predicted by the computations. However, the stepwise drop in reflectance is shifted up to 0.5 eV for Ag, showing the

importance of properly predicting the interband transition onset, a crucial parameter that defines the reflectance spectrum.

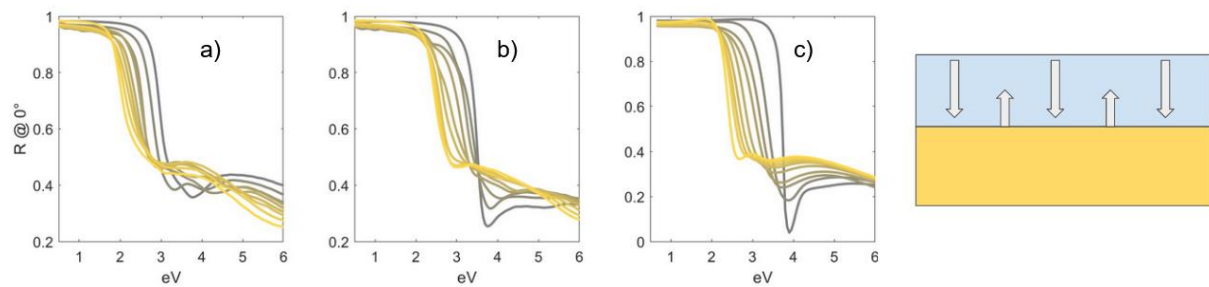


Figure 49. Reflectance of an air/metal (Au/Ag alloy) interface at normal incidence (schematically depicted on the right) as a function of the photon energy and alloy composition (in increments of 12.5%) using dielectric functions calculated employing a) PBE, b) GLLB-SC and c) experimental dielectric functions.<sup>152</sup>

Reflectance is also studied in the Kretschmann configuration, which is designed for exciting surface plasmon polaritons and used in sensing. The system consists of a thin metal film (40 nm in the simulations), that is in contact with a glass prism from one side and air on the other side. Monochromatic red light is directed at varying angles of incidence through the prism at the thin metal film and reflected off it. For all compositions there is a dip in the angular-dependent reflectance. When angle of incidence is larger than the critical angle an evanescent wave is created. Under the condition that there is momentum matching between light and the plasmon, the light is not reflected from the metal layer; instead the evanescent wave is able to excite the plasmon (using the incoming light energy) which leads to the drop in reflectance at the angle of incidence that ensures the momentum matching. Therefore the dip in Figure 50. corresponds to the excitation of a surface plasmon. For experimental data this dip becomes shallower, broader and shifts slightly to the larger angles of incidence as the composition changes from Ag to Au in the experiment-based results. A very similar trend is seen in the GLLB-SC-based results, although the peak does not become shallower with more Au present in the composition. PBE-based results show a much different behavior, even qualitatively. Only the results for Ag and Ag-rich alloys resemble the experiment-based results; for Au and Au-rich alloys the reflectance dip is present at larger angles of incidence and is extremely broadened, without becoming shallower. Considering that the width of the reflectance dip defines the figure of merit for the sensing purposes, this discrepancy is crucial and leads to a

large underestimation of the performance of a system in Kretschmann configuration for Au and Au-abundant alloys.

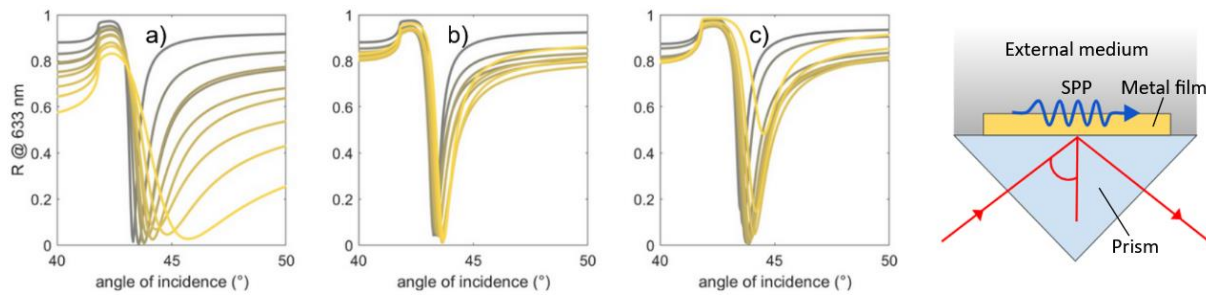


Figure 50. Reflectance of a glass/metal/air system (schematically depicted on the right), where the metal is an Au/Ag alloy with composition changing in 12.5% increments at 633 nm as a function of the incidence angle. a) shows the results based on PBE, b) the results based on GLLB-SC and c) shows the results based on experimental data.<sup>152</sup>

### 5.3. Elucidating a structure-property relationship

Insofar the results have shown that a DFT-based approach enables the prediction of material properties as well as optical and plasmonic properties of alloys requiring very little to no empirical parameters. In achieving that some unexpected effects, such as interband transitions below the d-sp threshold, have also been uncovered. Another beneficial property of DFT is that it can also provide fundamental physical insights into the electronic structure changes that happen upon alloying, thus enabling a multi-layered structure-property relationship to be formed. In doing so, the alloy structure, the electronic structure and the optical properties can be connected. Indications regarding the electronic structure changes upon alloying have been gained recently by two methods: calculating the alloy band structure as in the work by Gong *et al.*<sup>136</sup> and by calculating the DOS as in the work of Rahm *et al.*<sup>175</sup> Since each method carries its unique value in this work we used both of them and showed that they are complementary, providing added value when used in tandem.

#### 5.3.1. Band structure calculations

Band structures were calculated for all of the pure and alloyed systems using both GLLB-SC and PBE. Due to a large amount of figures, for better legibility and conciseness the figures containing all the band structures are placed in the appendix, and the reader is referred to them when needed. The figures shown in this chapter are only the partial results chosen to supplement the text.

In the Figure 51 the band structures of Au-Ag alloy systems are shown between  $\Gamma$  and  $X$  special symmetry points. Only this part of the band structure is shown in this figure since optimizing the unit cell leads to unit cell symmetry changes and thus different high-symmetry paths. Only the  $\Gamma$ - $X$  band path is shared between all unit cells so it is used for comparison. It should be noted that consequently the band structures in the Figure 51 do not contain full information regarding the electronic structure, but are sufficient to observe some of the trends and important features. Expanded band structures are shown in the appendix.

The d-bands can be identified as a closely spaced and relatively flat cluster of bands below the Fermi level. It is visible that, moving from pure Au to pure Ag, the d-bands cluster more together and as a collective become narrower. Furthermore, moving from pure Au to pure Ag the upper edge of the d-bands, important as it is involved in the onset of d-sp

---



interband transitions, moves downwards, deeper below the Fermi level. This is in line with the known results, both experimental and theoretical, and explains the shift in the part of the dielectric function that is connected with the interband transitions onset (or threshold). However, changes in the d-bands are not sufficient to explain the appearance of the low-energy part coming from the interband contribution to the dielectric function. Two specific features in the band structures of alloys have been identified as the reasons for emergent interband transitions at low energies: band folding and band splitting.

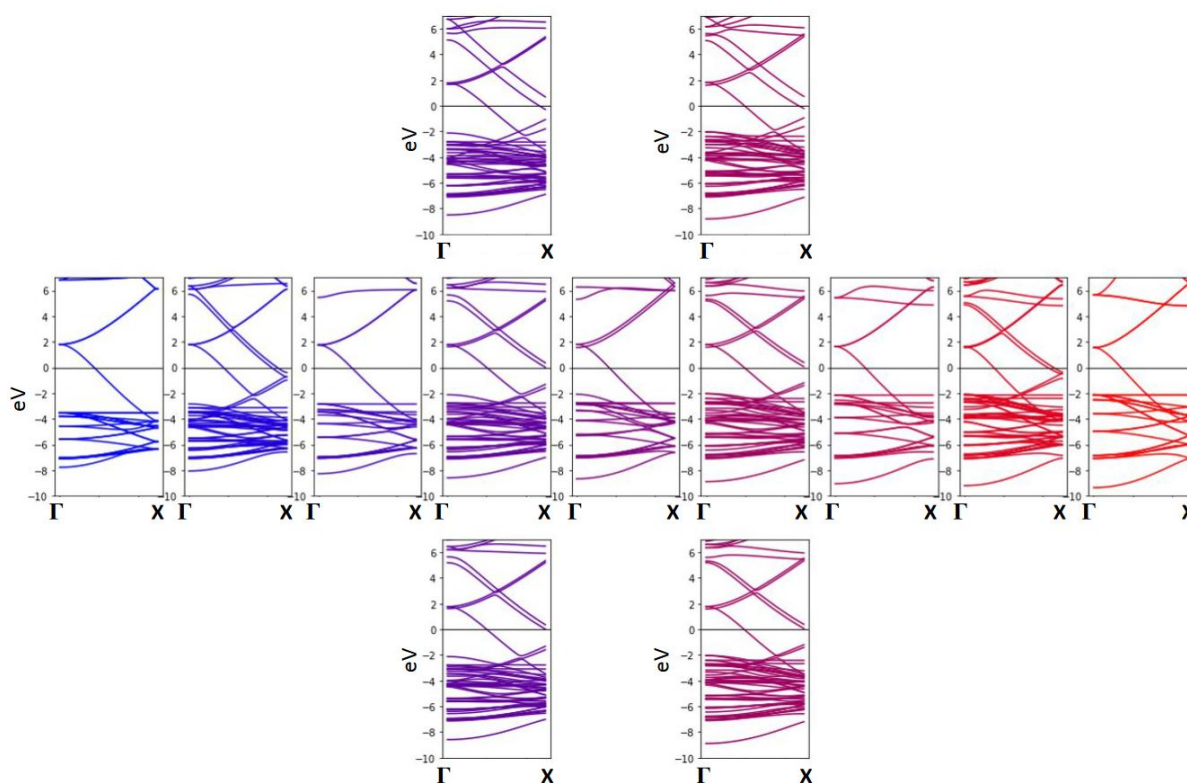


Figure 51. Band structures for Au-Ag alloy system, starting from Ag (left) and ending with Au (right). For two different ratios three configurations were used to represent the system, so their band structures are aligned vertically and for each the same color code is used. Due to different unit cell symmetries only the high symmetry path between  $\Gamma$  and X points is shown, since that part of the high symmetry path exists for all of the studied systems.

Band folding happens as a consequence of the translational symmetry loss upon alloying. When the unit cell is expanded, in reciprocal space the unit cell (Brillouin zone) is reduced. Since the bands are plotted in the reciprocal space, the same states are plotted on a shorter path, and thus they “fold” upon themselves. In the band structure this is reflected in the band, instead of proceeding down the high symmetry path, at some point “returning” in



the reverse direction with states positioned at the same k-point but at different energies. Figure 52 exemplifies this behavior for a primitive 1-atom FCC unit cell of Au and for the 4-atom FCC unit cell (supercell) reproducing the same crystal structure. It is important to note that GPAW detects that the 4-atom cell isn't the primitive unit cell and does not enable transitions between folded bands in a supercell. Therefore the dielectric function calculated based on both representations is identical. However, in an alloy the transitions between the folded-like bands are allowed since now the larger (i.e. 4-atom) cell is the primitive unit cell. In a substitutional alloy, a primitive unit cell consisting of more than one atom is needed to reproduce the crystal structure, thus expanding the minimum size of the cell. This reduces the Brillouin zone and leads to band folding. When the exact point of band folding appears near the Fermi energy, interband transitions are possible at a continuous energy range starting from near-zero. Such features are present near the Fermi energy for all alloys, as can be seen in the band structure figures in the appendix, and even on all of the band structures in the Figure 51.

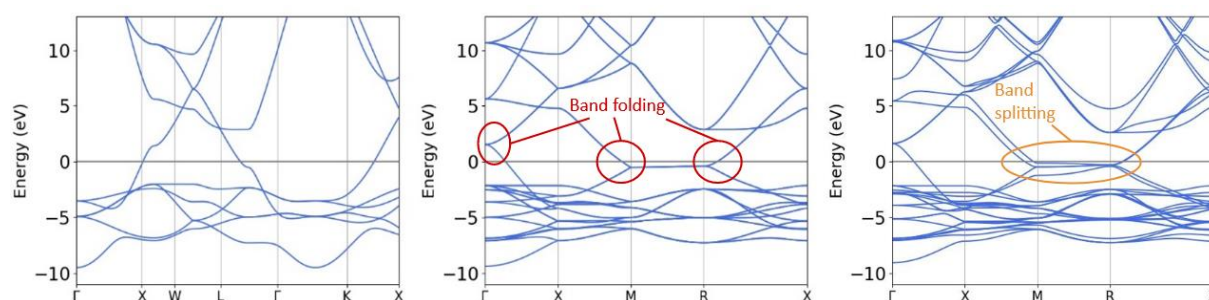


Figure 52. Band structure of bulk Au calculated using only the primitive (one atom) unit cell (left) and band structure of bulk Au calculated using four-atom face centered cubic unit cell that recreates the same lattice as the primitive one (middle). Band folding near the Fermi level can be observed on the middle picture. Band structure of  $\text{Au}_3\text{Ag}$  system (right) has a very similar four atom unit cell as the four atom bulk Au face centered cubic unit cell, with the band structure also being rather similar. However, band splitting caused by a substitution of one Au atom by one Ag atom can be observed near the Fermi level. GLLB-SC was used in these calculations.

Band splitting happens when a perturbation (such as atom substitution) is introduced in the periodic potential, thus breaking the degeneracy of certain states. In the studied alloys the perturbation is relatively mild due to atoms of similar elements being present in the lattice. As a consequence, the states are “split” only slightly, resulting in non-degenerate but very closely

spaced and almost parallel bands (Figure 52, right). When split bands cross the Fermi level, pairs of filled and unfilled states close in energy are available at the same k-point, thus enabling low-energy interband transitions. This effect can also, to varying degrees, be observed on all of the alloy band structures shown in the appendix, and is evident on some of the bands along the  $\Gamma$ -X path shown in the Figure 51. Although it is hard to grasp subtle trends from band structures containing a different number of bands and plotted along the different high symmetry paths, the band splitting seems to be slightly stronger for the alloys containing similar amounts of both elements, possibly explaining the trend of increasing losses at the  $\epsilon_2$  minimum for closed d-shell alloys (generally between 1 and 2 eV) - providing the main contribution below the onset of d-sp transitions and at the region where the Drude term has a very low influence.

In fact, these effects can be generalized and similar consequences found for different perturbations. For example, Malola *et al.* have observed that upon symmetry breaking of the Au nanocrystal, there is smearing of electronic states near the Fermi energy<sup>176</sup>. Another example is from the work of Gjerding *et al.*<sup>177</sup> in which a defect was introduced in the pure Ag (bulk) crystal lattice by removing one atom in the unit cell, leading to the appearance of the joint density of states (meaning newly allowed interband transitions) in the IR range.

Our results are corroborated by the ellipsometric data and computational considerations of AuCu<sub>3</sub> system<sup>121</sup> showing optical losses in the infrared range as well as JDOS below the d-sp interband transition onset in the alloyed structure. This work shows that the findings regarding the AuCu<sub>3</sub> system were not an exception but an indication of a general property of closed d-shell alloys, caused by band folding and band splitting due to alloying. Furthermore, the results imply that more precision might be needed when discussing the interband transition onset in alloys. What is typically referred to as the interband transition onset in alloys is actually only the onset of the transitions starting from the d-bands (d-sp transitions), as discussed above. These two terms are equivalent for pure closed d-shell metals. However, for alloys the interband transitions are allowed at very low energies (defining the actual onset) and below the energy of d-sp transitions. Besides that, these transitions happen between conduction bands, usually of sp-character. Therefore, the feature of the alloy dielectric function that is typically called interband transition onset should more precisely be called the d-sp interband transition onset for alloys of closed d-shell metals.

---

The band structures for Au-Cu and Ag-Cu alloys are in general rather similar to the results of the Au-Ag alloy system (see appendix) so they are not individually analyzed further in here. The reason for that is mostly in them being closed shell element alloys, suggesting a tentative classification of elements in terms of their electronic structure might be reasonable to simplify the view on some general alloy properties.

On the other hand, the alloys of Pd and Au show different behavior due to Pd being an open shell element (in the pure bulk metal form). As such it has high-lying d-states which cross the Fermi level, with both filled and empty states available at the same k-points, meaning that the interband transitions are allowed continuously from very low energies in the IR range and extend through visible to UV range with the involvement of other bands. Even with a rather low ratio of Pd in the alloy with Au, the imaginary part of the dielectric function (due to interband contribution) shows an abrupt rise in the region between 1 and 2 eV, where the Au  $\epsilon_2$  has a minimum. This shift can be partially explained by observing the dielectric function change for the PdAu<sub>7</sub> alloy (Figure 53, left).

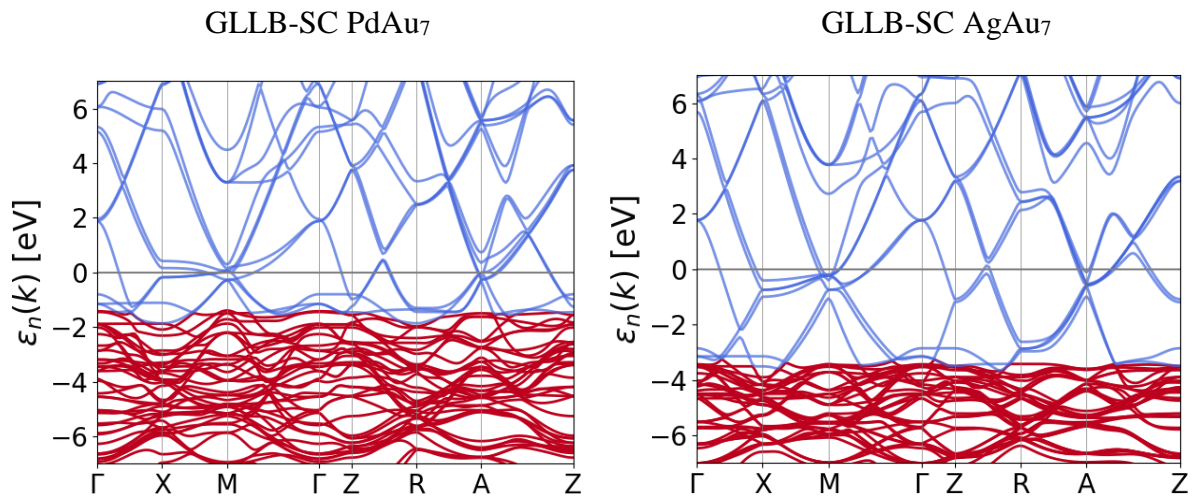


Figure 53. Band structure of PdAu<sub>7</sub> alloy system (left) and of AgAu<sub>7</sub> alloy system. Nominal d-bands are colored red to increase legibility of the figure but it should be noted that there is substantial hybridization near the Fermi level so an exact classification by orbital type can not be made.

It is visible that band folding and splitting is present around the Fermi energy, similarly as for the closed d-shell element alloys, with band splitting being seemingly slightly stronger. This might partially account for the observed behavior by enabling vertical transitions at the energy

of about 1 eV. Perhaps a more notable change that helps understand the abrupt shift in the dielectric function is the introduction of high-lying d-states characteristic for Pd. On Figure 53 the band structures of PdAu<sub>7</sub> and AgAu<sub>7</sub> alloys calculated by GLLB-SC are compared, with the d-bands colored differently for clarity. It can be seen that the upper edge of the d-states lies approximately 1 eV below the Fermi level. Moreover, along with the d-bands some of the (nominally) sp-bands below the Fermi level are also pushed upwards and lie relatively flatly above the d-states, possibly providing a high number of filled states available for transitions at low energies given that there are unfilled states directly above them. It should be taken into consideration that the distinction between sp- and d-states close in energy below the Fermi level in this case might be somewhat arbitrary since because of a possibly mixed orbital character of these states due to hybridization. This issue is more closely discussed in the part of this work related to the orbital-resolved DOS calculations. In contrast to the PdAu<sub>7</sub> band structure, for the AgAu<sub>7</sub> band structure the upper edge of the d-bands and the flat sp-bands lies about 2 eV below the Fermi energy, thus not being able to allow transitions in the 1-2 eV range where PdAu<sub>7</sub> alloy shows an abrupt shift in the  $\epsilon_2$ . Therefore, the main contribution to the abrupt shift with the addition of a small ratio of Pd in the alloy with Au can be assigned to the introduction of high-lying states characteristic for Pd. As the ratio of Pd increases, so does the upper edge of the d-states. Further increase is gradual, again in line with the observed behavior for the Pd-Au dielectric function.

Although the emergent properties of alloying discussed above also exist in this type of alloy - containing one open and one closed shell element - the main changes in the dielectric function can be ascribed to properties inherent to one of the constituent element and its characteristic electronic structure. This further validates the classification of elements due to their electronic structure to explain and predict some of the broad changes in their optical and plasmonic properties, both individually and in alloys.

It has to be noted that both band splitting and folding are predicted with both functionals (PBE and GLLB-SC), once again showing that DFT in general gives qualitatively correct results for alloyed systems. Focusing on the area near the Fermi level (since that is the area where relevant transitions occur), some differences are visible, but in terms of absolute discrepancy they are much smaller than the differences in d-band positions. This is unsurprising keeping in mind that the bands in question are of s and p-character, which are, unlike d-bands, usually fairly well described by standard GGA functionals such as PBE.

---

### 5.3.2. Density of states calculations

Density of states calculations were also performed using both PBE and GLLB-SC functionals. In GPAW the DOS calculations can be resolved by atomic orbitals, by atoms, and by elements in the unit cell. Therefore, not only the total DOS was studied but also the collective contributions of s, p, and d-states and the relative contributions of constituent elements of an alloy at different energies. Similarly as for the band structure calculations, the amount of relevant figures is large and not practical to fit in the main body of the thesis. For that reason the figures are placed in the Appendix, and only the most relevant figures are shown in the text below.

For the Au-Ag system the most notable change in the DOS upon alloying happens to the d-bands. As already indicated by the band structures, the trend of d-band DOS change shows that the collective band width contracts and the upper edge gradually moves further below the Fermi level as the alloy content changes from pure Au to pure Ag. It should be noted that when there is a small amount of Au in the alloy, the d-states highest in energy are disproportionately related to Au (Figure 54). This is not surprising since in its pure form Au in general has higher d-states than Ag. As the alloy composition approaches equal amounts of each element and continues towards the pure Au, the highest lying d-states are almost exclusively Au states. In other words, the d-band edge is dominated by the states coming from Au atoms. Moreover, in comparison to the rapid DOS drop with energy increase at the very edge of high-lying d-bands for pure Au and Ag, the DOS reduces progressively more slowly and smoothly as the composition reaches equal amounts of both elements. This fact might be connected to the smoother shape of the imaginary part of the dielectric function from the onset to the peak of the part related to d-sp interband transitions.

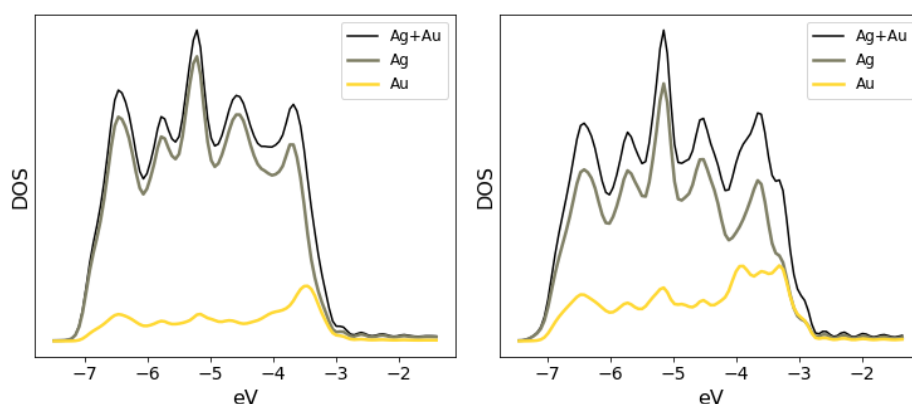


Figure 54. DOS projected on  $\text{Ag}_7\text{Au}$  (left) and  $\text{Ag}_3\text{Au}$  (right) d-bands resolved by element contribution.

There is little difference in the position and shape of the DOS projected on the p-orbitals between Au and Ag, so most of the changes upon alloying are not particularly notable. Still, there is a difference near the Fermi level, and since that area might be of particular importance it has to be mentioned that the Ag DOS projected on p-orbitals has almost double the value in comparison with Au, although in both cases the values are rather low. With alloying there is a gradual change between these two limiting values (Figure 55).

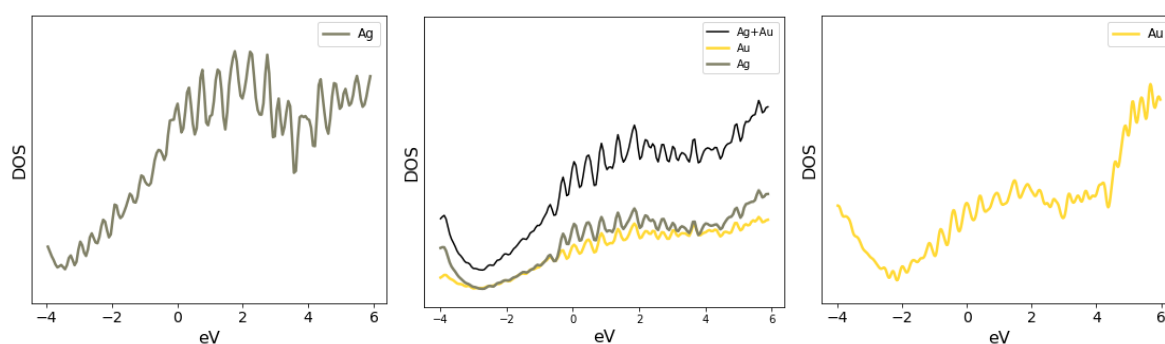


Figure 55. DOS projected on the p-orbitals of pure Ag (left), alloy of equal ratio of Au and Ag (middle), and pure Au (right), showing the contribution of each element in the system.

DOS projected on the s-orbitals shows similar features at similar energies, with a few notable differences: one is around the Fermi level where for both elements the s-orbital projected DOS (PDOS) has mostly smooth features but with slight differences, and the other is the abrupt increase that follows, likely the consequence of relatively flat unfilled band(s) at that energy. Around the Fermi level Ag s-orbital PDOS has a shape resembling a negative parabola, peaking almost exactly at the Fermi level. Conversely, the Au s-orbital PDOS steadily rises when crossing the Fermi level, with s-orbital PDOS at the Fermi level being very similar for both elements. The abrupt increase in the s-orbital PDOS is located near the 3.5 eV for Ag and near 3 eV for Au. With alloying it becomes smoother than for pure elements. Interestingly, when a small amount of Au is present in an alloy, a separate small peak forms at the energy slightly lower than the original PDOS increase for pure Ag, and the element-resolved PDOS shows that it is almost fully due to Au contribution. This small peak merges with the larger Ag-based peak thus making the overall PDOS increase less abrupt. Also, that way the increase in the s-orbital PDOS shifts closer to the Fermi level, possibly impacting the optical properties as it could be involved in the transitions excited by photon energy in the visible range.

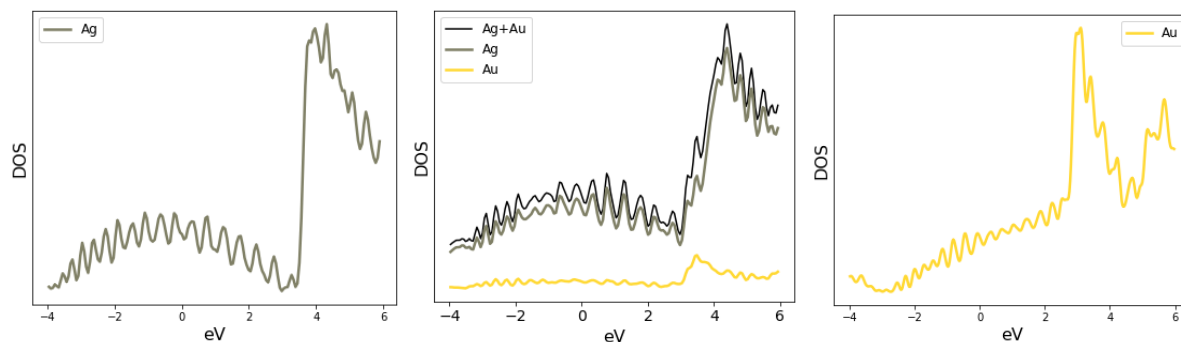


Figure 56. DOS projected on the s-orbitals of pure Ag (left), pure Au (right), and AgAu<sub>7</sub> alloy (middle), showing the contribution of each element in the system.

Comparing the overall contributions of s, p, and d-orbitals to the total DOS is relatively straightforward below the Fermi energy since d-bands dominate, even in the area where the nominal upper d-band edge ends. In fact, it is very interesting to note that even at Fermi energy the d-orbital contribution to the total DOS is comparable to both s and p-orbital contributions. For Ag, the p-orbital PDOS is dominant at the Fermi energy with s and d-orbital contribution being lower and almost the same, respectively. For Au GLLB-SC predicts almost the same contributions of all three orbital types while PBE predicts d-orbital contribution to be the highest (Figure 57). In general, the difference of calculated DOS using PBE and GLLB-SC is mostly reflected in the propensity of GLLB-SC to predict deeper d-band edge and lower bandwidth of the d-bands, in line with the band structure calculations.

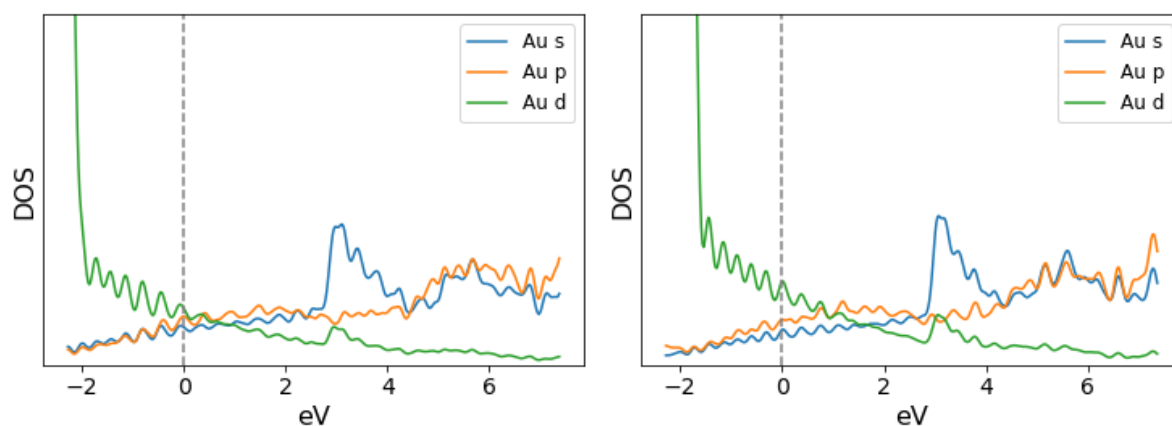


Figure 57. DOS projected on atomic orbitals of Au calculated by GLLB-SC (left) and PBE (right).

Figure 57 indicates that higher d-band contribution for Au at Fermi energy is likely connected to overall higher energy of the Au d-bands, leading to the unexpected implication that the position of the d-band might be connected to the total DOS at the Fermi energy despite the seemingly large distance of the d-band edge (2 eV or more) from the Fermi energy. Regardless of the functional used, these results challenge the notion of conduction band being (just) sp-hybridized. They imply that d-orbital contribution remains relevant near the Fermi energy, especially below it, but in some cases even slightly above it. It is possible, however, that some of the PDOS might be falsely attributed to different atomic orbitals due to imperfect projections. Nonetheless, these results provide guidelines for both theoretical and practical considerations of alloy electronic structure and the possibility of engineering it. Analysis of the d-character of the PDOS near the Fermi energy for Cu-Au and Cu-Ag systems shown on the Figure 58 provides more evidence in line with this assumption. Both Cu and Au have the upper d-band edge at similar energies, so at the Fermi level the amount of d-orbital character in the total DOS is very similar for both elements and changes little with alloying. Conversely, Cu-Ag system follows the trend of the Au-Ag system with a declining amount of d-orbital character in the total DOS as the ratio of elements moves towards Ag.

---



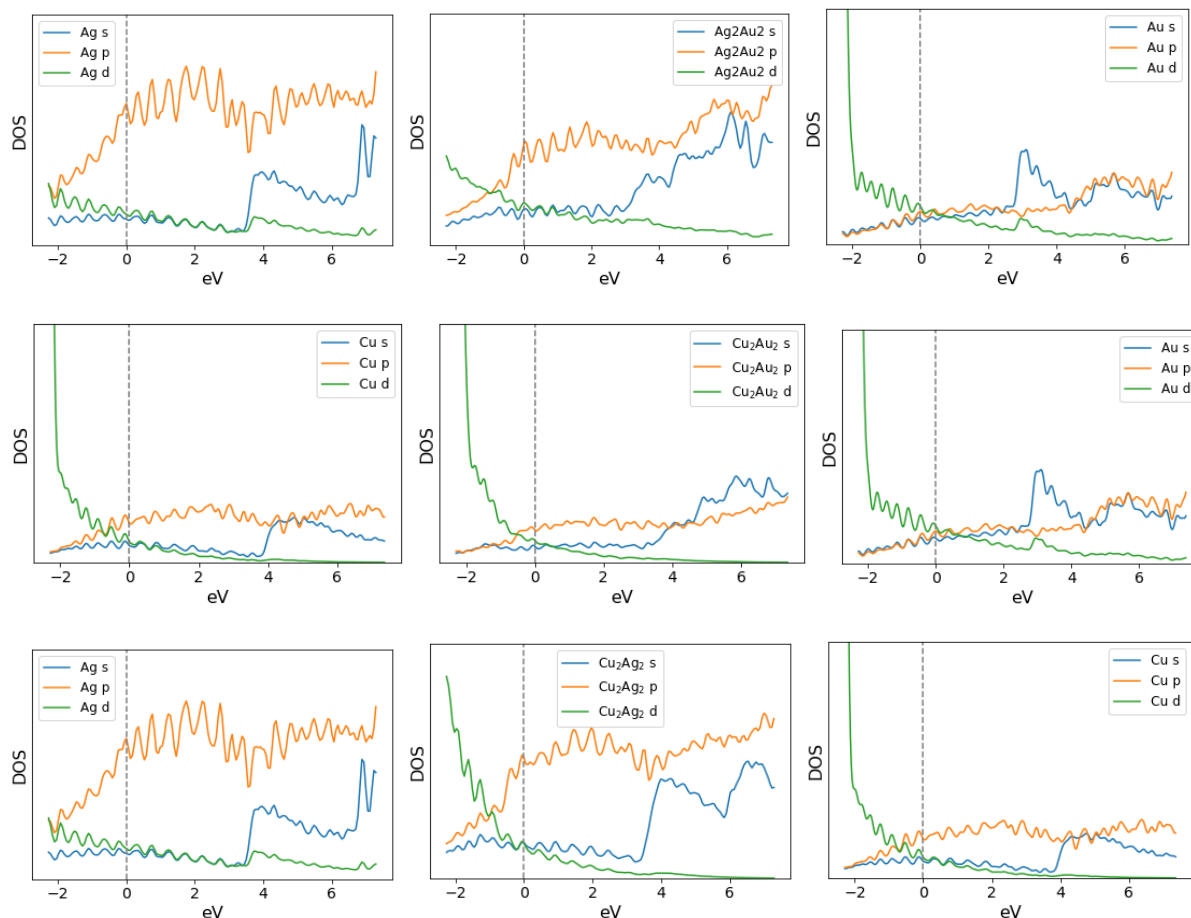


Figure 58. DOS projected on atomic orbitals of pure Au, Cu, and their alloys with the equal ratio of both elements.

As expected, the Pd-Au system is a different case, since the d-band edge of Pd actually crosses the Fermi energy. Nonetheless, the reasoning based on patterns observed in the aforementioned cases can, in good part, also be applied to this system. For example, the results of band structure calculations have shown that, in the case of alloyed systems with much less Pd than Au, the upper edge of the d-band lies below the Fermi energy (Figure 53). However, following the same reasoning as above, due to higher proximity of the d-band edge to the Fermi level, it is expected that the total DOS at the Fermi level has a higher d-orbital contribution than any alloy or pure element in Au-Ag, Au-Cu and Ag-Cu systems. This is indeed the case, as can be seen on the Figure 59.

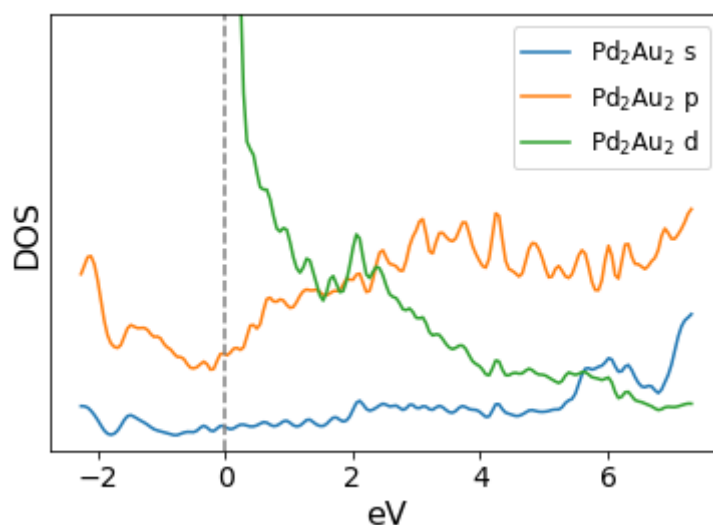


Figure 59. DOS projected on atomic orbitals of pure  $\text{Pd}_2\text{Au}_2$  system.

Indeed, at the Fermi level the d-orbital contribution dominates, and remains larger than the p and s-orbital contributions up to 2 eV - the majority of the energy range relevant for optical excitations. This relatively high density of d-like states results in a rapid increase of the total DOS near the Fermi level in comparison with pure Au DOS in that range. Supplementing the discussion based on band structure results, these findings confirm that the increase of the DOS at the Fermi level caused by the shift in the d-band position could be one of the reasons for the abrupt increase of the  $\epsilon_2$  in the 1-2 eV range upon alloying a small amount of Pd with Au. Moreover, it is evident that, although there is an abrupt drop in the contribution of the d-orbital character after the nominal d-band edge (in this case about 1 eV below the Fermi level), substantial contribution remains way above the Fermi level, suggesting that the conduction bands of such a system should not be classified as (just) sp-bands.

As the ratio of Pd in the Pd-Au alloy increases, the d-character dominance at the Fermi level also increases, with the (nominal) d-band edge coinciding with the Fermi level at about 50% element ratio, resulting in very high DOS at that energy. This remains so for element ratios where Pd dominates, likely remaining a defining feature for the optical properties until 100% of Pd is reached, and explaining the slowdown in the change of optical properties as a function of composition for Pd-dominant alloys.

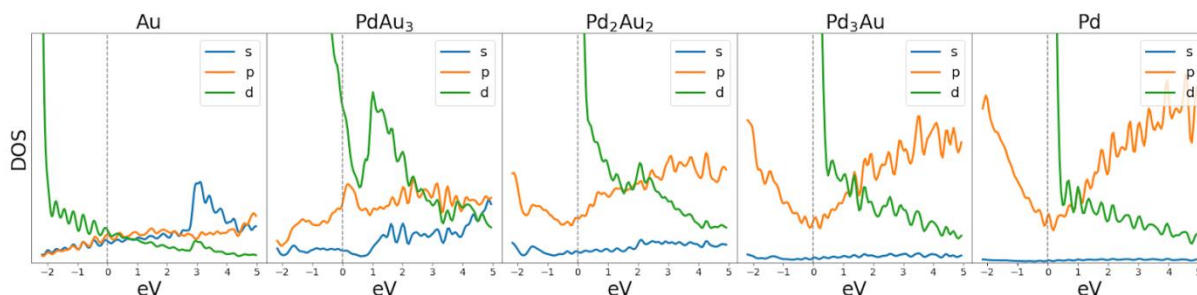


Figure 60. DOS projected on atomic orbitals of Au, Pd, and their alloys.

Element-resolved d-band PDOS in the Figure 61 helps elucidate the reason for the quick shift in the position towards higher energies even with a small amounts of Pd in alloy with Au. It can be seen that the Pd-related states localize in a sharp peak on a small energy range and make up a majority of the upper d-band edge. Observing the DOS contribution of the individual atoms shows this fact even more clearly, with sharply localized DOS related to the only Pd atom in the 8-atom cell. When the element ratios are reversed the element contribution to DOS is also reversed, with Au-related DOS now localized near the lower edge of the d-bands. Interestingly, for the equiatomic unit cell the element resolved d-band DOS shows a relatively clear segregation of Au-related states at lower energies and Pd-related states at higher energies, which stands in contrast to the results of the Au-Ag alloy system.

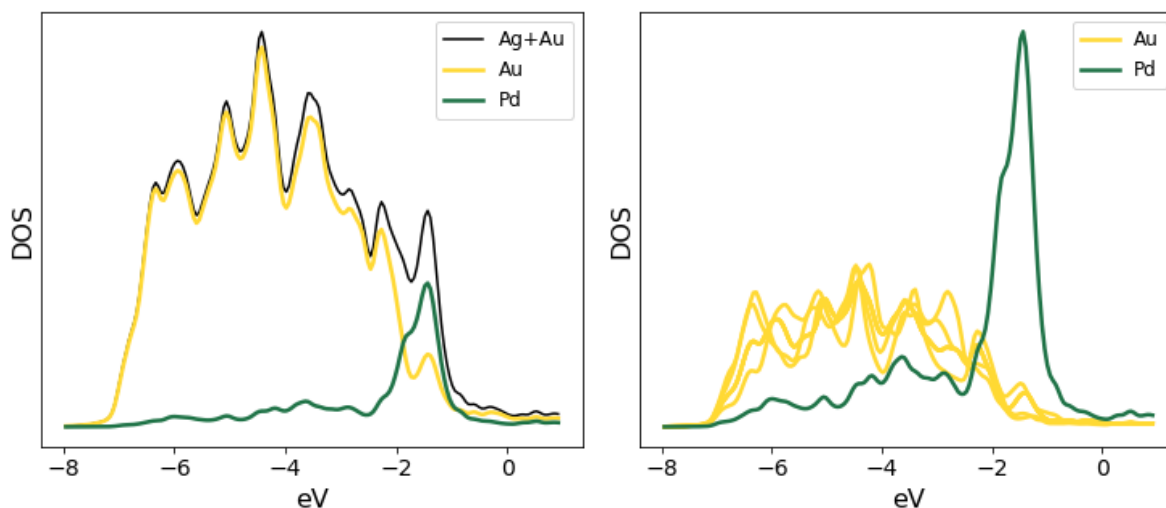


Figure 61. DOS projected on  $\text{Au}_7\text{Pd}$  (left) d-bands, showing the total contribution of each element, and atom-resolved DOS of the same system depicting the individual contributions of each atom in the unit cell to the total DOS.

Interestingly, similar behavior can be observed for Cu-Au and Cu-Ag alloys. Unlike the other studied elements, Cu has a d-band DOS highly skewed towards the upper band edge. When alloyed as a minority constituent with both Au and Ag it creates a localized and sharp peak in the d-band DOS, resembling the behavior of Pd in Pd-Au alloys. When alloyed with both Au and Ag in similar ratios the element contribution to the d-band DOS also segregates, with Cu contributing more to the higher energy states and other two elements more to the lower energy states. This behavior is especially pronounced for equiatomic Ag-Cu cells where the d-band takes a double-peaked shape, with DOS of two elements showing the least overlap, and both contributing slightly below -4 eV with respect to the Fermi level, thus visually almost “splitting” the d-band DOS (Figure 62). Similar effects have been previously observed for Au-Pd alloys and attributed to the interplay of band repulsion and hybridization<sup>178</sup>. However, this behavior does not strongly affect the optical properties in the visible range, but it could be expected to have some effect in the UV range where the dip in the DOS might reflect in the transitions excited by photons of energies higher than 4 eV (approximately over 300 nm). Such effects in the DOS are not observed for the s and p-contribution to the DOS in any alloy, which is in all cases quite similar regardless of the element.

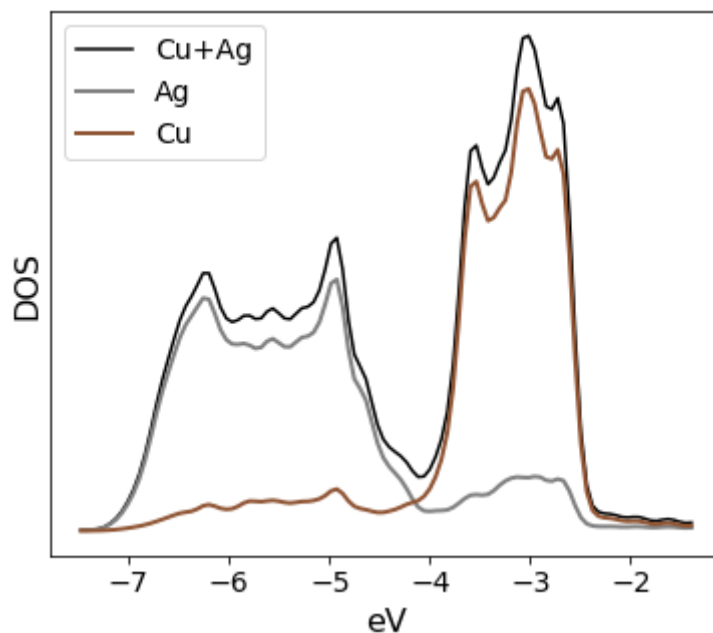


Figure 62. DOS projected on Ag<sub>2</sub>Cu<sub>2</sub> d-bands showing the segregation of the contribution of each element to the total DOS.

Insights regarding the influence of configuration on the DOS can be drawn from unit cells where atom ratio is constant but configuration changes. Overall, some influence can be observed, but it does not affect the DOS strongly. The relevant features of the DOS generally remain rather similar. For example, the upper d-band edge, as can be seen on the Figure 63, where it remains at almost exactly -2 eV below the Fermi level for the  $\text{Cu}_3\text{Au}_5$  system. This finding is in line with the observed small influence of the configuration change on the dielectric function.

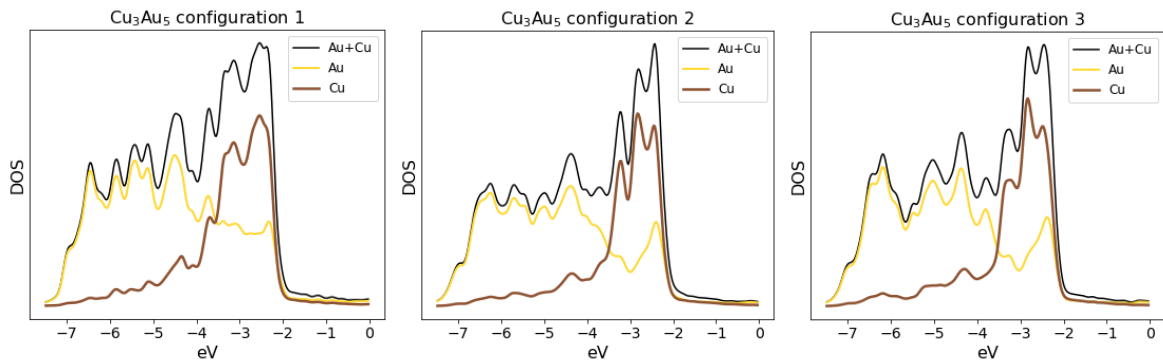


Figure 63. DOS projected on the d-bands of  $\text{Cu}_2\text{Au}_5$  system with three different unit cell configurations.

## 5.4. Influence of alloying on hot carrier generation

### 5.4.1. Comparison of the DOS and the JDOS-based approach

Obtaining a structure-property relationship encompassing the alloy composition, plasmonic and optical properties, and electronic structure of the system enables finding the reasoning behind the obtained DFT-based predictions and experimental results. The results of the DFT approach used in this work show that low energy interband transitions appear as an emergent property of alloying. It is also shown that they are enabled by band splitting and folding. Changes in the electronic structure that lead to the abrupt shift in the dielectric function of the Pd-Au alloys were also identified. It was also shown that elements can conceptually be classified by their electronic configuration/structure (in the bulk state). The findings regarding changes governing electronic transitions imply that hot carrier generation should also be affected by the said changes, with the classification of elements a useful approach to deliberately tune the hot carrier generation by combining the elements of appropriate classes. Since it is notoriously hard to study hot carrier generation experimentally due to the transient nature of these extremely short-lived charge carriers, DFT has become an especially important

---

research method in the field. While the hot carrier generation by alloys has rarely been studied, one method based on DOS calculations has been used several times to estimate the hot carrier energy distribution<sup>95,147,148</sup>. While popularized by its simplicity, this method is highly approximative, neglecting the momentum conservation condition as well as transition matrix elements and, in essence, treating both interband and intraband transitions the same. Our results show that alloying closed shell materials results in substantial changes in the band structure (leading to new interband transitions) but small changes in DOS, thus implying that a stricter method would be more suitable to study alloy hot carrier generation. A joint-density of states (JDOS)-based method was created for this purpose, and compared to the results of the DOS-based method in Figure 64. All of the results connected to hot carrier generation were obtained using GLLB-SC functional since we have hitherto shown that it performs better than PBE for properties relevant to this research.

---

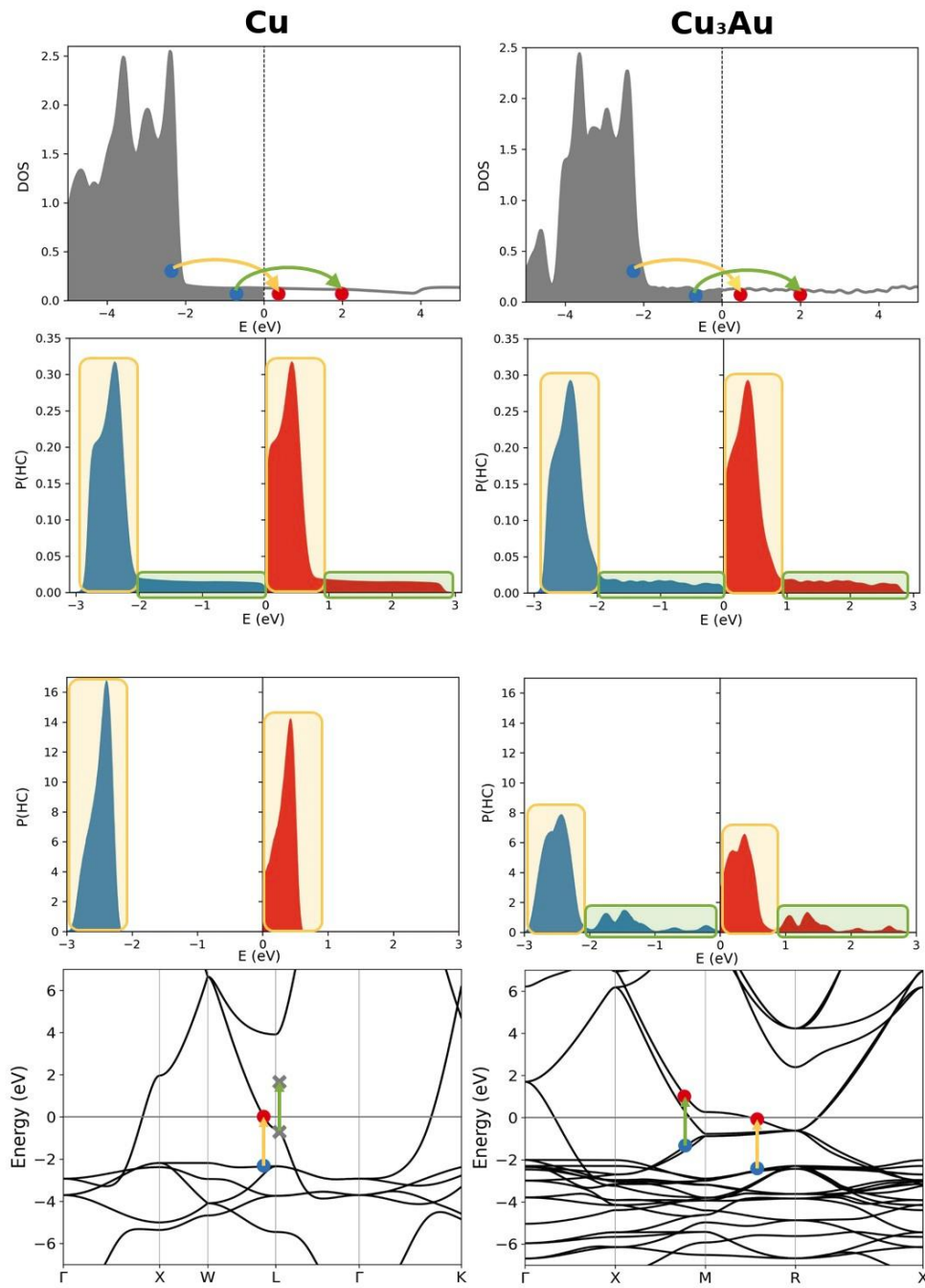


Figure 64. Comparison of hot carrier energy distributions given in arbitrary units, obtained by a DOS-based method that neglects momentum conservation (top two rows) and our method that takes it into account (bottom two rows). Yellow arrows show the d-sp transitions, with the corresponding part of the hot carrier distribution shaded yellow. Green arrow shows sp-sp transitions with green shading showing the corresponding parts of the hot carrier distribution. Hot hole distributions are shown in blue and hot electron distributions in red. Fermi level is set to 0 eV.<sup>179</sup>

Our method is focused on observing the changes in direct interband transitions because, as stated above, they are far more affected by the electronic structure changes. Furthermore, they carry a great deal of information regarding the total hot carrier generation since they dominate interband transitions above the interband transitions threshold. The systems of choice are Cu and Cu<sub>3</sub>Au - a pure closed shell metal and an alloy of two closed shell metals for which an experimentally observed ordered L1<sub>2</sub> structure exists. This means that the idealized DFT model of that alloy is a very close representation of a real system.

The results demonstrate the importance of accounting for momentum conservation: Hot carrier distributions that correspond to 2.8 eV light excitation obtained by the DOS-based method are almost identical for pure Cu and its alloy with Au, while those obtained by the JDOS-based method show significant differences. The similarity in the distributions obtained by the DOS-based method are due to very small changes of the DOS in the relevant energy range (Figure 64, first row). Abundant hot electron generation is predicted near the Fermi energy, and abundant hot hole generation deep below the Fermi energy. This part of the distribution is caused by the transitions starting from the high density of d-states and ending at the lowest energy unfilled states in the conduction band. Much lower hot carrier generation is predicted at higher energy (up to the photon energy) for hot electrons and in the less negative energy range (up to the Fermi level) for hot holes. This part of the hot carrier energy distribution comes from the transitions starting and ending in the conduction band. However, when momentum conservation is accounted for, only the transitions on the same k-point are allowed. For pure Cu, the only available direct transitions at 2.8 eV are the d-sp transitions, starting near the top of the d-band and ending near the Fermi energy, resulting in the abundant generation of highly energetic hot holes and less energetic hot electrons, near the Fermi level. In the alloy the bands are both folded and split near the Fermi level, allowing transitions almost continuously between different pairs of initial and final states separated by 2.8 eV. The high energy “tail” of hot electrons and low energy “tail” of hot holes is therefore absent in the hot carrier distribution for pure Cu, but present for Cu<sub>3</sub>Au alloy. Both Au and Ag, being closed d-shell elements, have a similar band structure to Cu, and thus the same features are obtained by these pure metals and their alloys (shown later). Therefore, the hot carrier “tail”, can also be viewed as an emergent property of alloying. This distinction in hot carrier generation is missed by the DOS-based method since it neglects momentum conservation.

---



#### 5.4.2. Influence of unit cell configuration and disorder modeling

To evaluate the influence of unit cell configuration and complexity, especially related towards modeling disordered systems, we compared the hot carrier distribution obtained by a 2-atom ordered CuAu alloy of  $L1_0$  crystal structure and the 8-atom SQS with the same atom ratio (Figure 65). Since many alloys containing good plasmonic metals exist as solid solutions or otherwise highly disordered structures this evaluation is important to make, especially since, unlike for the dielectric functions, no literature data exists for comparison.

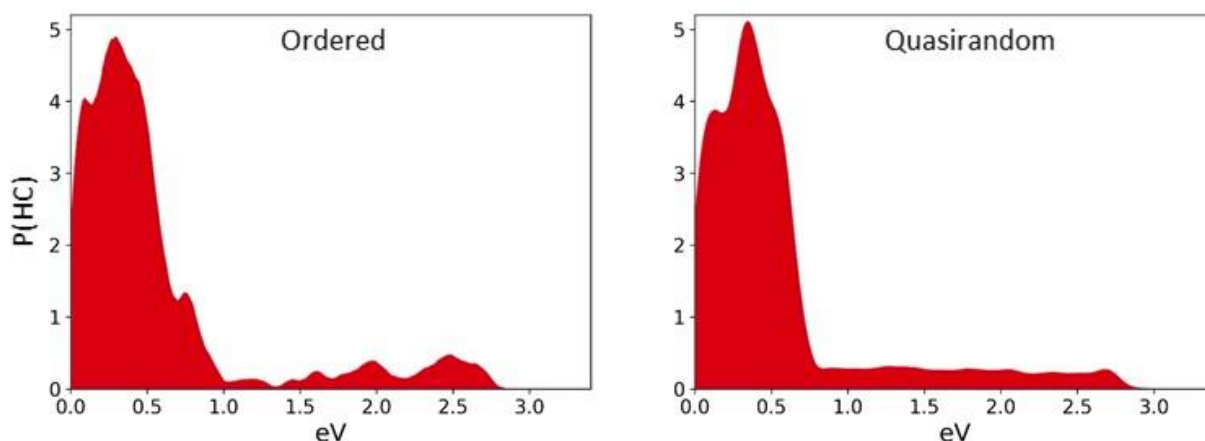


Figure 65. Hot electron energy distribution (in arbitrary units) for ordered AuCu alloy calculated using a simple 2-atom unit cell (left) and using a special quasirandom structure representing disordered alloy (right). Fermi level is set to 0 eV.<sup>179</sup>

Figure 65 shows that the hot electron distributions obtained using a very simple 2-atom unit cell and a larger unit cell with a quasirandom atom configuration show qualitatively very similar behavior. The same features are present in both cases - abundant hot electron generation near the Fermi level, and a high-energy tail. The differences are mostly in the higher smoothness of the hot carrier distribution obtained by a quasirandom unit cell. The low energy part is of practically same height and very similar shape in both cases, with a small additional peak present near 0.7 eV for the 2-atom unit cell. In the higher energy region the hot electron distribution obtained by using a simple unit cell shows a discontinuous lineshape, with several peaks and valleys. Such features are much smoother or not present in the results for the quasirandom unit cell. The reason for these differences is most likely in the much more diverse local environment of atoms in the larger, quasirandom unit cell. Furthermore, due to much more band folding for the larger and more complex unit cell, the pairs of states that are 2.8 eV (photon energy for this calculation) apart, are more smeared and thus spread more

equally. With further increase in the quasirandom unit cell it is expected that there would be further smoothing of the hot carrier energy distribution, until reaching convergence. However, even the simplest possible 2-atom alloy unit cell provides qualitatively the same features as the quasirandom one, and the complexity increase results primarily in smoothing. Since the small unit cell provides a satisfactory representation of the hot carrier generation, containing both important features (abundant low energy generation and the high energy tail), in the rest of the calculations we used the simple unit cells.

#### *5.4.3. Effects of combining closed d-shell elements on hot carrier distribution*

As discussed in the comparison of DOS and JDOS-based methods for the case of Cu and Cu<sub>3</sub>Au alloy and 2.8 eV photon energy, two features of hot carrier distribution can be observed: abundant generation on the narrow energy range and a more scarce generation on the wider energy range. To explore in more detail how hot carrier features of closed d-shell element alloys can be tuned with alloy composition, the Au-Ag alloy system was studied (Figure 66). The d-band positions are not as similar for Au and Ag as they are for Au and Cu, which makes the Au-Ag system more suitable for observing the effects of d-band position change on the hot carrier energy distribution.

---

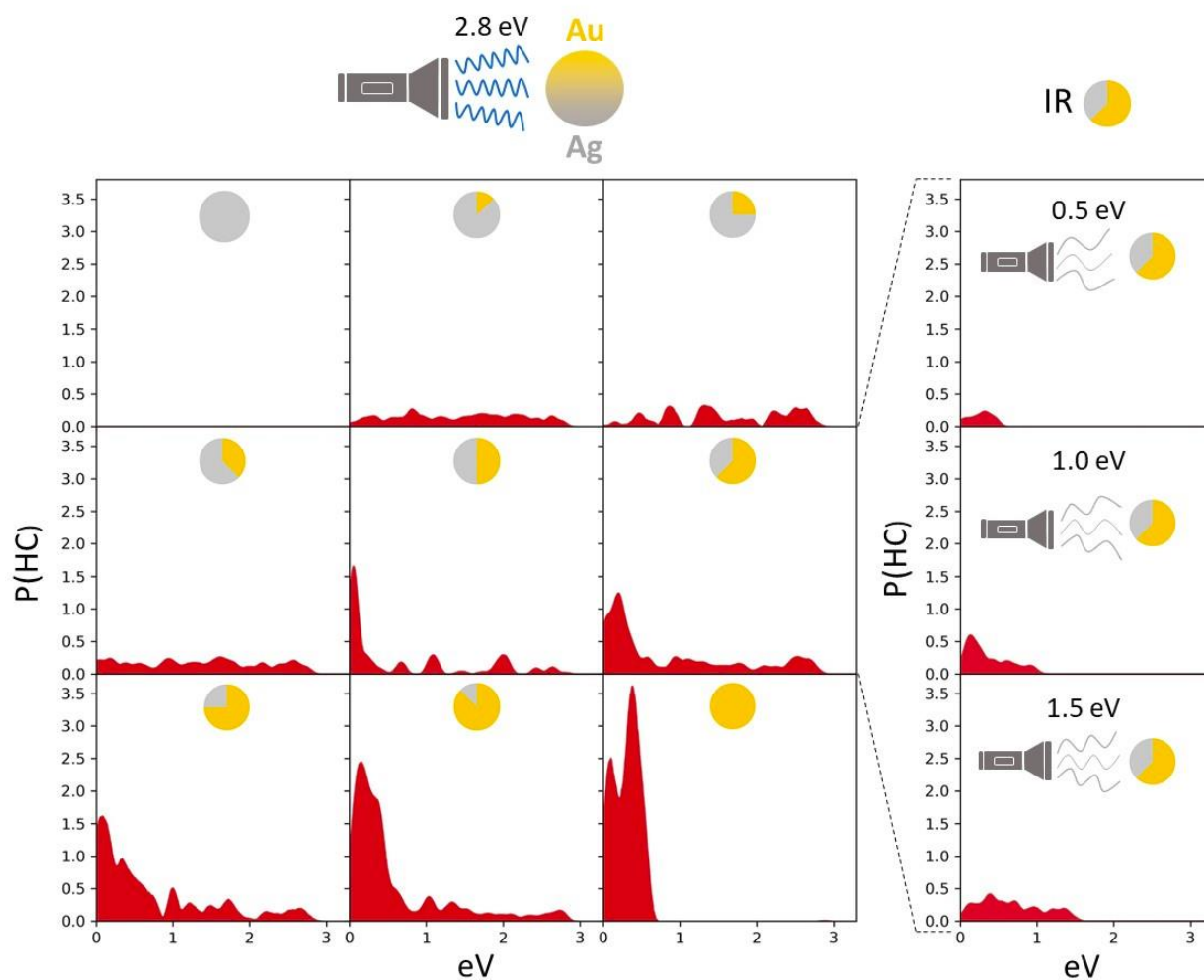


Figure 66. Hot electron energy distribution (in arbitrary units) due to excitation with 2.8 eV light for Au-Ag alloy systems with the composition changing in 12.5% increments from pure Au to pure Ag (three columns on the left). The column on the right shows that hot electron distributions can be obtained by IR light excitations for a fixed alloy composition  $\text{Au}_{0.625}\text{Ag}_{0.375}$ , far below the nominal d-sp direct transition onset. Fermi level is set to 0 eV.<sup>179</sup>

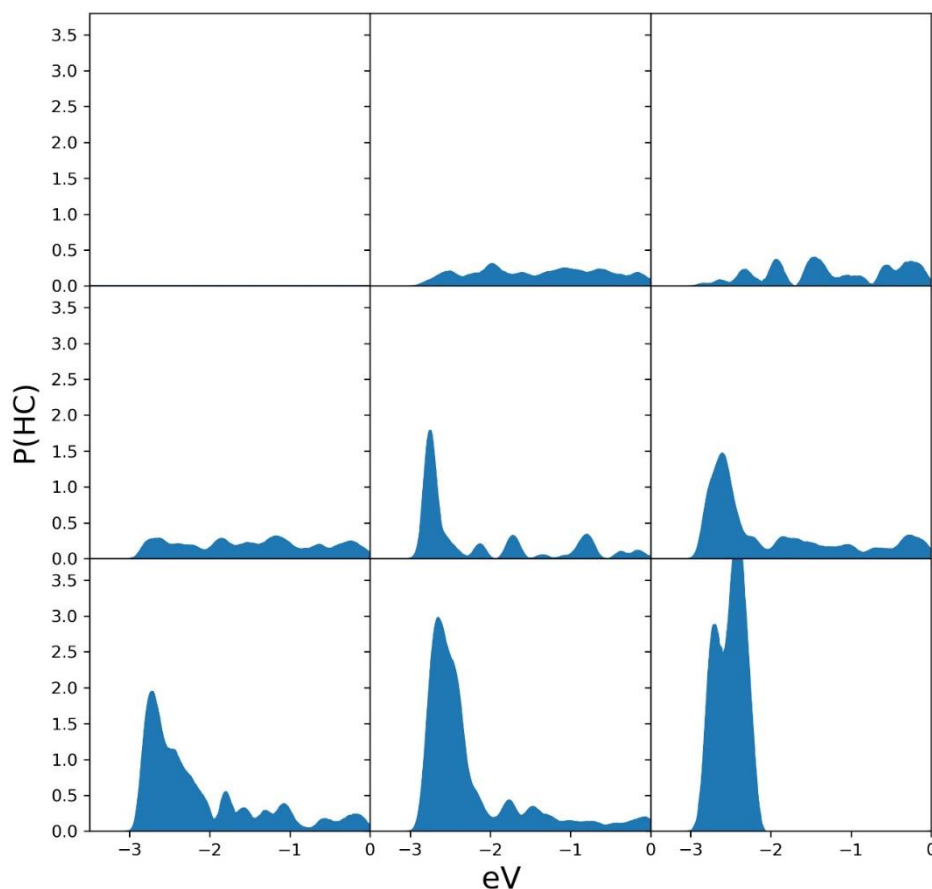


Figure 67. Hot hole energy distribution due to excitation with 2.8 eV light for Au-Ag alloy systems with the composition changing in 12.5% increments from pure Au to pure Ag. Fermi level is set to 0 eV.<sup>179</sup>

It can be seen that no interband transitions are allowed for pure Ag when photon energy is insufficient to excite electrons from the d-states to the unfilled states in the conduction bands. Therefore there is no hot carrier production related to interband transitions for pure Ag. When a small ratio of Au is present in the Ag-Au alloy, only the feature related to band structure folding and splitting is present in the hot carrier distribution since the upper edge of the alloy d-bands still lies too far (more than 2.8 eV, the photon energy) below the Fermi level and the first available unfilled states. However, at the ratio of 50% of both elements a more abundant hot electron generation near the Fermi level can be seen, with a similar feature present about photon energy below the Fermi level in hot hole energy distribution. This feature, characteristic of d-sp interband transitions, signifies that the upper edge of the d-bands increased to about 2.8 eV as more Au is present in the alloy. Indeed, as the ratio of Au and Ag

skewes more towards Au, this feature becomes more prominent. Finally, for pure Au, same as for the pure Cu, this is the only feature of hot carrier energy distribution. It can be seen that the smooth and gradual shift of the d-band edge upon changing the composition of an Au-Ag alloy enables smooth tuning of the feature characterized by the abundant generation of hot carriers. It has to be noted that the 2.8 eV energy was chosen as it lies between the plasmon resonance energy of small spherical Au and Ag nanoparticles. However, with the composition the plasmon resonance also gradually changes and this would have to be taken into account for tuning. Nonetheless, the photon energy in this case was held constant for demonstration purposes. While the hot electrons created by these transitions have relatively low energy, the corresponding hot holes are very energetic. This indicates that they might be particularly useful for injection into molecules or semiconductors, particularly of n-type. It has to be noted that the high energy of deep d-band hot holes partially remedies the issue of their low mobility (due to high effective mass in the relatively flat bands), which otherwise limits their usefulness.

The milder hot carrier generation that arises due to excitations to and from conduction bands is present for all Au-Ag alloys. Although some differences can be observed in terms of the more continuous or discontinuous nature of this feature, in general this feature does not seem to be highly tunable with alloy composition. Regardless, it is a modulation of hot carrier generation with regards to pure metals, a property of alloys that can function as an augmentation of the functionality present in pure metals. This is particularly important for hot electron generation since, unlike for hot electron energy distribution in pure metals, the feature unlocked by alloying extends to high energy range, up to the photon energy. There are several benefits to the production of very highly energetic hot electrons by interband transitions:

1. Hot electrons with energies close to the photon energy would otherwise be created only by less efficient interband transitions and by surface-assisted transitions whose relative contribution quickly diminishes as the size of the nanoparticles increases. Availability of direct transitions that produce high energy hot electron should therefore significantly improve the electron-injection properties of medium to large nanoparticles.
  2. Probability of injection of hot electrons over the Schottky barrier is increased in two ways. Firstly, the proportion of hot electrons with an energy sufficient to cross the
-

Schottky barrier increases. Secondly, the probability of injection increases with the excess kinetic energy (the larger the hot electron energy is in comparison to the Schottky barrier). Increase in the injection probability is the consequence of expanding the injection cone. In the ballistic picture of hot carrier injection, it is defined by the angle that the electron can have with respect to the semiconductor interface to still retain a perpendicular component of momentum large enough for injection.

3. Chemical reactions that are initiated by an injection of an electron in the high energy orbital benefit disproportionately from the availability of hot electrons of sufficient energy.
4. Even if only low energy hot electrons are needed for the desired process (for example hydrogen molecule desorption), the high energy tail of hot electron distribution provides an outsized contribution due to hot electron multiplication. As electrons scatter the energy that is contained in the highest energy hot electrons dissipates to several other electrons thus leading to a large increase in the number of relatively lower energy hot electrons.

The hot electron generation unlocked by band folding and splitting has another important property, it is available for excitations at any photon energy even if it is below the d-sp interband threshold. This is visible for 2.8 eV excitation and alloys that are Ag-abundant on the Figure 66. However, as shown on the right column of the Figure 66 in case of  $\text{Au}_{0.625}\text{Ag}_{0.375}$  alloy the hot carrier generation extends from visible to IR range. This is an expected consequence of the emergent interband transitions that were observed in the dielectric function calculations and confirms the hypothesis that the interband transition threshold reduction in alloys also meaningfully affects the hot carrier generation. The availability of interband transitions in the IR range becomes very important because the resistive losses otherwise make up a large proportion of all losses (up to 50%) in that energy range<sup>70</sup>. Since resistive losses do not result in hot carrier generation, a competing plasmon decay channel that enables hot carrier generation increases the efficiency of hot carrier generation. Greater proportion of hot carriers generated at low energies due to availability of interband transitions was observed in pure aluminum<sup>70</sup> and due to efficiency of interband transitions leading to approximately 25% of electrons decaying to create hot carriers by interband transitions. There are similarities to Al band structure and the band structure of

---

binary alloys of closed d-shell elements that can be connected to continuous availability of interband transitions. Namely, the band crossing near the W point in the band structure of Al can be likened to the conduction band folding present in the closed d-shell alloys. Both features of the band structure involve bands located one above another crossing or almost crossing near the Fermi energy. Since the Al was, for the aforementioned reasons, highlighted as a potentially very good material for plasmonic applications by Brown *et al.*<sup>70</sup>, the alloys of closed d-shell elements should also carry the same benefits, and thus the same potential.

#### 5.4.4. *Effects of combining open and closed d-shell elements on hot carrier distribution*

As was shown insofar, the addition of an open d-shell element such as Pd in an alloy with a closed d-shell element such as Au results in an increase of the DOS near the Fermi level, characteristic of the open d-shell elements. Such a change in the electronic structure also strongly affects the hot carrier generation, as can be observed in the Figure 68 in the case of a Pd-Au alloy. This alloy system exhibits a rather abundant and continuous hot carrier energy distribution. Such a distribution is especially important for high-energy hot electron production. Unlike in the case of alloys of two closed d-shell elements, where the transitions enabled by low DOS of split and folded conduction bands around the Fermi level result in a relatively scarce hot carrier production, the presence of abundant high-lying d-states in the alloy containing an open d-shell element enables much higher and relatively continuous hot electron distribution all the way up to the photon energy. Reiterating the previously stated point, availability of very high energy electrons can be rather useful, particularly when injection in a high-lying state or over a high-lying barrier is required.

---

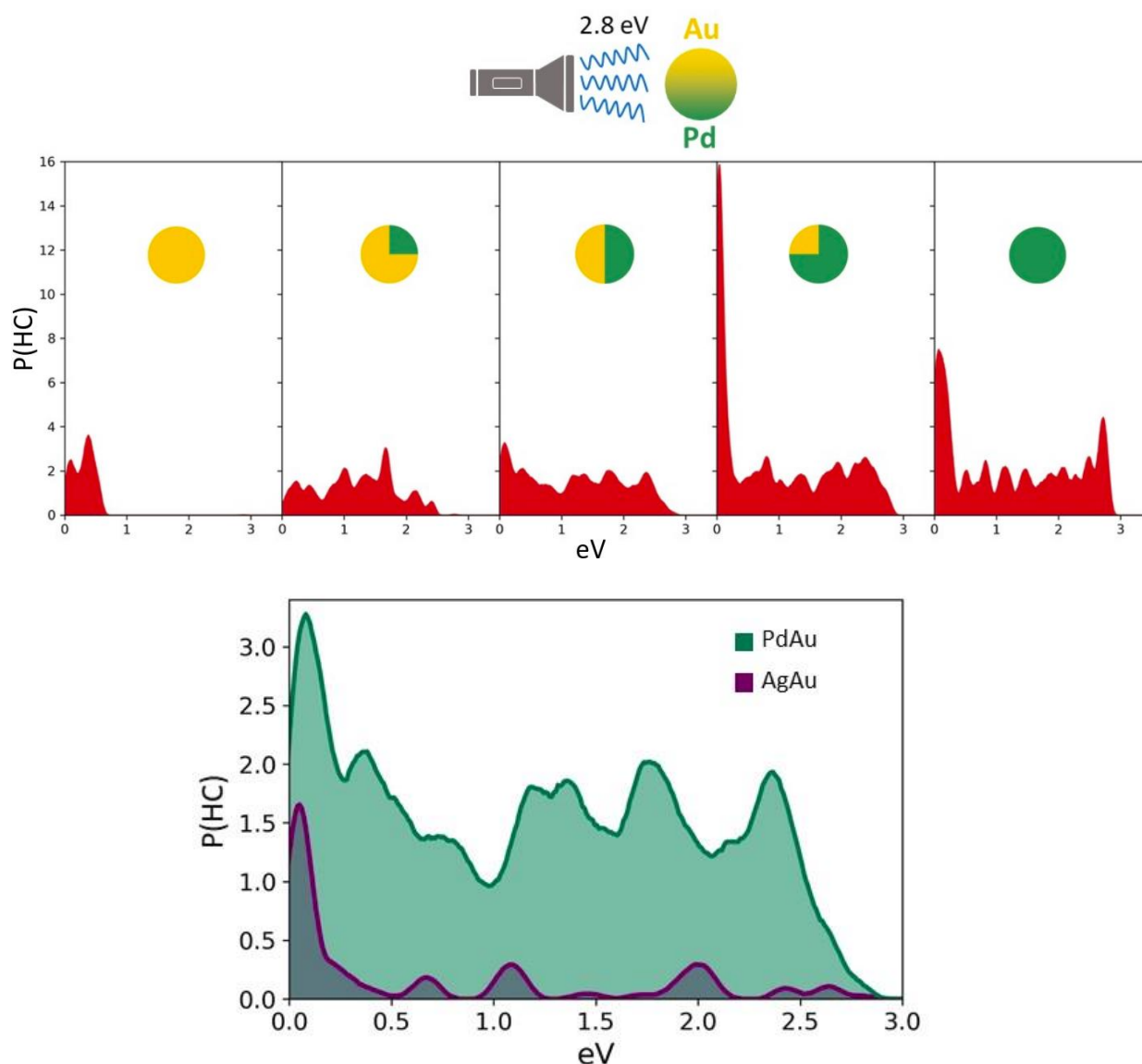


Figure 68. Top: Hot electron energy distributions (given in arbitrary units) obtained with a 2.8 eV excitation of Pd-Au systems ranging in composition from pure Pd to pure Au. The composition is varied in 25% increments. Bottom: Comparison of hot electron energy distributions obtained after 2.8 eV excitation of PdAu system (pale green) and AgAu system (purple). Fermi level is set to 0 eV.<sup>179</sup>

Hot electron energy distributions obtained by an  $\text{Au}_{0.5}\text{Ag}_{0.5}$  and an  $\text{Au}_{0.5}\text{Pd}_{0.5}$  system are compared in the bottom part of the Figure 68, showing approximately an order of magnitude increase in the hot electron production in the high-energy range when Pd is present instead of Ag. Alloying an open d-shell metal with a traditionally good plasmonic metal such as Au can therefore be considered as a potential strategy for increasing the efficiency of hot electron



production given a similar field enhancement. However, taking the change in the field enhancement into account presents a considerable caveat in maximizing the hot electron production. The increased availability of interband transitions around Fermi level as a result of increased DOS at that energy due to the presence of an open d-shell element also presents a very efficient plasmon decay channel. This causes quenching of the plasmonic response and, consequently, the reduction in the field enhancement. Since this can result in a lower amount of photons available for the absorption by the nanoparticle, the very same effect which would, (given the same field enhancement) be expected to increase the hot carrier generation, actually reduces the field enhancement and thus diminishes the the increase of, or even possibly adversely affects the generation of hot carriers. Hence, a tradeoff seems to exist between the amount of absorbed photons and the efficiency of using them for hot carrier generation and finding the satisfactory compromise (a “sweet spot”) is important. Aside from affecting the hot carrier generation, alloying open d-shell metals with closed d-shell metals could be used to expand the properties of plasmonic nanoparticles. Open d-shell metals are oftentimes good catalytic metals, with Pd and Pt being important examples. On the other hand, Au and Ag - good plasmonic metals - do not find as prominent use in traditional (non-plasmonic) catalysis. Thus, mixing a good (traditional) catalytic metal in an alloy with a good plasmonic metal opens the possibility of blending and utilizing both properties and expands the variety of nanoparticle functionality.

The differences in hot carrier distribution that appear upon alloying only closed d-shell metals and combining open and closed d-shell metals point to the ability to influence the hot carrier distribution by choosing elements of suitable electronic structure. However in all such cases fully or almost fully filled d-bands predominantly define the alloy properties. To expand upon the idea of connecting electronic structure to hot carrier distribution we also performed several case studies involving s and p-block elements.

#### *5.4.5. Effects of combining s-block and closed d-shell elements on hot carrier distribution*

Some experimental and several computational studies have, in the last couple of years, highlighted the promising plasmonic properties of the s-block elements<sup>180,181</sup>. The main factor preventing their utilization in practice is their poor chemical stability. However, alloying s-block elements with much more stable noble and coinage (filled d-shell) metals holds potential of stabilizing the atoms of s-block elements and lengthening the lifetime of metal

---

nanoparticles that contain them, in the same time making use of their good plasmonic properties.

Analysis of the DOS features characteristic of the s-block elements provides a basis for hypothesizing how they might influence the hot carrier distribution when alloyed with a filled d-shell element. In the relevant energy range, several eV around the Fermi level, the s-block elements have only the filled s-states, with unfilled s and p-states above the Fermi level. As exemplified by Na DOS, the density of unfilled states tends to rise with the rising energy above the Fermi level (Figure 69 a). Increasing number of unfilled states that electrons could be excited to at higher energies hints at the possibility of increasing the number of high energy hot electrons in an alloy containing Na. Keeping in mind that alloy DOS is not just a linear combination of the DOS of constituent metals, there is a reasonable correlation of the DOS features present for pure constituent metals and the DOS of their alloy. Closed d-shell metals exhibit a relatively flat and continuous DOS of unfilled states of s and p-character which can in part explain the (generally) continuous hot electron energy distribution without a clear trend of increase or decrease up to the photon energy. However, adding an element such as Na might result in a DOS skewed upwards at higher energies, and the consequent hot electron distribution that is also skewed towards higher energy electrons. To test whether such a rational engineering of hot carrier distribution is possible based on the knowledge of electronic structure a  $\text{Na}_8\text{Au}_4$  alloy system was chosen. Since Na and Au do not make a simple FCC-like substitutional alloy, as opposed to all the alloy unit cells used insofar, the unit cell that was used as a basis for calculation was created using a crystal structure that was experimentally found<sup>182</sup>. An added benefit to using a known crystal structure is in achieving better comparability to a real system.

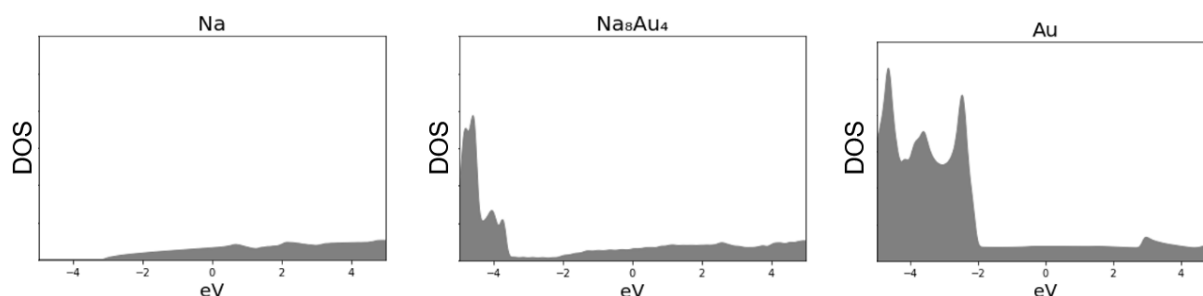


Fig 69. DOS calculated for pure Na (left),  $\text{Na}_8\text{Au}_4$  alloy (middle) and pure Au (right). Fermi level is set to 0 eV<sup>179</sup>

As can be seen from Figure 69, that hypothesis is indeed confirmed for the case of  $\text{Na}_8\text{Au}_4$  alloy system. The alloy indeed retains a skewed DOS towards higher energies. Additionally, it is visible that the d-band edge of the  $\text{Na}_8\text{Au}_4$  is much lower than the d-band edge of pure Au. Therefore, it is reasonable to assume that the d-band position can also be tuned by utilizing an alloy that contains s-block elements and d-block elements.

The hot electron distribution can be seen on the Figure 70. Further showing the importance of understanding the fundamental properties of metals to rationally influence the hot carrier energy distribution, it is visible that the range of hot electron distributions corresponding to photon energies in the visible and UV spectrum indeed do show skewness towards higher energies. A comparison with the hot electron energy distribution of the  $\text{Ag}_5\text{Au}_3$  alloy system (Figure 70 b) demonstrates the skewness when compared to the distribution obtained by an alloy of two closed d-shell metals. It can also be seen that the abundant generation of low energy carriers is not present for  $\text{Na}_8\text{Au}_4$  until rather high photon energies. Only at 3.8 eV (bottom right picture of Figure 70) the feature characteristic of transitions from the d-band edge appears, exactly coinciding with the d-band edge position from the DOS calculation shown in the Figure 69 b. This could be useful considering that the larger proportion of the absorbed photons is used to create high energy electrons instead of relatively low energy hot electrons, near the Fermi level. Thus, pushing the d-band further below the Fermi level by an addition of an s-block element could be another useful way to tune the hot carrier generation by alloying.

---

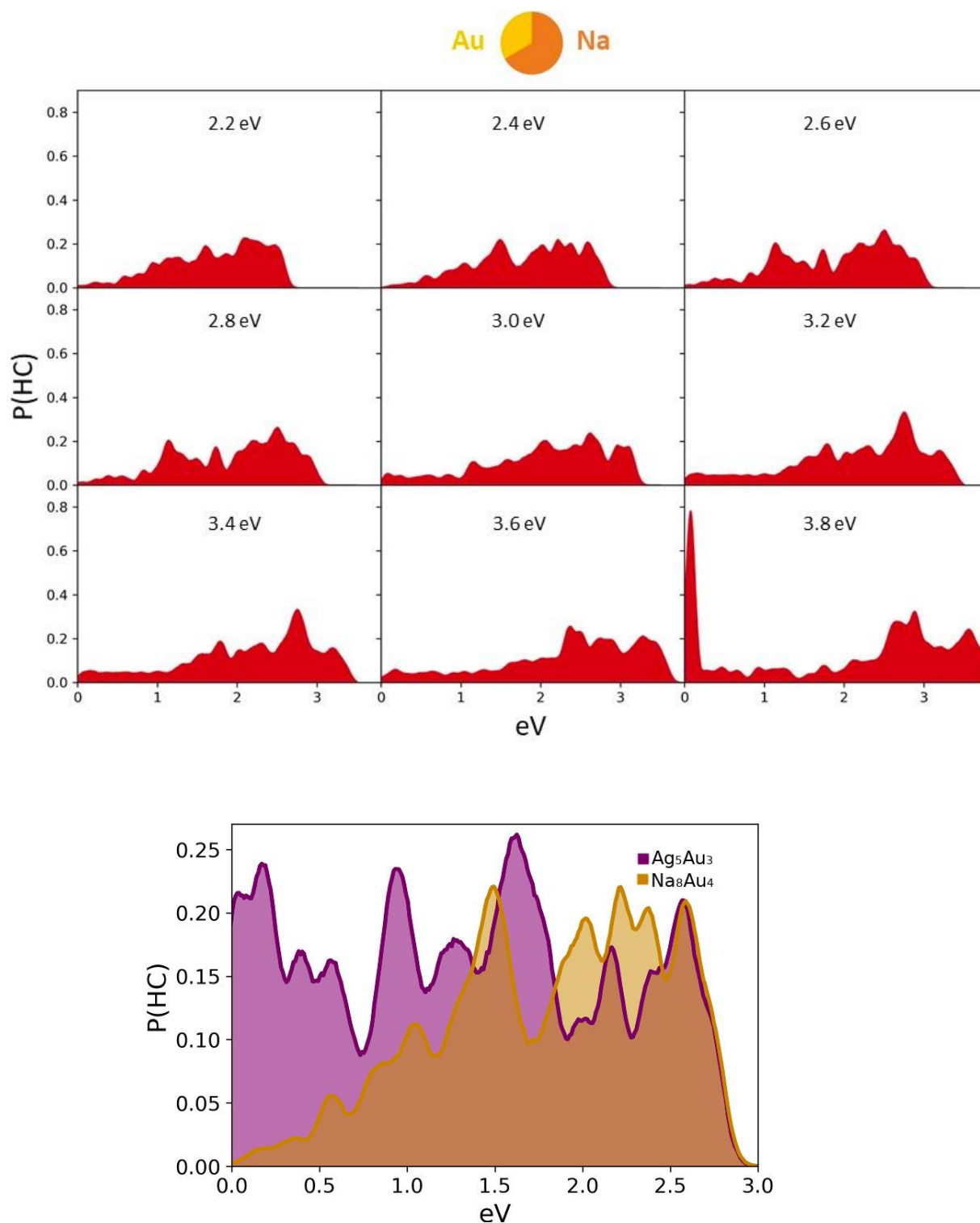


Figure 70. Hot electron energy distributions (in arbitrary units) calculated for excitation of  $\text{Na}_8\text{Au}_4$  alloy system with light of energy ranging from 2.2 eV to 3.8 eV with a 0.2 eV increments (top). Comparison of hot electron distributions obtained by 2.8 eV light for  $\text{Na}_8\text{Au}_4$  and  $\text{Ag}_5\text{Au}_3$  systems (bottom). Fermi level is set to 0 eV.<sup>179</sup>

#### 5.4.6. Effects of combining p-block and closed d-shell elements on hot carrier distribution

Out of p-block elements, Al is the by far the most utilized in plasmonics and seems to be the most promising one. For that reason, we chose to study Al in an alloy with Cu for a case study of p-block and closed d-shell element alloy. As for the case of  $\text{Na}_8\text{Au}_4$  a particular, experimentally determined, crystal structure was used to build the alloy system<sup>183</sup> since the substitutional FCC-like Cu-Al alloy structure only occurs in a very small composition range<sup>184</sup>. Although Al shows an increasing DOS towards the higher energies, the nontrivial nature of shaping the DOS by combining different elements becomes apparent in the Cu-rich  $\text{Cu}_6\text{Al}_2$  alloy. In this case, the features characteristic of Cu DOS are more apparent, both in the low energy range, with the prominent d-bands dominating the DOS, and even in the higher energy range, with slightly decreasing DOS followed by a small peak (near at about 4 eV for Cu and 3.5 eV for  $\text{Cu}_6\text{Al}_2$  alloy, Figure 71). However, the average DOS after the d-band edge is slightly higher in the alloy when compared to pure Cu DOS, which can likely be attributed to the influence of increased relative density of high-lying states of s and p-character contributed by the Al. However, similarly as for the alloy of an s-block element with a closed d-shell element, in this case the d-band edge is also lowered in comparison with the DOS of the pure d-block metal. While in the case of the  $\text{Na}_8\text{Au}_4$  the d-band edge was lowered by approximately 1.5 eV, in the case of  $\text{Al}_2\text{Cu}_6$  the shift is smaller, less than 1 eV. This might be attributed to the different ratios of the non-d-block element in the alloy and points to the possibility of finely tuning the d-band edge by elemental ratio. However, more research is needed to explore this possibility.

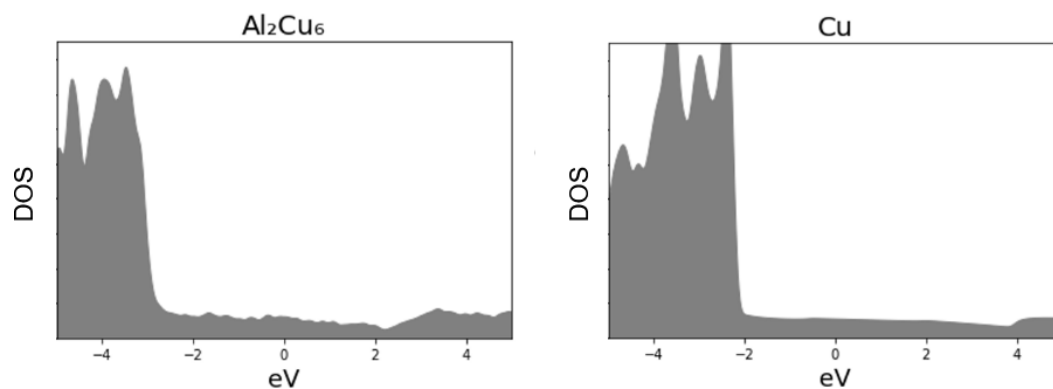


Figure 71. DOS calculated for pure Cu (left) and  $\text{Al}_2\text{Cu}_6$  alloy (right). Fermi level is set to 0 eV.<sup>179</sup>

It is visible from the Figure 72 that the resulting hot carrier distribution is more abundant than in case of mixing closed d-shell elements but less abundant than in case of open and closed d-shell elements mixing. The more abundant hot carrier generation can not, in this case, be ascribed to substantial density of high-lying d-states, but probably to higher relative density of sp-states. Furthermore, it is visible that the d-bands of Cu become lower upon alloying with Al (Figure 71). The alloy thus inherits the potential for asymmetry of hot hole and hot electron distribution that is characteristic for closed d-shell elements, with the possibility of tuning said asymmetry by the addition of Al.

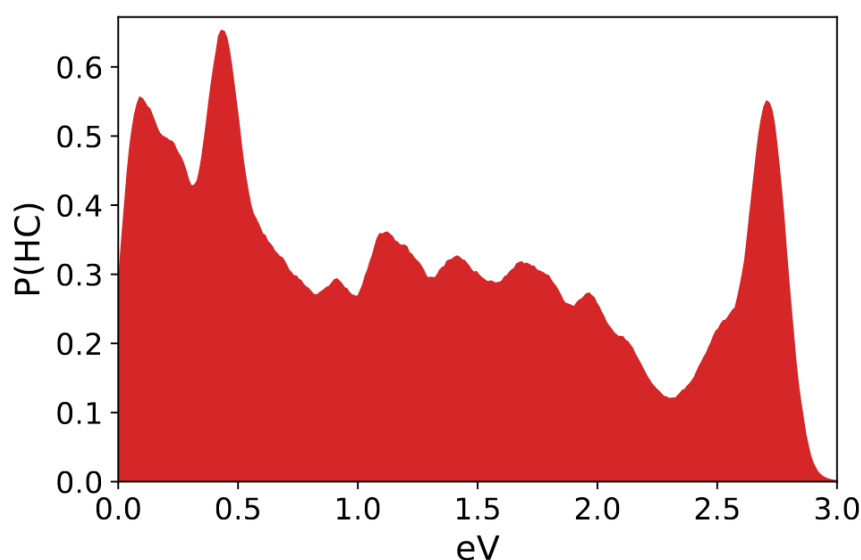


Figure 72 Hot electron energy distribution (in arbitrary units) for  $\text{Al}_2\text{Cu}_6$  alloy upon excitation with 2.8 eV light. Fermi level is set to 0 eV.<sup>179</sup>

The hot electron distribution obtained for the  $\text{Al}_2\text{Cu}_6$  system is, when compared to previous results, intermediately high (Figure 72.). The values are, on average, clearly higher than for the high energy distribution for  $\text{Na}_8\text{Au}_4$  and closed d-shell alloys, and clearly lower than for the abundant generation at lower energies attributed to the d-sp transitions in closed d-shell alloys, as well as the energy distribution in the entire range for the Pd-Au alloys. Since the d-band edge lies a bit below the 2.8 eV, which is chosen as the photon energy in this case, the intermediate hot carrier energy distribution can be attributed to a higher relative density of the s and p-states due to presence of Al, when compared to pure Cu. Alloying Al with a closed d-shell element such as Cu thus presents a way to achieve intermediate hot electron distribution when d-bands are not involved, with an abundant high energy hot hole and low energy hot

electron generation likely present for photon energies higher than the depth of the d-band edge.

#### 5.4.7. Effects of combining p-block and open d-shell elements on hot carrier distribution

As an example of open d-shell and p-block element alloy, an  $\text{Al}_3\text{Pd}_2$  system was chosen<sup>185</sup>. The combined DOS shows a very interesting behavior, with the feature that can be identified as a d-band edge lying far (more than 3 eV) below the Fermi level, although for the pure Pd, the d-band edge crosses the Fermi level. The DOS above the d-band edge is generally higher than in the case of d-shell metals studied insofar, possibly due to the influence of states primarily attributed to Al.

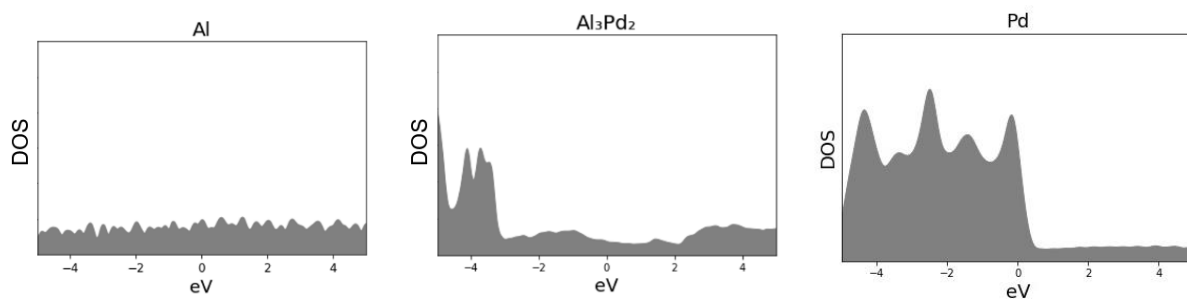


Figure 73. DOS for Al (left),  $\text{Al}_3\text{Pd}_2$  (middle) and Pd (right). Fermi level is set to 0 eV.<sup>179</sup>

The hot electron distribution (Figure 74) of  $\text{Al}_3\text{Pd}_2$  system obtained for 2.8 eV photon excitation can be roughly classified as an intermediately high, similarly to the case of  $\text{Al}_2\text{Cu}_6$ , with the main difference being the increase in the hot electron production at higher energies.

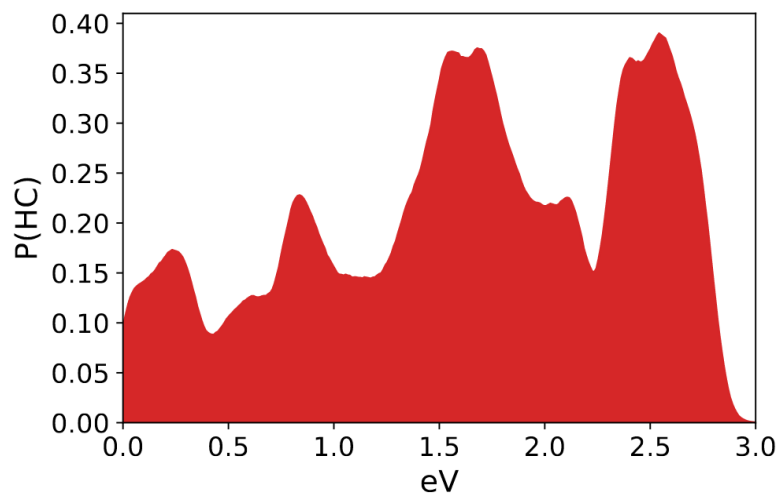


Figure 74. Hot electron energy distribution (in arbitrary units) for  $\text{Al}_3\text{Pd}_2$  alloy upon excitation with 2.8 eV light. Fermi level is set to 0 eV.<sup>179</sup>

In general, it seems that mixing Al, a p-block element with the d-block elements, both closed and open shell, leads to a lowering of the d-band edge, especially prominent for the open d-shell element such as Pd, and to a slight increase in the DOS above the d-band edge. The resulting hot carrier distribution is thus intermediately high. The strong downward shift of the d-band edge observed for the  $\text{Al}_3\text{Pd}_2$  system implies that the optical losses due to interband transitions become weaker in the large part of the relevant energy range, since the contribution of abundant transitions starting from the d-bands is not present. Since this very fact disqualified Pd and Pt from being good plasmonic metals, alloying with Al might present an opportunity for reintroducing these metals, as well as others with similar characteristics, to plasmonic applications. Lowering the average cost of material by intermixing Al with these pricy metals further highlights the potential of such alloys for plasmonic applications, and highlights the need for future investigation.



## § 6. CONCLUSION

In this work a computational framework for efficient determination of optical and plasmonic properties of alloys has been established. A special attention was given to the choice of the exchange-correlation functional in several steps of the computational scheme: First in the optimization procedure, where PBEsol was chosen over PBE, and the importance of the proper choice was shown since even small differences in lattice parameters affect the interband transition onset of the pure metals. Afterwards, in the benchmarking on dielectric functions of pure metals where GLLB-SC performed the best. Finally, for alloyed systems and for calculation of both dielectric functions and properties related to the electronic structure, where GLLB-SC was shown to be universally better than the standardly used PBE.

A database of dielectric functions for several binary alloy systems was produced and compared to experimentally available data. It was shown that the DFT-based approach can be qualitatively very good, predicting the trends well but in some cases lacking quantitative agreement with the experimental data. Nonetheless, the results are very well suited as a basis for screening, and can serve as a good guideline for experiment design. Furthermore, emergent properties of alloying, helping explain the increased optical losses in the infrared, have also been predicted, showing that the DFT approach helps elucidate the origin of puzzling experimental observations.

Optical and plasmonic properties of different nanostructures were simulated for the Au-Ag alloy system based on the results of the calculations and the empirical data. The ability of GLLB-SC to better predict the position of the d-bands and the corresponding onset of interband transitions between the upper d-band edge and the unfilled states in the conduction bands was shown to have an outsized influence on the quality of prediction of optical and plasmonic properties, with PBE in some cases failing almost to qualitatively predict the results. GLLB-SC enables qualitative prediction of the trends relatively well, although there are quantitative discrepancies with the experiment-based data in most cases. Overall, based on the results, this work highlights GLLB-SC as the same-cost alternative to the PBE and the potential new standard in for efficient calculations in the field of plasmonics.

---

Newly allowed interband transitions were identified as the reason for the increase of optical losses in the infrared region, providing connection with the electronic structure of the alloy. This connection was further explored by calculating the DOS and the band structures for studied alloys. Band splitting and folding due to alloying was presented as the reason for the emergent interband transitions. These results show that the traditional considerations of interband transition onset for alloys of Cu, Ag, and Au moving with the upper edge of the d-band position is not valid, since there are allowed interband transitions between split and folded conduction bands present at much lower energies, extending into IR. Furthermore, it was shown that these conduction bands have a considerable amount of d-orbital character near the Fermi energy even though the nominal d-band edge lies one or more eV below the Fermi energy. The distance of the d-band edge from the Fermi energy was shown to correlate with the amount of the d-character in the conduction bands, as well as the total DOS at the Fermi energy. Tying to that observation, alloying was shown to provide a tunability of the d-band edge in the range defined by the d-band edges of the constituent elements. This shift is smooth and gradual in the case of alloys of closed d-shell elements, and more abrupt and nonlinear when Pd, an open d-shell metal (in its bulk state) is present in the alloy. This points to classification of the metals by their electronic structure as a suitable approach to rationally design the alloy properties.

Effects of unit cell configuration on the dielectric function and the electronic structure were shown to be relatively minor for the studied substitutional binary alloys. The effects of modeling disorder by the use of large SQS structures were obtained indirectly, by comparing small unit cells used in this work and large SQS of the same stoichiometry used in the literature, with very similar results obtained by both methods. Therefore it can be concluded that the small unit cells offer a good ratio of accuracy and efficiency and are suitable for studies involving a large number of alloyed systems aimed for exploring a vast composition space.

By connecting the findings, a multilayered structure-property relationship was created by linking the alloy structure, the corresponding electronic structure of the material and the resulting optical and plasmonic properties.

Due to the implications of low energy interband transitions unlocked by alloying, and by using the conceptual framework of classifying the elements by their electronic structure, the effects of alloying on the hot carrier energy distributions were studied. Alloys of two

---

closed d-shell metals exhibited asymmetrical abundant hot carrier generation due to transitions from the d-band to conduction bands, with very energetic hot holes and less energetic hot electrons created. This feature of hot carrier generation was tunable by alloy composition due to shift in the d-band position. Additionally, a more symmetrical and continuous scarce hot carrier generation was observed and explained by band folding and splitting. The importance of this feature lies in the creation of high energy hot electrons, up to the photon energy.

A much more abundant hot carrier energy distribution is obtained for an alloy of open and closed d-shell metals due to much higher DOS particularly due to high-lying d-states, crossing the Fermi level. However, this also introduces an efficient decay pathway that could result in plasmon quenching.

Mixing s and p-shell metals with both open and closed d-shell metals seems to lower the d-band edge with respect to the Fermi level. This can be used as a way to tune the amount of asymmetric and abundant hot carrier generation characteristic for transitions starting from the d-bands, and is especially interesting as a way to tune the properties of open d-shell elements. The hot carrier generation that involves conduction bands is relatively scarce but skewed towards higher energy electrons in the case of the Na-Au alloy system that was studied. Said observations could be useful for utilizations that benefit mostly from very high energy hot electrons such as injection into semiconductors with a high Schottky barrier and high energy molecular orbitals. Hot carrier energy distribution resulting from conduction bands in alloys with Al, a p-shell metal and both open and closed d-band metals was of intermediate value. Overall, the findings provide way to match the metals, categorized by their electronic structure, to create alloys of desired hot carrier distribution, or in other words, a deliberate hot carrier distribution engineering.

---

## § 7. LIST OF ABBREVIATIONS

CPA	Coherent potential approximation
DFT	Density functional theory
DOS	Density of states
FCC	Face centered cubic
GS	Gustoća stanja
HC	Hot carrier
IC	Infracrveno
IR	Infrared
JDOS	Joint density of states
PAW	Projector augmented wave
PDOS	Projected density of states
RPA	Random phase approximation
SPP	Surface plasmon polariton
VNN	Vrući nosioci naboja

---

## § 8. REFERENCES

1. S. Hayashi and T. Okamoto, *Journal of Physics D: Applied Physics* **45** (2012) 433001
  2. N. J. Halas, *PNAS* **106** 3643-3644
  3. Q. Duan, Y. Liu, S. Chang, H. Che, and J.-h. Chen, *Sensors* **21** (2021) 5262
  4. J. Leuthold, C. Hoessbacher, S. Muehlbrandt, A. Melikyan, M. Kohl, C. Koos, W. Freude, V. Dolores-Calzadilla, M. Smit, I. Suarez, J. Martínez-Pastor, E.P. Fitrakis, and I. Tomkos, *Optics & Photonics News* **24** (2013) 28-35
  5. J. B. Khurgin and G. Sun, *Applied Physics Letters* **96** (2010) 181102
  6. P. R. West, S. Ishii, G. V. Naik, N. K. Emani, V. M. Shalaev and A. Boltasseva, *Laser & Photonics Reviews* **4** (2010) 795-808
  7. S. V. Boriskina, T. A. Cooper, L. Zeng, G. Ni, J. K. Tong, Y. Tsurimaki, Y. Huang, L. Meroueh, G. Mahan and Gang Chen, *Advances in Optics and Photonics* **9** (2017) 775-827
  8. Y. Hattori, J. Meng, K. Zheng, A. M. de Andrade, J. Kullgren, P. Broqvist, P. Nordlander and J. Sá, *Nano Letters* **21** (2021) 1083-1089
  9. H. Tang, C.-J. Chen, Z. Huang, J. Bright, G. Meng, R.-S. Liu and N. Wu, *The Journal of Chemical Physics* **152** (2020) 220901
  10. A. O. Govorov, H. Zhang and Y. K. Gun'ko, *Journal of Physical Chemistry C* **117** (2013) 16616–16631
  11. Y. Sun and Z. Tang, *MRS Bulletin* **45** (2020) 20-25
  12. M. L. Brogersma, N. J. Halas and P. Nordlander, *Nature Nanotechnology* **10** (2015) 25-34
  13. I. Fabijanić, V Janicki, J. Ferré-Borrull, M Bubaš, V. B. Bregović, L. F. Marsal and J. S. Parramon, *Coatings* **9** (2019) 382
  14. J. R. Cole, N. A. Mirin, M. W. Knight, G. P. Goodrich and N. J. Halas *Journal of Physical Chemistry C* **113** (2019) 12090–12094
  15. Y. Zhang, C. Min, X. Dou, X. Wang, H. P. Urbach, M. G. Somekh and X Yuan *Light: Science & Applications* **10** (2021) 59
  16. S.A. Mezzasalma, J. Kruse, S. Merkens, E. Lopez, A. Seifert, R. Morandotti and M. Grzelczak, *Advanced Materials* **35** (2023) 2302987
  17. R. Hoffman, *Solids and Surfaces: A Chemist's View of Bonding in Extended Structures*, Wiley-VCH, New York, 1991, str. 3-20
  18. K. Fujii, *Semiconductors and Semimetals* **97** (2017) 139-183
  19. P. Hohenberg and W. Kohn, *Physical Review* **136** (1964) 864-871
  20. W. Kohn and L. J. Sham, *Physical Review* **140** (1965) A1133-A1138.
  21. J. P. Perdew and K. Schmidt, *AIP Conference Proceedings* **577** (2001) 1-20
  22. P. Borlido, T. Aull, A. W. Huran, F. Tran, M. A. L. Marques and S. Botti, *Journal of Chemical Theory and Computation* **15** (2019) 5069-5079
-

23. J. P. Perdew, R. G. Parr, M. Levy and J. L. Balduz, Jr, *Physical Review Letters* **49** (1982) 1691-1694
  24. J. P. Perdew and M. Levy, *Physical Review Letters* **51** (1983) 1884-1887
  25. P. E. Blöchl, C. J. Först and J. Schimpl, *Bulletin of Materials Science*, **26** (2006) 33-41
  26. P. E. Blöchl *Physical Review B* **50** (1994) 17953-17979
  27. C. Rostgaard, arXiv:0910.1921 [cond-mat.mtrl-sci]
  28. G. Mie, *Annalen der Physik*, **25** (1908) 377-445
  29. C. F. Bohren and D. R. Huffman, John Wiley & Sons, 2008.
  30. V. Myroshnychenko, J. Rodríguez-Fernández, I. Pastoriza-Santos, A.M. Funston, C. Novo, P. Mulvaney, L.M. Liz-Marzán and F. J. De Abajo, *Chemical Society Reviews* **37** (2008) 1792-1805
  31. F. G. De Abajo, and A. Howie, *Physical Review B* **8** (2002) 115418.
  32. U. Hohenester and A. Trügler, *Computer Physics Communications* **183** (2012) 370-381
  33. J.M. Gérardy and M. Ausloos *Physical Review B* **25** (1982) 4204
  34. S. A. Maier, *Plasmonics: fundamentals and applications*, Springer, New York 2007 22-45
  35. H. Wang, H. Li, S. Xu, B. Zhao and W. Xu, *Scientific Reports* **7** (2017) 14630
  36. S. D. Rezaei, J. Ho, R. J. H. Ng, S. Ramakrishna, and J. K. W. Yang, *Optics Express* **25** (2017) 27652-27664
  37. Q. Duan, Y. Liu, S. Chang, H. Chen and J.-h. Chen, *Sensors* **21** (2021) 5262
  38. J.-F. Masson, *ACS Sensors* **2** (2017) 16-30
  39. Commercializing plasmonics, *Nature Photonics* **9** (2015) 477
  40. P. Moitra, M. Alafeef, K. Dighe, M. B. Frieman and D. Pan, *ACS Nano* **14** (2020) 7617–7627
  41. D. Quesada-González and M. A., *Biosensors & bioelectronics* **73** (2015) 47–63
  42. P. Estrela, K. M. Koczula and A. Gallotta, *Essays in Biochemistry* **60** (2016) 111–120
  43. H. S. Han and K. Y. Choi, *Biomedicines* **9** (2021) 305
  44. A. R. Rastinehad, H. Anastos, E. Wajswol, J. S. Winoker, J. P. Sfakianos, S. K. Doppalapudi, M. R. Carrick, C. J. Knauer, B. Taouli, S. C. Lewis, A. K. Tewari, J. A. Schwartz, S. E. Canfield, A. K. George, J. L. West, N. J. Halas, *PNAS* **116** (2019) 18590–18596
  45. A. Y. Lin, E. Yang, J. S. Rink, D. Xu, S. Miller, L. I. Gordon, *Blood* **142** (2023) 2825
  46. A. Pujari T. Tomas, *Sustainable Materials and Technologies* **27** (2021) e00250
  47. X. Geng, M. Abdellah, R. B. Vadell, M. Folkenant, T. Edvinsson and J. Sá, *Nanomaterials* **11** (2021) 3329
  48. Z. C. Su, C. H. Chang, J.-C. Jhou, H.-T. Lin and C.-F. Lin, *Scientific Reports* **13** (2023) 5388
  49. K. H. W. Ho, A. Shang, F. Shi, T. W. Lo, P. H. Yeung, Y. S. Yu, X. Zhang, K.-y. Wong and D. Y. Lei, *Advanced Functional Materials*, **28** (2018) 1800383
  50. S. Cantero-Palacios, A. Jiménez-Solano and H. Míguez, *ACS Energy Letters* **1** (2016) 323-331
  51. D. Zhang, W. C. H. Choy, F. Xie, W. E. I. Sha, X. Li, B. Ding, K.i Zhang, F. Huang and Y. Cao, *Advanced Functional Materials*, **23** (2013) 4255-4261
  52. M. A. Alkhalayfeh, A. Abdul Aziz, M. Z. Pakhuruddin, *Renewable and Sustainable Energy Reviews*, **141** (2021) 110726
  53. N. J. Halas, *Faraday Discussions* **214** (2019) 13-33
  54. E. A. Monyoncho, M. Dasog, *Advanced Energy and Sustainability Research* **2** (2021) 2000055
-

- 
55. A. Marimuthu, J. Zhang and S. Linić, *Science* **339** 1590-1593
  56. V.-H. Nguyen, B.-S. Nguyen, Z. Jin, M. Shokouhimehr, H. W. Jang, C.a Hu, P. Singh, P. Raizada, W. Peng, S. S. Lam, C. Xia, C. C. Nguyen, S. Y. Kim, Q. V. Le, *Chemical Engineering Journal*, **402** (2020) 126184
  57. K. Kołataj, J. Krajczewski and A. Kudelski, *Environmental Chemistry Letters*, **18** (2020) 529-542
  58. S. Lal, S. Link, N. Halas, *Nanoscience and Technology*, (2019) 213-220
  59. D. K. Gramotnev and S. I. Bozhevolnyi, *Nature Photonics* **4** (2010) 83-91
  60. C. Kim, C. Favazza and L. V. Wang, *Chemical Reviews* **110** (2010) 2756–2782
  61. Y. Cheng, A. C. Samia, J. D. Meyers, I. Panagopoulos, B. Fei and C. Burda, *Journal of American Chemical Society* **130** (2008) 10643-10647
  62. K.-C. Lee, S.-J. Lin, C.-H. Lin, C.-S. Tsai, Y.-J. Lu, *Surface and Coatings Technology* **202** (2008) 5339-5342
  63. L. K. Sørensen, D. E. Khrennikov, V. S. Gerasimov, A. E. Ershov, S. P. Polyutov, S. V. Karpov and Hans Ågren, *Journal of Physical Chemistry C* **126** (2022) 39
  64. U. Kreibig, M. Vollmer, *Optical Properties of Metal Clusters*, Springer Series in Materials Science page. 30
  65. F. Benz, R. Chikkaraddy, A. Salmon, H. Ohadi, B. de Nijs, J. Mertens, C. Carnegie, R. W. Bowman and J. Baumberg, *Journal of Physical Chemistry Letters* **7** (2016) 2264-2269
  66. R. S. Geonmonond, A. G. M. da Silva, T. S. Rodrigues, I. C. de Freitas, R. A. Ando, T. V. Alves, P. G. C. Camargo, *ChemCatChem* **10** (2018) 3447-3452
  67. A. R. Shafiq, A. A. Aziz and B Mehrdel, *Journal of Physics: Conference Series* **1083** (2018) 012040
  68. P. K. Jain, K. S. Lee, I. H. El-Sayed and M. A. El-Sayed, *Journal of Physical Chemistry B* **110** (2006) 7238–7248
  69. A. Manjavacas, J. G. Liu, V. Kulkarni and P. Nordlander, *ACS Nano* **8** (2018) 7630–7638
  70. A. M. Brown, R. Sundararaman, P. Narang, W. A. Goodard 3rd, H. A. Atwater, *ACS Nano* **10** (2016) 957-966
  71. W, Cao, T. Huang, X.-H. N. Xu and H. Elsayed-Ali, *Journal of Applied Physics* **109** (2011) 034310
  72. H.-P. Liang, L.-J. Wan, C.-L. Bai and L. Jiang, *Journal of Physical Chemistry B* **109** (2005) 7795–7800
  73. Genç, J. Patarroyo, J. Sancho-Parramon, R. Arenal, M. Duchamp, E. E. Gonzalez, L. Henrard, N. G. Bastús, R. E. Dunin-Borkowski and V. F. Puntes and Jordi Arbiol, *ACS photonics* **3** (2016) 770–779
  74. D. Radziuk and H. Moehwald, *Physical Chemistry Chemical Physics* **17** (2015) 21072-21093
  75. S. A. Mezzasalma, M. Grzelczak, J. Sancho-Parramon, *ACS Photonics* **7** (2020) 1551-1559
  76. H. Yockell-Lelièvre, F. Lussier and J.-F. Masson, *Journal of Physical Chemistry C* **119** (2015) 28577–2858
  77. Ángela I. López-Lorente, *Analytica Chimica Acta* **1168** (2021) 338474
  78. T. P. Rossi, P. Erhart and M. Kuisma, *ACS Nano* **14** (2020) 9963–9971
  79. D. Chahinez, T. Reji and R. Andreas, *RSC Advances* **8** (2018) 19616
  80. R. D. Babli Debnath, *Spectrochimica Acta Part A: Molecular and Biomolecular Spectroscopy* **249** (2021) 119306
-

81. A. Mizuno and A. Ono, *ACS Applied Nano Materials* **4** (2021) 9721–9728
  82. H. Cha, D. Lee, J. H. Yoon and S. Yoon *Journal of Colloid and Interface Science* **464** (2016) 18-24
  83. S. Kessentini, D. Barchiesi, C. D'Andrea, A. Toma, N. Guillot, E. D. Fabrizio, B. Fazio, O. M. Maragó, P. G. Gucciardi and M. L. de la Chapelle, *Journal of Physical Chemistry C* **118** (2014) 3209–3219
  84. J. H. Kim, J. Y. Lee, E. S. Kim and M. Y. Jeong, *PhotonIX*, **4** (2023) 8
  85. K. L. Kelly, E. Coronado, L. L. Zhao and G. C. Schatz, *Journal of Physical Chemistry B* **107** (2003) 668-677
  86. N. Fukoka and K. Tanabe, *Nanomaterials* **9** (2019) 1235
  87. H. Yu, Y. Peng, Y. Yang and Z.-Y. Li, *npj Computational materials*, **5** (2019) 45
  88. U. Guler, V. M. Shalaev and A. Boltasseva, *MaterialsToday* **18** (2015) 227-237
  89. B. Doiron, M. Mota, M. P. Wells, R. Bower, A. Miah, Y. Li, L. F. Cohen, N. McN. Alford, P. K. Petrov, R. F. Oulton and S. A. Maier, *ACS Photonics*, **6** (2019) 240-259
  90. A. Moores and F. Goettmann, *New Journal of Chemistry* **30** (2006) 1121–1132
  91. S. Eustis and M. A. El-Sayed, *Chemical Society Review* **35** (2005) 209–217
  92. M. B. Cortie and A. M. McDonagh, *Chemical Reviews* **111** (2011) 3713–3735
  93. M. Bubaš, V. Janicki, S. A. Mezzasalma, M. C. Spadaro, J. Arbiol, J. Sancho-Parramon, *Applied Surface Science* **564** (2021) 1520260
  94. M. Bubaš, I. Fabijanić, A. Kendel, S. Miljanić, M. C. Spadaro, J. Arbiol, V. Janicki, J. Sancho-Parramon, *Sensors and Actuators B: Chemical* **380** (2023) 133326
  95. T. Gong and J. N. Munday, *Optical Materials Express* **5** (2015) 2501-2512
  96. L. J. Krayner, K. J. Palm, C. Gong, A. Torres, C. E. P. Villegas, A. R. Rocha, M. S. Leite and J. N. Munday, *ACS Photonics* **7** (2020) 1689–1698
  97. J. G. Liu, H. Zhang, S. Link, P. Nordlander, *ACS Photonics* **5** (2018) 2584–2595
  98. P. Narang, R. Sundararaman and H. Atwater, *Nanophotonics* **5** (2016) 96-111
  99. O. A. Douglas-Gallardo, M. Berdakin, T. Frauenheim and C. Sánchez, *Nanoscale* **11** (2019) 8604-8615
  100. C. Sánchez and M. Berdakin, *Journal of Physical Chemistry C* **126** (2022) 10015–10023
  101. M. Zhang, H. Xiang, X. Zhang and G. Lu, *Journal of Physics: Condensed Matter* **28** (2016) 155302
  102. M. Pogodaeva, S. V. Levchenko, V. P. Drachev, I. R. Gabitov, *Journal of Physics: Conference Series* **1890** (2021) 012008
  103. R. Sundararaman, P. Narang, A. S. Jarmyn, W. A. Goddard 3rd and Harry Atwater, *Nature Communications* **5** (2014) 5788
  104. X. Blase, I. Duchemin, D. Jacquemin and P.-F. Loos, *Journal of Physical Chemistry Letters* **11** (2020) 7371–7382
  105. M. Bernardi, J. Mustafa, J. B. Neaton and S. G. Louie, *Nature Communications* **6** (2015) 7044
  106. T. Rangel, D. Kecik, P. E. Trevisanutto, G.-M. Rignanese, H. Van Swygenhoven and V. Olevano, *Physical Review B*, **86** (2012) 125125
  107. B. Himmetoglu, A. Floris, S. de Gironcoli and M. Cococcioni, *International Journal of Quantum Chemistry* **114** (2014) 14-49
  108. I.-B. Lin, T. W.-H. Sheu and J.-H. Li, *Optics Express* **25** (2014) 30725-30734
-

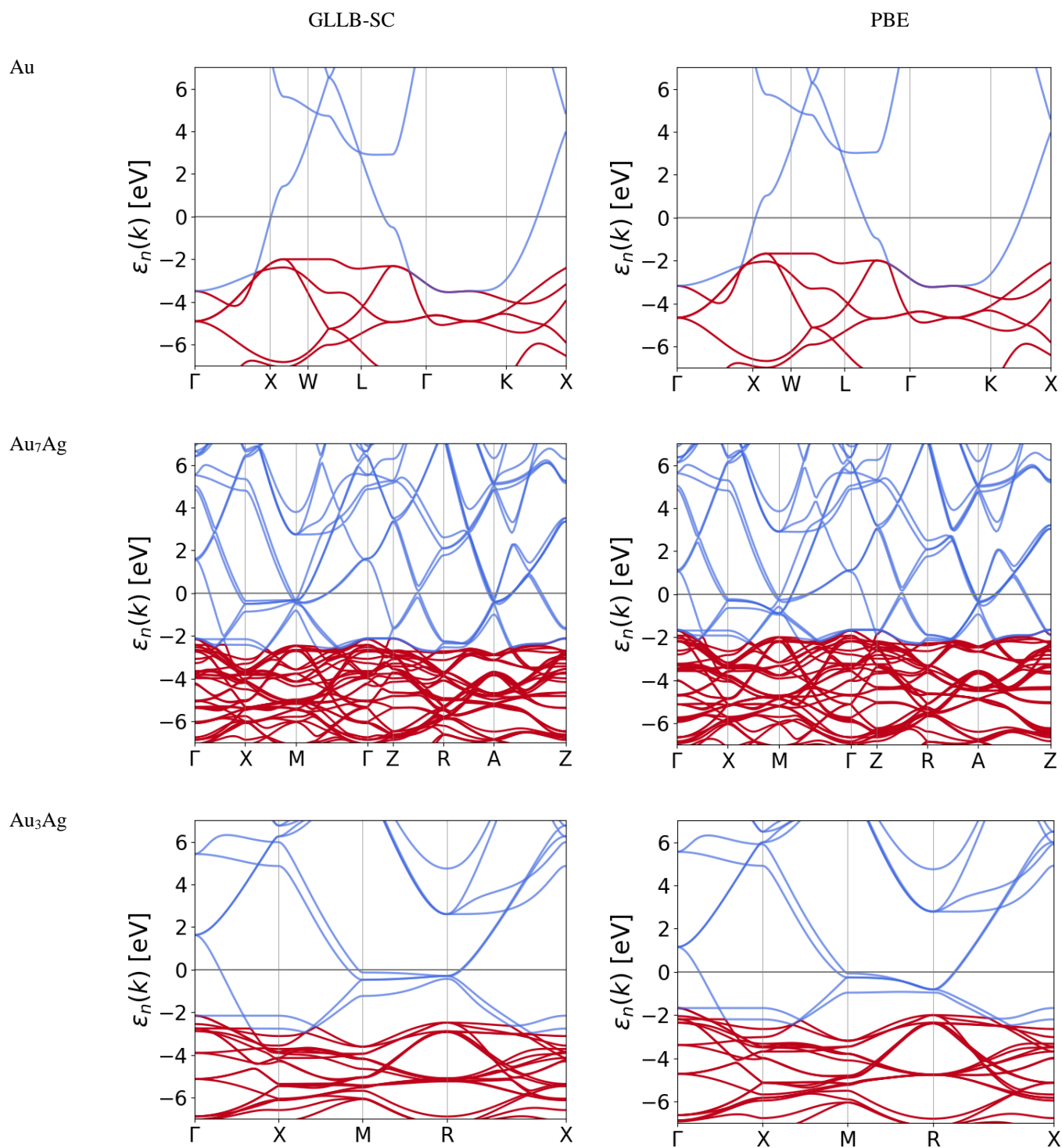


- 
109. M. Kuisma, A. Sakko, T. P. Rossi, A. H. Larsen, J. Enkovaara, L. Lehtovaara and T. T. Rantala, *Physical Review B* **91** (2015) 115431
  110. J. Yan, K. W. Jacobsen and K. S. Thygesen, *Physical Review B* **84** (2011) 235430
  111. J. Yan and K. S. Thygesen, *Physical Review B* (2012) **86** 241404
  112. O. Gritsenko, R. van Leeuwen, E. van Lenthe and E. J., *Physical Review A* **51** (1995) 1944
  113. M. G. Blaber, M. D. Arnold and M. J. Ford, *Journal of Physics: Condensed Matter* **21** (2009) 144211
  114. V. J. Keast, K. Birt, C.T. Koch, S. Supansomboon, M. B. Cortie, *Applied Physics Letters* **99** (2011) 111908
  115. M. G. Blaber, M. D. Arnold and M. J. Ford, *Journal of Physics: Condensed Matter* **22** (2010) 095501
  116. V. J. Keast, R. L. Barnett and M. B. Cortie, *Journal of Physics: Condensed Matter* **26** (2014) 305501
  117. M. Kumari and U. P. Verma, *Journal of Magnesium and Alloys* **5** (2017) 454-459
  118. G. Prandini, G.-M. Riganese and N. Marzari, *npj Computational Materials* **5** (2019) 129
  119. J. Rivory, *Journal de Physique Colloques* **35** (1974) C4-51-C4-56
  120. K. S. B. De Silva, A. Gentle, M. Arnold, V. J. Keast and M. B. Cortie, *Journal of Physics D: Applied Physics* **48** (2015) 215304
  121. L. K. Skriver and H. P. Lengkeek, *Physical Review B* **19** (1979) 900-910
  122. W. R. Scott and L. Muldrew, *Physical Review B* **14** (1976) 4426-4430
  123. Köster, W. and R. Stahl, *Zeitschrift für Metallkunde* **58** (1967) 768
  124. A. Zunger, S.-H. Wei, L.G. Ferreira and J. E. Bernard, *Physical Review Letters*, **65** (1990) 353
  125. Z.W. Lu, S.-H. Wei and A. Zunger, *Physical Review B* **44** (1991) 19
  126. A. van Walle, P. Tiwary, M. de Jong, D. L. Olmsted, M. Asta, A. Dick, D. Shin, Y. Wang, L.-Q. Chen and Z. K. Liu, *Calphad* **42** (2013) 13-18
  127. L. Bellaiche and D. Vanderbilt, *Physical Review B* **61** (2000) 7877
  128. S. Wang, J. Xiong, D. Li, Q. Zeng, M. Xiong and X. Chai, *Materials Letters* **282** (2021) 128754
  129. J. Banhart, *Physical Review Letters* **82** (1999) 2139
  130. S. J. Oh and T.-U. Nahm, *Journal of Electron Spectroscopy and Related Phenomena* **78** (1996) 43-48
  131. S. K. F. Stofela, O. Kizilkaya, B. T. Diroll, T. R. Leite, M. M. Taheri, D. E. Willis, J.n B. Baxter, W. A. Shelton, P. T. Sprunger and K. M. McPeak, *Advanced Materials* **32** (2020) 1906478
  132. Y. Zhang, G. M. Stock, K. Jin, C. Lu, G. Bei, B. C. Sales, L. Wang, L. K. Béland, R. E. Stoller, G. D. Samolyuk, M. Caro, A. Caro and W. J. Weber, *Nature Communications* **6** (2015) 8736
  133. I. M. Lifshitz, *Soviet Physics Uspekhi* **7** (1964) 549-573
  134. V. Popescu and A. Zunger, *Physical Review B* **85** (2012) 085201
  135. S. G. Mayo, F. Yndurain and Jose M. Soler, *Journal of Physics: Condensed Matter* **32** (2020) 205902
  136. C. Gong, A. Kaplan, Z. A. Benson, D. R. Baker, J. P. McClure, A. R. Rocha and M. S. Leite, *Advanced Optical Materials* **6** (2018) 1800218
  137. B. Ginatempo, G.Y. Guo, W.M. Temmerman, J.B. Staunton and P.J. Durham, , Volume **42**, (1990) 5
  138. R. Stahl, H.-J. Spranger and H.-P. Auba, *Zeitschrift für Metallkunde* **60** (1969) 933
  139. P.-O. Nilsson and C. Norris, *Physics Letters A* **29** (1969) 22
  140. Y. Zhang, *Journal of Physical Chemistry A* **125** (2021) 9201–9208
  141. L. Ranno, S. Dal Forno, J. Lischner, *npj Computational Materials* **4** (2018) 31
-

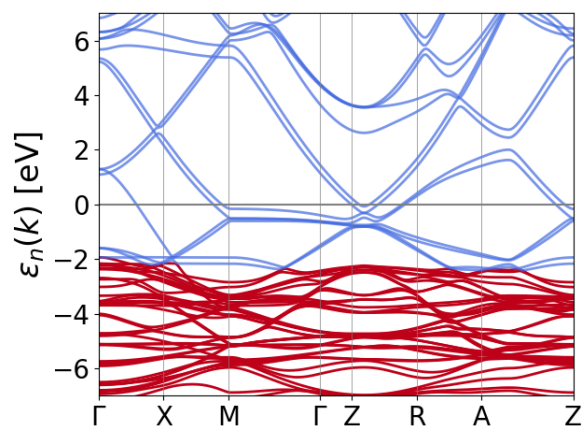
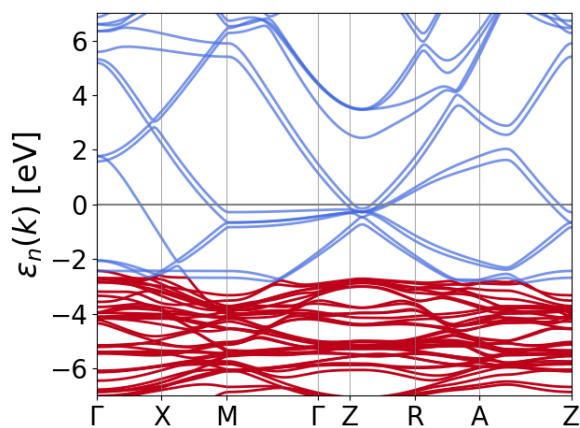
- 
142. M. Berdakin, O. A. Douglas-Gallardo and Cristián G. Sánchez, *Journal of Physical Chemistry C* **124** (2020) 1631–1639
143. J. Fojt, T. P. Rossi, M. Kuisma and P. Erhart, *Nano Letters* **22** (2022) 8786–8792
144. P. V. Kumar, T. P. Rossi, K. Kuisma, P. Erhart, D. J. Norris, *Faraday Discussions* **214** (2019) 189–197
145. M. Berdakin, G. Soldano, F. B. Bonafé, V. Liubov, B. Aradi, T. Frauenheim and C. G. Sánchez, *Nanoscale* **14** (2022) 2816–2825
146. S. Dal Forno, L. Ranno and J. Lischner, *Journal of Physical Chemistry C* **122** (2018) 8517–8527
147. T. P. White and K. R. Catchpole, *Applied Physics Letters* **101** (2012) 073905
148. S. K. F. Stofela, O. Kizilkaya, B. T. Diroll, T. R. Leite, M. M. Taheri, D. E. Willis, J. B. Baxter, W. A. Shelton, P. T. Sprunger and K. M. McPeak, *Advanced Materials* **32** (2020) 1906478
149. J. Enkovaara, C Rostgaard, J J Mortensen, J Chen, M. Dułak, L. Ferrighi, J. Gavnholt, C. Glinsvad, V. Haikola, H. A Hansen, H. H. Kristoffersen, M. Kuisma, A. H. Larsen, L. Lehtovaara, M. Ljungberg, O. Lopez-Acevedo, P.G. Moses, J. Ojanen, T. Olsen, V. Petzold, N. A. Romero, J. Stausholm-Möller, M. Strange, G. A. Tritsarlis, M. Vanin, M. Walter, B. Hammer, H. Häkkinen, G. K. H Madsen, R. M. Nieminen, J. K. Nørskov, M. Puska, T. T. Rantala, J. Schiøtz, K. S. Thygesen and K. W. Jacobsen, *Journal of Physics: Condensed Matter* **22** (2010) 253202
150. A. H. Larsen, J. J. Mortensen, J. Blomqvist, I. E Castelli, R. C., M. Dułak, J. Friis, M. N. Groves, B. Hammer, C. Hargus, E. D. Hermes, P. C Jennings, P. B. Jensen, J. Kermode, J. R Kitchin, E. L. Kolsbjerg, J. Kubal, K. Kaasbjerg, S. Lysgaard, J. Bergmann M., T. Maxson, T. Olsen, L. Pastewka, A. Peterson, C. Rostgaard, J. Schiøtz, O. Schütt, M. Strange, K. S. Thygesen, T. Vegge, L. Vilhelmsen, M. Walter, Z. Zeng and K. W Jacobsen, *Journal of Physics: Condensed Matter* **29** (2017) 273002
151. H. J. Monkhorst and J. D. Pack, *Physical Review B* **13** (2008) 5188
152. M. Bubaš, J. Sancho-Parramon, *Journal of Physical Chemistry C* **125** (2021) 24032–24042
153. R. Fletcher, *Practical Methods of Optimization (2nd ed.)*, John Wiley & Sons, New York 1987
154. J. P. Perdew, K. Burke, M. Ernzerhof, *Physical Review Letters* **77** 3865–3868
155. J. P. Perdew, A. Ruzsinszky and G. I. Csonka, *Physical Review Letters* **100** (2008) 136406
156. J. P. Perdew and Y. Wang, *Physical Review B* **45** (1992) 13244
157. B. Hammer, L. B. Hansen, J. K. Nørskov, *Physical Review B* **59** (1999) 7413
158. M. Dion, H. Rydberg, E. Schröder, D. C. Langreth and B. I. Lundqvist, *Physical Review Letters* **92** 246401
159. M. Kuisma, J. Ojanen, J. Enkovaara and T. T. Rantala, *Physical Review B* **82** (2010) 115106
160. O. Peña-Rodríguez, M. Caro, A. Rivera, J. Olivares, J. M. Perlado and A. Caro, *Optical Materials Express* **4** (2014) 403–410
161. R. M. A. Azzam, N. M. Bashara, *Ellipsometry and Polarized light*, North Holland publishing company (1997)
162. J. Gérardy and M. Ausloos, *Physical Review B* **25** (1982) 4204
163. U. Hohenester and A. Trügler, *Computer Physics Communications* **183** (2012) 370–381
164. <https://spglib.readthedocs.io/en/stable/python-interface.html> (downloaded 10th of April 2024.)
165. P. Haas, F. Tran and P. Blaha *Physical Review B* **79** (2009) 085104
-

- 
166. G. I. Csonka, J. P. Perdew, A. Ruzsinszky, P. H. T. Philipsen, S. Lebègue, J. Paier, O. A. Vydrov and J. G. Ángyán, *Physical Review B* **79** (2009) 155107
  167. V.A. Lubarda, *Mechanics of Materials* **35** (2003) 53-68
  168. J. W Arblaster, *Metals Review* **56** (2012) 181-189
  169. E. D. Palik, *Handbook of Optical Constants of Solids*, Academic Press (1998)
  170. Y. Jiang, S. Pillay and M. A. Green, *Optics Express* **23** (2015) 2133–2144.
  171. R. L. Olmon B. Slovick,; T. W. Johnson, D. Shelton, S.-H. Oh, G. D. Boreman and M. B. Raschke, *Physical Review B* **86** (2012) 235147
  172. W. Köster and R. Stahl, *Zeitschrift für Metallkunde* **58** (1967) 768–777
  173. J. Rivory and M. L. Theye, *Journal de Physique Lettres* **36** (1975) 129-132
  174. H. P. Myers, L. Walldén and Å. Karlsson, *The Philosophical Magazine: A Journal of Theoretical Experimental and Applied Physics* **18** (1968) 725-744
  175. M. J. Rahm, C. Tiburski. T. P. Rossi, F. A. A. Nugruho, S. Nilsson. C. Langhammer and P. Erhart, *Advanced Functional Materials* **30** (2020) 2002122
  176. Malola, S.; Kaappa, S.; Häkkinen, H., *Journal of Physical Chemistry C*, **123** (2019) 20655–20663
  177. Gjerding M., Pandey M. and K. S. Thygesen, *Nature Communications* **8** (2017) 15133
  178. Z. W. Lu, S.-H. Wei and A. Zunger, *Physical review B* **44** (1991) 19
  179. M. Bubaš, J. Sancho-Parramon, *Journal of Physical Chemistry C*, **128** (2024) 3924–3934
  180. E. R Hopper, C. Boukouvala, J. Asselin, J. S. Biggins and E. Ringe, *Journal of Physical Chemistry C* **126** (2022) 10630–10643
  181. M. Kuisma, B. Rousseaux, K. M. Czajkowski, T. P. Rossi, T. Shegai, P. Erhart, and T. J. Antosiewicz, *ACS Photonics* **9** (2022) 1065–1077
  182. W. Haucke, *Naturwissenschaften* **25** (1937) 61–61
  183. N. Shahcheraghi, V. Keast, A. Gentle, M. Arnold and M. Cortie, *Journal of Physics: Condensed Matter* **28** (2016) 405501
  184. G. Kurdjumov, V. Mireckij and T. Stelleckaja, *Zhurnal Tkhnicheskoi Fiziki* **8** (1938) 1959-1972
  185. M. Ellner, U. Kattner and B. Predel, *Journal of the Less-Common Metals* **87** (1982) 117-133
-

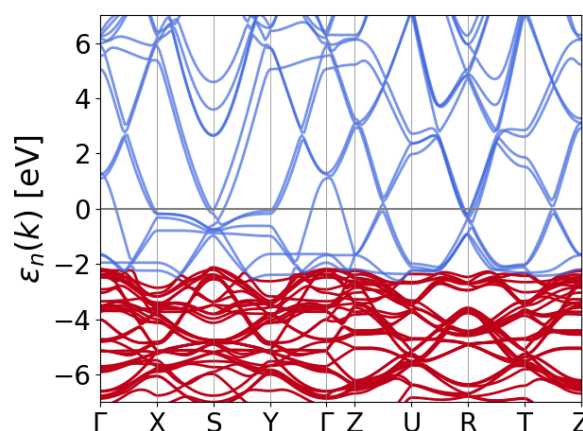
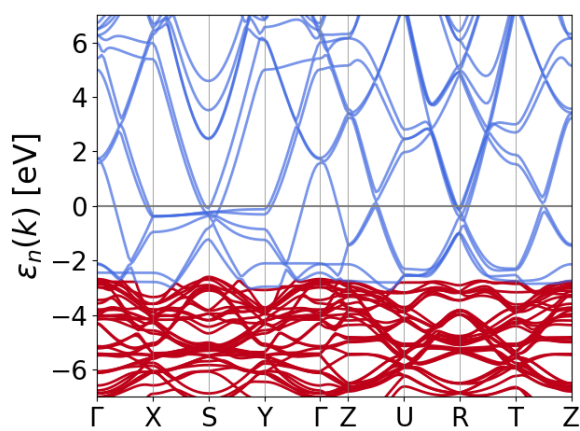
## § 9. APPENDIX



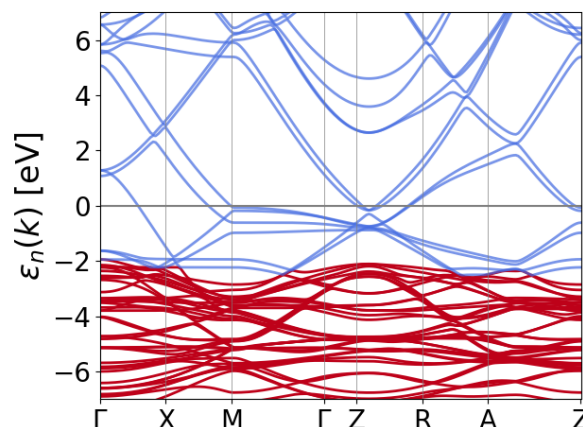
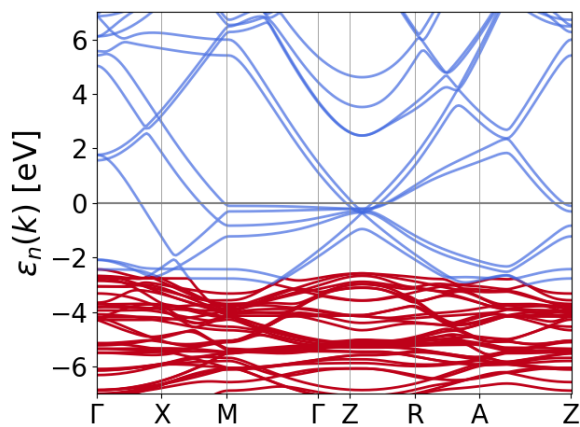
Au<sub>5</sub>Ag<sub>3</sub> 1



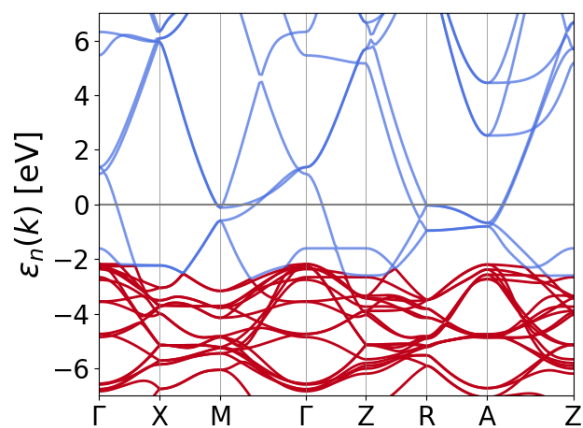
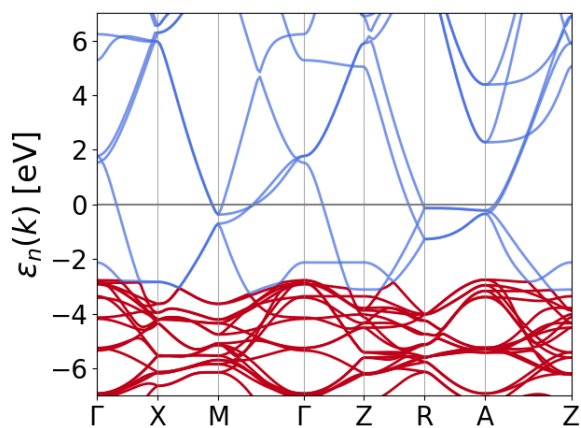
Au<sub>5</sub>Ag<sub>3</sub> 2



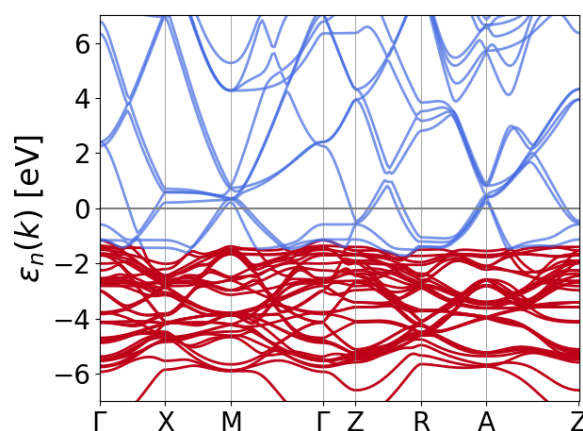
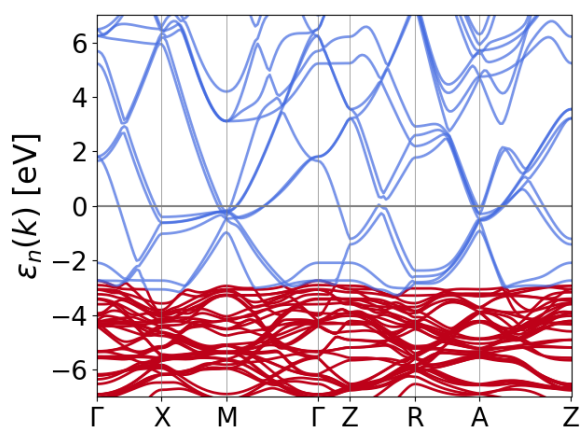
Au<sub>5</sub>Ag<sub>3</sub> 3



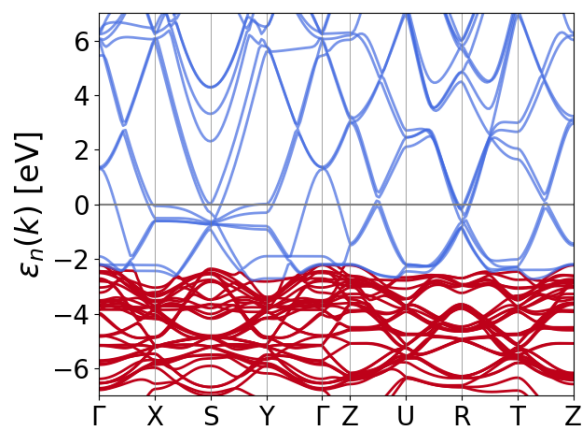
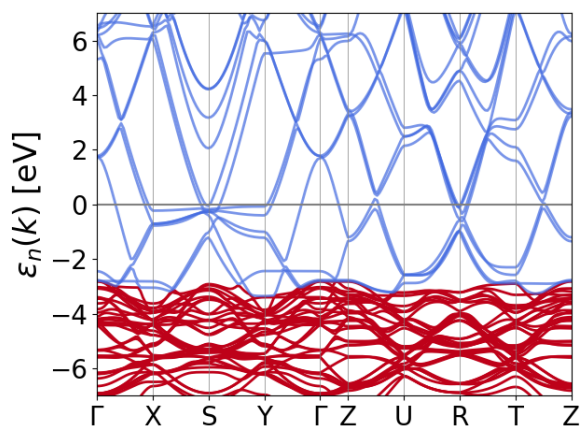
Au<sub>2</sub>Ag<sub>2</sub>



Au<sub>3</sub>Ag<sub>5</sub> 1

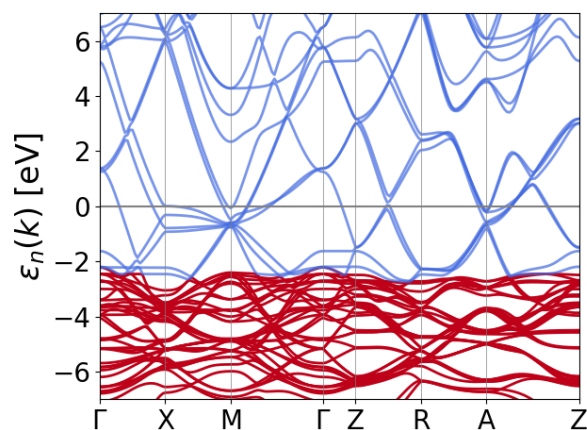
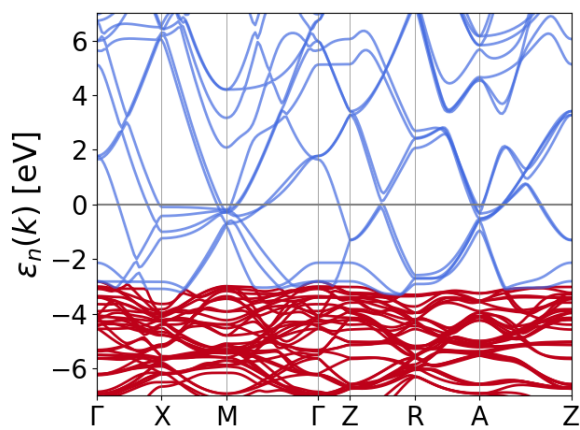


Au<sub>3</sub>Ag<sub>5</sub> 2

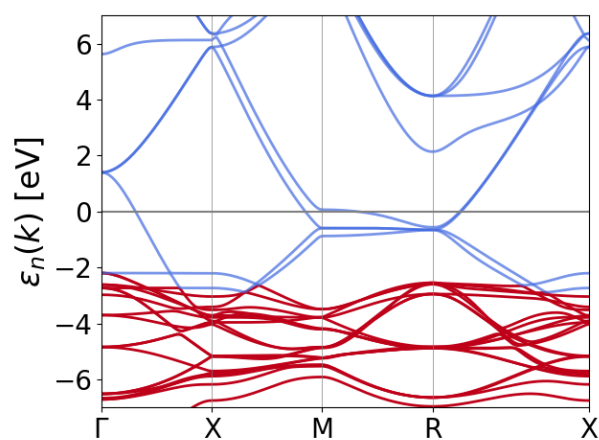
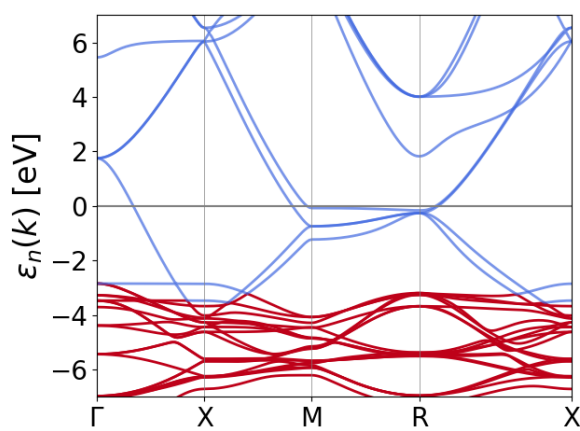




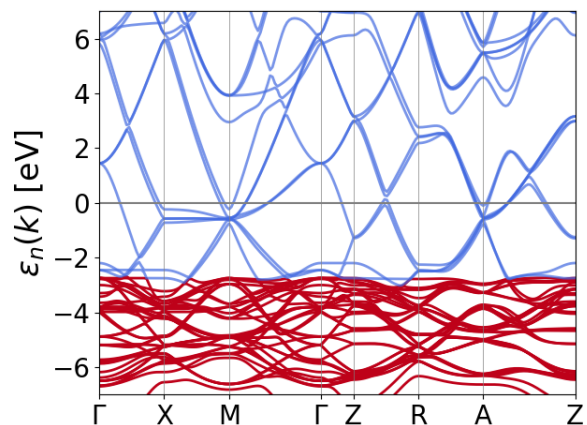
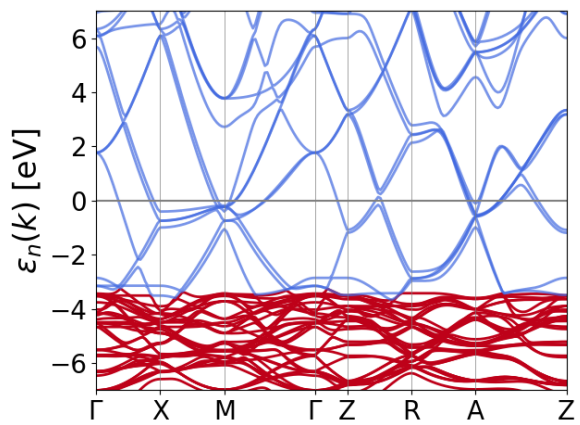
Au<sub>3</sub>Ag<sub>5</sub> 3



AuAg<sub>3</sub>



AuAg<sub>7</sub>



Ag

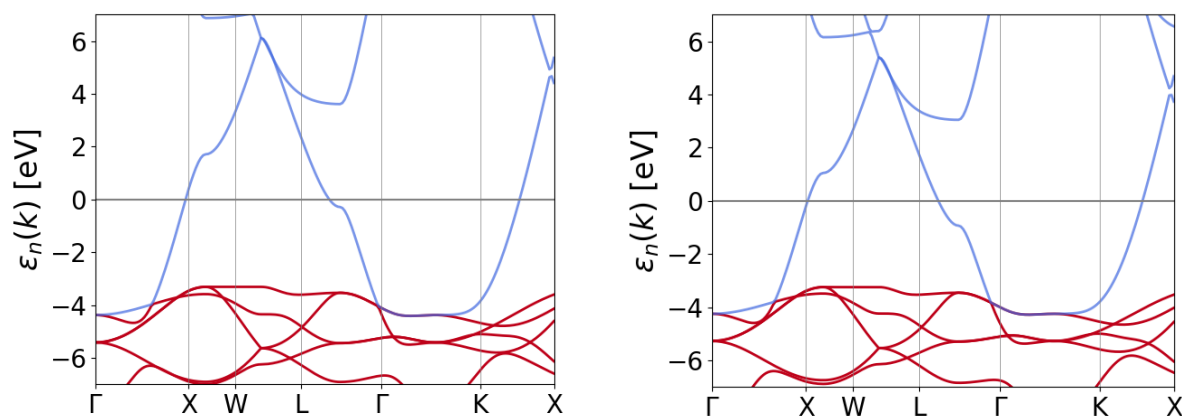
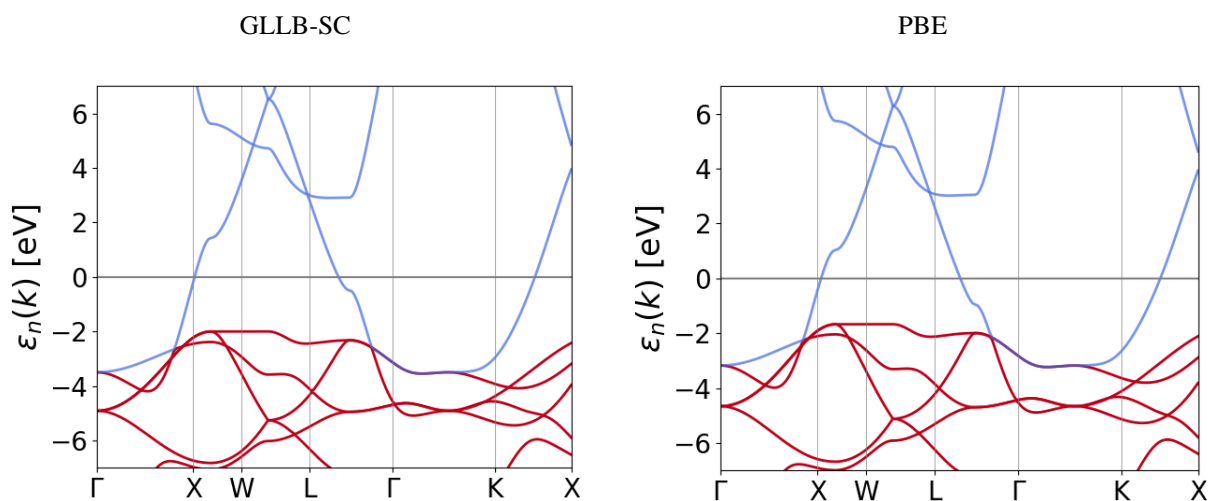
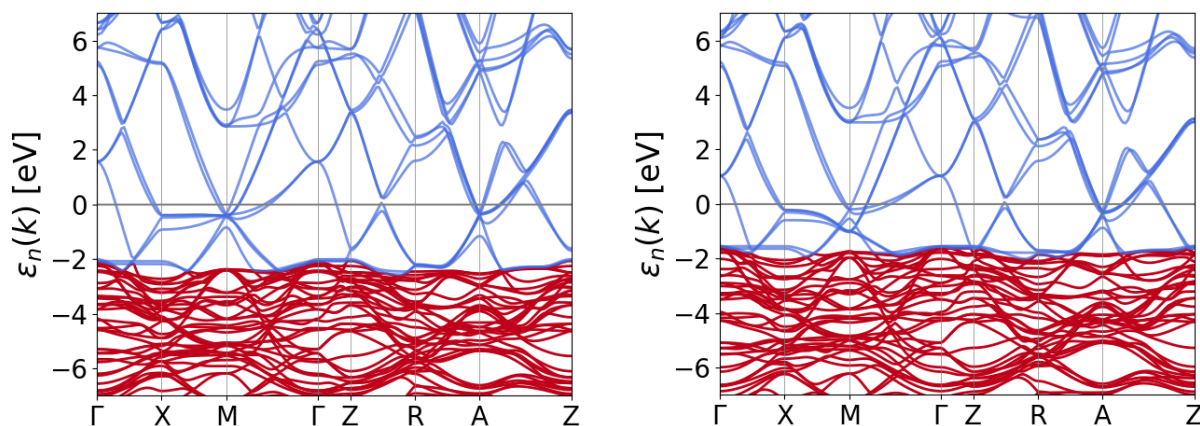


Figure A1. Band structures of Au-Ag alloys calculated by GLLB-SC and PBE. Fermi level has been set to 0 eV and the energy axis shifted accordingly. Nominal d-bands are shown in red and the rest are shown in blue. It has to be noted that this distinction is in part artificial due to hybridization, especially near the Fermi level.

Au

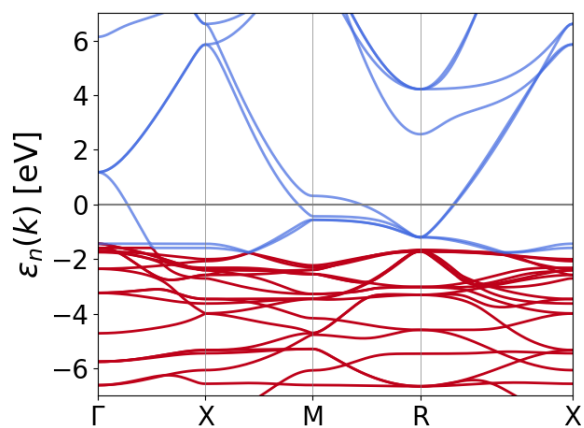
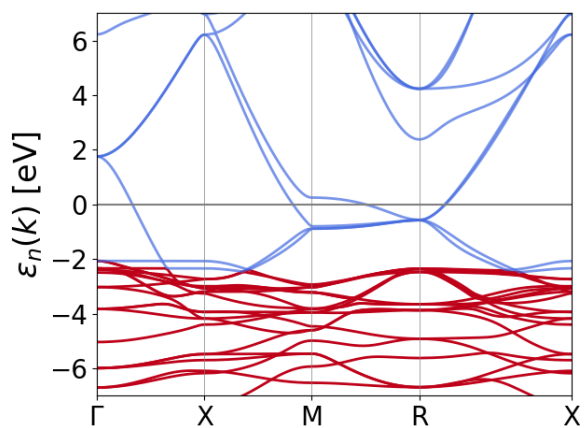


Au<sub>7</sub>Cu

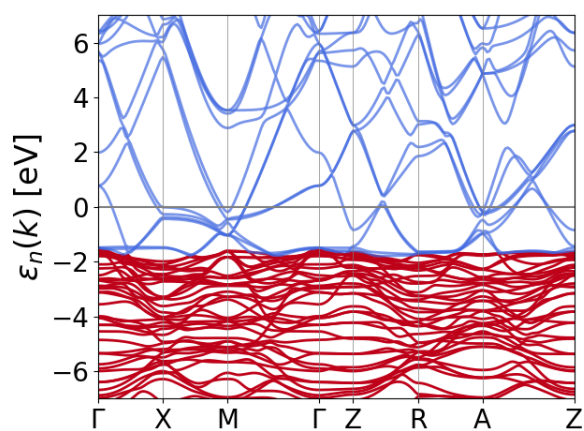
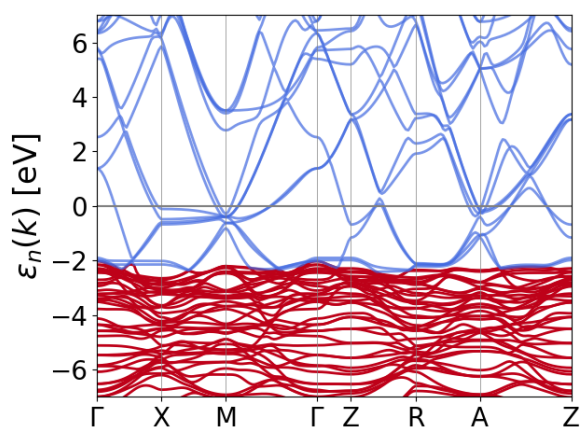




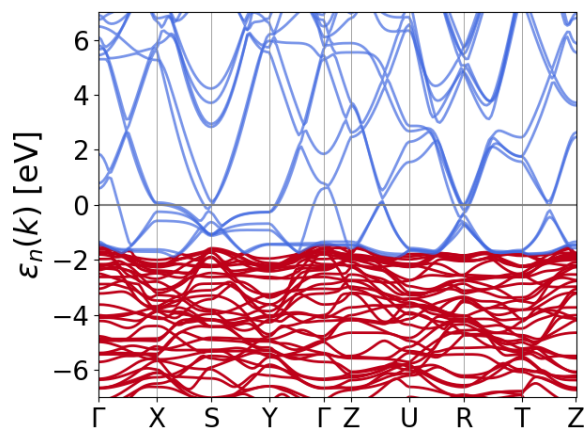
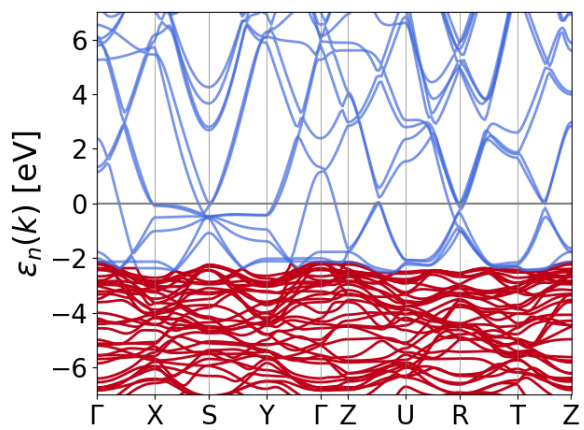
Au<sub>3</sub>Cu



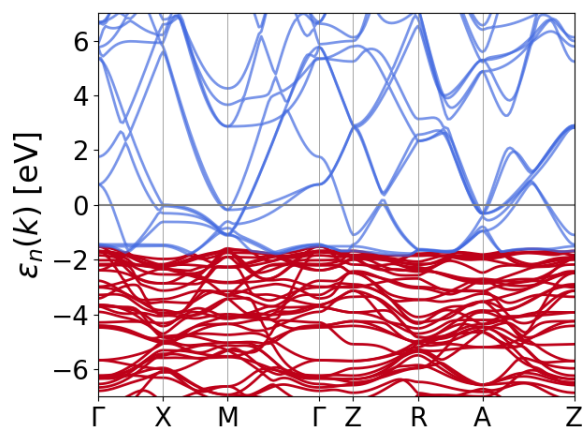
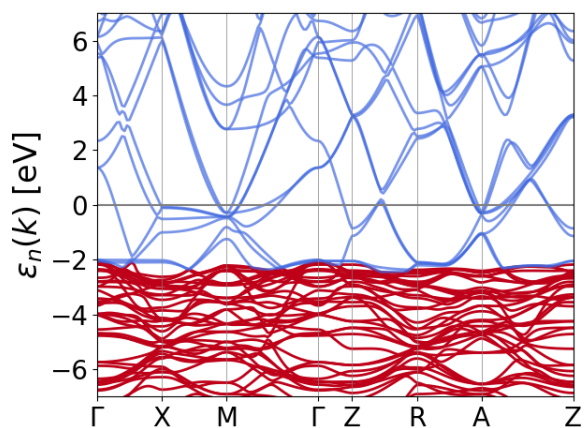
Au<sub>5</sub>Cu<sub>3</sub>  
1



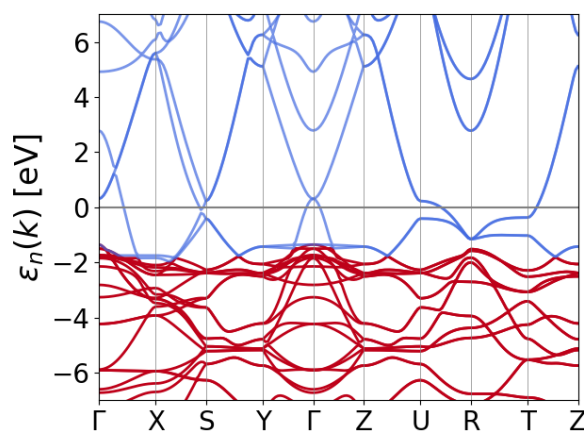
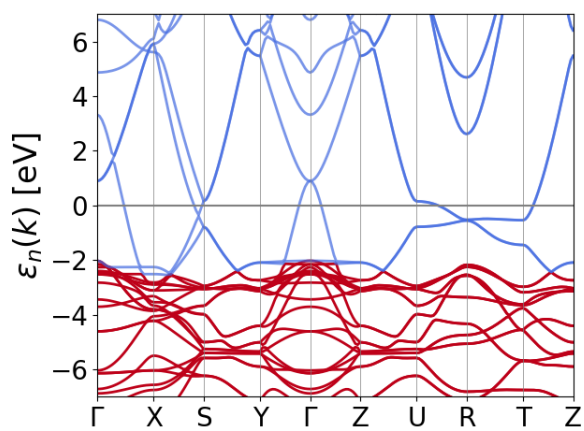
Au<sub>5</sub>Cu<sub>3</sub>  
2



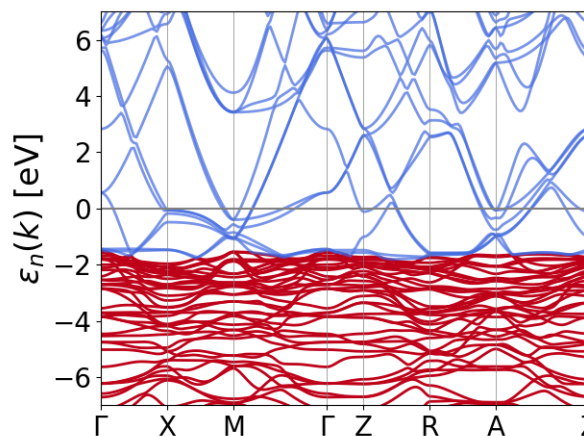
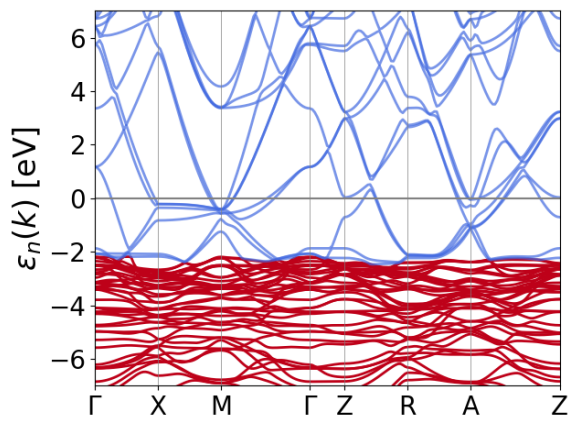
Au<sub>5</sub>Cu<sub>3</sub>  
3



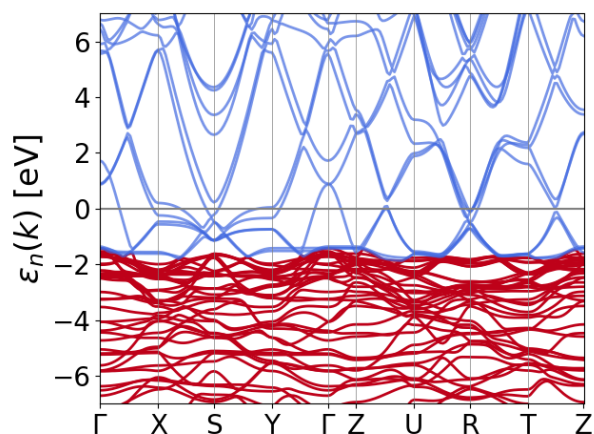
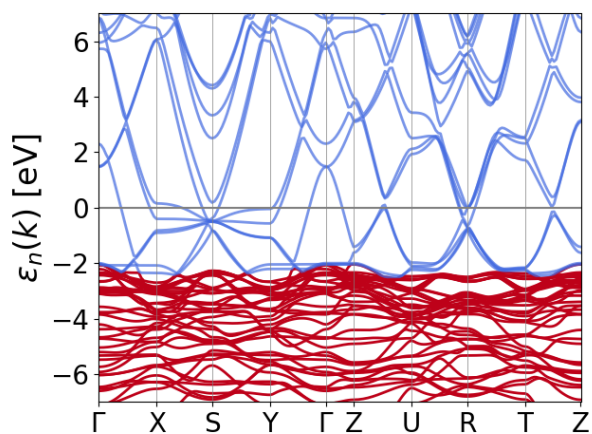
Au<sub>2</sub>Cu<sub>2</sub>



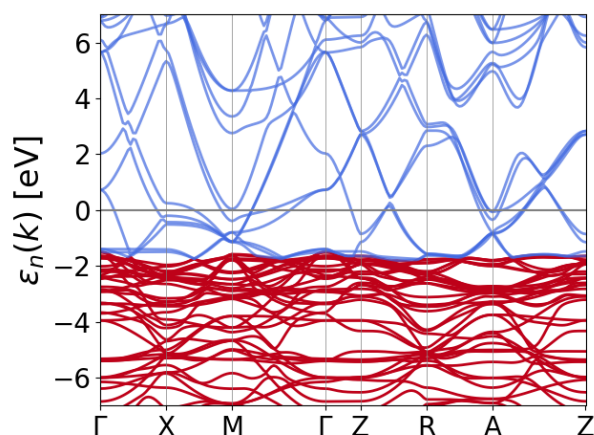
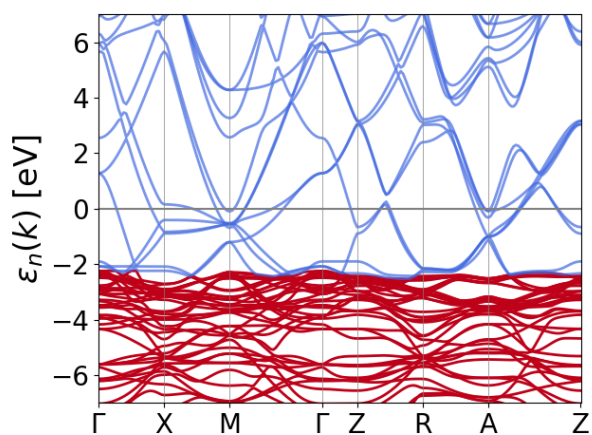
Au<sub>3</sub>Cu<sub>5</sub>  
1



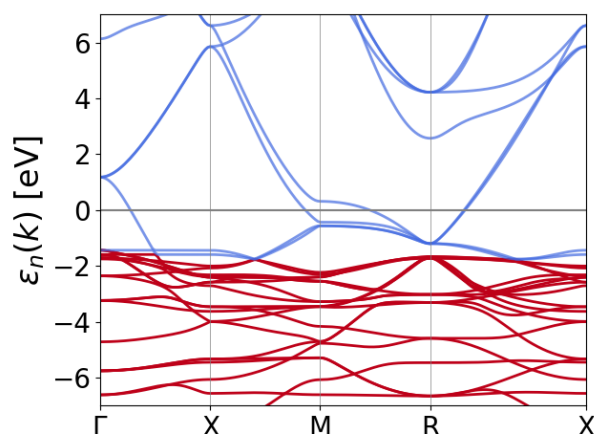
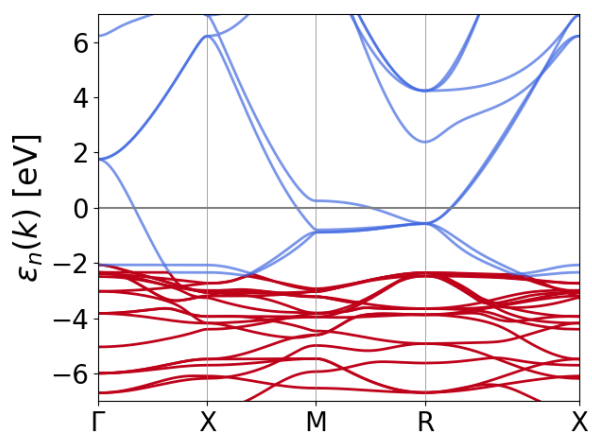
$\text{Au}_3\text{Cu}_5$   
2



$\text{Au}_3\text{Cu}_5$   
3



$\text{AuCu}_3$



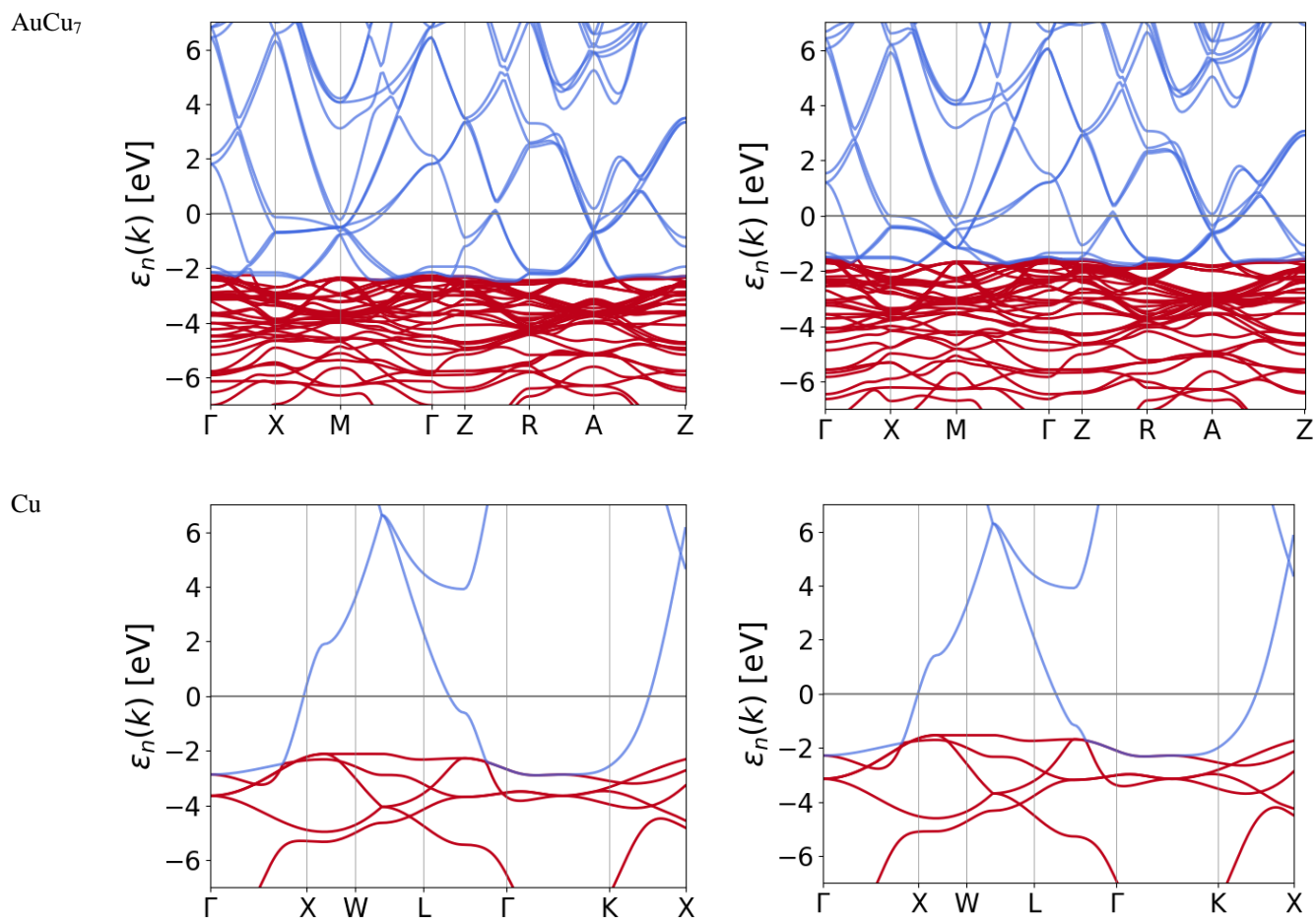
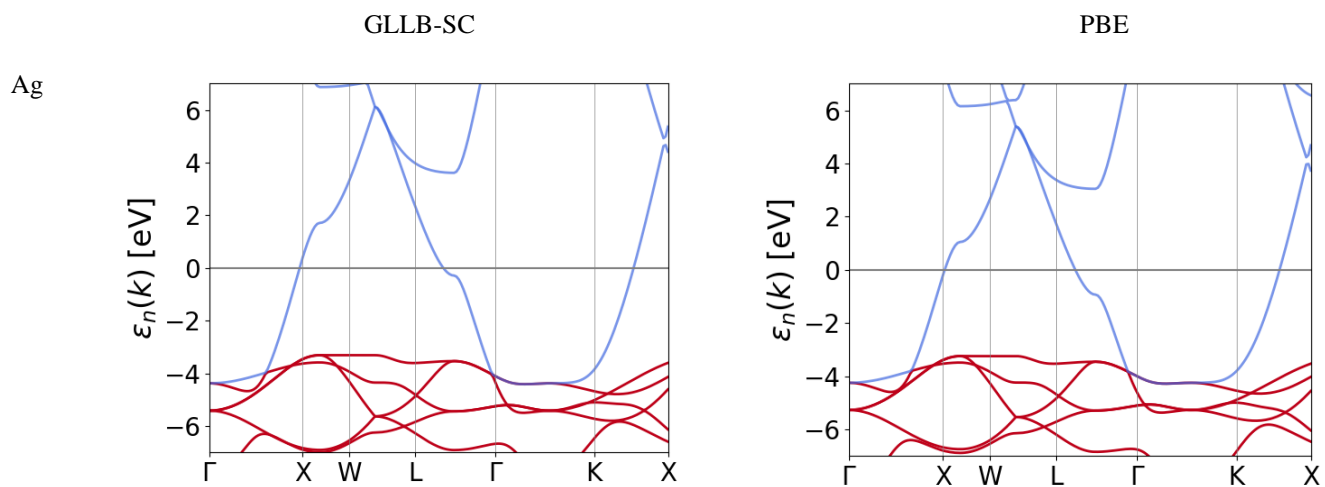
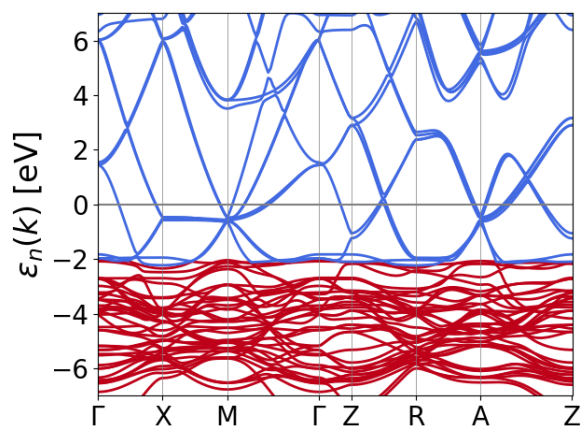
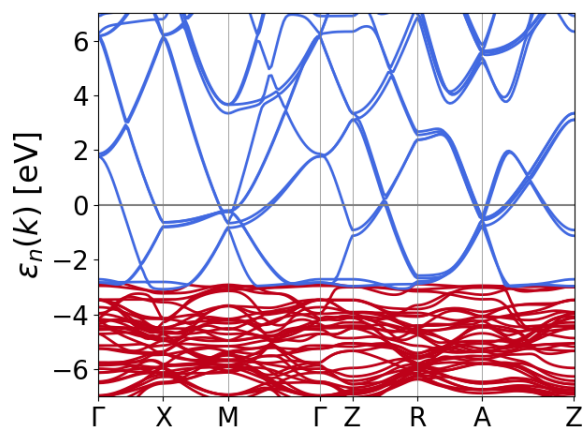


Figure A2. Band structures of Au-Cu alloys calculated by GLLB-SC and PBE. Fermi level has been set to 0 eV and the energy axis shifted accordingly. Nominal d-bands are shown in red and the rest are shown in blue. It has to be noted that this distinction is in part artificial due to hybridization, especially near the Fermi level.

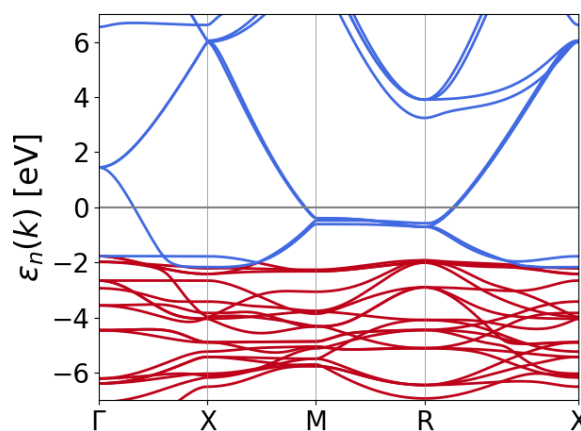
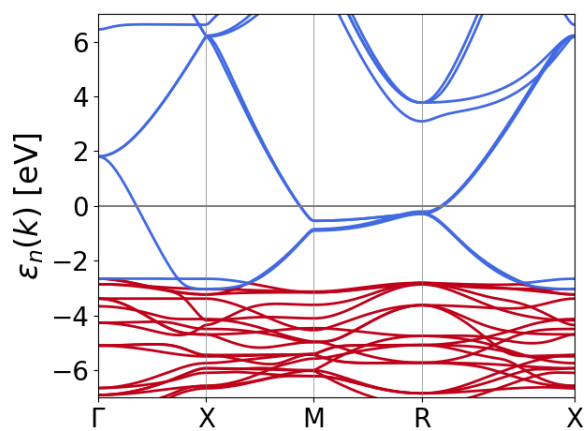




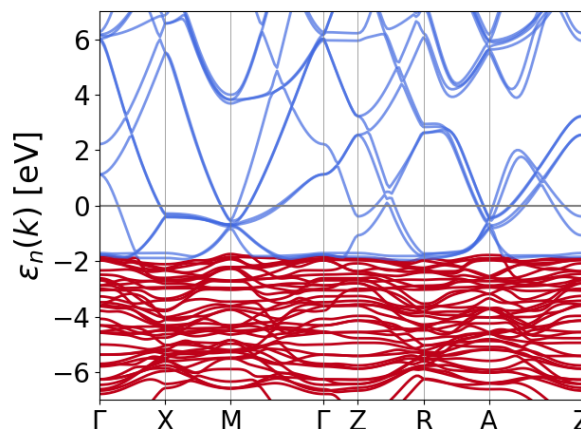
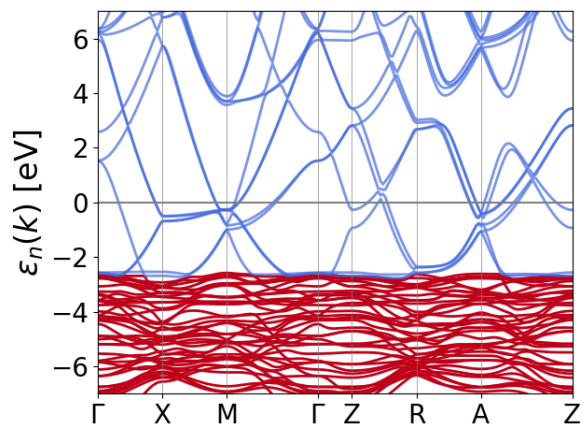
Ag<sub>7</sub>Cu



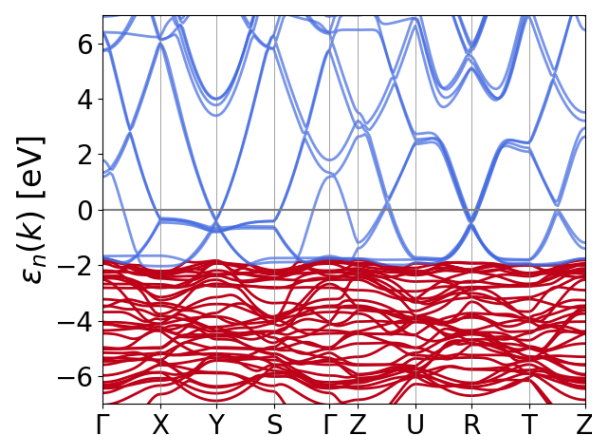
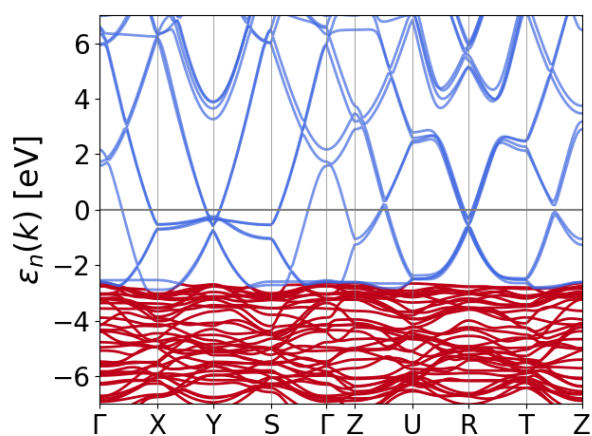
Ag<sub>3</sub>Cu



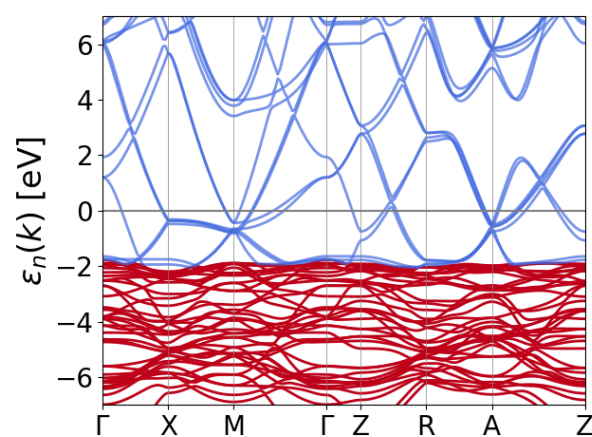
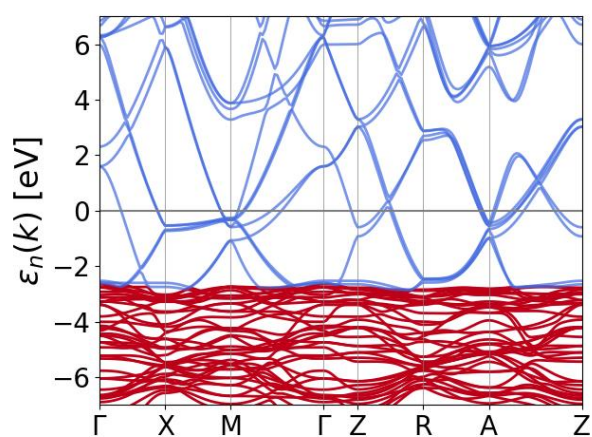
Ag<sub>5</sub>Cu<sub>3</sub>  
1



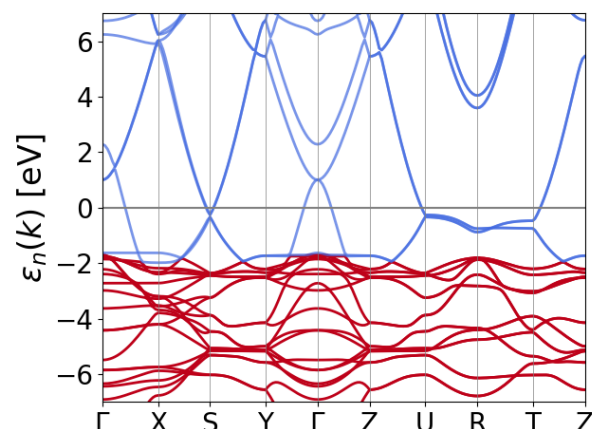
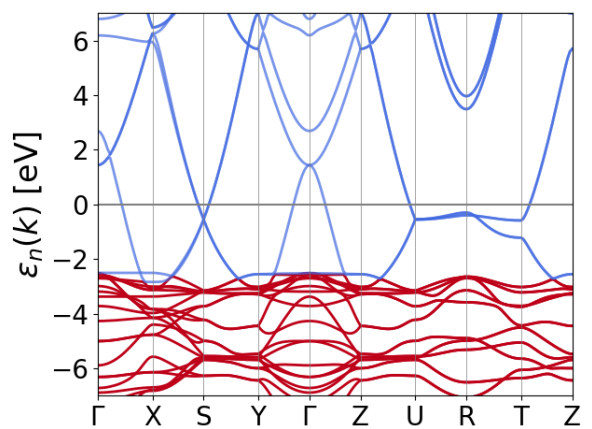
$\text{Ag}_5\text{Cu}_3$   
2



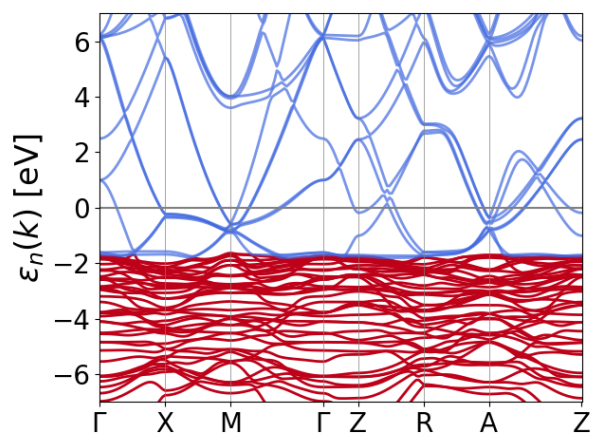
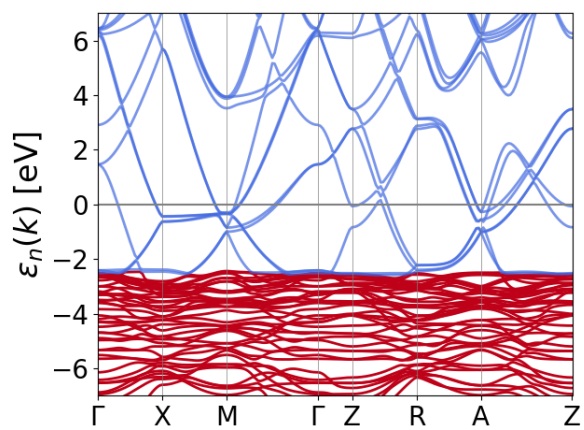
$\text{Ag}_5\text{Cu}_3$   
3



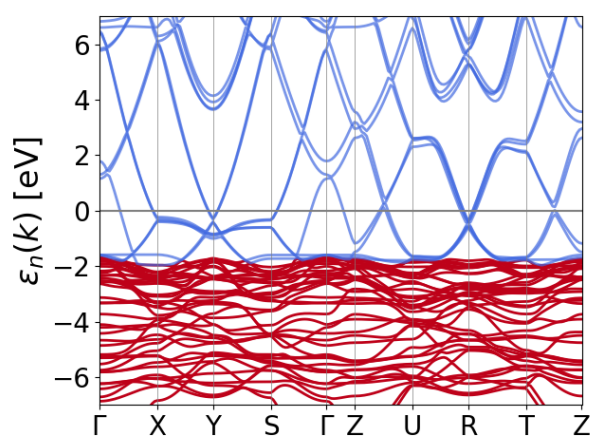
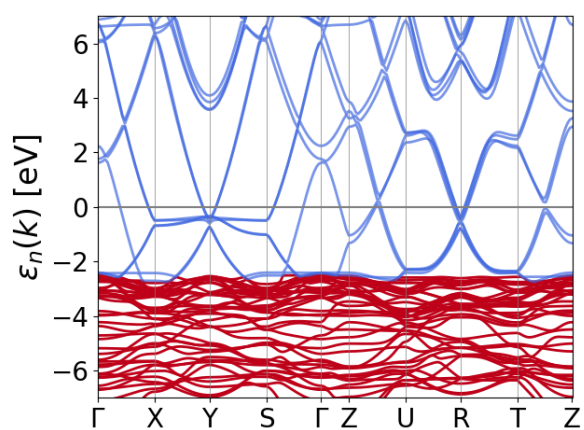
$\text{Ag}_2\text{Cu}_2$



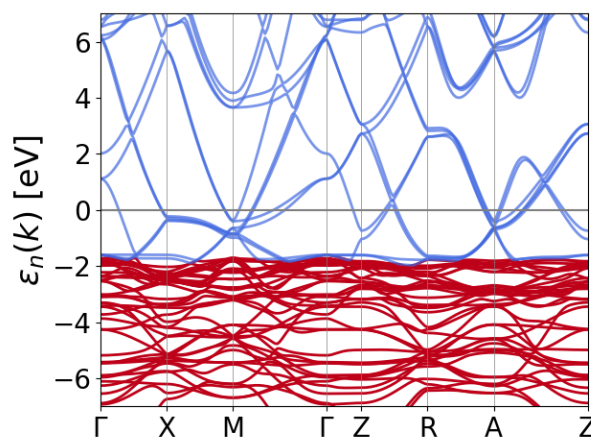
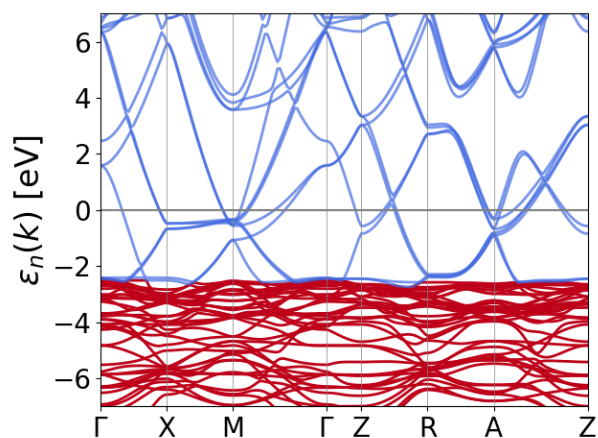
$\text{Ag}_3\text{Cu}_5$   
1



$\text{Ag}_3\text{Cu}_5$   
2



$\text{Ag}_3\text{Cu}_5$   
3



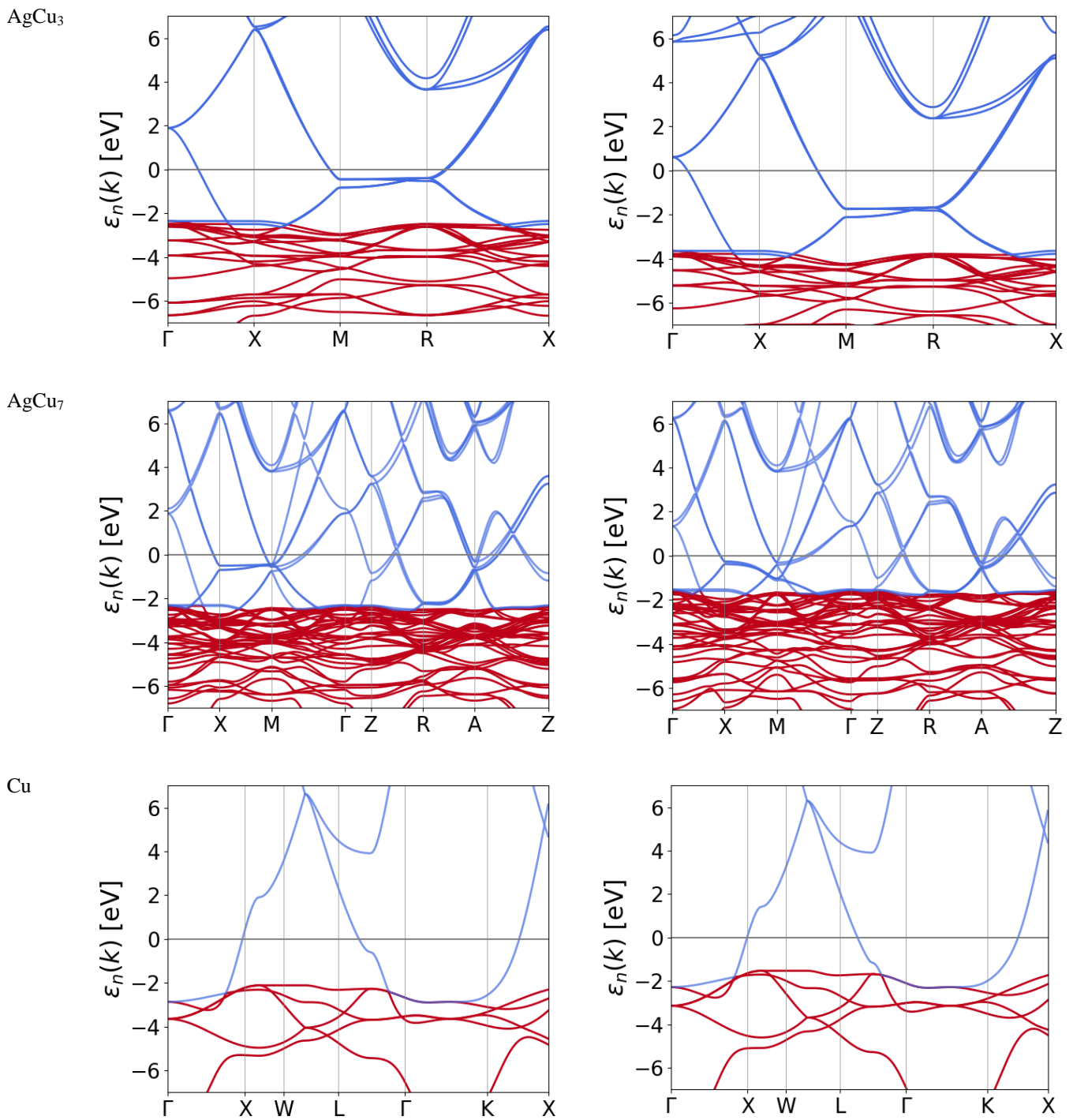
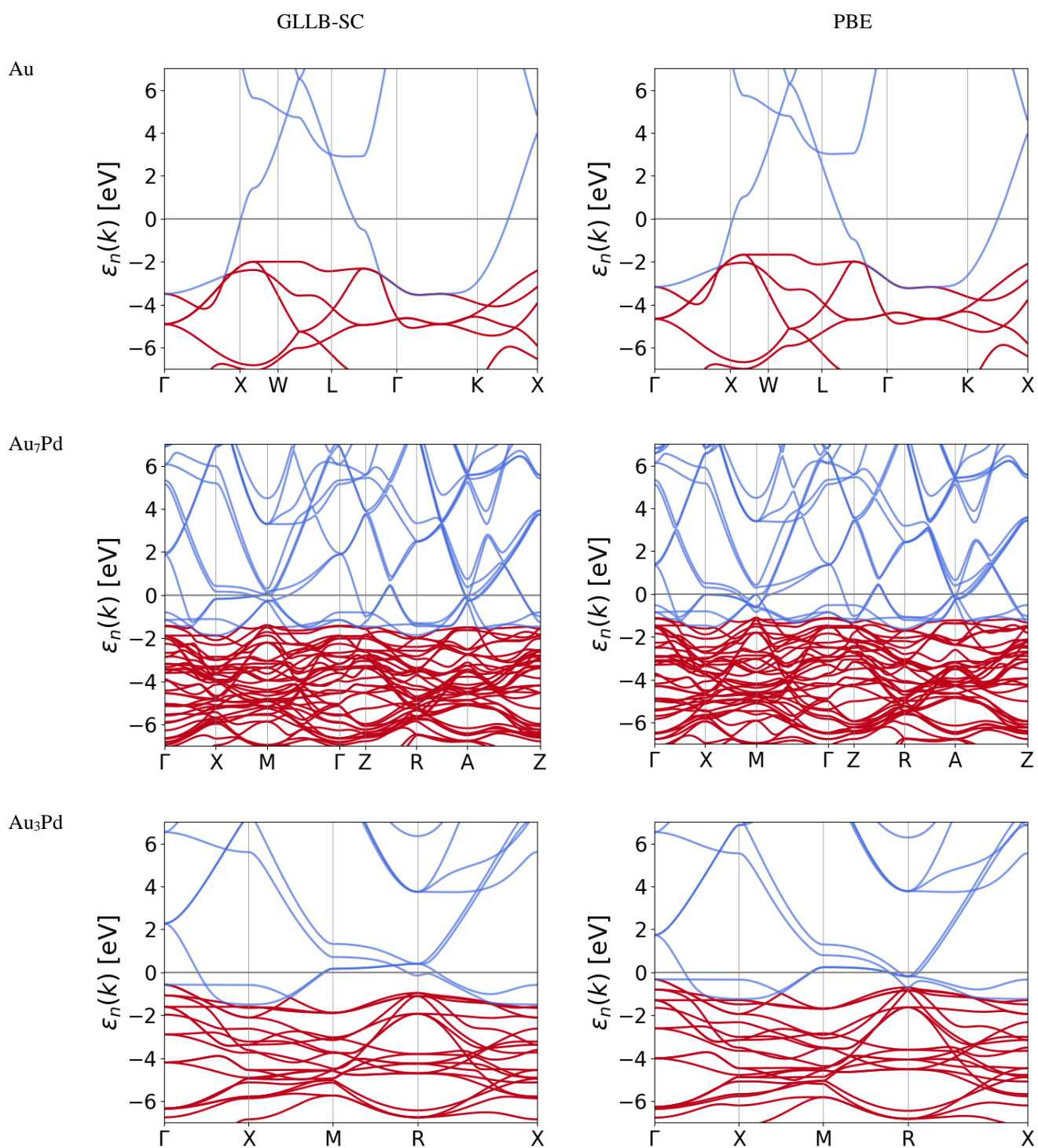
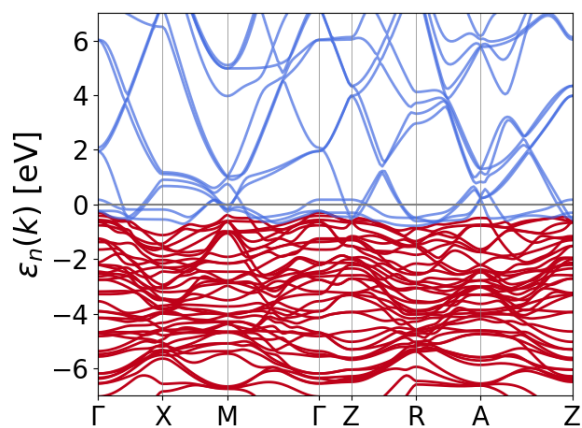
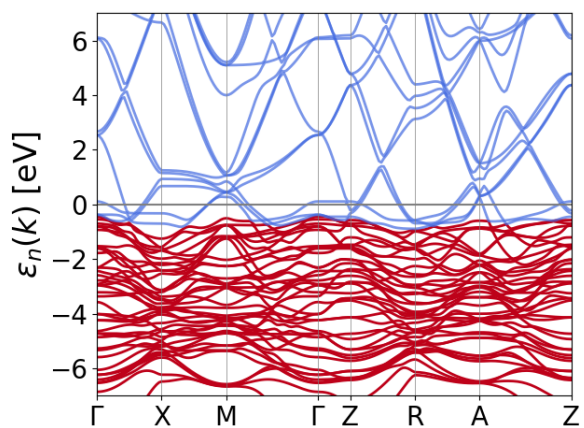


Figure A3. Band structures of Ag-Cu alloys calculated by GLLB-SC and PBE. Fermi level has been set to 0 eV and the energy axis shifted accordingly. Nominal d-bands are shown in red and the rest are shown in blue. It has to be noted that this distinction is in part artificial due to hybridization, especially near the Fermi level.

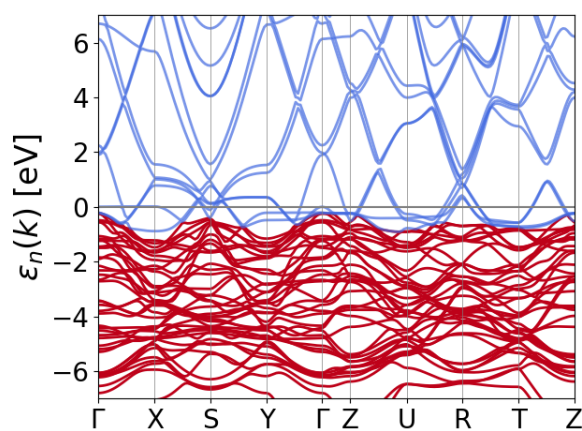
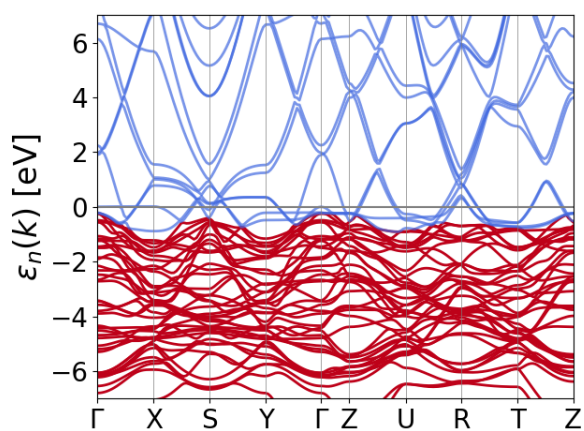




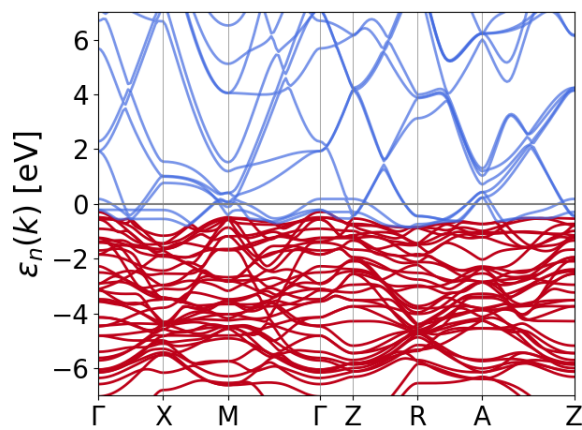
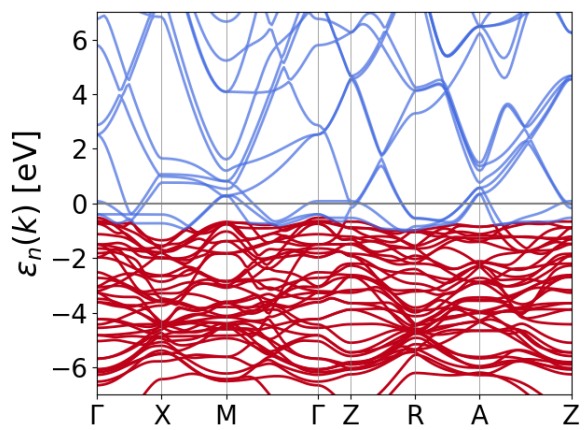
Au<sub>5</sub>Pd<sub>3</sub>  
1



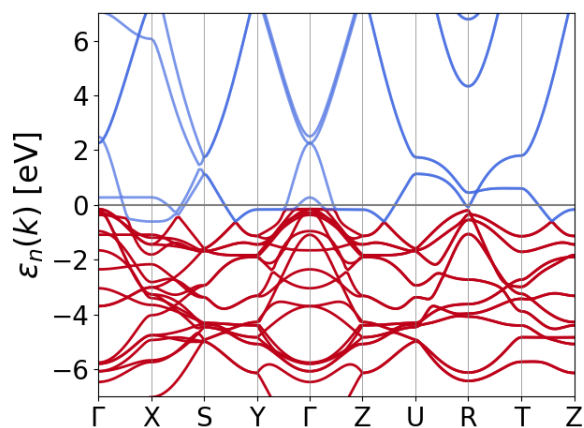
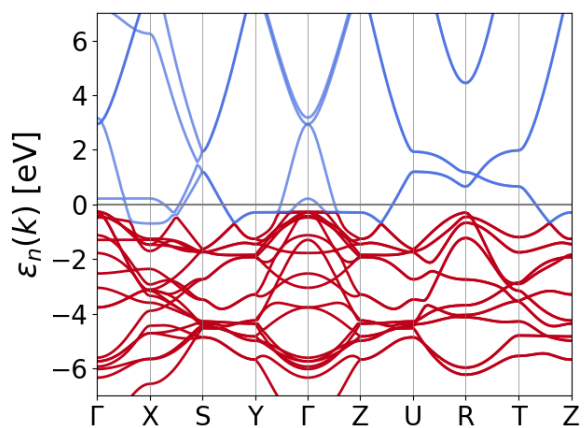
Au<sub>5</sub>Pd<sub>3</sub>  
2



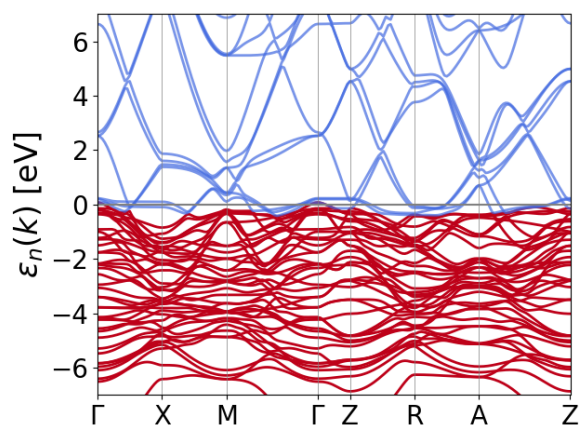
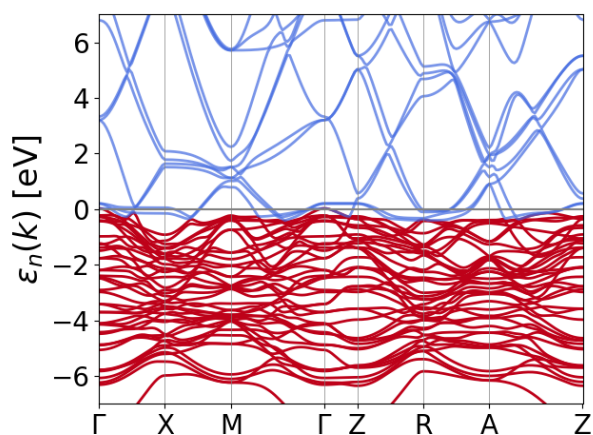
Au<sub>5</sub>Pd<sub>3</sub>  
3



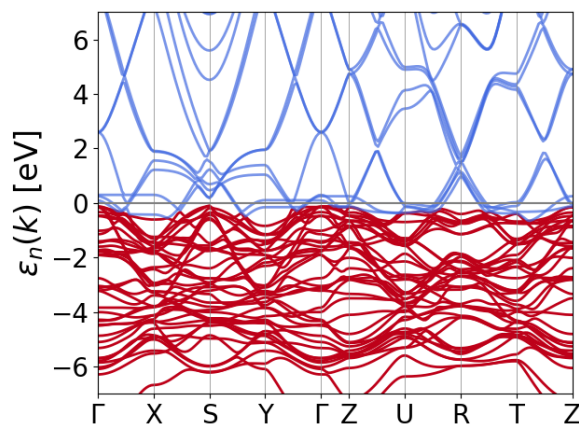
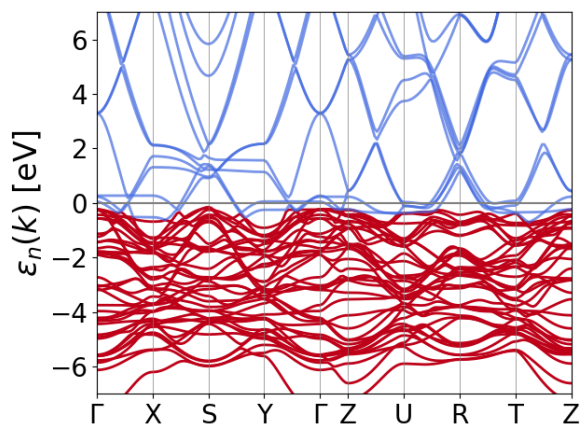
Au<sub>2</sub>Pd<sub>2</sub>



Au<sub>3</sub>Pd<sub>5</sub>  
1

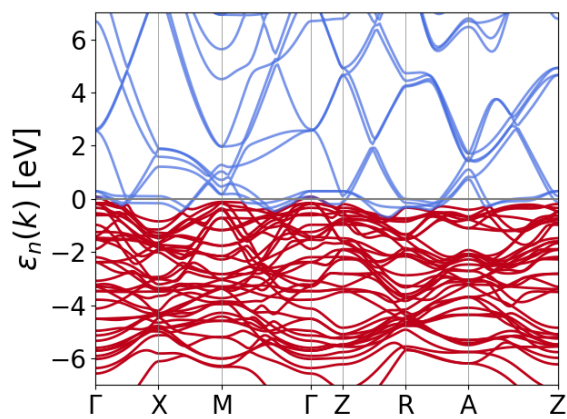
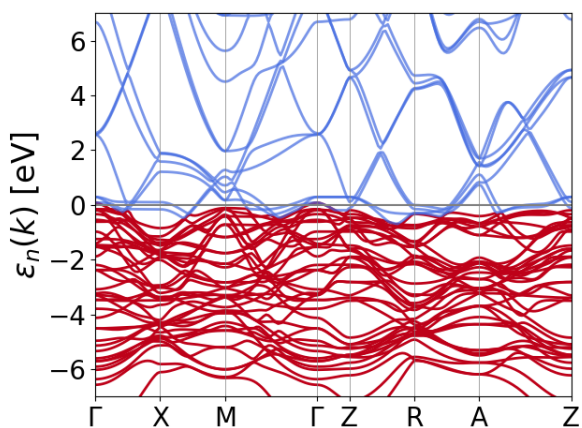


Au<sub>3</sub>Pd<sub>5</sub>  
2

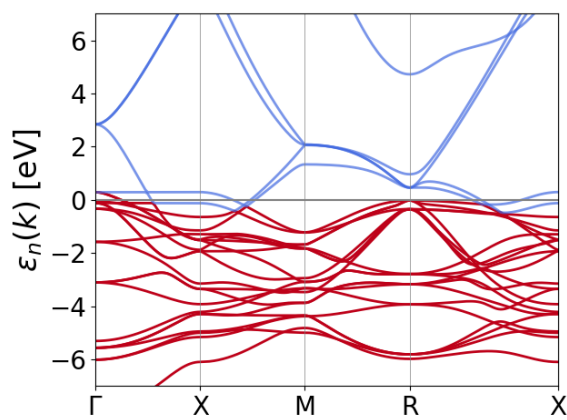
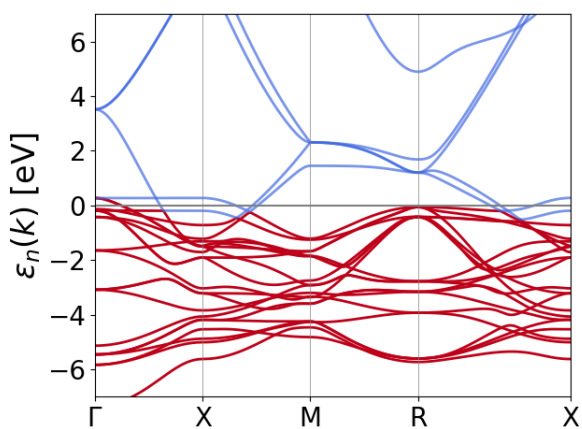




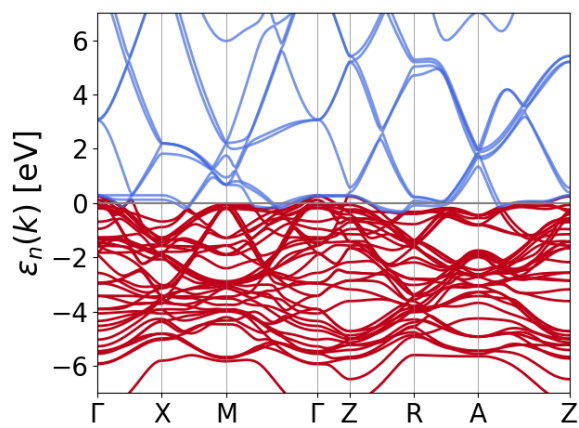
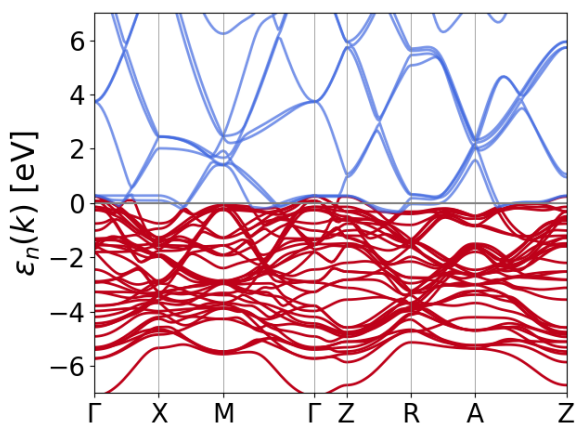
$\text{Au}_3\text{Pd}_5$   
3



$\text{AuPd}_3$



$\text{AuPd}_7$



Pd

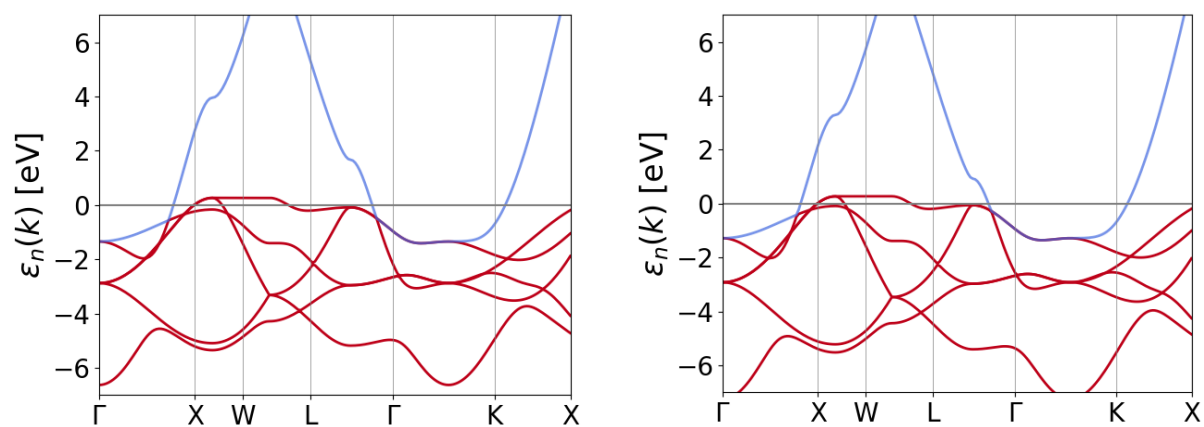


Figure A4. Band structures of Au-Pd alloys calculated by GLLB-SC and PBE. Fermi level has been set to 0 eV and the energy axis shifted accordingly. Nominal d-bands are shown in red and the rest are shown in blue. It has to be noted that this distinction is in part artificial due to hybridization, especially near the Fermi level.

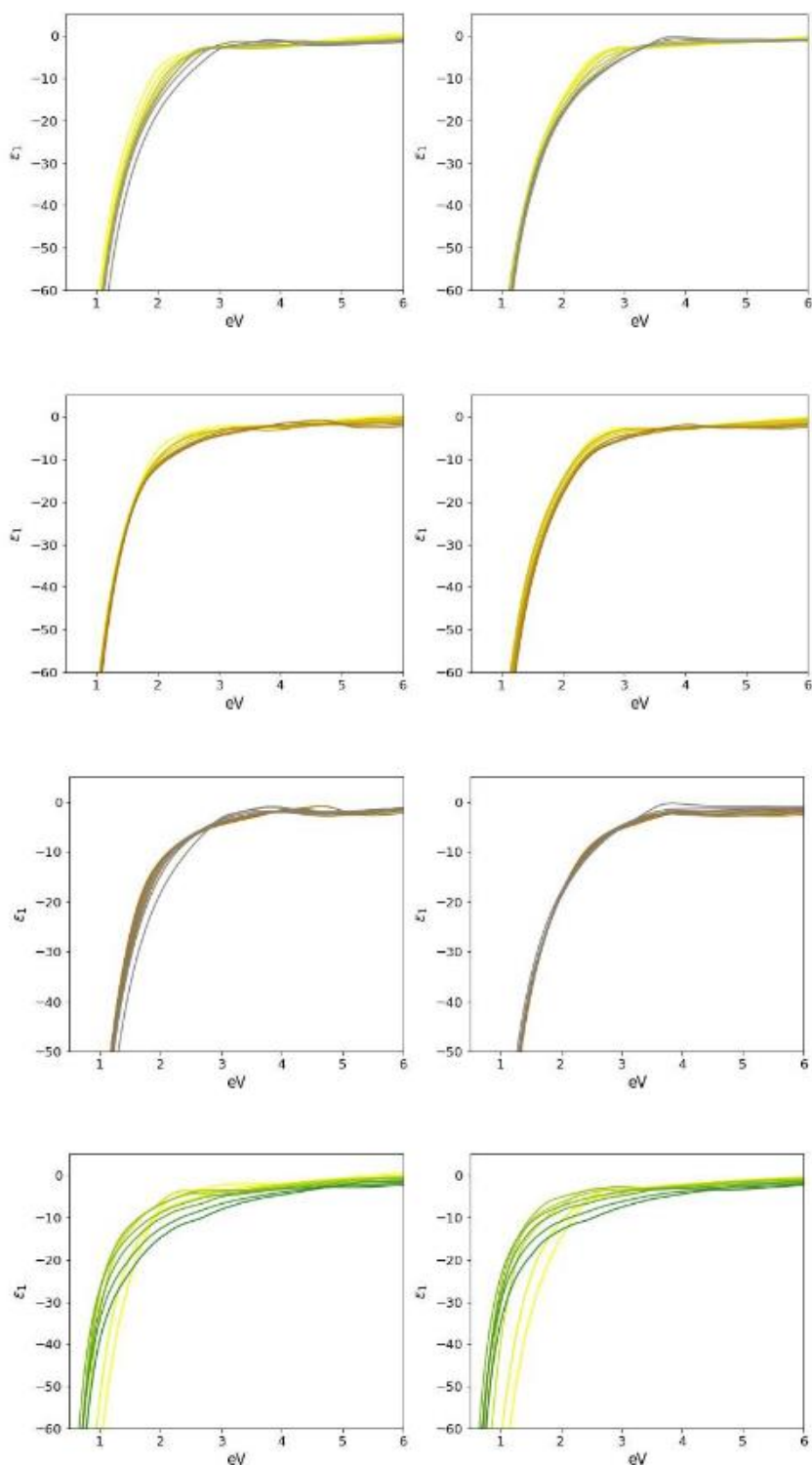
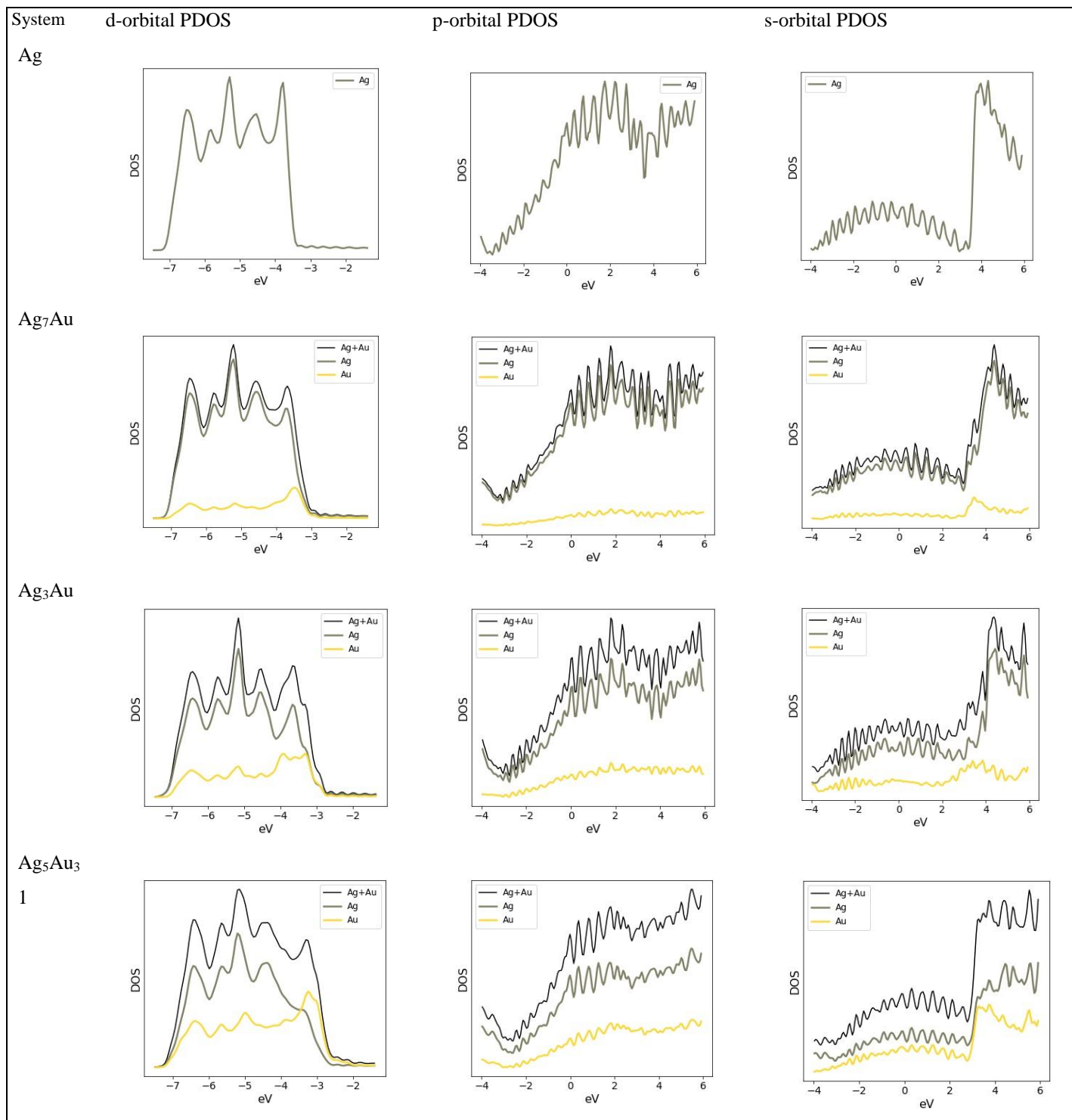


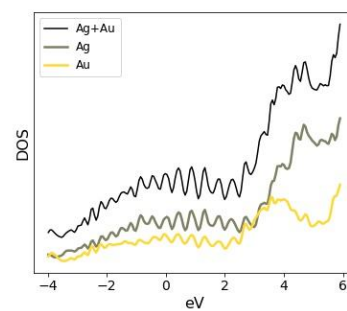
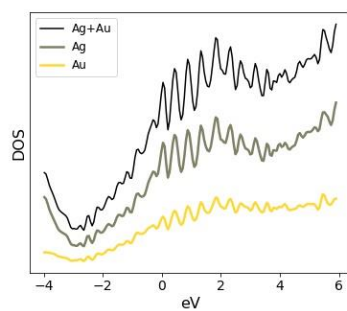
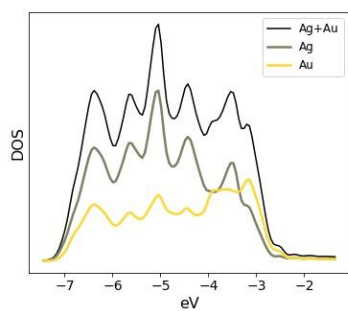
Figure 33. Real part of the alloy dielectric functions for Au-Ag (first row), Au-Cu (second row), Ag-Cu (third row) and Au-Pd (fourth row). Results obtained using PBE are on the left and using GLLB-SC are on the right. Dielectric function is shaded progressively more yellow for increasing Au content, brown for Cu content, gray for Ag content and dark green for Pd content.<sup>152</sup>

Table A1. Element resolved projected density of states for the Ag-Au alloy system. The projected density of states is not normalized with respect to the orbital type so results are comparable only between the same orbital type. The results are obtained using GLLB-SC functional.



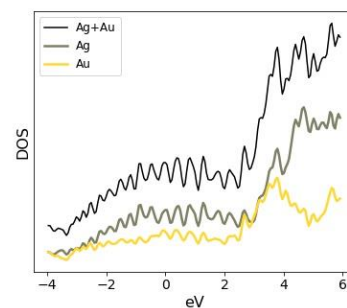
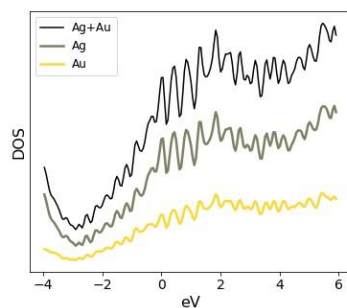
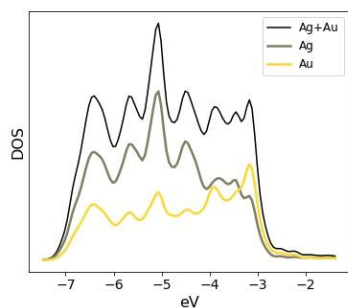
Ag<sub>5</sub>Au<sub>3</sub>

2

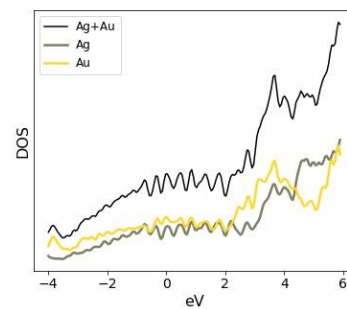
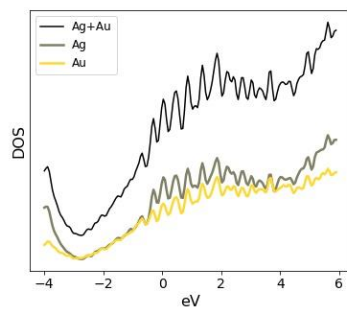
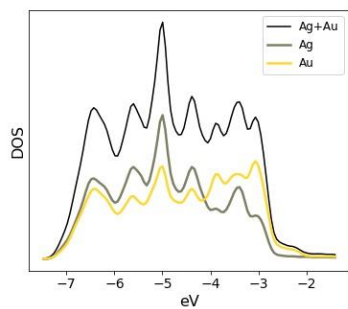


Ag<sub>5</sub>Au<sub>3</sub>

3

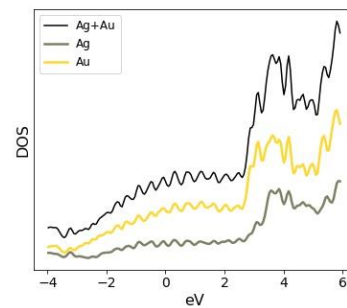
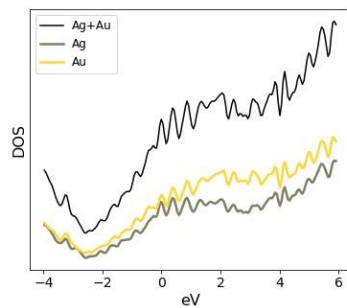
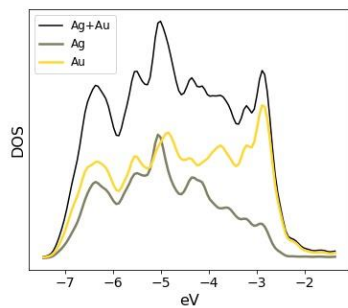


Ag<sub>2</sub>Au<sub>2</sub>



Ag<sub>3</sub>Au<sub>5</sub>

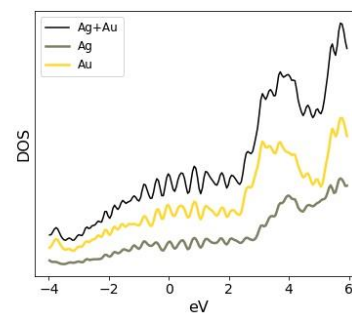
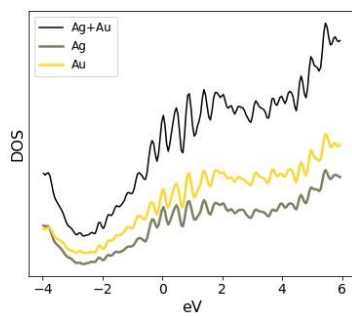
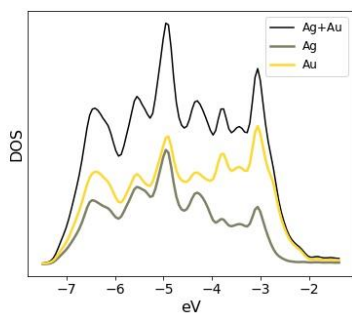
1





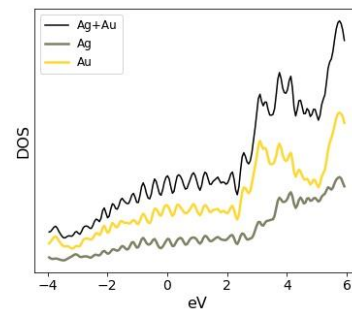
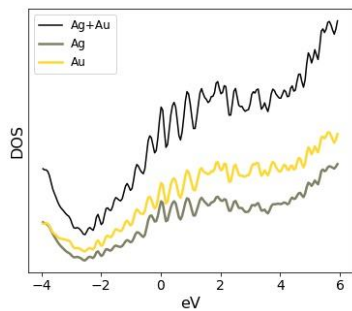
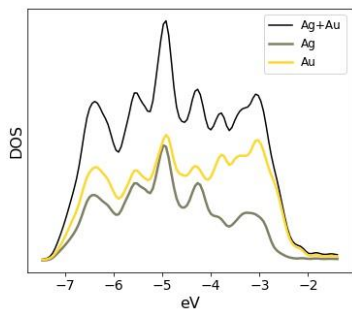
Ag<sub>3</sub>Au<sub>5</sub>

2

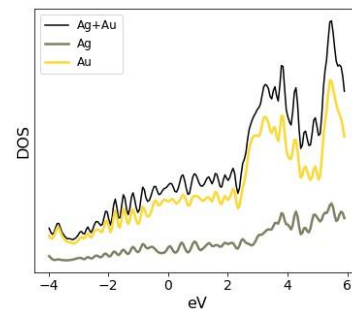
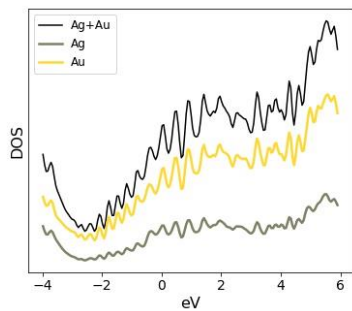
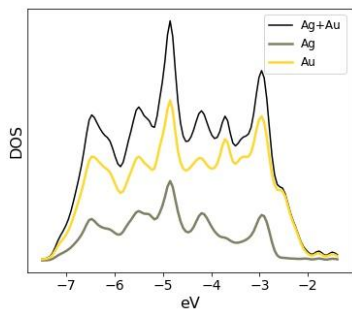


Ag<sub>3</sub>Au<sub>5</sub>

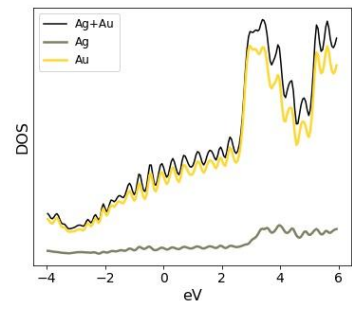
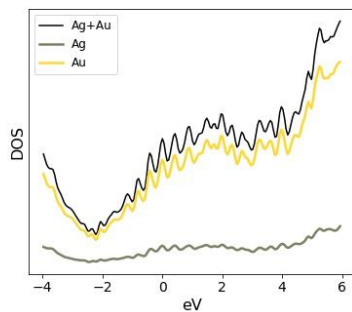
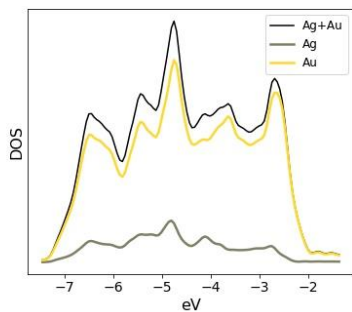
3



AgAu<sub>3</sub>



AgAu<sub>7</sub>



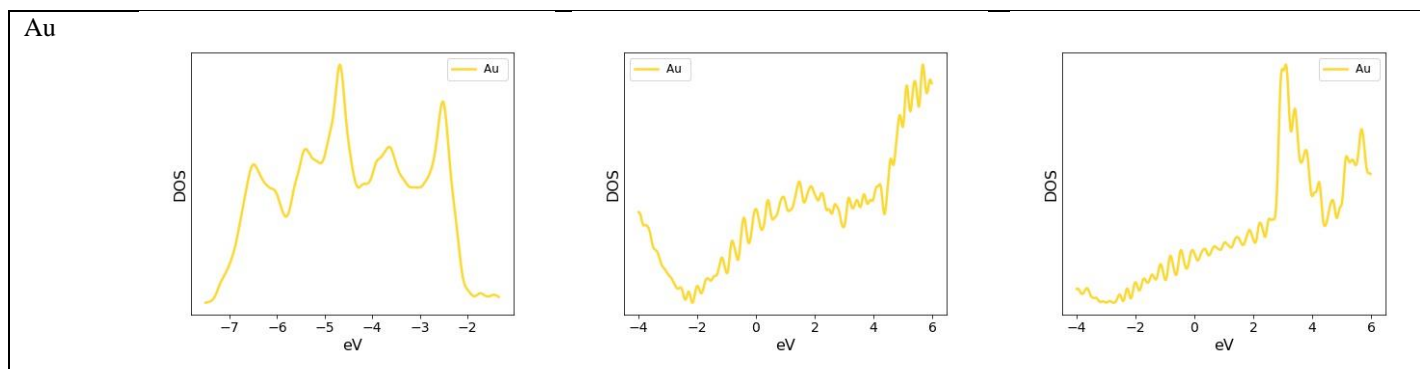
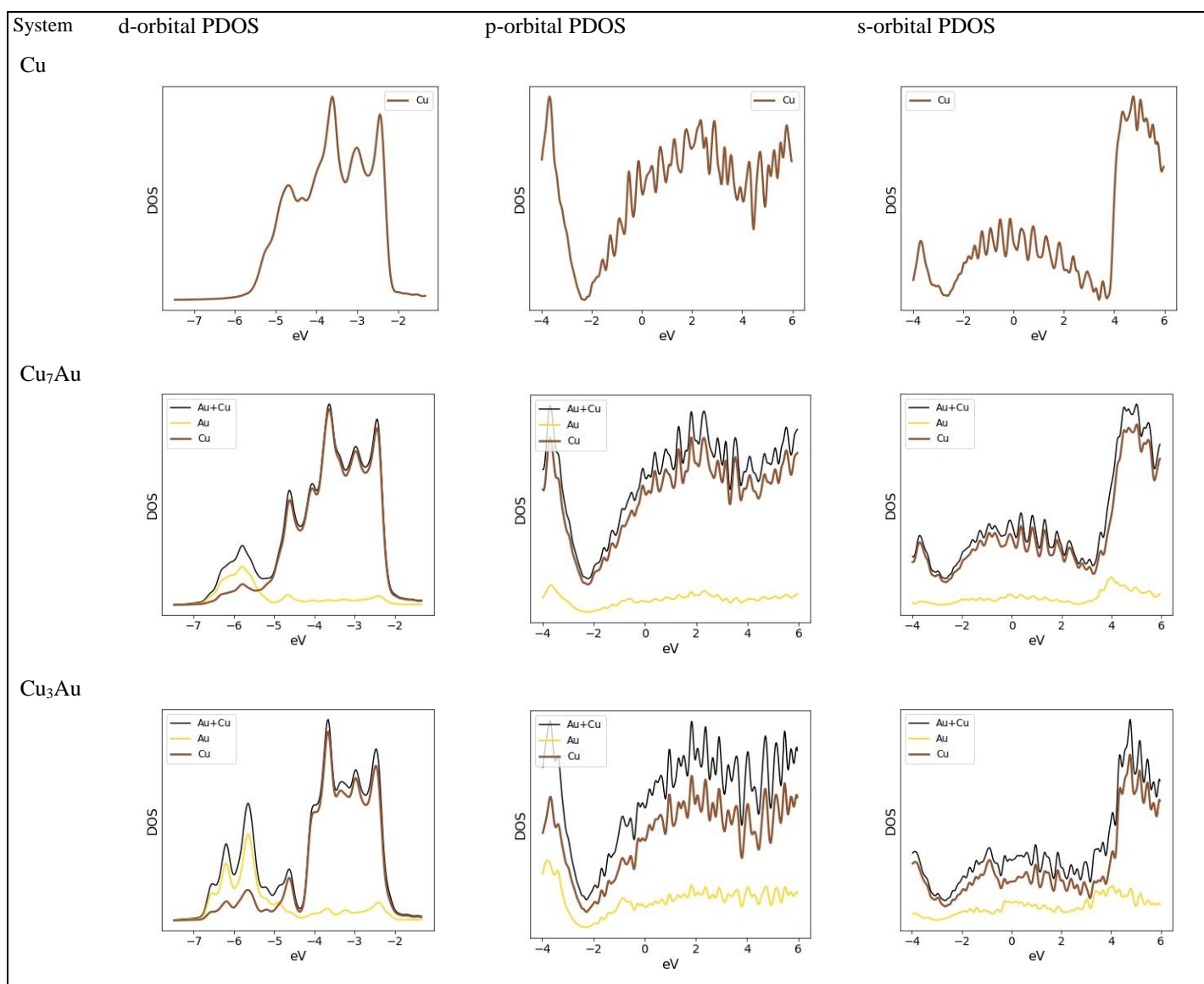
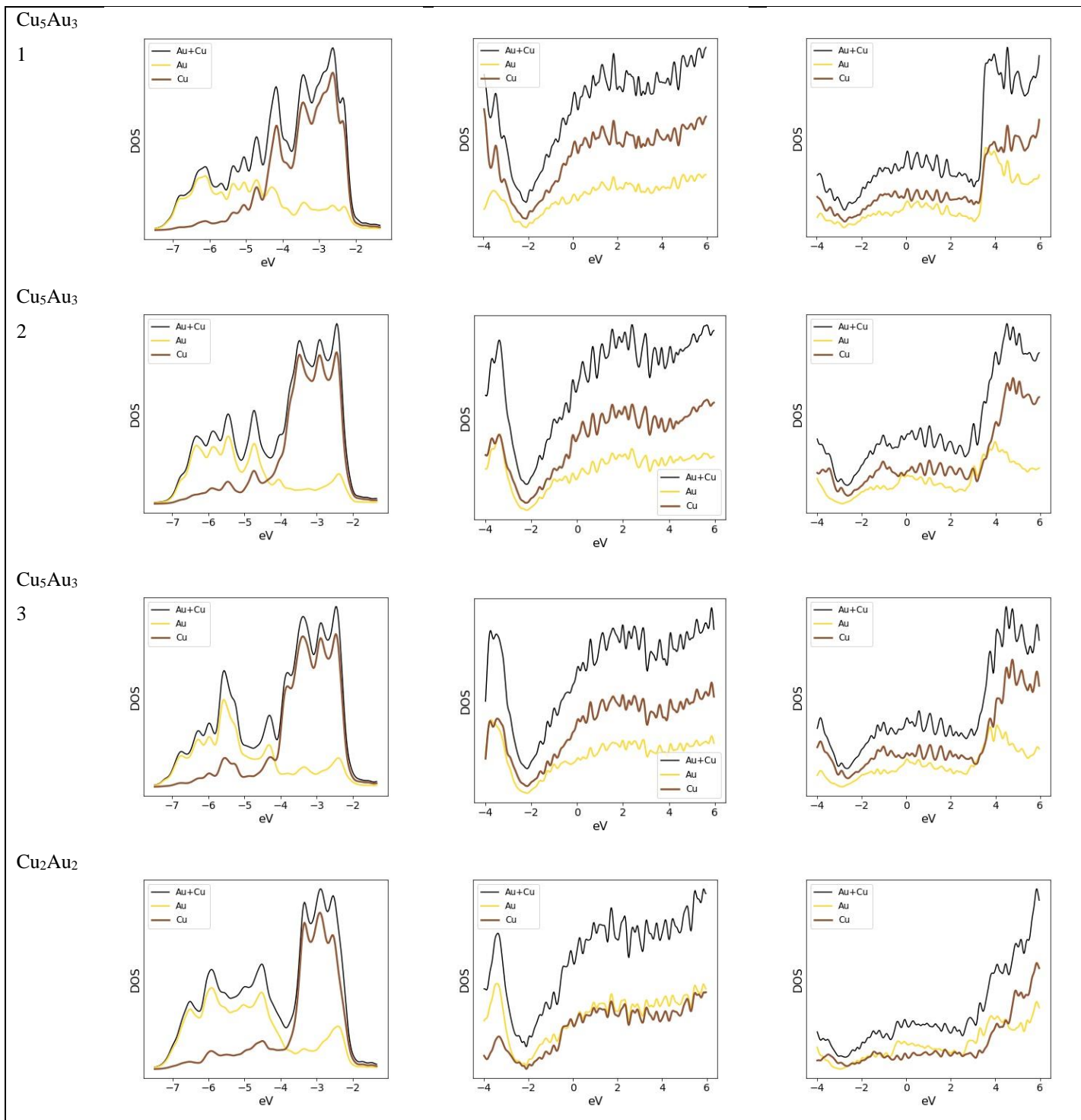
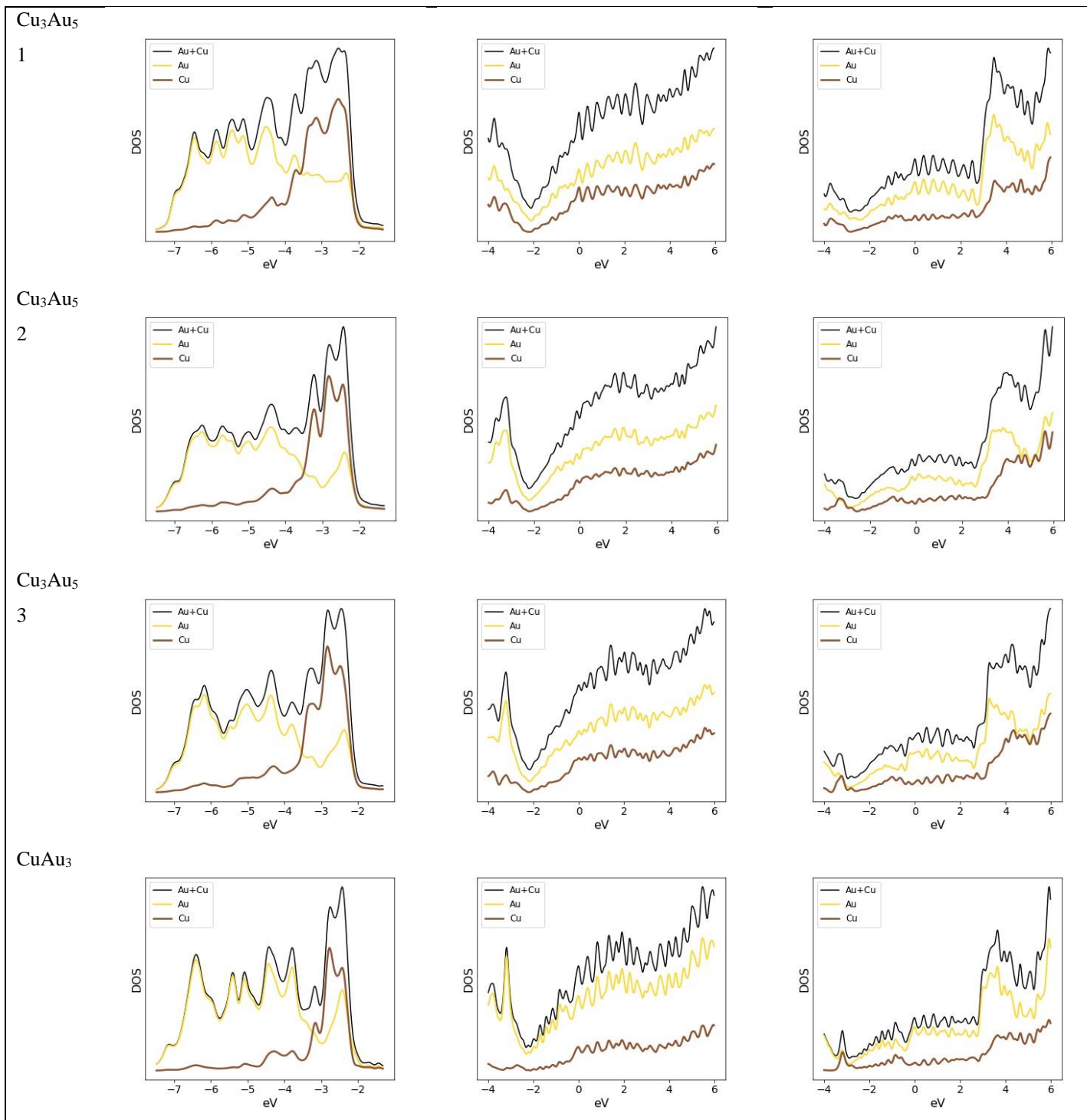


Table A2. Element resolved projected density of states for the Cu-Au alloy system. The projected density of states is not normalized with respect to the orbital type so results are comparable only between the same orbital type. The results are obtained using GLLB-SC functional.







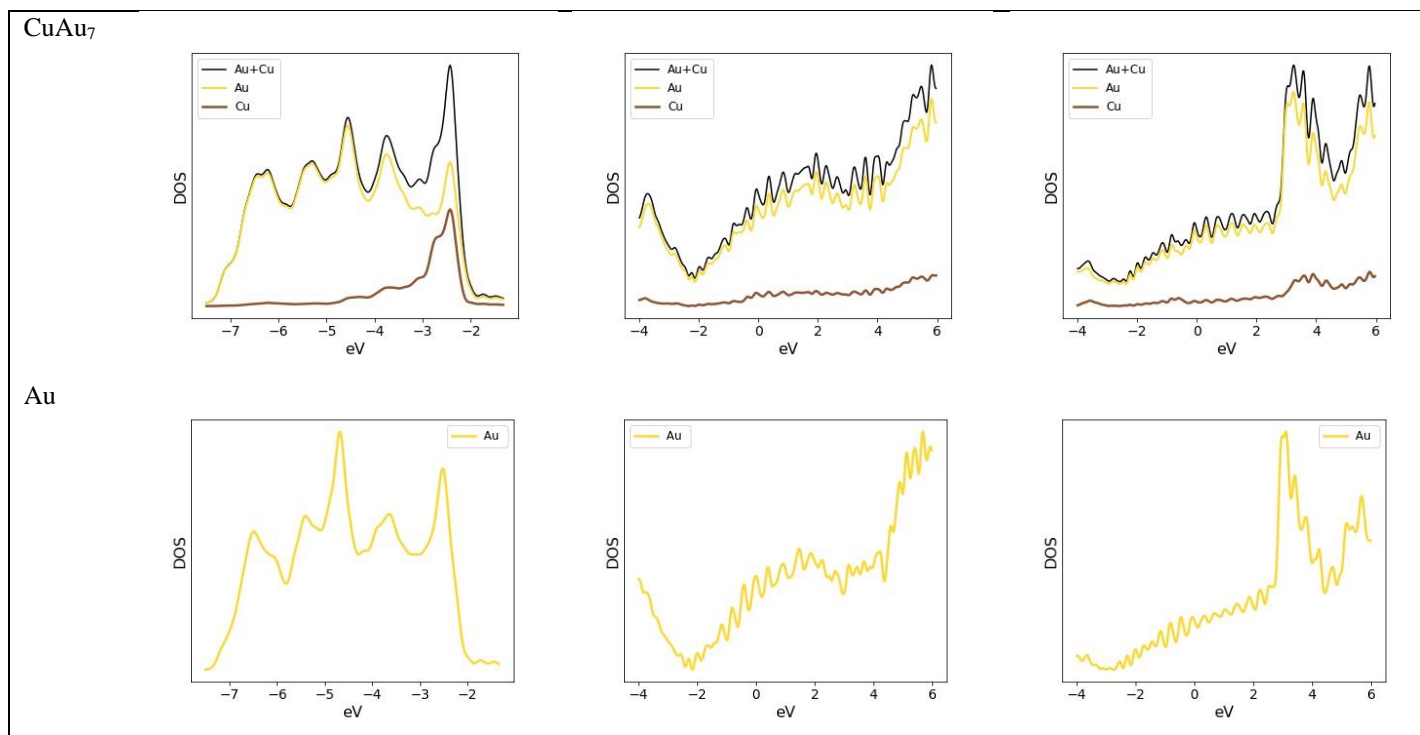
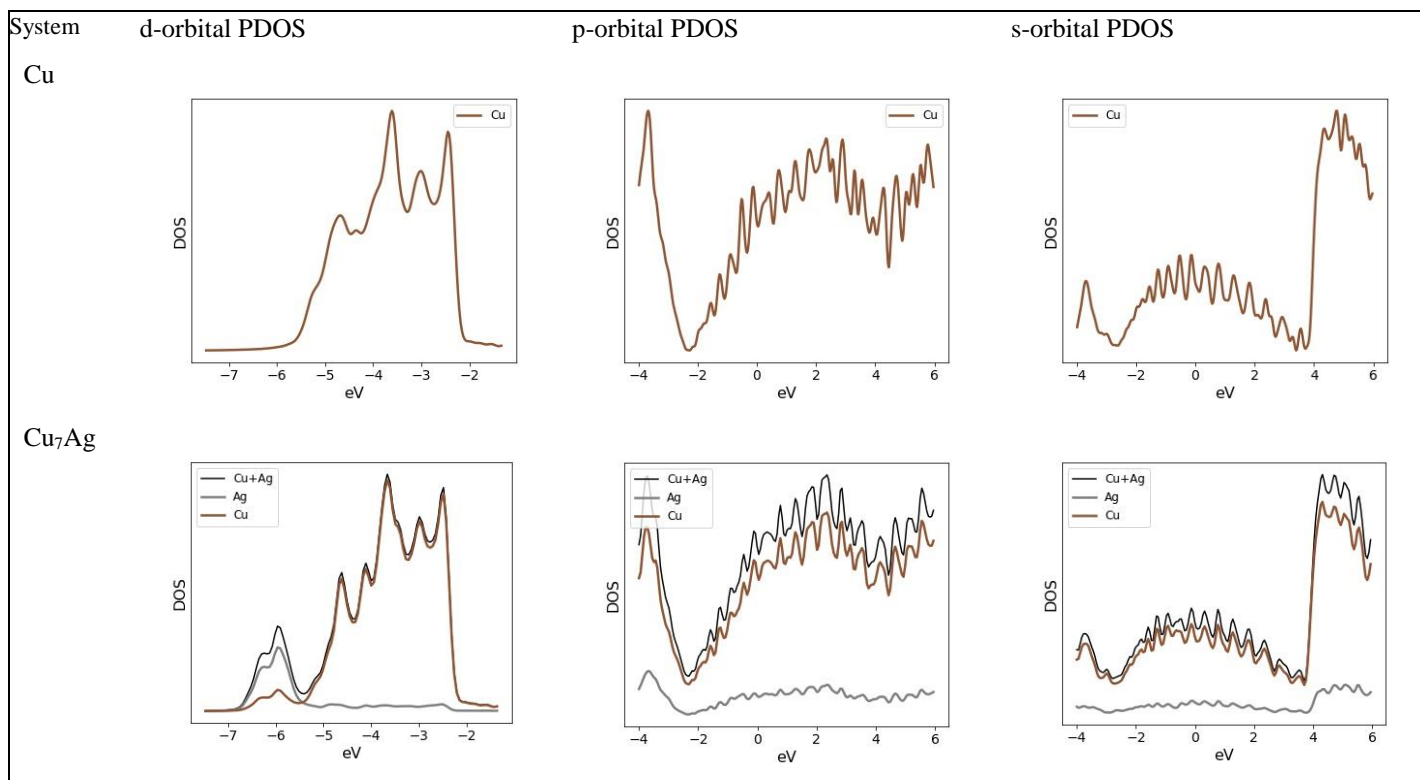
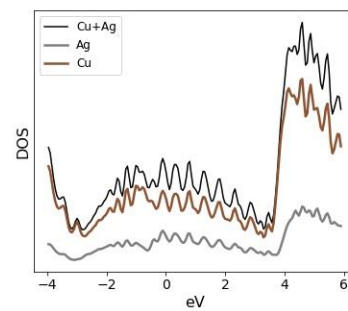
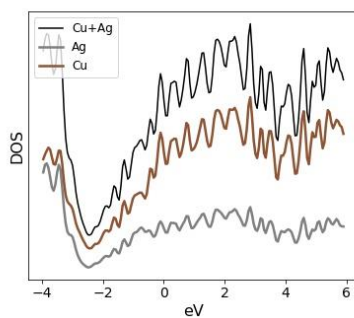
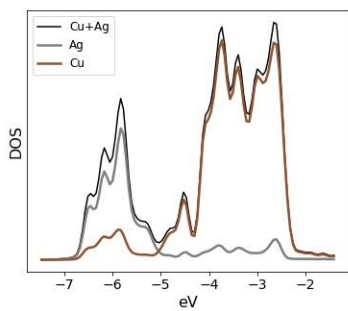


Table A3. Element resolved projected density of states for the Cu-Ag alloy system. The projected density of states is not normalized with respect to the orbital type so results are comparable only between the same orbital type. The results are obtained using GLLB-SC functional.



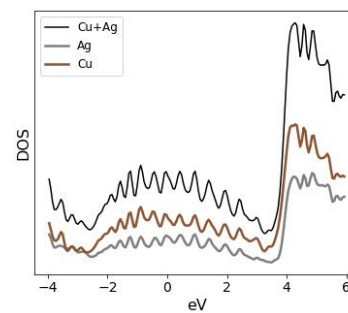
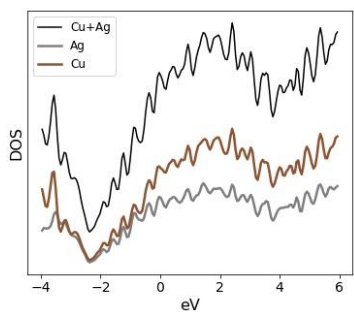
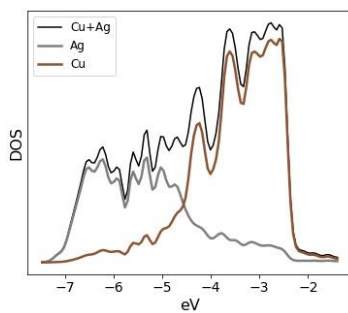


Cu<sub>3</sub>Ag



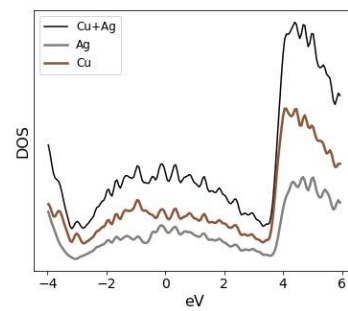
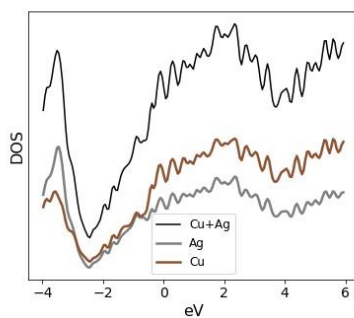
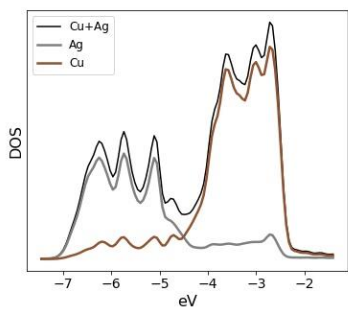
Cu<sub>5</sub>Ag<sub>3</sub>

1



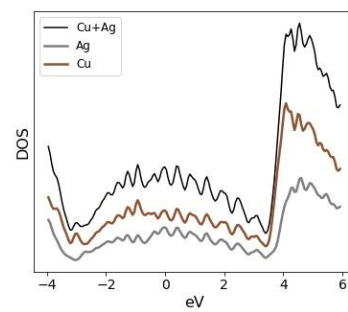
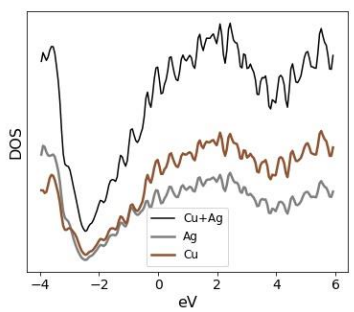
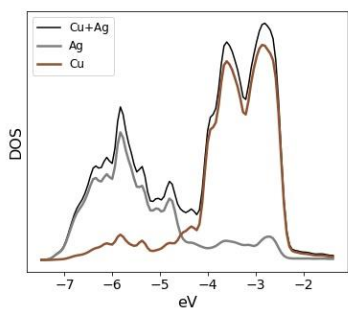
Cu<sub>5</sub>Ag<sub>3</sub>

2

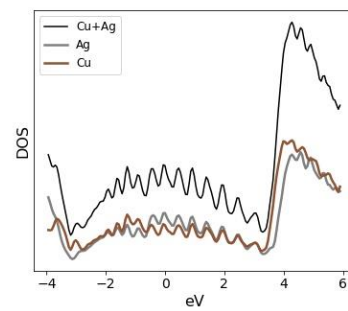
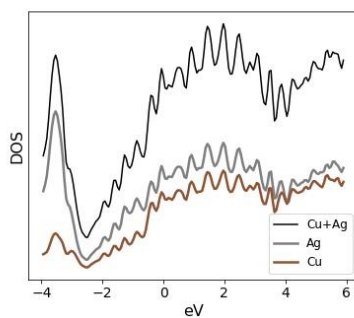
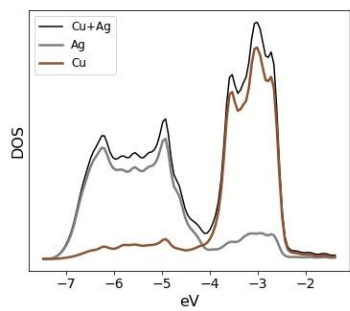


Cu<sub>5</sub>Ag<sub>3</sub>

3

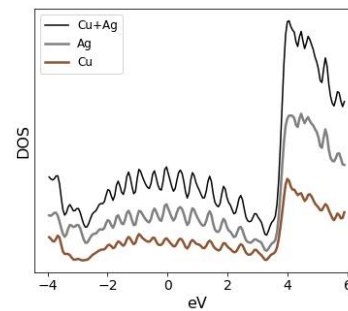
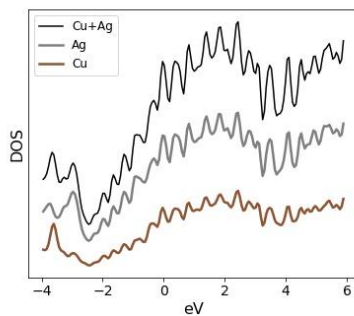
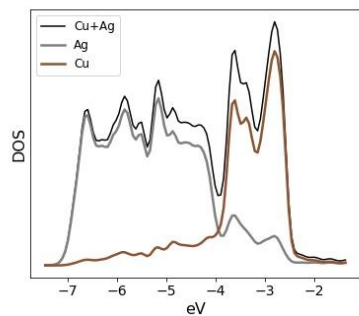


$\text{Cu}_2\text{Ag}_2$



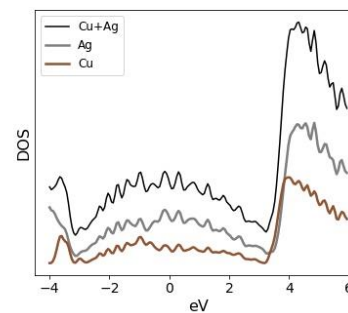
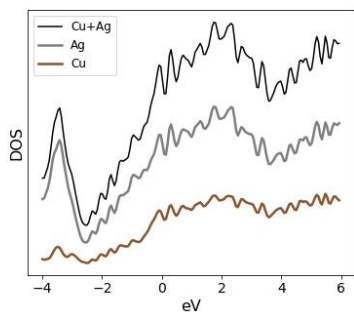
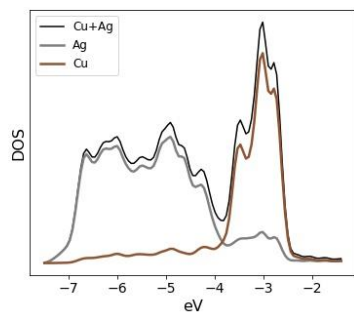
$\text{Cu}_3\text{Ag}_5$

1



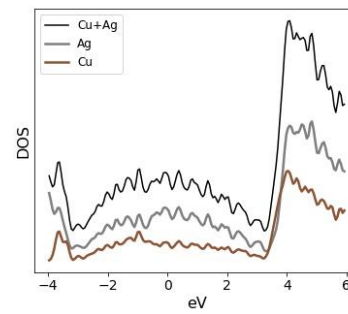
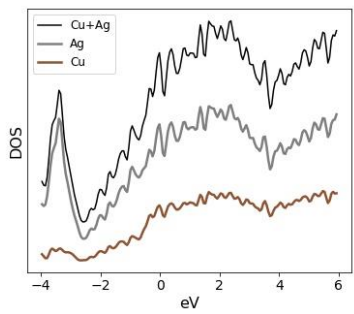
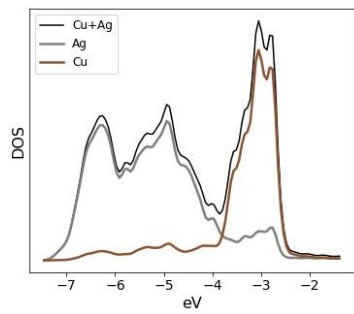
$\text{Cu}_3\text{Ag}_5$

2



$\text{Cu}_3\text{Ag}_5$

3



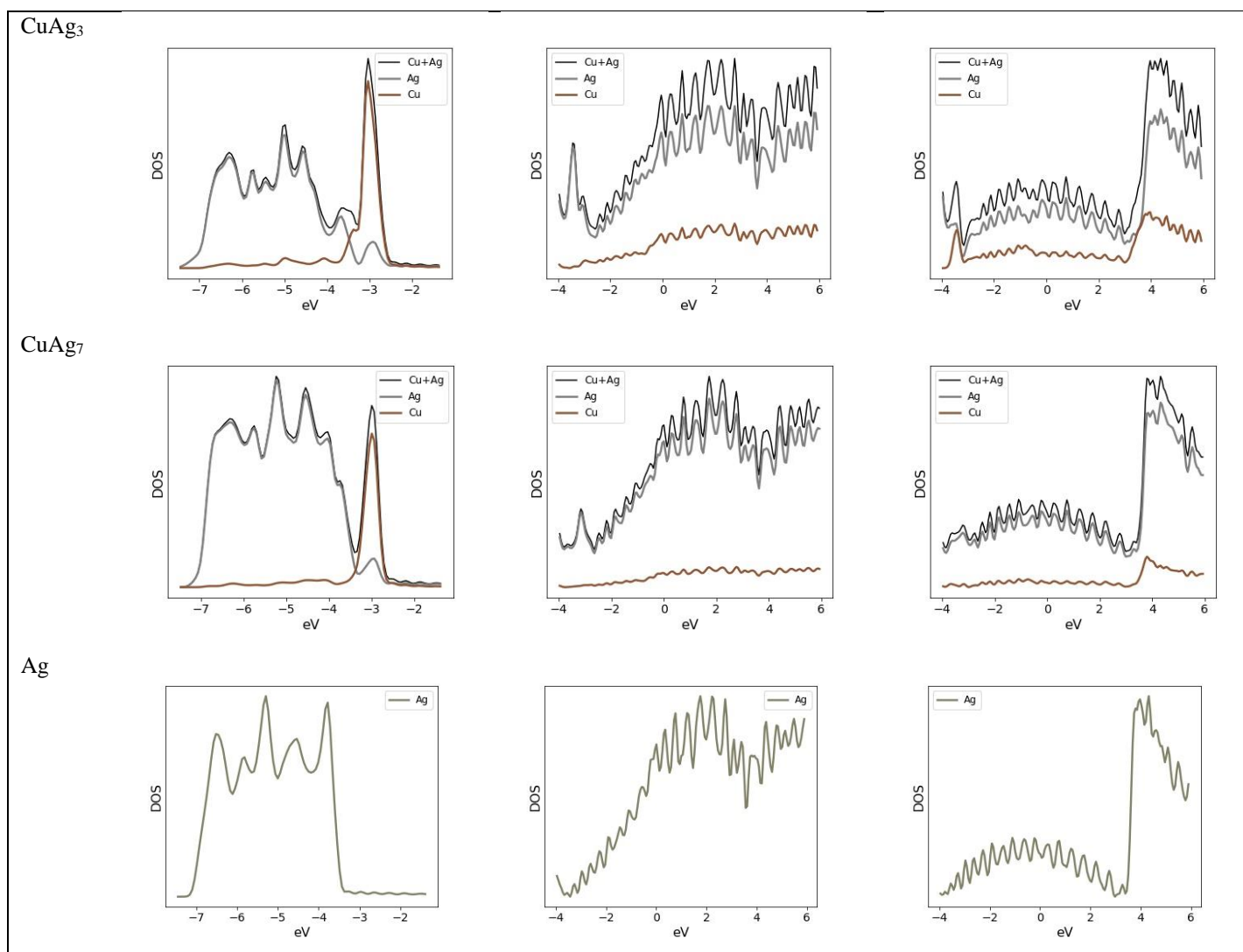
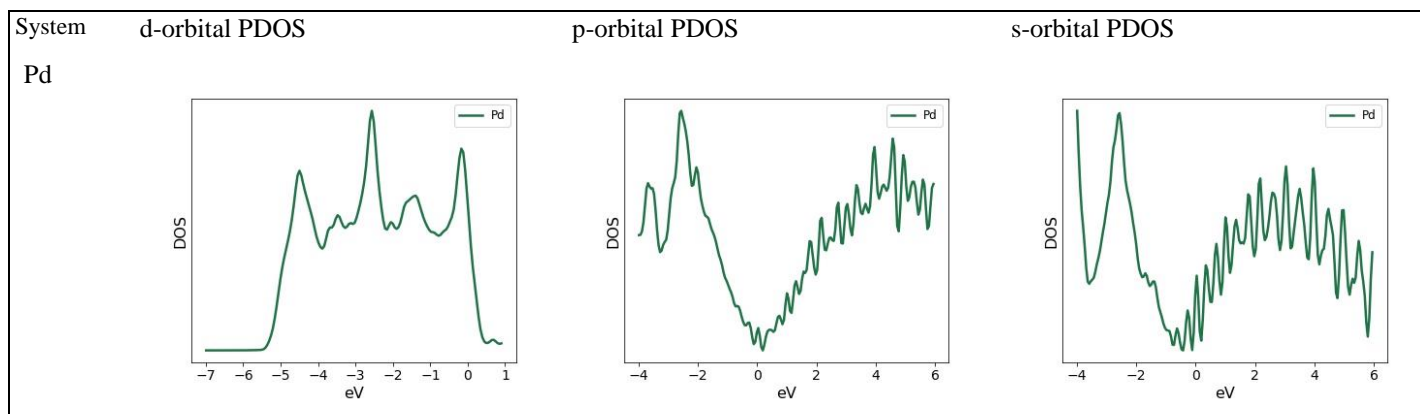


Table A4. Element resolved projected density of states for the Pd-Au alloy system. The projected density of states is not normalized with respect to the orbital type so results are comparable only between the same orbital type. The results are obtained using GLLB-SC functional.

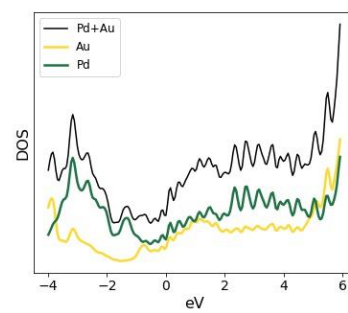
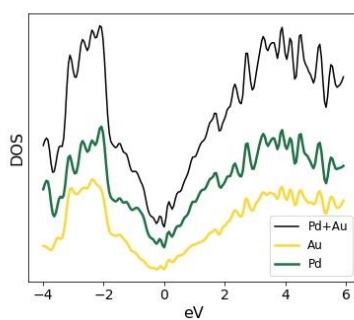
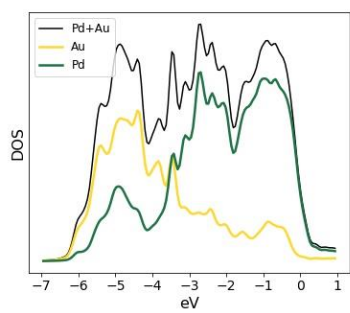




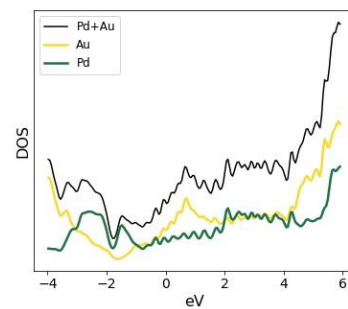
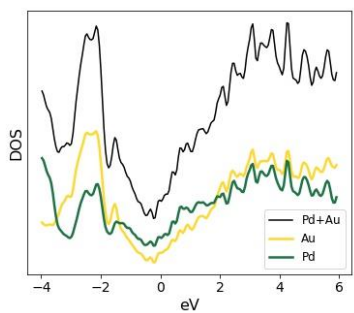
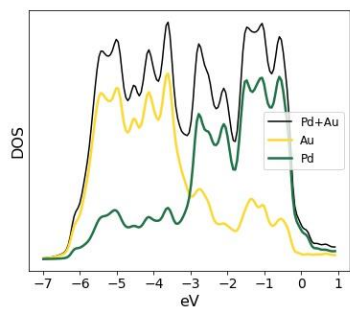


Pd<sub>5</sub>Au<sub>3</sub>

3

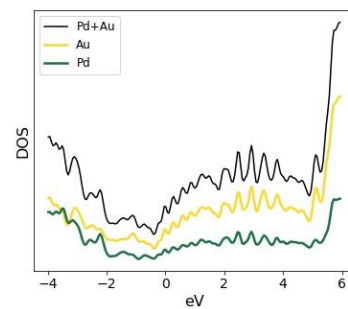
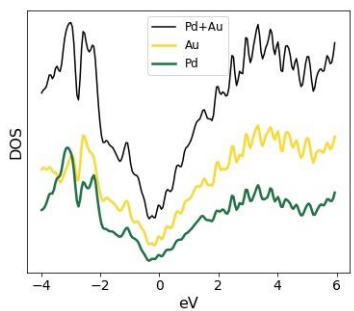
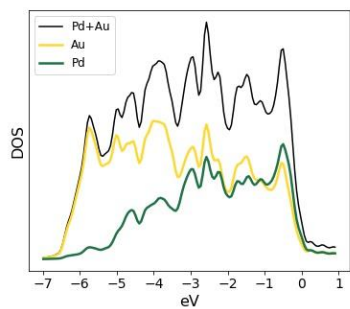


Pd<sub>2</sub>Au<sub>2</sub>



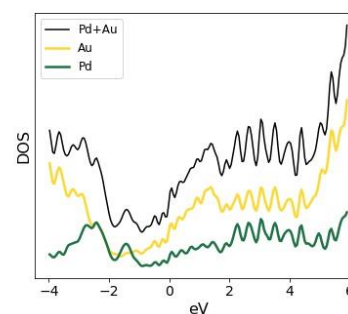
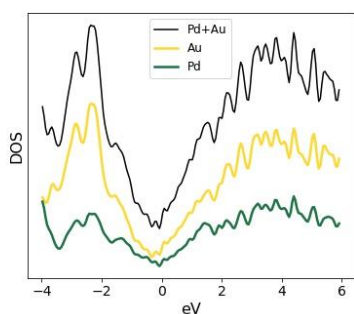
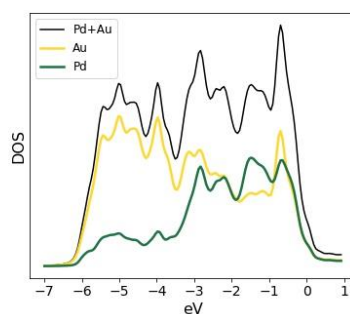
Pd<sub>3</sub>Au<sub>5</sub>

1



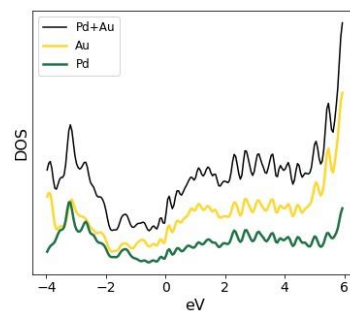
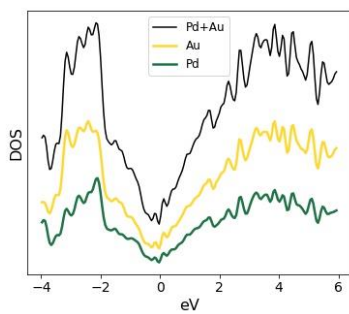
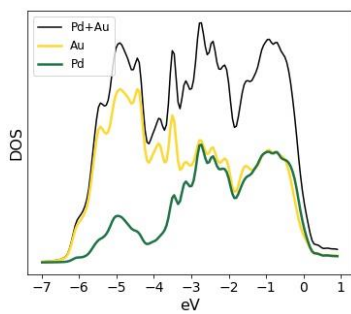
Pd<sub>3</sub>Au<sub>5</sub>

2

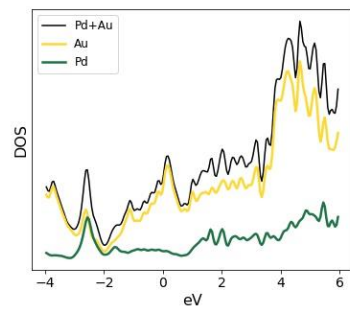
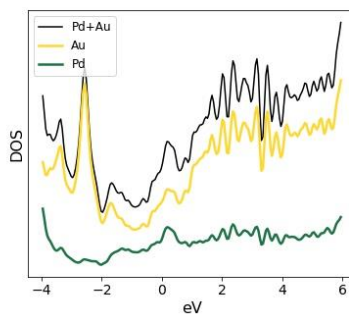
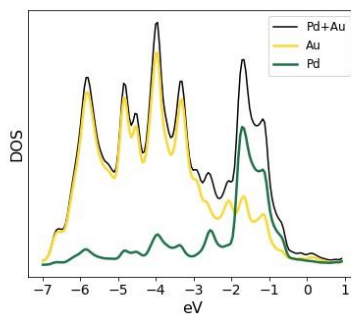


Pd<sub>3</sub>Au<sub>5</sub>

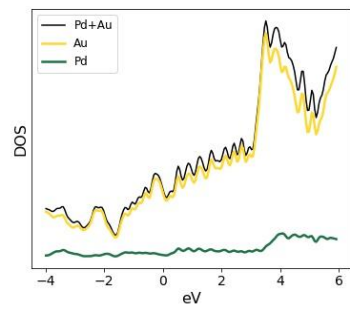
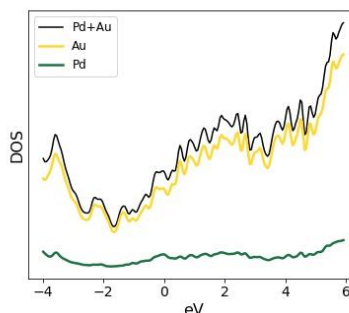
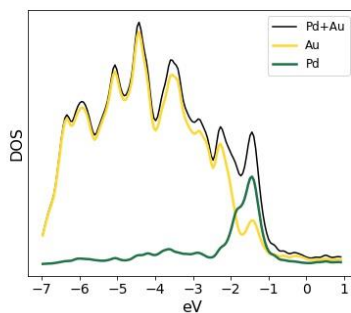
3



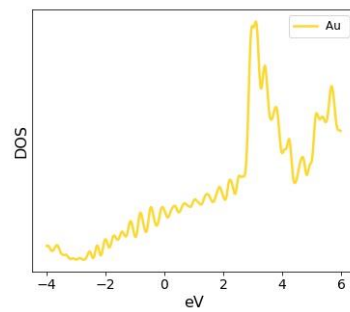
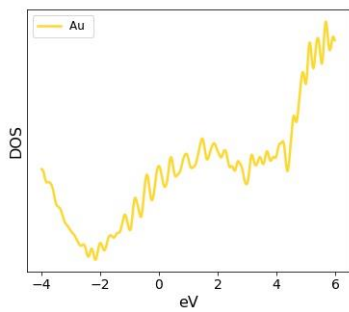
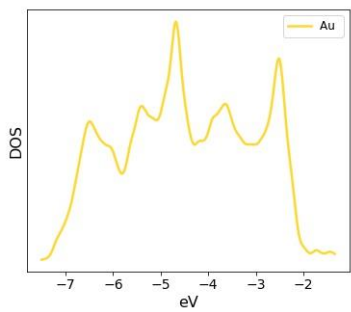
PdAu<sub>3</sub>



PdAu<sub>7</sub>



Au



## § 10. CURRICULUM VITAE

### Work experience

- Senior professional associate at the National Institute of Chemistry, Department of inorganic chemistry and technology, Ljubljana, Slovenia (June 2024-present)
- External associate at the Laboratory for Optics and optical thin films, Materials physics department, Ruđer Bošković Institute, Zagreb, Croatia (December 2023-present)
- Visiting researcher at the National Institute of Chemistry in Ljubljana, Slovenia (November-December 2023)
- Research Assistant at the Laboratory for Optics and optical thin films, Materials physics department, Ruđer Bošković Institute, Zagreb, Croatia (June 2018-December 2023)
- Student assistant lecturer at the courses Organic chemistry Lab 2 (2016-2017) and Molecular modelling (2013-2014)

### Education

- PhD course in chemistry at the Faculty of science, University of Zagreb (2018-today)
- Masters in chemistry at the Faculty of science, University of Zagreb (2014-2017)
- Baccalaureate in chemistry at the Faculty of science, University of Zagreb (2010-2014)

### Acknowledgements and awards

- Author of two papers that received the “Best scientific papers of year 2021” award by Ruđer Bošković Institute (2022)
- Rector’s award for individual scientific work (2016)
- Award for student’s scientific work by the Department of Chemistry (2016)
- Special Rector’s award for a group project (2013)

### Publications

- Author of **11 scientific papers**, including the one published in the prestigious journal Applied Catalysis B: Environment and Energy

### Poster presentations

- First author of **11 poster presentations** which includes the presentation titled “Tuning the plasmonic properties by alloying: Insights from a DFT approach” chosen in the hot topic category for 2021 MRS Fall Meeting, Boston, Massachusetts, USA (2021)
- Coauthor of **4 poster presentations**

### Oral presentations

- First author of **9 oral presentations** including the invited lecture titled “Hybrid metal nanoislands as plasmon-based sensors” at the 8th International scientific Meeting on Vacuum Science and Technique (2022)
- Coauthor of **3 oral presentations**

### Other notable activities and achievements

**Science popularization** by taking part in projects Magic in science (2010-2011), Open Chemistry day (2013-2016) and Open day of Ruđer Bošković Institute (2019); scientific communication and popularization at 3 radio and TV shows (2023); **Reviewer for journals** Sensors and actuators B: Chemical (2024), Scientific reports (2024) and Chemistry in industry (2019); **Training and specialization** at 4 workshops and 3 winter/summer schools; **Elected as Assistant council representative** for the department of Materials physics at the Ruđer Bošković Institute (2022); **Member of the organizing committee** for the Workshop on Solar Energy Materials (2019)

---

**List of publications (WoS):**

1. M. Bubaš, J. Sancho-Parramon, *Journal of Physical Chemistry C* **125** (2021) 24032–24042
  2. M. Bubaš, J. Sancho-Parramon, *Journal of Physical Chemistry C*, **128** (2024) 3924–3934
  3. M. Bubaš, V. Janicki, S. A. Mezzasalma, M. C. Spadaro, J. Arbiol, J. Sancho-Parramon, *Applied Surface Science* **564** (2021) 1520260
  4. M. Bubaš, I. Fabijanić, A. Kendel, S. Miljanić, M. C. Spadaro, J. Arbiol, V. Janicki, J. Sancho-Parramon, *Sensors and Actuators B: Chemical* **380** (2023) 133326
  5. M. Tkalčević, I. Periša, K. Marušić, K. Salamon, M. Bubaš, S. Bernstorff, M. Mičetić, *Sensors and Actuators A: Physical*, **363** (2023), 114745
  6. L. Matasović, B. Panić, B. Matej; H. Vancik, I. Biljan, I. Rončević *Journal of Materials Chemistry C*, **10** (2022), 14; 5433-5446
  7. K. Lorber, J. Zavašnik, J. S. Parramon, M. Bubaš, M. Mazaj, P. Djinović, *Applied Catalysis B: Environmental*, **301** (2021), 120745, 11
  8. I. Fabijanić, M. Mičetić, M. Bubaš, V. Janicki, S. Bernstorff, J. S. Parramon, *Surf. Interfaces*, **27** (2021), 101483, 6
  9. M. Tkalčević, J. S. Parramon, L. Basioli, M. Bubaš, G. Dražić, P. Nadazdy, P. Siffalovic, M. Mičetić *Microporous and Mesoporous Materials*, **325** (2021), 111306
  10. M. Tkalčević, L. Basioli, K. Salamon, I. Šarić, J. S. Parramon, M. Bubaš, I. Bogdanović-Radović, S. Bernstorff, Z. Fogarassy, K. Balazsi, Katalin Soar. *Energy Materials and Solar. Cells*, **218** (2020), 110722
  11. I. Fabijanić, V. Janicki, J. Ferré- Borrull, M. Bubaš, V. Blažek Bregović, L. F. Marsal, J. S. Parramon, *Coatings*, **9** (2019), 382
-